Universitat de Girona

ANALYSIS AND SIMULATION OF TRANSVERSE RANDO FRACTURE OF LONG FIBRE REINFORCED COMPOSITES

Daniel TRIAS MANSILLA

ISBN: 84-689-3089-X
Dipòsit legal: GI-764-2005
http://hdl.handle.net/10803/7762

Universitat de Girona
Escola Politècnica Superior
Dep. d'Enginyeria Mecànica i de la Construcció Industrial

Analysis and Simulation of Transverse Random Fracture of Long Fibre Reinforced Composites

Ph. D. Thesis

Daniel Trias Mansilla

January 2005

The present work has been funded by the Universitat de Girona under research grant BRAE00/02. Also, it has been partially funded by the Spanish Government under research projects MAT2000 − 00741−C02 − 01 and MAT2003 − 09768−C03 − 01.

The research stays of the author at the University of California at Berkeley (UCB), Technische Universität Hamburg-Harburg - TUHH (Technical University Hamburg-Harburg, Germany) and Politeknika Łódźka (Polytechnical University of Lodz, Poland) have been economically funded, respectively, by Patronat de l'Escola Politècnica Superior of the University of Girona, the program Sonderforschungsbereich 371 "Micromechanics of Multiphase Materials" at TUHH, and University of Girona.

Agraïments - Aknowledgements

The subject of this work starts from the ideas of my thesis advisors, Dr. Josep Costa Balanzat, Associate Professor of the Department of Physics, University of Girona and Dr. Jorge Eduardo Hurtado Gómez, professor at the National University of Colombia at Manizales ,who detected the industrial and scientific interest in relating the behavior of composite materials and the random distribution of the fibre within them. The support and ideas of both have influenced the development of the present thesis and I render thanks to them.

A l'Universitat de Girona he tingut la possibilitat de treballar amb membres del Departament de Física, Departament d'Enginyeria Mecànica i de la Construcció Industrial i del grup de recerca AMADE, que en tot moment han facilitat la meva feina. En especial, haig d'agraïr l'amistat, complicitat, disposició i bons consells de Joan Andreu Mayugo, a Norbert Blanco per ser més que un company, a Victor Martínez, per ser tot un personatge, i a Albert Turon, Pere Maimí, Benigne Corbella, Sergi Ortiz, Marc Masó i Pep Vicens, per crear un molt bon ambient de treball. Dins l'Universitat de Girona també haig d'agraïr al Servei de Microscòpia, especialment a Jordi Blàvia i Dani Fernández la seva ajuda i bons consells, a Rafa García i Cristina Roura, del Grup de Robòtica i Visió per Computador, la bona feina feta amb el programes de mosaiquing i de tractament d'imatges i a Vera Pawlowsky per atendre les meves consultes estadistíques amb tanta amabilitat.

During the years I have been working in my Ph.D. degree I have been lucky to establish some interesting and advantageous scientific contacts in different universities. I must express here my gratitude to professor Robert L. Taylor and Ignacio Romero, at the University of California at Berkeley, to Andreas Gägel, Bodo Fiedler and Karl Schulte at Technische Universität Hamburg-Harburg, to Marcin Kamiński at Politeknika Łódźka, to Sergio Oller and Fernando Zalamea at Universitat Politècnica de Catalunya. Also, I must express my aknowledgements to the composites group in the University of Porto for providing some of the materials analyzed in this work.

Per sort, durant aquest temps també m'han acompanyat molts amics, especialment en Quim, amb qui he compartit grans (bons i menys bons) moments, cerveses i sol·lituds, la Maria Luisa, companya de cafès, confessions i cinema, i també en Miquel, la Cristina, en Xavier Martinez-Falero ("Fafa") i en David, amb els que sempre he pogut comptar.

Sense cap mena de dubte no hauria arribat a assolir aquesta fita sense l'ajut de la meva família: els meus pares, Eduard i Joana, que han confiat sempre en mi, i els meus germans, Rosalia i Albert, amb qui he viscut tants moments inesborrables.

And last but not least, haig d'agraïr a l'Airu haver suportat les meves absències durant aquests darrers mesos, encomanar-me el seu llenguatge, i haver-me obert les portes del seu petit món.

Contents

List of symbols

NOTE: The Greek letter *sigma* is used traditionally in both Mechanics and Statistics with different meanings. While in Mechanics denotes *stress* in Statistics denotes the standard deviation or the variance (if squared). The author has preferred to keep this usual notation and to avoid confusion a *sigma* with any subscript (σ_{ij} or σ_i) will denote a stress component, a boldface *sigma* ($\boldsymbol{\sigma}$) will denote the stress tensor, and when denoting the standard deviation or the variance it will appear as an operator: $\sigma(\cdot)$, for instance $\sigma(x)$, $\sigma^2(x)$.

Acronyms

APTA	polyoxy propyleneamine
CFRP	Carbon fiber reinforced polymer
CSR	Complete Spatial Randomness
CDF	Cumulative distribution function
DDS	4,4-diaminodiphenyl sulphone (curing agent)
DGEBA	Diglycidyl ether of bisphenol A (epoxy)
DETA	Diethylenetriamine (curing agent)
ECA	Embedded Cell Approach
FEM	Finite Element Method
MHPA	HY 917, produced by Ciba-Geigy (curing agent)
RVE	Representative Volume Element
RCP	Random Close Packing
ROM	Rule of Mixtures
SRVE	Statistical Representative Volume Element
TGDDM	Tetraglycidyl-4,4-diaminodiphenyl methane epoxy

Mechanics symbols

E	Young's elasticity modulus
ν	Poisson's ratio
$E^{(f)}, E^{(m)}$	Young's elasticity modulus of the fibre and matrix, respectively
λ, k, μ	Lamé constants
σ_{yc}	Material compression yield limit
σ_{yt}	Material tension yield limit
$\boldsymbol{\sigma}$ with components σ_{ij}	Stress tensor
$\sigma_1, \sigma_2, \sigma_3$	Principal components of the stress tensor.
$\boldsymbol{\varepsilon}$ with components ε_{ij}	Strain tensor
$\mathbf{s}$ with components s_{ij}	Deviatoric stress tensor
$\mathbf{e}$ with components e_{ij}	Deviatoric strain tensor
$\mathbf{u}$ with components u_i	Displacement vector
$\mathbf{C}$ with components C_{ijkl}	Elastic constitutive tensor
$\mathbf{S}$ with components S_{ijkl}	Compliance constitutive tensor
$\mathbf{L}$	Elasticity matrix, following Hill's notation
$\mathbf{M}$	Compliance matrix, following Hill's notation
$\delta = L/r$	Dimensionless parameter to measure the Representative Volume size
L	Length of the side of the Representative Volume Element
d	Fiber diameter
r	Fiber radius
ρ	Density of the material
v_f	Fibre volume fraction
U_v	Dilatational energy density
U_d	Distortional energy density
I_1	First invariant of the stress tensor
$\langle I_1^0 \rangle$	Mean of I_1 in the matrix of a microstructure model with arbitrary value of the boundary conditions.

Statistics symbols

$\mu(x), < x >, \bar{x}$	Mean of the random variable x
$\sigma^2(x), \mathrm{Var}(x)$	Variance of the random variable x
$\sigma(x)$	Standard deviation of the random variable x
$B(h)$	Covariance function of a second-order stationary field or stationary variance
τ_r	r-th moment
λ	Poisson parameter
$K(h)$	Second-order intensity function or Ripley's K-function
$g(h)$	Pair distribution function
$D(h)$	Nearest-neighbor distribution function
$d(h)$	Nearest-neighbor density function
$D^k(h)$	k-th Nearest-neighbor distribution function
α, β	Parameters of a Weibull function
α^0, β^0	Parameters of a Weibull function, obtained from a microstructure model with arbitrary value of the boundary conditions.

List of Figures

List of Tables

List of Algorithms

Chapter 1

Introduction and objectives

1.1 Composite materials: a brief historical perspective

Composite materials are new materials obtained from the mixture of different materials during the manufacturing process. That is, the material is created at the same time that the mechanical or structural component is manufactured. This availability of designing and creating a new material opens a wide range of possibilities for the mechanical engineer and, since the material design implies the choice of a set of desired material properties, changes somehow the entire design process.

The key material properties for usual engineering mechanics applications are: *stiffness*, which could be defined as the capacity of the material to offer resistance to be stretched or compressed; *strength* or the capacity of the material to avoid being broken; and the *density* or weight per unit volume. When designing a mechanical component, the engineer considers which loads or forces (wind, reactions from other components, weights,...) will act on it and, considering the geometry restrictions, looks for a material stiff enough to avoid deformations or strains which would make the component not useable and strong enough to avoid breakage, under the considered loads. The weight of the component is very important in the case of dynamic applications (components of engines, energy generators, blades,...) and, depending on the used material, even in static applications (edification components, for instance).

Historically, metals (specially in machines and tools) minerals and ceramics (specially in edification) have been used as engineering materials. The designer chose what he thought was the most convenient material for each application and could improve slightly its properties with some treatments (usually thermal treatments based on heating and cooling at definite temperatures and times). The in-depth study of this treatments, which are usually closely-related to the atomic arrangements of the material, is one of the classic fields of the Materials Science.

But, by the first half of the 20th century a new methodology appears with the steel reinforced concrete[1], which may be seen as the first wide-used *artificial* composite mate-

[1] Concrete itself can be seen as a composite, since it is a mixture of stones, called aggregate, and cement,

rial. The combination of steel and concrete allowed engineers to take advantage of the more useful properties of each one: high stiffness and strength (in the case of steel) and reasonably low weight (concrete). Due to its low density, concrete can be used in bulk to provide the structure of the required dimensions and geometry and steel is used to reinforce it only with the necessary amount and direction. Since a *new material* can be designed for each component of the edification the possibilities increase immensely and a more efficient design can be obtained: if material meets better the necessities of the application the cost (the material itself and sometimes the production) decreases.

Nevertheless, some applications, specially aircrafts, need stiffness-weight ratios which clearly cannot be provided with concrete. By the 1940s industry was capable to produce new *artificial* materials: plastics or polymers. These have normally low stiffness but, very reduced weight. In the early 1960s carbon fibres, which have very high stiffness, were developed in UK and started to be used in combination with polymers in aviation industry. Since aircraft components normally have more complex geometries than those used in edification, the possibility of composite materials of *designing* the material together with the component turns out to be even more attractive.

The application of composite materials, specially long fiber reinforced polymers, has experienced a great increase and nowadays are widely used in some industries, like aircraft and wind turbine components, but also in leisure applications like sportive cars and crafts. Generally, composites are used to improve stiffness/weight or strength/weight ratio of structural members. For this reason and its undeniable industrial usefulness, composite materials are taught in many under-graduate and graduate courses in universities around the world, and there exist many descriptive textbooks which cover the generalities like the one by Matthews and Rawlings [103], their mechanic behavior like those by Christensen [38] and, recently, by Kollár and Springer [91], among many others.

1.2 Manufacturing of composite materials

Long fibre composites are usually made with carbon or glass fibers embedded in a polymer, commonly epoxy. The fibers are stiff and have high strength and they are expected to carry the loads to which the component or structure is submitted. The matrix has low stiffness and low strength and it gives the shape to the component but also, and this is an important task, it transfers the loads to the fibers and between them.

A single layer of composite have a width of about $0.05 - 0.2mm$, and, consequently, in order to obtain usable engineering mechanics components, some layers have to be stacked to form a *lamina*, as shown in Figure 1.1. A lamina with fibers in an only direction is called a unidirectional lamina. Usually, laminae with fibers in different directions are used to form a laminate. The directions of the fiber in each part of the mechanical component can be chosen by the designer to give the component a better efficiency in cost or weight.

---

which holds them together

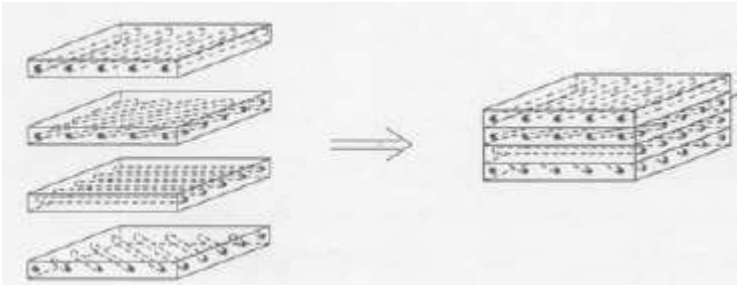

Figure 1.1: Stacking of single laminae (left) form a laminate (right) (Figure taken from Kollar and Springer [91])

One of the basic methods of fabrication of a laminate is to spread the fibers, which are normally distributed in rolls of layers, following a stacking sequence, which is defined in the design process, over a mold and then, to pour the liquid epoxy mixed with some curing agent. The pouring of the epoxy on the fibers can be done by several methods: by hand (manually spreading epoxy through the fibre layers) or automatically spreading the epoxy using a vacuum process called Resin Transfer Moulding or RTM. Also, there exist some pre-impregnated tissues of fibres (called *pre-pregs*) which have a small quantity of epoxy soaking the fibres and allow to obtain high volume fractions of fibre. Finally, the liquid epoxy has to cure during some time and controlled temperature and pressure conditions to solidify. Usually the different manufacturing processes lead to slightly different mechanical properties, even using the same constituents, since. In part, these differences are related to the achieved fibre volume fraction or to the presence (or absence) of micro-bubbles or voids. For instance, the combination of a RTM process and pressure controlled epoxy curing can reduce enormously or even eliminate the voids or air micro-bubbles produced by a non-uniform epoxy spreading.

1.3 Mechanical design with composite materials

The usual design criteria for composite materials is based on trying to align the fibers with the most critically loaded directions of the mechanical component. Nevertheless, the behavior of the composite in the transverse or perpendicular plane is also of importance because normally transverse layers are used in the laminate. Also, in applications with non-regular shapes the stress state may vary from a point to another, and some of the layers may be loaded mainly in the transverse direction.

As it was said formerly, long fibre reinforced polymers are today widely used in wind turbines, aircrafts, small or sportive vessels and crafts. Nevertheless there are still many phenomena related to composite materials which are not fully understood and which are the subject of research. Those phenomena may be macroscopical like *damage* (loss of strength and/or stiffness) and *fatigue* (loss of strength under cyclic loads), but also local or microscopical like *delamination* (loss of adherence between laminae), *debonding* (loss of adherence between fiber and matrix) and *matrix cracking*. The main difficulty is that usually these phenomena may take place at the same time and that they are related: fatigue

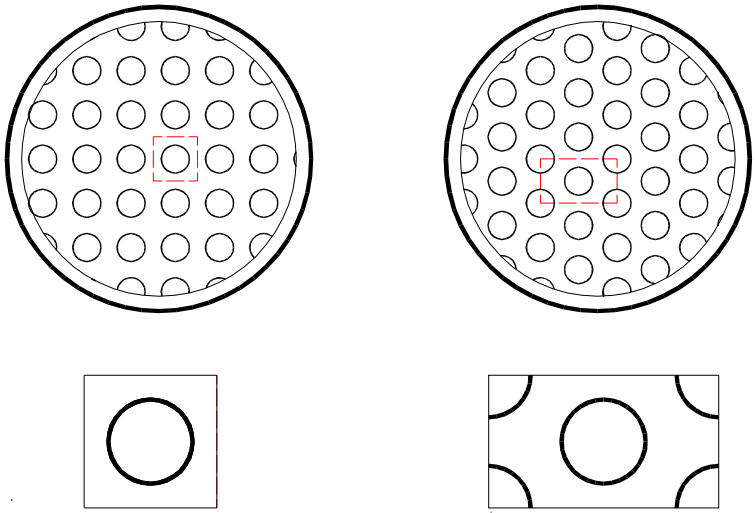

Figure 1.2: Typical composite unit cells (Source: Zalamea [160])

depends on all of them and so, the life prediction of composites with cyclic loads is one of the milestones of the researchers. Furthermore, damage may be seen as the consequence of the combination of matrix cracking, debonding and delamination in different stages of the load application.

According to the existence of two scales, the analysis of composite materials can be undertaken from two different approaches: micromechanical and macromechanical. In the macromechanical approach the properties of the composite are obtained by averaging or smearing and a set of properties similar to that of homogeneous materials is produced. Also failure criteria for the design are normally produced from this approach. Macromechanical analysis requires quite geometrically simple models but is unable to reproduce some of the phenomena related to the constituents and their interface. Another important drawback is that the obtention of the composite properties requires an important amount of experimentation which is usually destructive[2].

Although they may not always provide design criteria, micromechanical models are desirable since they may improve the understanding of the physical mechanisms involved. Classical micro-models have considered regular distributions of the fiber. As shown in Figure 1.2, several distributions which lead to different periodic unit cells can be considered. This periodic models have achieved partially good results but usually results obtained using this periodic models depend on the chosen geometry [129].

On the other hand, the in-depth analysis of these microscale phenomena has to consider the random nature of composite materials. This approach is included into a scientific

[2]In the sense that the samples used for these experiments are broken as a part or as the conclusion of the experiment

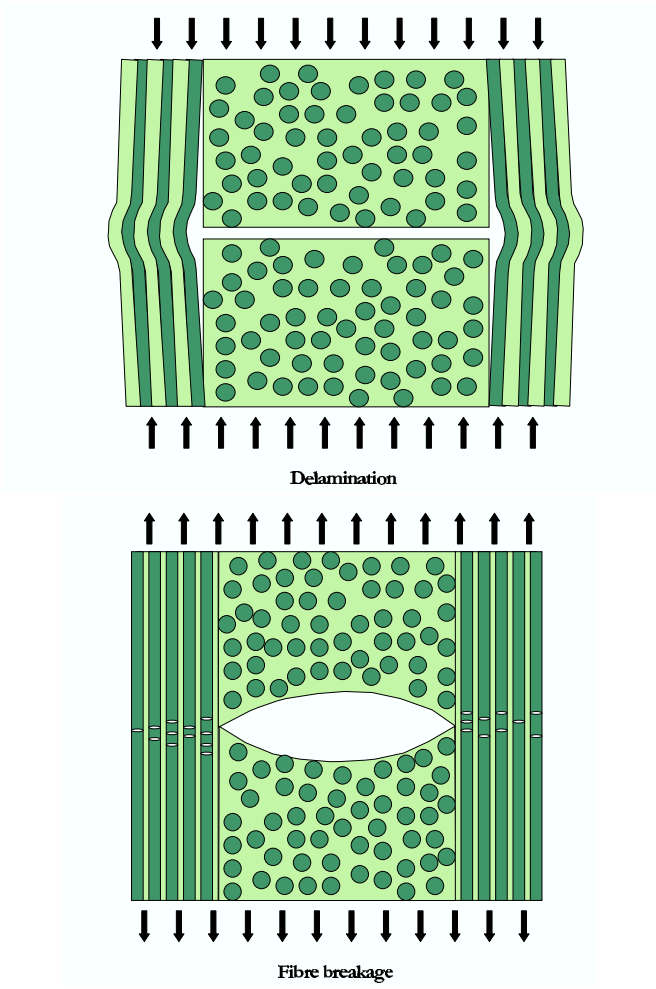

Figure 1.3: Consequences of matrix cracking (Figure concept taken from Gamstedt [56])

area called micromechanics of random media, which has been object of special issues of *Applied Mechanics Reviews* [122], *International Journal of Solids and Structures* [77] and recent books, like the one edited by Jeulin and Ostoja-Starzewski [80]. Some authors, like Matsuda et al. have already observed that [102]:

> Transverse randomness of fibre distribution has small effect in the macroscopical behavior of composite laminates but strong effect in the microstructural stress distributions. Consequently, it is important to consider the randomness of fibre distribution for studying microscopic problems such as interfacial damage, microscopic failure, etc.

Since in usual designs the main loads are parallel to fibre direction, transverse failure of composites is normally not critical but, of course, it has to be verified in the design and also contributes to other degradation phenomena like delamination or fibre breakage, as shown in Figure 1.3.

1.4 Probabilistic methods in engineering mechanics

The analysis of the phenomena just described involves a close understanding of the micromechanical features and the macroscopic performance. The use of microstructural characterization techniques have been widely applied in both traditional and composite materials in extending this understanding. There also exist some interesting books with this scope, focused on composite materials, like the one by Summerscales [143].

As it will be detailed in Section 1.5, the main purpose of this work is to relate the microstructure of the transverse section of long fiber reinforced composites, specially Carbon fiber reinforced polymers (CFRP), with its probability of failure. The field of engineering mechanics which, among many other targets, derives expressions and computational or numerical methods aiming to obtain probabilities of failure and reliability is usually referred as *probabilistic mechanics* or *probabilistic engineering mechanics*.

The importance of probabilistic methods in nowadays computational mechanics is not only proved by the international publication (*Probabilistic Engineering Mechanics* [1]) which shows the existence of a full scientific field, but also by special issues of general computational mechanics publications like *Engineering Fracture Mechanics* [62, 63] or *Computers and Structures* [49]. One of the reasons for this interest on applying probabilisic techniques to the mechanics of engineering materials, as pointed out by Ostoja-Starzewski [62, 63] is because "all fracture processes are characterized, to a greater or lesser extent, by randomness".

Another proof of the industrial interest on this field, is the fact that recently, commercial finite element related companies like ANSYS [4], MSC [3] and Altair [2] have developed modules for probabilistic computing and analysis. In fact, the use of reliability and probability methods in large mechanical systems and production or power plants, is nowadays quite spread. Nevertheless there is still a lot of work to do to approach the available techniques to the industry and engineering, specially in the field of the mechanics of materials.

Probabilistic mechanics usually distinguishes two different sources of randomness within any physical system: external sources and internal sources. Typical external sources are loads such as produced by wind, earthquakes, etc. Internal sources can also by divided into geometric (for instance, any plate manufactured through usual production systems can have considerable variations of its width at the micro-level) and material. This work is focused in a material source of randomness: the distribution of the fibres within the composite at the microscale.

1.5 Objectives

The present work has been developed in the composite materials branch of the research group AMADE (Analysis of Advanced Materials for Structural Design). Provided the research group detected the industrial and engineering interest on finding probability of failure of composite materials , the objectives of this work were established as the follows:

1. To develop a technique of simulation for the failure in the transverse direction of long fibre reinforced composite materials

2. To develop a methodology which allow to obtain statistical information concerning the fibre distribution of the transverse section of composite materials.

3. To analyze the distribution of the fibres in the transverse section of composite materials

4. To simulate through finite element models which correctly represent the randomness due to fibre distribution of the microscale the stress-strain fields present in the transverse section of long fibre reinforced composites, and to compare the results from the simulation of the elastic behavior of a periodic model and a random model to determine if the modelling could affect the failure results.

5. To use the developed technique and the statistical information from the microstructure of the composite material for obtaining the probability of fracture of simple geometries of composite materials.

6. To evaluate the influence of the microstructure on the transverse fracture behavior of the analyzed fibre reinforced composites.

1.6 Thesis layout

This work is divided in three parts. First part includes the state-of-the-art and the theory on which the research work is based.

Chapters 2 and 4 review the different approaches for finding the elastic properties of composite materials through macroscopic and microscopic methods and some approaches which try to find the size of a Representative Volume Element (Chapter 2) and the methods of analysis of random composite materials (Chapter 4). Chapter 3 reviews some macroscale and microscale failure criteria for composite materials.

The chapters included in Part II try to fulfill the objectives described in the former section. Chapter 6 describes the experimental method for microscopy image processing and analysis of carbon fibre reinforced composite materials (Objectives # 2 and # 3). Chapter 5 develops a *Statistical Representative Volume Element* and determines its finite size by analyzing the convergence of some mechanical and statistical variables (Objective # 1).

The periodic modelling and the random modelling of the transverse section of composite materials are compared in Chapter 7. This Chapter may be seen as a motivation or justification of the rest of the work. It could have been placed as the first Chapter of Part II, but since the modelling method is explained in Chapter 5, the author has preferred to place it next to this.

The simulation of transverse random failure of composite materials is achieved in Chapter 8 where the simulation results are compared with some test data provided by the

composites group of the Technical University of Hamburg-Harburg (TUHH).

This work tries to be self-explanatory and, for this reason, Appendixes A and B cover the essentials which may help to understand the main chapters to the reader with some mathematics and engineering background.

In Appendix C the whole set of results of the analysis of digital images of the transverse section of fibre reinforced composites is given.

Part I

Theory review and State-of-the-Art

Chapter 2

Mechanics of Composite Materials

2.1 Composite materials

A composite is a material composed by distinct constituents or phases. Each of these phases can be taken as uniform, with known constitutive properties. Although the number of constituents involved may be greater, in engineering mechanics usually composite materials are manufactured by embedding one material (usually called *the reinforcement*) in another one, called *the matrix*.

Every point of the composite is occupied by some phase (the cavities can be taken into account by including one phase with zero properties), and the phases are taken to be firmly bonded across interfaces. Behavior of individual phases may be nonlinear.

According to Hashin [67] there are two kinds of information which determine the properties of the composite: the internal phase geometry and the physical properties of each phase. Considering the geometry of the phases, composite materials can be classified in particulate materials (in which the reinforcement phase appears in form of particles) or in fibrous materials, in which the reinforcement is in the form of fibres. These fibres can be *short* and have random orientation or can be *long* and have a designed or intentional orientation. Unless it was specified, in this work only long fibre reinforced composites are considered.

2.1.1 Micro, meso and macro scales

In the mechanics of composite materials several length scales may be taken to study. Some models are constructed from the point of view of only one of this scales, but in many cases it is necessary to relate events which happen at different length-scales. According to Alzebdeh and Ostoja-Starzewski [9], when developing computational methods for random composite materials, the three following length-scales have to be taken in account:

Micro-scale This is the scale of the heterogeneity (inclusion, fibre...) and it is usually denoted by d. In this scale each constituent material is homogeneous and the interaction is analyzed together with the stress and strain fields in this scale, which

provide useful information for modelling debonding, crack initiation and damage, etc.

Meso-scale Some models deal with groups of fibres, or with laminae (in long fibre reinforced composites). This scale intermediate scale is usually called *meso-scale*. Also, some computational models [9] [34] [52] work with finite elements which consider a group of fibres, then the length-scale of a single finite element defines the meso-scale.

Macro-scale This is the scale of the global structure or mechanical component under consideration.

2.1.2 The concept of equivalent homogeneity

Although material properties and material behavior strongly depend on the micro-scale, most of engineering mechanics problems have to be solved in the macro-scale. The macroscopic overall properties can be determined experimentally for usual materials, but it is also of interest to relate this overall behavior to more detailed behavior at the level of the microstructure, because this leads to a deeper knowledge of the material and can reduce the experimentation costs.

In the micro-scale composite materials are highly heterogeneous (in fact, any material is heterogeneous at a sufficiently small length scale) and taking into account all the information related to the micro-scale, when solving a macro-scale problem, would be a nearly impossible task. The usual way to overcome this difficulty is to introduce an equivalent homogeneous material hypothesis. This equivalent homogeneous material is assumed to have the same average properties than the heterogenous one, so computations can be performed in these one, avoiding the complex internal structure of the heterogeneous material. The condition just described is said to be that of effective or equivalent homogeneity [38] and it is graphically expressed in Figure 2.1. Other terms in common usage with the same implication are those of *macroscopic homogeneity* and *statistical homogeneity*.

Let us assume that it exists a intermediate length scale D, such that the properties can be averaged for this scale in some meaningful way. For computational purposes, it is very advantageous if there exists such a length scale of averaging, D , that is still small compared with the characteristic dimension of the body. In all further considerations it will be assumed that the scale D of properties averaging exists and is meaningful. This intermediate scale is usually called Representative Volume Element (RVE) and will be defined in depth in Section 2.1.3.

The development of methods which allow to obtain this average properties is one of the historical fields of the mechanics of composite materials [67]. Some of them will be summarized in the following.

2.1.3 Representative volume element (RVE) definitions

The mathematical description of dissipative phenomena in mechanics of solids needs of a formulation of continuum mechanics consistent with principles of thermodynamics. This

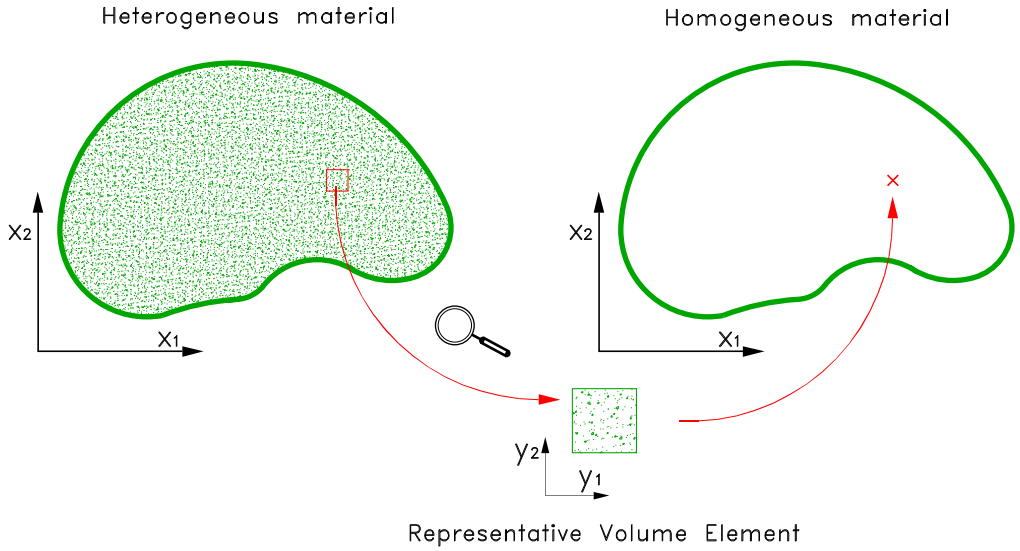

Figure 2.1: The equivalent homogeneous material hypothesis (figure concept taken from Zalamea [160])

theory is commonly called *thermomechanics* or *continuum thermodynamics* [104]. This field postulates the existence of a Representative Volume Element (RVE) which, briefly, can be defined using Jiang et al. [81] words and say that, "mathematically, the Representative Volume Element (RVE) is an infinite length scale limit, relative to the microscale in which the material appears uniform and the continuum concept [101] may be applied". However, the concept of Representative Volume Element (RVE) has been in constant evolution since the days of Hill who defined Representative Volume Element as [74]:

> "a sample that (a) is structurally entirely typical of the whole mixture on average, and (b) contains a sufficient number of inclusions for the apparent overall moduli to be effectively independent of the surface values of traction and displacement, so long as these values are "macroscopically uniform". That is, they fluctuate about a mean with a wavelength small compared with the dimensions of the sample, and the effects of such fluctuations become insignificant within a few wave-lengths of the surface. The contributions of this surface layer to any average can be made negligible by taking the sample large enough".

This two requirements are expressed in other words, using some statistical concepts, by Ostoja-Starzewski [121]:

1. statistical homogeneity and ergodicity[1] of the material; these two pro-

[1] As will be seen in Section 4.2.3, a material is suposed to be *ergodic* when any statistical information about it can be obtained from a single sample. A material is suposed to be statistically homogeneous if its probability functions depend only on the relative position

perties ensure the RVE to be *statistically representative* of the macro-response.

2. some scale L of the material domain, sufficiently large relative to the microscale d (inclusion size) so as to ensure the independence of boundary conditions.

According to Drugan and Willis [47] there exist to main groups of definitions of RVE:

> "One definition arises from the perspective that in order to characterize macroscopic composite constitutive response, one must recognize the statistical nature of the microstructure of actual composites. This perspective leads to the conclusion that the smallest RVE for which a macroscopic "effective" constitutive theory could apply is one that is sufficiently large to be statistically representative of the composite - that is, to include effectively a sampling of all possible microstructural configurations that occur in the composite. This is the perspective generally adopted and it leads to statements of the type that the RVE must include a very large number of the composite's microheterogeneities (such as grains, inclusions, voids, cracks, fibres, etc.).
>
> There is another, perhaps more pragmatic, definition of "representative volume element": the smallest material volume element of the composite for which the usual spatially constant "overall modulus" macroscopic constitutive representation is a sufficiently accurate model to represent mean constitutive response."

The latter one is the definition adopted by Drugan and Willis. According to their work [47], this definition leads to much smaller (and so, more attractive from the computational point of view) size of the RVE.

The definitions given here so far concern to ideal infinite-length Representative volume Elements and so not sufficient when using computational mechanics for the simulation of the behaviour of the micromechanics of materials. In this case some criteria which define somehow the minimum finite size of the RVE have to be found. Section 2.6.1 reviews some works which, using some of this criteria, find the finite size of the RVE.

2.1.4 The Hill condition

As will be seen later in Section 2.6.1 the Hill Condition may be useful to determine the minimal size of material which have to be analyzed theoretically to obtain the same results than the bulk material, so now is just exposed as a theoretical law but a *reprise* appears in Section 2.6.1.

The Hill condition or Hill principle poses the equivalence of energetically and mechanically defined effective properties of heterogeneous elastic materials. It can be expressed [92]:

$$\langle \boldsymbol{\sigma} : \boldsymbol{\varepsilon} \rangle = \langle \boldsymbol{\sigma} \rangle : \langle \boldsymbol{\varepsilon} \rangle \tag{2.1}$$

Equation 2.1 implies that the stress and strain fields are uncorrelated. Kröner [92] shows that this equation stands under the following conditions:

1. the local elastic compliances and surface force densities are bounded
2. the body is macroscopically homogeneous, infinite in the limit
3. no volume forces are present
4. no internal stresses are present[2]

The Hill Condition of equation 2.1 can be generalized for a nonlinear inelastic medium, as it is shown in [70].

No real body is infinite, however the Hill Condition will be a good approximation to real situations if the external dimensions of the composite are sufficiently large compared to the typical inclusion diameter. Clearly, this is the case of composite materials: the fibre size is much smaller than the size of any component of a mechanical system, to such an extent that, as seen in Section 2.1.1, different scales are involved on their analysis.

2.2 Effective properties of composite materials

As pointed out by Jiang et al.[81] the term *effective* should be reserved for the overall response of the RVE, in opposition to the term *apparent*, which should be used when working with domains which are smaller than the RVE. In the following, the basic expressions for computing the effective properties of a composite material are reviewed.

Under conditions of an imposed macroscopically homogeneous stress or deformation field on the representative volume element, the average stress is defined by:

$$\langle \sigma_{ij} \rangle = \frac{1}{V} \int_V \sigma_{ij}(x) \, \mathrm{d}v \tag{2.2}$$

and the average strain by:

$$\langle \varepsilon_{ij} \rangle = \frac{1}{V} \int_V \varepsilon_{ij}(x_i) \, \mathrm{d}v \tag{2.3}$$

where V is the volume of the RVE.

The average stress and strain fields, as defined in equations 2.2 and 2.3, can be related using the effective elastic moduli tensor $\bar{\mathbf{C}}$ and the effective compliance tensor $\bar{\mathbf{S}}$:

$$\langle \boldsymbol{\sigma} \rangle = \bar{\mathbf{C}} : \langle \boldsymbol{\varepsilon} \rangle \tag{2.4}$$

$$\langle \boldsymbol{\varepsilon} \rangle = \bar{\mathbf{S}} : \langle \boldsymbol{\sigma} \rangle \tag{2.5}$$

[2]The Hill Condition, as shown in Kröner [92], can be extended for the case when internal stresses, such like, thermal stresses, are present.

Consequently, $\bar{\mathbf{C}}$ and $\bar{\mathbf{S}}$ can be seen as the elastic tensors of an homogeneous material having the same macroscopic elastic behavior than the composite material and, therefore, to derive the effective properties of a composite material is equivalent to find the effective stress-strain relation. That is, for the elastic case, to find the effective tensors $\overline{\mathbf{C}}$ or $\overline{\mathbf{S}}$. For this purpose different methods can be followed. This methods can be classified in four main groups:

Micromechanics methods . They determine constitutive relations by setting up some hypotheses on the stress and strain fields at the micro-scale and analytically solving the elasticity problem. The first approach in this category is the well known rule of mixtures (ROM), described in section 2.3.1. Some other approaches are the self-consistent methods, reviewed in section 2.3.2.

Some classic papers in this field are those by Eshelby [50] and Mori and Tanaka [110]. Some reviews including this topic are those by Böhm [23] and Li [99].

Bounds for the effective properties This approach, instead of explicitly finding the effective properties of the material, finds upper and lower bounds for them. The Voigt and Reuss bounds (described in section 2.4.1) are the simplest ones. The only information needed about the distribution of the reinforcement is the volume fraction. By adding the hypothesis of statistical homogeneous distribution Hashin and Shtrikman [69] found narrower bounds, as described in Section 2.4.3. The more statistical information is used, the narrower are the bounds, and so, using second or third order statistics this bounds can be improved. Some of the most prolific researchers in this field are Willis and Talbot [148] [149] [158], Drugan and Willis [47], Ponte Castaneda [128] and Torquato [152] [153].

Homogenization methods . They consider the elasticity problem as a two-scale problem and derive the behavior of the heterogeneous material at the macroscale. They consider that the material is periodic at the micro-scale and have reached a high level of sophistication. The main researchers in this field are Sanchez-Hubert and Sanchez-Palencia [139] [138], Suquet, Michel et al. [144] [78] [79] and, more recently, Anthoine [10] [11], Feyel [52], Fish [54] [53], Lee and Ghosh [93] [94] [58] [59] and Zalamea [160] [161].

Computational approaches The evolution of computers gives place to methods which were unfeasible in the former decades. This methods try to find the effective behaviour of the material by "brute force" solving the problem in the microscale. This methods have been mainly used in solving problems for which no analytical solution is available, like the case of non-periodic inclusions. Some papers int his category are those by Ostoja-Starzewski and co-workers [124] [9] [8], Borbély [25], Kanit [88], Buryachenko [31], Byström [33], Graham [61], Knight [90]

The latter classification should be seen only for the organisation of the present chapter purposes. Usually the line dividing each category is not clear and so, the groups of approaches defined above have points in common.

2.3 Micromechanics methods

One of the classic approaches for finding the effective properties of composite materials consists on setting up hypotheses on the microgeometry of the material (such like geometry of the inclusions and the assumption of periodicity) and deriving from them analytical expressions for the effective properties. This section shortly resumes the basic approaches: the rule of mixtures and the self-consistent method. A comparison of this methods extended to viscoelastic materials was performed by Brinson [28].

2.3.1 The rule of mixtures (ROM)

A common and well known way to solve the problem of finding the effective properties of a long fibre reinforced composite is the use of the *rule of mixtures*. Let us assume that the domain of the solid under consideration can be subdivided in two subdomains, one related to the matrix and the other related to the fibre:

$$\Omega = \Omega_m \cup \Omega_f \tag{2.6}$$

Let us denote the volume of Ω by V and the volume occupied by the matrix and the fibre by V_m and V_f, respectively.

Finally, let us assume that the composite is loaded in the fibre direction. In this case and for this type of composite it is reasonable to assume the coupling of the strains of each constituent along the fibre direction:

$$\varepsilon_{11}^{(f)} = \varepsilon_{11}^{(m)} = \varepsilon_{11} \tag{2.7}$$

where the superscripts f and m denote the fibre and the matrix, respectively. Following this hypothesis, the fibre and the matrix are treated like parallel springs.

If we compute now the average stress in the fibre direction $\langle\sigma_{11}\rangle$ as defined in Equation 2.2:

$$\langle\sigma_{11}\rangle = \frac{1}{V}\int_{\Omega_m} \sigma_{11}\,\mathrm{d}\Omega + \frac{1}{V}\int_{\Omega_f} \sigma_{11}\,\mathrm{d}\Omega \tag{2.8}$$

we obtain:

$$\langle\sigma_{11}\rangle = \frac{V_m}{V}\langle\sigma_{11}^{(m)}\rangle + \frac{V_f}{V}\langle\sigma_{11}^{(f)}\rangle \tag{2.9}$$

where $\langle\sigma_{11}^{(m)}\rangle$ denotes the mean stress in the matrix and $\langle\sigma_{11}^{(f)}\rangle$ the mean stress in the fibre. Since the strain is assumed to be constant all over the domain, the effective value of the Young modulus in the fibre direction (E_{11}) can be found by dividing expression 2.9 by the average strain $\langle\varepsilon_{11}\rangle$:

$$\frac{\langle\sigma_{11}\rangle}{\langle\varepsilon_{11}\rangle} = \frac{V_m}{V}\frac{\langle\sigma_{11}^{(m)}\rangle}{\langle\varepsilon_{11}^{(m)}\rangle} + \frac{V_f}{V}\frac{\langle\sigma_{11}^{(f)}\rangle}{\langle\varepsilon_{11}^{(m)}\rangle} \tag{2.10}$$

Finally, if we define the volume fraction of each constituent as:

$$c_r = \frac{V_r}{V} \qquad r = f, m \tag{2.11}$$

We obtain the effective value of E_{11}:

$$\langle E_{11} \rangle = c_m E^{(m)} + c_f E^{(f)} \tag{2.12}$$

where $E^{(m)}$ and $E^{(f)}$ are, respectively, the Young's Modulus of the matrix and the fibre, which are both isotropic. The latter expression can be written in a more general form:

$$P = c_m P^{(m)} + c_f P^{(f)} \tag{2.13}$$

where P is any material property. The latter formula is usually called *the rule of mixtures*.

In the other hand, for the derivation of the effective properties in the transverse direction (that is, the direction perpendicular to the fibre axis) the composite is loaded in this direction and the matrix and the fibre can be treated as a series of springs. In this case, the total strain of the composite could be found by adding the total strain in the matrix and the total strain in the fibre, that is, fibre and matrix are treated like springs connected in series:

$$\varepsilon_{22} = \varepsilon_{22}^{(f)} + \varepsilon_{22}^{(m)} \tag{2.14}$$

Proceeding analogously and computing the average strain (Equation 2.3) instead of the average stress, the next expression can be found:

$$\frac{1}{\langle E_{22} \rangle} = c_m \frac{1}{E_{22}^{(m)}} + c_f \frac{1}{E_{22}^{(f)}} \tag{2.15}$$

According to the latter expression, under the hypothesis 2.14, the inverse of E_{22} follows the rule of mixtures:

$$P^{-1} = c_m [P^{(m)}]^{-1} + c_f [P^{(f)}]^{-1} \tag{2.16}$$

What happens in real long fibre reinforced materials is that the rule of mixtures is a good approximation for E_{11} (Equation 2.12), but it is not for E_{22} (Equation 2.15). One of the main reasons for this lack of accuracy is that neither equation 2.12 or equation 2.15 use any information about the geometry and distribution of the fibre within the composite.

For this reason, some modified expressions have been proposed [16] for unidirectional fibre-reinforced composites. Most of them depend on fitting values, like the Halpin-Tsai [65] relations:

$$P = \begin{cases} c_f P^{(f)} + c_m P^{(m)} & \text{for } E_{11} \text{ and } \nu_{12} \\ P^{(m)} \frac{1+\xi\eta c_f}{1-\eta c_f} & \text{for } E_{22}, G_{12} \text{ and } \nu_{23} \end{cases} \tag{2.17}$$

where ξ is a fitting factor and

$$\eta = \frac{\frac{P^{(f)}}{P^{(m)}} - 1}{\frac{P^{(f)}}{P^{(m)}} + \xi} \tag{2.18}$$

Another continuum mechanics-based approach can be found in the work by Oller et al. [116]. Considering that no real composite has not only a *series* behavior or a only a *parallel* behavior, they have proposed a *generalised rule of mixtures* which can also be applied when plasticity is considered [117] and, in general, to non-linear behavior

2.3.2 Self-Consistent Methods

Self-Consistent Methods provide approximate estimates of the effective elastic response by making use of the phase geometry. The main assumption is that any fibre in the composite is embedded in an homogenous body with unknown properties.

The basic self-consistent method employs a single fibre embedded in an infinite matrix, following the classical Eshelby [51] approach[3] which can be found in [38]. Some Self Consistent approaches are modifications of the Eshelby formula for finite concentration effects.

The Mori-Tanaka approach [110] is a well-known self-consistent method. It considers an isolated fibre embedded in an infinite matrix which is subjected to a far-field load σ_0. An interesting reformulation of this method was provided by Benveniste [20], assuming that the isolated inclusion is loaded by average stress in the matrix. Then, the stress in the fibre is given by:

$$\boldsymbol{\sigma}^{(f)} = \mathbf{W}^{(f)} : \boldsymbol{\sigma}^{(m)} \tag{2.19}$$

where $\mathbf{W}^{(f)}$ is a partial concentration factor, given by:

$$\mathbf{W}^{(f)} = \mathbf{L}^{(f)} \left[\mathbf{I} + \mathbf{S} : [\mathbf{L}^{(m)}]^{-1} : (\mathbf{L}^{(f)} - \mathbf{L}^{(m)})\right] \tag{2.20}$$

where $\mathbf{L}^{(f)}$ and $\mathbf{L}^{(m)}$ are tensors following Hill's notation for plane strain[4] for the fibre and the matrix, respectively, $\mathbf{I}$ is the identity tensor and $\mathbf{S}$ can be expressed through a polarisation tensor $\mathbf{P} = \mathbf{S} : [\mathbf{L}^{(m)}]^{-1}$ which for cylindrical fibres [162] has components:

$$\begin{gathered} P_{22} = P_{33} = \frac{k^{(m)}+4m^{(m)}}{8m^{(m)}(k^{(m)}+m^{(m)})} \quad P_{23} = P_{32} = \frac{-k^{(m)}}{8m^{(m)}(k^{(m)}+m^{(m)})} \\ P_{44} = \frac{k^{(m)}+2m^{(m)}}{2m^{(m)}(k^{(m)}+m^{(m)})} \qquad P_{55} = P_{66} = \frac{1}{2m^{(m)}} \end{gathered} \tag{2.21}$$

where $m^{(m)}$ is the torsion modulus of the matrix (G) and $k^{(m)}$ can be written as $k = 2\lambda/\nu$.

Then, the effective compliance relation can be expressed using the compliance relations of the fiber ($\mathbf{M}^{(f)}$) and the matrix ($\mathbf{M}^{(m)}$):

[3] Eshelby derived some formulae which describe the elastic relations for an inclusion (fibre) embedded in an infinite matrix

[4] See Section A.5.1 in Appendix A for a short description of Hill's notation

$$\mathbf{M} = \frac{c_m \mathbf{M}^{(f)} : \mathbf{W}^{(f)} + c_m \mathbf{M}^{(m)}}{c_m \mathbf{I} + c_f \mathbf{W}^{(f)}} \tag{2.22}$$

Finally, the effective stiffness tensor $\mathbf{L}$ can be obtained by inverting the compliance tensor $\mathbf{L} = \mathbf{M}^{-1}$.

2.4 Bounds on effective properties of composite materials

Instead of explicitly computing the effective properties of the composite by assuming some geometry or periodicity, some methods consider that the composite material has random geometry and give upper and lower bounds od the effective properties.

2.4.1 Voigt and Reuss bounds

The first to consider a random material was W. Voigt, in 1887. By assuming a constant strain through the material, he found an expression for the effective properties. Some years later, in 1929, Reuss found another equation for the effective properties by assumig a constant stress through the material. Finally in 1952, R. Hill proved that under the assumption[5]:

$$\langle \boldsymbol{\sigma} : \boldsymbol{\varepsilon} \rangle = \langle \boldsymbol{\sigma} \rangle : \langle \boldsymbol{\varepsilon} \rangle \tag{2.23}$$

the Voigt and Reuss approximations provide upper and lower bounds for the effective moduli. In this section, Voigt's upper bound and Reuss' lower bounds for the elastic constitutive tensor C_{ijkl} will be derived thorugh some energy principles.

Strain energy

It is known [38] [104] that the stress can be expressed as the derivative of the strain energy with respect to strain as:

$$\sigma_{ij} = \frac{\partial W}{\partial \varepsilon_{ij}} \tag{2.24}$$

where the strain energy W is given by:

$$W(\varepsilon_{ij}) = \frac{1}{2} C_{ijkl} \varepsilon_{ij} \varepsilon_{kl} \tag{2.25}$$

$$W(\varepsilon_{ij}) \leq 0$$

The strain energy of Equation 2.25 can be also expressed as a function of the stress components:

$$W(\sigma_{ij}) = \frac{1}{2} S_{ijkl} \sigma_{ij} \sigma_{kl} \tag{2.26}$$

[5]This assumption is usually called *The Hill Condition* and it has been reviewed in Section 2.1.4

Theorem of minimum potential energy

Let us consider the elasticity boundary value problem of section (A.3). We define the potential energy functional:

$$U_\varepsilon = \int_\Omega \left[W(\varepsilon_{ij}) - F_i u_i\right] \,\mathrm{d}\Omega - \int_{\partial\Omega_\sigma} \bar{f}_i u_i \,\mathrm{d}\partial\Omega \tag{2.27}$$

where F_i are the body forces, $\bar{f}_i$ the prescribed forces, u_i the displacement field, Ω is the dominium under consideration and $\partial\Omega$ its boundary.

Theorem 1 (Theorem of minimum potential energy) *Of the displacement fields which satisfy the boundary conditions, the one that also satisfies the equations of equilibrium makes the potential energy functional (2.27) an absolute minimum.*

Theorem of minimum complementary energy

Let us define the complementary energy functional as:

$$U_\sigma = \int_\Omega \left[W(\sigma_{ij})\right] \,\mathrm{d}\Omega - \int_{\partial\Omega_u} \sigma_i \bar{u}_i \,\mathrm{d}\partial\Omega \tag{2.28}$$

where $\bar{u}_i$ are the prescribed displacements.

Theorem 2 (Theorem of minimum complementary energy) *Of the stress fields which satisfy the boundary conditions, the one that also satisfies the equations of equilibrium makes the complementary energy functional (2.28) an absolute minimum.*

Voigt's upper bound

Let us suppose that we impose some displacement $\hat{\mathbf{u}}$ in the boundary of the body and let us assume that this displacement causes uniform strain field in the composite $\widehat{\boldsymbol{\varepsilon}} = \overline{\boldsymbol{\varepsilon}}$ (where $\overline{\boldsymbol{\varepsilon}}$ is the average strain as defined in Equation 2.3) . Then, the potential energy functional 2.27, can be written:

$$\begin{aligned} U^{\text{VOIGT}} &= \frac{1}{2}\int_{\Omega_f} \widehat{\boldsymbol{\varepsilon}} : \mathbf{C}^{(f)} : \widehat{\boldsymbol{\varepsilon}} \,\mathrm{d}\Omega + \frac{1}{2}\int_{\Omega_m} \widehat{\boldsymbol{\varepsilon}} : \mathbf{C}^{(m)} : \widehat{\boldsymbol{\varepsilon}} \,\mathrm{d}\Omega \\ &= c_f \cdot \left[\overline{\boldsymbol{\varepsilon}} : \mathbf{C}^{(f)} : \overline{\boldsymbol{\varepsilon}}\right] + c_m \cdot \left[\overline{\boldsymbol{\varepsilon}} : \mathbf{C}^{(m)} : \overline{\boldsymbol{\varepsilon}}\right] \end{aligned} \tag{2.29}$$

Since $\widehat{\boldsymbol{\varepsilon}}$ does not necessarily satisfy the equilibrium equation, the real energy, following Theorem 1, has to be lower or equal to that energy computed following the assumption of homogeneous strain:

$$U_\varepsilon \leq U^{\text{VOIGT}} \qquad \rightarrow \qquad \overline{\boldsymbol{\varepsilon}} : \overline{\mathbf{C}} : \overline{\boldsymbol{\varepsilon}} \leq \overline{\boldsymbol{\varepsilon}} : \left[c_f \cdot \mathbf{C}^{(f)} + c_m \cdot \mathbf{C}^{(m)}\right] : \overline{\boldsymbol{\varepsilon}} \tag{2.30}$$

then:

$$\overline{\mathbf{C}} \leq c_f \mathbf{C}^{(f)} + c_m \mathbf{C}^{(m)} \tag{2.31}$$

where $\overline{\mathbf{C}}$ denotes the effective stiffness tensor, as defined in Equation 2.4. Comparing equations 2.13 and 2.31 we can say that the rule of mixtures for the stiffness tensor gives an upper bound for the effective stiffness tensor. The analogy between the Voigt upper bound development and the rule of mixtures were clear from the beginning since the hypotheses of homogeneous strain is the same for both.

Reuss' lower bound

Let us consider we impose the body surface to traction forces $\hat{\mathbf{f}}$ which cause a stress field $\widehat{\boldsymbol{\sigma}}$. Let us also assume that this stress field is equivalent to the average stress $\overline{\boldsymbol{\sigma}}$ of the real solution, computed by equation 2.2. Then, the complementary strain energy 2.28 can be computed:

$$\begin{aligned} U^{\text{REUSS}} &= \frac{1}{2}\int_{\Omega_f} \widehat{\boldsymbol{\sigma}} : \mathbf{S}^{(f)} : \widehat{\boldsymbol{\sigma}}\, \mathrm{d}\Omega + \frac{1}{2}\int_{\Omega_m} \widehat{\boldsymbol{\sigma}} : \mathbf{S}^{(m)} : \widehat{\boldsymbol{\sigma}}\, \mathrm{d}\Omega - \int_{\partial\Omega} \hat{\mathbf{f}} \cdot \mathbf{u}\, \mathrm{d}\partial\Omega = \\ &= c_f \cdot \left[\overline{\boldsymbol{\sigma}} : \mathbf{S}^{(f)} : \overline{\boldsymbol{\sigma}}\right] + c_m \cdot \left[\overline{\boldsymbol{\sigma}} : \mathbf{S}^{(m)} : \overline{\boldsymbol{\sigma}}\right] - \int_{\partial\Omega} \hat{\mathbf{f}} \cdot \mathbf{u}\, \mathrm{d}\partial\Omega \end{aligned} \tag{2.32}$$

Since the stress field $\widehat{\boldsymbol{\sigma}}$ does not necessarily satisfy the strain compatibility requirements, the energy U^{REUSS} will be greater or equal to that of the real solution:

$$U \leq U^{\text{REUSS}} \qquad \rightarrow \qquad \overline{\boldsymbol{\sigma}} : \overline{\mathbf{S}} : \overline{\boldsymbol{\sigma}} \leq \overline{\boldsymbol{\sigma}} : \left[c_f \cdot \mathbf{S}^{(f)} + c_m \cdot \mathbf{S}^{(m)}\right] : \overline{\boldsymbol{\sigma}} \tag{2.33}$$

and, so:

$$\overline{\mathbf{S}} \leq c_f \cdot \mathbf{S}^{(f)} + c_m \cdot \mathbf{S}^{(m)} \tag{2.34}$$

and:

$$\overline{\mathbf{C}} = \left[\overline{\mathbf{S}}\right]^{-1} \geq \left[c_f \cdot \mathbf{S}^{(f)} + c_m \cdot \mathbf{S}^{(m)}\right]^{-1} \tag{2.35}$$

Once again, by comparing equations 2.16 and 2.35, we can say that the rule of mixtures for the inverse of the compliance tensor gives a lower bound for the effective stiffness tensor. Both Reuss bound development and the inverse rule of mixtures development use the same hypothesis of homogeneous stress field.

2.4.2 Hill's bounds

The expression of the upper bound of Voigt together with the lower bound of Reuss in a tensorial form is usually known as the Hill bounds [23]:

$$\left[\sum_{i=1}^{N} c_i \cdot \mathbf{S}^{(i)}\right]^{-1} \leq \overline{\mathbf{C}} \leq \sum_{i=1}^{N} c_i \cdot \mathbf{C}^{(i)} \tag{2.36}$$

2.4.3 Hashin-Shtrikman bounds

This section exposes the variational principles which were developed by Hashin and Shtrikman in 1963 [69] for linear media. Talbot and Willis extended this principles for non linear media in 1985 (See references [47], [147] and [158]).

The basic idea of the Hashin-Shtrikman principle is to express the stress, strain and displacement field of the medium relative to a comparison medium. This comparison medium is subjected to those boundary conditions of the problem under consideration. Let $\mathbf{C}_0$ be the elastic constitutive relation for this comparison medium and $\boldsymbol{\varepsilon}$ any strain field which satisfy the boundary conditions. We can express a stress tensor $\hat{\boldsymbol{\sigma}}$ which satisfies the equilibrium equation as follows:

$$\hat{\boldsymbol{\sigma}} = \mathbf{C}_0 : \boldsymbol{\varepsilon} + \boldsymbol{\tau} \tag{2.37}$$

$\boldsymbol{\tau}$ is sometimes called *polarization stress* and for:

$$\boldsymbol{\tau} = (\mathbf{C} - \mathbf{C}_0) : \boldsymbol{\varepsilon} \tag{2.38}$$

the exact solution for the heterogeneous medium under consideration is obtained. Recalling the theorem of minimum potential energy (Theorem 1):

$$U \leq \frac{1}{2} \sum_{r=1}^{N} \int_{V_r} \boldsymbol{\varepsilon} : \mathbf{C}_r : \boldsymbol{\varepsilon} \, \mathrm{d}V \tag{2.39}$$

defining $\langle \boldsymbol{\varepsilon}_r \rangle$ as the volume average strain over V_r and the deviation of the strain in V_r with respect to its average value, $\boldsymbol{\varepsilon}'_r$:

$$\boldsymbol{\varepsilon}'_r = \boldsymbol{\varepsilon} - \langle \boldsymbol{\varepsilon}_r \rangle \tag{2.40}$$

and using the next three expressions, which relate the strain volume average over V_r ($\langle \boldsymbol{\varepsilon}_r \rangle$) by means of the tensor $\hat{\mathbf{A}}_r$, the strain volume average ($\langle \boldsymbol{\varepsilon} \rangle$), the elastic relation of each constituent ($\mathbf{C}_r$) and the average constitutive stiffness tensor of the heterogeneous material ($\overline{\mathbf{C}}$):

$$\langle \boldsymbol{\varepsilon}_r \rangle = \hat{\mathbf{A}}_r : \langle \boldsymbol{\varepsilon} \rangle \tag{2.41}$$

$$\sum_{r=1}^{N} \mathbf{C}_r : \widehat{\mathbf{A}}_r = \mathbf{I} \tag{2.42}$$

$$\widehat{\mathbf{C}} = \sum c_r \mathbf{C}_r : \widehat{\mathbf{A}}_r \tag{2.43}$$

where $I_{jkl} = \frac{1}{2} \left[\delta_{ik} \delta_{jl} + \delta_{il} \delta_{jk} \right]$

Before some manipulation (which can be found in [38]), the theorem of minimum potential energy of 2.39 can be rewritten:

$$\overline{\boldsymbol{\varepsilon}} : (\mathbf{C} - \widehat{\mathbf{C}}) : \overline{\boldsymbol{\varepsilon}} \leq -\frac{1}{V} \sum_{r=1}^{N} \int_{V_r} \boldsymbol{\varepsilon}'_r : (\mathbf{C}_0 - \mathbf{C}_r) : \boldsymbol{\varepsilon}'_r \, \mathrm{d}v \tag{2.44}$$

In the latter expression $\mathbf{C}$ is the effective properties tensor. From the inequality 2.44, bounds for $\mathbf{C}$ can be found. This is done by finding solutions for $\widehat{\mathbf{C}}$, by imposing or restricting $\boldsymbol{\tau}$ some value or condition. Using the Eshelby formula [38] for this purpose and assuming the material is statistically homogeneous[6], the following explicit bounds for the Lamé constants[7] can be found:

$$k \leq \left[\sum_{r=1}^{N} c_r (k_g^+ + k_r)^{-1}\right]^{-1} - k_g^+ \tag{2.45}$$

$$\mu \leq \left[\sum_{r=1}^{N} c_r (\mu_g^+ + \mu_r)^{-1}\right]^{-1} - \mu_g^+ \tag{2.46}$$

where:

$$k_g^+ = \frac{4}{3}\mu_{max} \tag{2.47}$$

$$\mu_g^+ = \frac{3}{2}\left(\frac{1}{\mu_{max}} + \frac{10}{9k_{max} + 8\mu_{max}}\right) \tag{2.48}$$

where μ_{max} and k_{max} are the maximum values of the properties for the N phases.

$$k \geq \left[\sum_{r=1}^{N} c_r (k_g^- + k_r)^{-1}\right]^{-1} - k_g^- \tag{2.49}$$

$$\mu \geq \left[\sum_{r=1}^{N} c_r (\mu_g^- + \mu_r)^{-1}\right]^{-1} - \mu_g^- \tag{2.50}$$

where:

$$k_g^- = \frac{4}{3}\mu_{min} \tag{2.51}$$

$$\mu_g^- = \frac{3}{2}\left(\frac{1}{\mu_{min}} + \frac{10}{9k_{min} + 8\mu_{min}}\right) \tag{2.52}$$

where μ_{min} and k_{min} are the minimum values of the properties for the N phases.

As pointed out by Hashin in [67] the Hashin-Shtrikman bounds provide good approximations for phase stiffness mutual ratios up to 10.

The analogies between the self-consistent method, the Hashin-Shtrikman bounds and the Mori-Tanaka method are shown in [48].

[6] Statistics definitions are given in the section 4.2 of Chapter 4. For the present, statistical homogeneity means that the basic statistics such as the mean, the variance and the density function are constant all over the material.

[7] Lamé constants are defined in the Appendix A

2.4.4 Second and third order bounds

The latter development can be generalized to non-linear materials if the constitutive linear expression in 2.37 is replaced by a general constitutive relation. If the strain energy of the comparative medium is $W_0(\boldsymbol{\varepsilon}, \mathbf{x})$, Equation 2.37 can be rewritten:

$$\sigma_{ij} = \frac{\partial W_0}{\partial \varepsilon_{ij}} + \tau_{ij} \tag{2.53}$$

Let us define:

$$(W - W_0)^* = \sup_{\boldsymbol{\varepsilon}} \{\boldsymbol{\tau}\boldsymbol{\varepsilon} - (W - W_0)(\boldsymbol{\varepsilon}, \mathbf{x})\} \tag{2.54}$$

so that,

$$W(\boldsymbol{\varepsilon}, \mathbf{x}) \geq W_0(\boldsymbol{\varepsilon}, \mathbf{x}) + \boldsymbol{\tau} : \boldsymbol{\varepsilon} - \boldsymbol{\sigma}_0 : \boldsymbol{\varepsilon} - (W - W_0)^*(\boldsymbol{\tau}, \mathbf{x}) \tag{2.55}$$

Then,

$$U_\varepsilon \geq \inf_{\varepsilon \in K} \int_\Omega \{W_0(\boldsymbol{\varepsilon}, \mathbf{x}) + \boldsymbol{\tau} : \boldsymbol{\varepsilon} - \boldsymbol{\sigma}_0 : \boldsymbol{\varepsilon} - (W - W_0)^*(\boldsymbol{\tau}, \mathbf{x})\} \, \mathrm{d}\mathbf{x} \tag{2.56}$$

The so-called bounds of Hashin-Shtrikman type are obtained by ensemble averaging expression 2.56:

$$\langle U_\varepsilon \rangle \geq \langle \inf_{\varepsilon \in K} \int_\Omega \{W_0(\boldsymbol{\varepsilon}, \mathbf{x}) + \boldsymbol{\tau} : \boldsymbol{\varepsilon} - \boldsymbol{\sigma}_0 : \boldsymbol{\varepsilon} - (W - W_0)^*(\boldsymbol{\tau}, \mathbf{x})\} \, \mathrm{d}\mathbf{x} \rangle \tag{2.57}$$

The polarisation stress $\boldsymbol{\tau}$ is now piece-wise defined and depends on each phase location. So, the ensemble average of equation 2.57 depends on the two point probability function.

Third order bounds were obtained in the general case by Beran[21] and later for two-phase materials by Milton [105]. The incorporation of more and more statistical information on the distribution of heterogeneities in random materials gives closer bounds as suggested by the theory of Kröner [92].

There are numerous publications devoted to analytically find closer bounds, using second or third order statistics, like references [128],[48] and [149]. In this latter work Talbot and Willis show that the third order bounds can be seen as a generalization of those by Hashin-Shtrikman. A development of 2.56 which depends on three-point statistics and gives closer bounds was also given by Talbot and Willis [148].

According to Kanit et al. [88] for microstructures whith phases with quantitatively very different properties, the usual bounds do not give a useful estimation of the effective properties. The work of Kanit et al. [88] show how to use homogenization techniques to obtain more accurate bounds.

2.5 Homogenization

The term *homogenization* can be defined as the process in which an heterogeneous material is replaced by an homogeneous one having an equivalent mechanical behaviour within a usual range of loads.

In the Ph.D. thesis by Zalamea [160] the main approaches to the homogenization problem are summarized. All of them work with two scales [8]: a macroscopical scale (whose coordinate system will be denoted by $\mathbf{x}$) and a microscopical scale (with coordinate system $\mathbf{y}$). For instance in a laminate the microscopical scale would consider the matrix, the fiber, the interface between them, possible delamination or debonding phenomena between fibre and matrix, bubbles in the matrix, etc.[156].

Microscopical scale is usually characterized by being submitted to stress and strain fields which present fluctuations and oscillations with a wave-length which is related to de size of the components. This oscillations are not seen in the macroscale but some phenomena which affect the material in the macroscale (such as damage, fracture and crack nucleation) are closely-related to them.

Homogenization methods can be roughly divided into two groups: *Mean methods* and *Asymptotical methods*. Although these are the classical approaches new computational-based methods are worth to mention like the Voronoï Finite Element Method proposed by Ghosh and Moorthy [58] [59] [109] and the methods by Zalamea [160], by Michel [78] and by Feyel [52].

2.5.1 Spatial averages approach

Let V be the volume of a representative domain of the heterogeneous media. The main hypothesis of the *mean methods* stands that the macroscopic variables of the problem (stresses and strains) can be obtained computing the mean[9] of their microscopical values within the domain:

$$\boldsymbol{\sigma}^{\mathbf{x}} =< \boldsymbol{\sigma} >_V \qquad \text{or} \qquad \boldsymbol{\varepsilon}^{\mathbf{x}} =< \boldsymbol{\varepsilon} >_V \tag{2.58}$$

Where the superscript $\mathbf{x}$ denotes the macroscopic scale. Because the dependency on the macroscopic and microscopic scale we write:

$$\boldsymbol{\sigma}^{\mathbf{x}}(x) =< \boldsymbol{\sigma}(x,y) >_V \qquad \text{or} \qquad \boldsymbol{\varepsilon}^{\mathbf{x}}(x) =< \boldsymbol{\varepsilon}(x,y) >_V \tag{2.59}$$

As pointed out by Zalamea [160], the main differences between the homogenization problem and the classical boundary value problem are:

1. In the homogenization problem the loads are field averages instead of displacements or mass or surface loads

2. The boundary conditions do not exist, or they are not stated clearly.

[8] Usually the terms of *homogenization* and *multi-scale methods* are employed with the same meaning

[9] The mean operator $< \cdot >$ is defined $\langle \mathbf{f}(x,y) \rangle := \frac{1}{V} \int_V \mathbf{f}(x,y) dV$

In a general form, an elastic constitutive law for an heterogeneous material as a function of the macroscopical and microscopical scales can be written:

$$\sigma_{ij}(x,y) = C_{ijkl}\varepsilon_{kl}(u(x,y)) \tag{2.60}$$

where $\mathbf{C}$ is the elastic constitutive tensor. As stated in Eq. 2.58 it is assumed that stresses in the macroscopical scale can be obtained computed the mean of the stress field in the microscopical scale:

$$\boldsymbol{\sigma}^{\mathbf{x}}(x) =< \boldsymbol{\sigma}(x,y) >_V =< \mathbf{C}(x,y)\boldsymbol{\varepsilon}(u(x,y)) >_V \tag{2.61}$$

where it is assumed that the microscopical strain $\boldsymbol{\varepsilon}(u(x,y))$ can be expressed as a lineal function of the macroscopical strain $\boldsymbol{\varepsilon}(u^x(x,y))$, then:

$$\boldsymbol{\varepsilon}(u(x,y)) = \mathbf{d} : \boldsymbol{\varepsilon}(u^x(x)) \tag{2.62}$$

where $\mathbf{d}$ is a transformation tensor called *strain concentration tensor*. By using Eq. 2.62 in Eq. 2.61:

$$\boldsymbol{\sigma}^x(x) = \mathbf{C}^x(x) : \boldsymbol{\varepsilon}(u^x(x)) \tag{2.63}$$

where $\mathbf{C}^x =< \mathbf{C} : \mathbf{d} >_V$ is the effective constitutive tensor of the heterogeneous media. So, the homogenisation law is indeed a weighted mean of the microscopical constitutive law, using the strain concentration tensor $\mathbf{d}$ as the weight. Since the homogenization law depends on $\mathbf{d}$, this tensor has to be obtained.

Hill-Mandel method

Let us consider the boundary value problem in the microscopical scale:

$$\begin{array}{lll} \boldsymbol{\sigma}(y) = \mathbf{C} : \boldsymbol{\varepsilon}(u(y)) \quad ; & \varepsilon_{ij} = \frac{1}{2}\left(\frac{\partial u_i}{\partial y_j} + \frac{\partial u_j}{\partial y_i}\right) & \text{in V} \\ \frac{\partial \sigma_{ij}(y)}{\partial y_i} = 0 & & \text{Equilibrium equation in V} \\ \bar{u}_i(y) = \varepsilon^x_{ij} y_j & & \text{Boundary condition on } \partial V \end{array} \tag{2.64}$$

Considering only the linear problem, the displacement field is a linear function of the imposed strain field $\boldsymbol{\varepsilon}(u^x)$, and then:

$$u_i(y) = v_i^{kl}(y)\varepsilon_{kl}(u^x) \tag{2.65}$$

where v_i^{kl} is the ith component of the displacement vector $\mathbf{v}^{kl}$ which is the solution of the problem 2.64 for a unit strain state defined by:

$$\varepsilon_{ij}(u^x) = I_{ij}^{kl} = \frac{1}{2}(\delta_{ik}\delta_{jl} + \delta_{il}\delta_{jk}) \tag{2.66}$$

where I_{ij}^{kl} is a second order tensor whose components (ij) are defined in a similar manner to the fourth order identity tensor $I_{ij}^{kl} = I_{ijkl}$.

From Eq. 2.65 we can obtain the strain field:

$$\varepsilon_{ij}(u(y)) = \varepsilon_{ij}(v^{kl}(y))\varepsilon_{kl}(u^x) \tag{2.67}$$

and so, by comparing equations 2.62 and 2.67 we find the tensor **d**:

$$d_{ijkl} = \varepsilon^y_{ij}(v^{kl}(y)) \tag{2.68}$$

Once **d** is known, it can be used to obtain the constitutive tensor **C**:

$$C^x_{ijkl} =< C_{ijpq}(y)d_{pqkl} >_V \tag{2.69}$$

It can be shown [160][144] that the elastic tensor **C** keeps the following symmetries:

$$C^x_{ijkl} = C^x_{jikl} = C^x_{klji} \tag{2.70}$$

The former development can be extended for periodic material, by considering the force field *anti-periodic* (which is justified by the action-reaction principle) in the microscale and by considering the displacement field periodic in the microscale. The extension for periodic materials can be found in [160]. In the same reference a stress-based development can be found.

2.5.2 Asymptotic methods

The asymptotic methods for homogenization are detailed in the works by Sanchez-Palencia et al [139] [138]. As remarked in [139], the two-scale asymptotic expansions is a classical method in mechanics of vibrations, for instance, the motion of a pendulum with a damper, which is plotted in Figure 2.2 can be seen as a exponential function in the macroscale and a sinus funtion in the microscale.

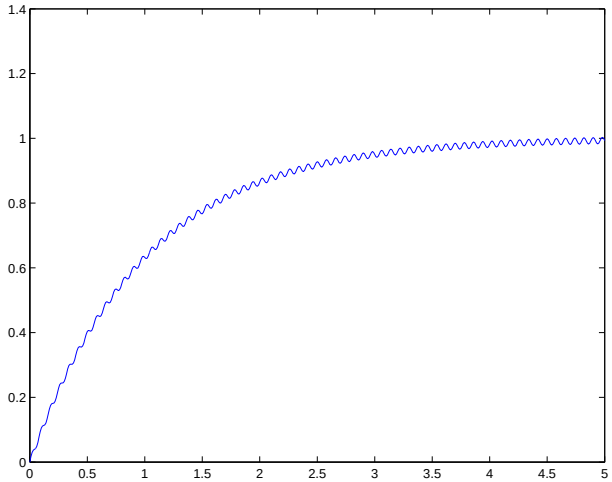

Figure 2.2: Macro and microscales

This approach obtains asymptotical developments for the heterogeneous medium in the both macro and micro scales. The problem is developed in both scales by using continuum mechanics formulae [101]. At the macro scale, it has to be satisfied:

$$\nabla\boldsymbol{\sigma} + \rho\mathbf{b} = 0 \qquad \text{in } \Omega \tag{2.71}$$

$$\begin{aligned} \boldsymbol{\sigma} &= \mathbf{C} : \boldsymbol{\varepsilon}(\mathbf{u}) \\ \boldsymbol{\sigma} \cdot \mathbf{n} &= \mathbf{t} \qquad \text{in } \Omega_t \\ \mathbf{u} &= \mathbf{0} \qquad \text{in } \Omega_u \end{aligned}$$

where ρ is the material density, $\mathbf{b}$ are the body forces (such as gravity or magnetic fields), $\mathbf{n}$ is the outward normal vector to the boundary surface, $\mathbf{t}$ is the traction vector and $\mathbf{u}$ the displacement field.

The problem 2.71 has a single solution and, consequently, $\mathbf{u}$ and $\boldsymbol{\sigma}$ can be obtained, but if the microscale is too small it is impossible to compute the displacements $\mathbf{u}$. The adopted solution is to obtain a limit by means of an asymptotical expansion. The equilibrium equations for the microscale are re-written in function of this asymptotical expansion, assuming periodicity of the unit cell. A set of vectors which relate the microscale and the macroscale can be found by solving the problem at the microscale. By using this vectors the homogenized constitutive elastic tensor for the macroscopic scale can be computed. The elastic problem can be solved at the macroscale by using this tensor and the macroscopic stress $\boldsymbol{\sigma}$ and strain $\boldsymbol{\varepsilon}$ fields can be obtained.

From the macroscopic stress field $\boldsymbol{\sigma}$, one can obtain a stress field $\boldsymbol{\sigma}(x, y)$ which for a constant $\mathbf{x}$ represents the mean stress in a microscale periodic subdomain. The set of equations to solve depend on the constitutive relation at the microscale of the problem: inelastic strain, debonding between fiber and matrix or damage [54].

Within the researchers, as pointed out in the Ph. D. thesis by Zalamea [160], some of them have published works in which the utility of these methods is questioned in some conditions. For example, when the dimensional relation between the scales has a finite instead of infinitesimal value. Terada and Kikuchi [151] question the accuracy of these approaches in non-linear applications and proposes a general method for non-linear problems based in energy functionals.

2.5.3 Computational approaches for the homogenization problem

Zalamea [160, 161] proposed a general computational method for solving homogenization problems by implementing a two-scale method within a Finite Element code with parallelization. The method is general because the consitutitve relation in the microscale (unit cell) is obtained by solving a finite element problem in this scale, where the boundary conditions are set up to configure a periodic media.

Car [34] and Zalamea [160], [161] compare the solution given by the method with experimental values and show the good agreement between them. Similar two-scale FE-based approaches are those by Michel [78, 79] and Feyel [52].

Some approaches have used homogenization techniques for the estimation of elastic properties of random composites. These approaches are based on the averaging in some window, as can be seen in the work by Huyse and Maes [76], or Baxter and Graham [17]

[18], where a moving window is used. An analogous technique is used by Graham and Baxter for the simulation of local composite properties [61].

2.6 Computational approaches

When a composite material is considered non-periodic or random[10], for the analysis of inclusion clustering, stress or strain concentration, etc. most of the analytic techniques are not useful. For this reason, some computational approaches which analyze the microstructure by means of numerical methods (normally, the Finite Element Method [164]) have been developed. This section reviews some of this techniques, a larger decription of which can be found in the review by Mishnaevsky et al.[84].

Since the size of the RVE is a crucial point for this techniques some approaches for its determination are also reviewed.

2.6.1 The size of the RVE

As seen in Section 2.1.3, the Representative Volume Element is thought to ideally have an infinite length, related to that of the microstructure. When applying computational methods, this infinite length scale limit has to be relaxed and a finite length for the RVE has to be found. From the computational point of view a *small* RVE is desired, but from the mechanics point of view a *big enough* RVE which satisfies certain representativeness criteria is needed.

In other words, starting from the definitions of the RVE given in section 2.1.3, from the computational mechanics point of view, a question arises: *Which is the smallest size of a valid RVE for a composite material?* This section reviews different approaches trying to give an answer to the latter question.

Convergence of effective properties

According to Hill's definition of Section 2.1.3, the Representative Volume Element is expected to have the same effective properties that the whole material. Following this characteristic convergence studies can be performed with increasing size RVEs.

Gusev [64] considered spherical reinforcements and computed the effective properties for increasing size RVEs, with the same volume fraction (RVEs having 8, 27 and 64 inclusions with $c_f = 0.27$). The ratio between the Young modulus of the inclusion and the matrix was constant ($E^{(f)}/E^{(m)} = 23.3$) Although the spheres were randomly distributed inside the RVE, periodic boundary conditions were used. The periodic boundary condition can be used since the average behaviour is expected to be the same in any subdomain of

[10] Although in this section some techniques for the analysis of random microstructures are reviewed, the description of this techniques is done from the point of view of mechanics. Statistical approaches and criteria are reviewed in Chapter 4

the material. Monte Carlo simulations[11] were performed for the different RVE sizes and the effective properties and its scatter were computed. The obtained effective properties were compared with theoretical formulae results. The dimensionless L/d measure for the RVE size was used, were L is the length of the unit cell edge and d the sphere diameter. The results showed that, for those conditions, a cell with 27 inclusions (which corresponds to $L/d = 3.75$) could be used as a RVE.

Terada and co-workers [150] performed a convergence analysis which shows that homogenization theory is still valid when the material is considered non-periodic. In this case a sufficiently large RVE is used instead of the periodic cell. In the referenced work three different types of boundary conditions (displacement, force and periodic)[12] were applied to increasing-size representative volume elements with randomly placed circular inclusions. The results showed the convergence of the obtained effective properties when increasing the size of the RVE . The effective properties obtained by means of the three different boundary conditions can be considered equivalent, and consequently, that the homogenization method is convergent, when the RVE size approaches 15-20 times the microscopic scale length (in the example, the inclusion diameter, which means $L/d = 15 - 20$). The analysis was only performed for one ratio of the elastic properties of inclusion and matrix ($E^{(f)}/E^{(m)} = 10$).

Monte Carlo Simulation of effective properties

In accordance with Kanit et al. [88] the RVE must ensure a given accuracy of the estimated property obtained by spatial averaging of the stress, the strain, or the energy fields in a given domain V. In the same work Kanit et al. pose that smaller volumes of V can be used if the average behavior of several realizations of the microstructure is computed to get the same accuracy. Their study is applied to a solid composed by polycristals and grains, which they model by using three-dimensional Voronoï cells[13] to obtain estimates of the mean and variance of the elastic and thermal properties for materials with volume fraction $0.5, 0.7$ and 0.9. They perform Monte Carlo simulations and analyze the convergence of the thermal and elastic effective properties and the variance of the results when increasing the RVE size. The estimates of the effective properties are compared with Voigt-Reuss and Hashin-Shtrikman bounds. They conclude that by using Monte Carlo simulation for the effective properties computation, smaller sizes of the RVE can be used and that the size of the RVE depends on the number of realizations. That is, for smaller RVE sizes, greater number of realizations are required, and conversely.

Hill Condition and Convergence of effective properties

The following important conclusion related to the use of finite size RVEs is pointed out by Ostoja-Starzewski et al. [124]. Let us consider a dominium Ω and a subdominium of

[11] Although some improvements can be performed [136], Monte Carlo Simulation is based in the repetition of some experiment which depends on some random variables. Then, distribution functions for the output can be found.

[12] See Annex A for boundary conditions descriptions

[13] Voronoï cells are traingles or thetraedra which include an inclusion on void within. Ghosh and Moorthey [58] developed a special finite element formulation for Voronoï cells

it $\omega \in \Omega$ whose size is denoted by δ. This subdominium ω is used as a RVE to compute the effective elastic tensors. Two procedures can be applied for this purpose:

- Displacement boundary conditions (essential or Dirichlet boundary conditions) of the type of equation 2.72 are applied to the RVE:

$$u_i = \varepsilon_{ij} \cdot n_j \tag{2.72}$$

  where $\bar{\boldsymbol{\varepsilon}}$ is the volume-averaged strain. The condition 2.72 corresponds to the following interpretation of the Hooke's law, which is written from the standpoint of controllable strains:

$$\boldsymbol{\sigma} = \mathbf{C}^e_\delta : \bar{\boldsymbol{\varepsilon}} \tag{2.73}$$

  where the superscript e stands for *essential boundary conditions*. The former equation can be applied to each finite element in order to obtain an estimate of $\mathbf{C}^e_\delta$ and obtain the ensemble average of them $\langle \mathbf{C}^e_\delta \rangle$

- Force boundary conditions (natural or Neumann boundary conditions) of the type of equation 2.74 are applied to the RVE:

$$t_i = \bar{\sigma}_{ij} \cdot n_j \tag{2.74}$$

  where $\bar{\boldsymbol{\sigma}}$ is the volume-averaged stress and n_j the outer unit normal to the boundary. In this case the Hooke's law is written from the standpoint of controllable stresses:

$$\boldsymbol{\varepsilon} = \mathbf{S}^n_\delta : \bar{\boldsymbol{\sigma}}^{-1} \tag{2.75}$$

  where n denotes the natural boundary condition and δ the scale dependency. An estimate of $\mathbf{S}^n_\delta$ can be found for each element in the mesh, by using Equation 2.75. The ensemble average $\langle \mathbf{S}^n_\delta \rangle$ of this estimates could then be computed.

The following order relation is pointed out by Ostoja-Starzewski et al. [124][118]:

$$(\mathbf{S}^{\texttt{REUSS}})^{-1} \equiv \langle \mathbf{S}^n_1 \rangle^{-1} \leq \langle \mathbf{S}^n_\delta \rangle^{-1} \leq \mathbf{C}^{\text{eff}} \leq \langle \mathbf{C}^e_\delta \rangle \leq \langle \mathbf{C}^e_{\delta'} \rangle \leq \langle \mathbf{C}^e_1 \rangle \equiv \mathbf{C}^{\texttt{VOIGT}} \qquad \forall \delta' < \delta \tag{2.76}$$

where $\mathbf{S}^{\texttt{REUSS}}$ and $\mathbf{S}^{\texttt{VOIGT}}$ recall the Reuss and Voigt bounds of Section 2.4.1.

Expression 2.76 means that the larger the window scale δ the closer are the bounds, and in the limit $\delta \to \infty$, the bounds coincide and the difference between both types of boundary conditions disappears. The subscript $\delta = 1$ denotes the smallest scale. A proof for Equation 2.76, using the energy principles defined in Section 2.4.1, is given in reference [82]. In the same paper, the requirement of equivalency of the boundary conditions is shown to be an extension of the Hill Condition of Section 2.1.4.

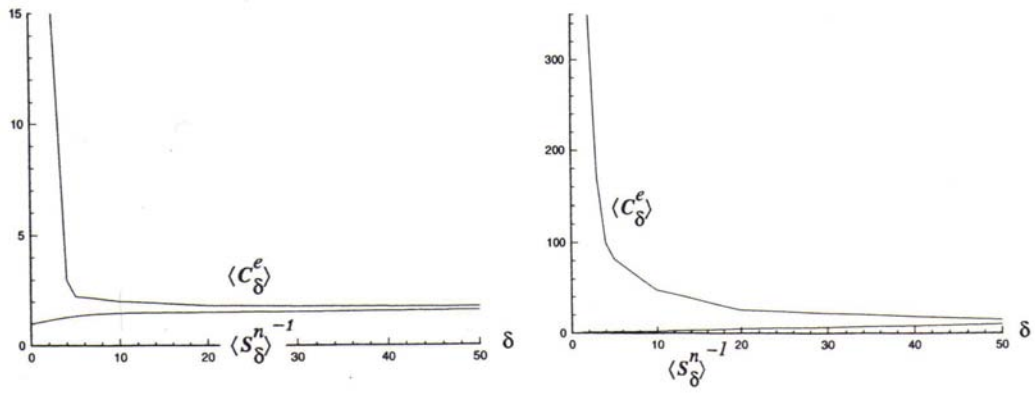

Figure 2.3: Convergence of bounds for the elasticity tensor
for the RVE increasing size for $C^f/C^m = 100$ (left) and $C^f/C^m = 10^4$ (right).
(Figure taken from Ostoja-Starzewski et al. [118])

Following this development, Ostoja-Starzewski and co-workers [118] [119] [125] and Jiang and Jasiuk [82] [81] devoted some papers to the determination of the RVE size and scale dependency of composite materials.

In reference [118] an extensive work is devoted to the determination of the RVE size. Several materials showing a wide range of contrast[14] values are considered, from rigid or stiff disks (having large values of the contrast) to holes (having near zero values). Elasticity Equations are solved using spring networks (Reviewed in Section 2.6.3). Figures plotting the convergence of stiffness and compliance tensors, which are computed by imposing essential (Equation 2.72) and natural (Equation 2.74) boundary conditions are given for each value of the contrast considered $(10^4, 100, 10^{-2}, 10^{-4})$. Fibre-reinforced composites, which are being considered in this work, normally have contrast in the range $100 - 10^4$, for which in the work by Ostoja-Starzewski, as shown in Figure 2.3, a size of the RVE of $L/d = 25 - 30$ seems to be enough. Further considerations on the inclusion shape are also given in the same work.

Variational principles

Drugan and Willis [47] give some quantitative values for the RVE size. Focusing on two-phase elastic composites with spherical and isotropic randomly distributed reinforcements and using the Hashin-Shtrikman variational principle the authors find the minimum RVE length needed for a given accuracy. As seen in Section 2.1.3, Drugan and Willis use explicitly a slightly different from the classical RVE definition, based only in the accuracy of the value of the effective property.

Their work is based on expressing the constitutive equation of the composite in the following non-local manner:

[14] In composite materials, usually the ratio between the elastic properties of the fiber and the matrix $(E^{(f)}/E^{(m)})$ is called *the contrast*.

$$< \boldsymbol{\sigma} > (\mathbf{x}) = \hat{\mathbf{L}} < \boldsymbol{\varepsilon} > (\mathbf{x}) - \frac{1}{2} < \tilde{\mathbf{T}} >_{,mn} (\mathbf{0}) \frac{\partial^2 < \boldsymbol{\varepsilon} > (\mathbf{x})}{\partial x_m \partial x_n} \tag{2.77}$$

Expressions for the fourth-rank tensors $\hat{\mathbf{L}}$ and $\tilde{\mathbf{T}}$ can be found in the same reference [47].

To perform the computation of the minimum RVE length for a given accuracy, they consider ensemble averaged strain fields $< \boldsymbol{\varepsilon} > (\mathbf{x})$ that vary with position and determine at what wavelength this variation will cause a variation in the first right-hand-side term in 2.77, which is, indeed, the local term. Therefore, they determine the RVE length by comparing the second right-hand-side term in 2.77 with the first.

As a result, they give the minimum RVE size for different accuracies, volume fractions of the reinforcement and different ratios of the elastic properties of the reinforcement and the matrix. They point out that for an accuracy of 1%, for volume fraction from 0.025 to 0.4 the RVE size should be at least 4.5 times the diameter of the reinforcement. For the same conditions, and for an accuracy of 5% the RVE should only be two times the inclusion diameter.

2.6.2 The Embedded Cell Approach (ECA)

The *Embedded Cell Approach* (ECA) is a computational method for the analysis of micromechanical stress and strain fields which combines macro and micromechanics modelling. The aim is to predict the microfields at high spatial resolution. It has been widely used for Metal Matrix Composites (MMC) [29] [90].

This technique models the heterogeneous material as a core which contains discrete phase arrangement (local heterogeneous region) and which is embedded within an outer region of homogeneous material to which far field loads or displacements are applied, as shown in Figure 2.4.

The inner region can be a highly detailed description of experimentally observed phase arrangement and the outer region may be described using some macroscopic constitutive law [90], determined self-consistently from the behaviour of the core [46], or even can be a coarse description of the global phase arrangement.

2.6.3 Spring networks

The use of the Finite Element Method in the analysis of microstructures requires of fine discretization and, consequently, a great number of finite elements which suppose large computation times. Instead of working with finite elements, Ostoja-Starzewski and coworkers [123][124] [8] use the *spring network* technique.

In this numerical technique the dominium is discretized in a regular network of springs. Inclusions (fibres) are forced to have its center in one of the network points. Then, mechanical properties are associated to each spring, depending on which material they represent.

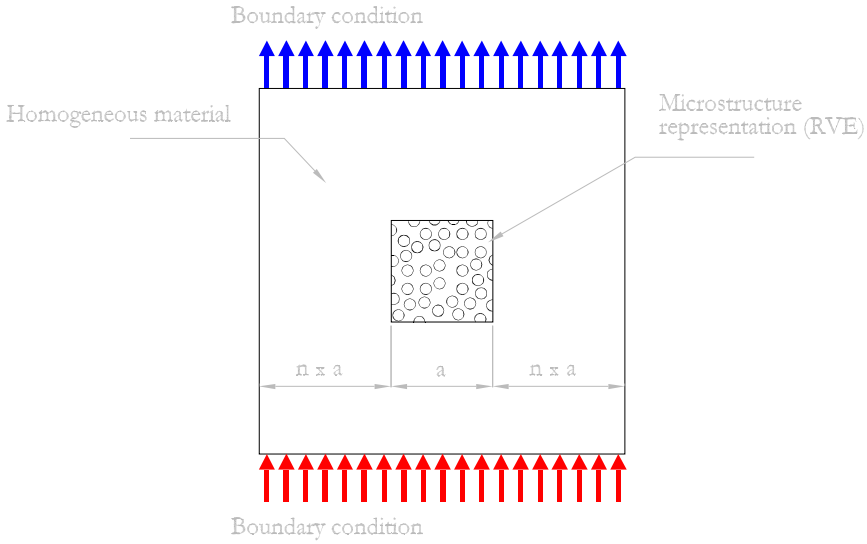

Figure 2.4: The Embedded Cell Approach

The equations of the springs are similar to those of the finite difference method [123].

Springs can have also an associated ultimate strength or strain and once they reach these value they are supposed to break and a zero value is given for its stiffness. Ostoja and co-workers have used this method for the simulation of damage evolution in random inclusion composites [124] and polycrystals [60].

Another important advantage of this approach is that, since fibres are forced to have its center in one of the network nodes, no re-meshing is needed.

2.7 Conclusions

In the present chapter, the main approaches for computing the effective properties of composite materials have been reviewed.

Although the Voigt and Reuss bounds of Section 2.4.1 give values which are far from real materials, can always be used as a necessary condition of any bound development. However, the Hashin-Shtrikman derived bounds for elastic two phase composite of Equations 2.45 - 2.52 give more accurate values and they will be used for the verification of the Statistical Volume Element developed in Chapter 5.

The different approaches of homogenization procedures imply periodicity of the geometry and so, cannot be used for the simulation of geometrically random materials.

The concept of Representative Volume Element (RVE) is of crucial importance in the

simulation of the microstructure of composite materials. Although in its theoretical definition, the RVE is an infinite limit, for the purposes of computational methods, a finite size volume RVE has to be found. From the mechanics standpoint there are several criteria which are applicable for this purpose and some work has been performed in this direction. Unfortunately, the works reviewed so far, which use different criteria for the RVE size determination, as summarized in Table 2.1 , lead to different RVE sizes which vary around from 4 to 20 times the fibre diameter.

The Embedded Cell Approach (Section 2.6.2) is a simulation technique for random microstructures which provides a solution to avoid boundary condition concentration effects.

Author	$\mathbf{c_f}$	$\mathbf{E^{(f)}/E^{(m)}}$	$\boldsymbol{\delta = L/r}$	**Type of Boundary Condition**	**Description**
Gusev [64]	0.27	23.3	7.5	Periodic	Convergence of effective properties. Spherical inclusions
Terada [150]	0.3	10	$30-40$	Displacement. Force. Periodic	Convergence of effective properties. Homogenization
Kanit [88]	$0.5, 0.7, 0.9$	200	Dependency on the number of simulations	Displacement. Force. Periodic	Monte Carlo Simulation. Grain - polycrystal. Voronoï Cell FEM
Drugan and Willis [47]	$0.025-0.4$	Voids (0), Rigid Particles (∞), ~ 10	9		Variational approach
Ostoja-Starzewski [118]	0.56	$100-10^4$	$50-60$	Force and Displacement	Convergence of effective properties. Fibre

Table 2.1: Summary on the different approaches to determine the RVE size

Chapter 3

Transverse Failure in Polymer Composites

3.1 Introduction

Fibre reinforced composites are normally composed of glass or carbon fibres and a polymer matrix. These fibres are much stronger than the polymer matrix and have as a main function to carry the load. The main function of the matrix is to transfer this load to the fibres.

As happened with the rule of mixtures[1], the failure behavior in the direction of the fibre is dominated by this constituent and, on the other hand, the failure behavior of the transverse direction[2] is influenced mainly by the behavior of the matrix. For this reason, and since the mechanisms involved in each one are uncorrelated[131] is is normally distinguished between:

- Fibre failure. Which affects laminae with main loads in fibre direction.
- Matrix failure. Which affects laminae with main loads in the transverse direction.
- Interface failure. Which causes loss of adhesion between fibre and matrix.

As was mentioned in the introduction chapter, the usual methods of design with composite materials try to align the load with the fibres but in complex geometries and in cross-ply laminates, loads and reactions may also take place in different directions to that of the fibres. Moreover, composites are seldom used exclusively in the transverse direction, but 90^o layers and off-axis ply layers are usually employed in common laminates. For these reasons, failure criteria for those plies are also required to reach a safe and efficient design.

From the point of view of damage mechanics the mechanical behavior of the transverse section is also of interest. It is generally accepted that the primary mechanisms of failure initiation in laminates are: fibre/matrix debonding and matrix failure and that

[1] Described in Section 2.3.1 of Chapter 2

[2] As has been used in the former chapters, the transverse direction or transverse plane is any direction or any plane perpendicular to the fiber direction

the predominant mechanism in the initial stage of mechanical degradation in composite laminates is the formation and growth of intralaminar matrix cracks in off-axis plies. As denoted by Asp et al. [13] [15], these cracks can be produced by yielding and cavitation and have an influence in stiffness degradation [6], damage [97, 73] and fatigue [35] and are related to delamination [113].

The close relation between the phenomena involved in the fracture initiation is expressed by Asp et al. [15], who affirms that:

> "in composites loaded in tension normal to fibers, three competing initiation mechanisms can be expected to occur: fiber/matrix debonding, yield in matrix and cavitation-induced brittle matrix failure. In a real composite, which may have an irregular distribution of fibers, it is expected that the local stress states would vary such a that the mix of deviatoric and dilatational stress components could vary from purely deviatoric to purely dilatational. Thus the matrix could yield in some regions while other regions could fail by cavitation-induced cracking."

Asp and co-workers are the responsible of an important set of papers [12, 13, 14, 15] regarding the initiation of matrix cracking transverse failure of long fibre reinforced composites. It is known -and it can be seen from the elasticity relations of Chapter 2- that transverse behavior of long fibre reinforced composites is matrix dominated but, as observed by Asp and co-workers [12, 14] and, in fact, the motivation for their work was that, the strain to failure of a transversely loaded composite (between 0.5 and 0.8%) is much lower than for the pure matrix in uniaxial tension (normally between 1.8 and 7%). In their works, they study the stress state in the matrix of fiber reinforced composites using the poker-chip test [12], they propose a criterion for crack initiation based on the dilatational energy density [13], and, using this criterion, they make predictions of matrix-initiated transverse failure for composites with different volume fractions and assuming different arrays of unit cells [14]. In another work [13], also using the proposed criterion, they analyze parametrically the influence of some other aspects like: the elastic modulus of the fibers and the presence of a fiber-matrix interphase. According to Asp and co-workers [12, 14, 15] the cavitation-induced brittle failure is assumed to occur at a point when the dilatational energy density attains a critical value. On the other hand, Asp and co-workers [12, 14, 15] use The Von-Misses criterion as a indicator of the beginning of the yielding in the matrix, although it is known that it overestimates the yield stress in the first quadrant of the stress plane, while in the other quadrants it is underestimated.

This chapter summarizes some micromechanical[3] failure criteria, specially the one developed by Asp and co-workers but, first reviews some macromechanical criteria.

3.2 Review of some macroscopic criteria

There already exist some in depth reviews of failure criteria for long fibre reinforced composites, like the one by Paris [126]. The purpose of this section is only to review those

[3]Micromechanical denotes here that these criteria can be applied to a single constituent

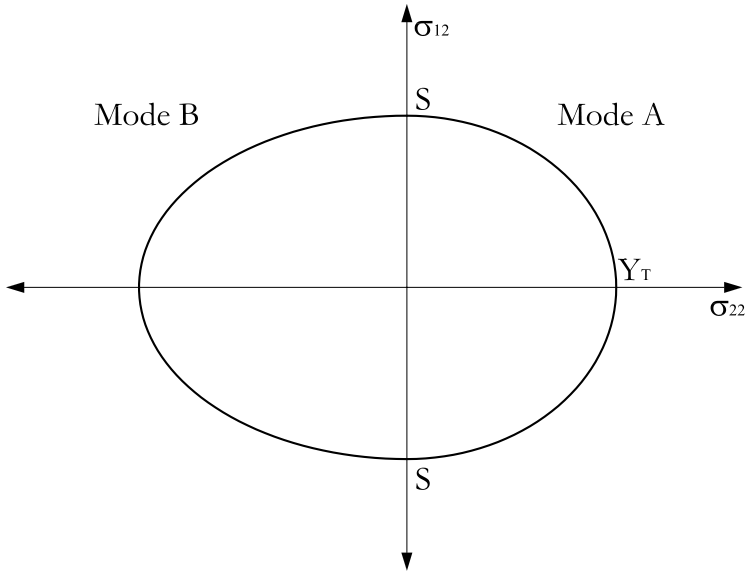

Figure 3.1: Hashin and Roten [68] criterion for matrix failure

which describe concepts which can be useful for this work.

3.2.1 Hashin's criterion

Usual transverse failure criteria for composites are concerned with strains and stresses which are present in the lamina, like the one proposed by Hashin and Roten [68]:

$$\left(\frac{\sigma_{22}}{Y}\right)^2 + \left(\frac{\sigma_{12}}{S}\right)^2 = 1 \tag{3.1}$$

where σ_{22} is the nominal stress in the lamina in the transverse direction, σ_{12} is the nominal shear stress in the plane of the lamina, S is the in-plane shear strength of the lamina and Y stands for the strength of the lamina in the transverse direction which must be replaced for the compression strength (Y_C) or tension strength (Y_T) if they are different. This criteria does not take into consideration interface failure and, as shown in Figure 3.1, poses that matrix failure mode can be modelled as a quadratic function of transversal and tangential stresses.

Hashin modified this criteria for the compressive mode [66]:

$$\left(\frac{\sigma_{22}}{2S_T}\right)^2 + \left[\left(\frac{Y_C}{2S_T}\right)^2 - 1\right]\frac{\sigma_{22}}{Y_C} + \left(\frac{\sigma_{12}}{S}\right)^2 = 1 \tag{3.2}$$

where S_T is the transversal shear strength, S is the shear strength and Y_C is the strength in the direction transversal to the fibres in absolute value while σ_{22} keeps its

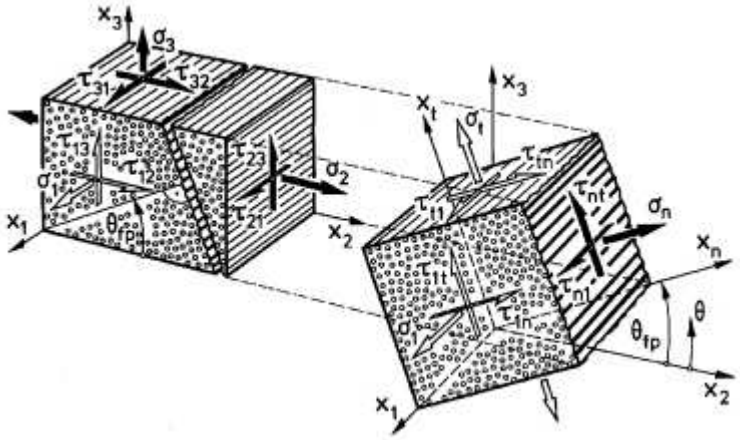

Figure 3.2: Stress components in a UD composite. In this figure σ_1 and σ_2 denote, respectively, σ_{11} and σ_{22} instead of principal components of the stress tensor as in the rest of this work . Source: Puck and Schürmann [131]

sign.

3.2.2 IFF Puck's criterion

Puck's criterion describes fibre failure (FF) and matrix or inter-fibre (IFF).In this section only the latter one will be considered, since it is the one related to the topic of this work.

Other approaches can be derived if the failure is assumed to happen in any plane parallel to the fibers where the stress vector has the components: σ_n, τ_{nl} (longitudinal direction or fiber direction) and τ_{nt} (transversal direction). A failure criteria can be written for this plane [131, 66]:

$$\left(\frac{\sigma_n}{Y}\right)^2 + \left(\frac{\tau_{nl}}{S}\right)^2 + \left(\frac{\tau_{nt}}{S_T}\right)^2 = 1 \tag{3.3}$$

where Y, S, S_T are, again, the allowable values for σ_n, τ_{nl} and τ_{nt}, respectively. From this starting point, Puck and Schürman made some improvements and proposed a new criteria for the transverse or inter-fiber failure [131]. Their starting point was to assume that failure happened at an inclined plane parallel to the fibres and, according to Mohr's theory[4] [107], they proceeded on the hypothesis that fracture is exclusively related to the stress components which act on the fracture plane: $\sigma_n, \tau_{nt}, \tau_{nl}$. Figure 3.2 plots these stresses for a general fracture plane θ.

These three stress components can be easily related to the stress components acting on the lamina:

$$\sigma_n = \sigma_{22} \cos^2 \theta \tag{3.4}$$

[4]Which will be reviewed later in this chapter

$$\tau_{nt} = -\sigma_{22}\sin\theta\cos\theta \tag{3.5}$$
$$\tau_{n1} = \sigma_{21}\cos\theta \tag{3.6}$$

Following Puck's nomenclature the stresses σ_n, τ_{nt} and τ_{n1} represent, respectively, a transverse stressing ($\sigma_\perp$), a transverse-transverse shear stressing ($\tau_{\perp\perp}$) and a transverse-longitudinal shear stressing ($\tau_{\perp\parallel}$). The subscripts of these *stressing* terms denote if they are perpendicular ($\perp$) or parallel ($\parallel$) to the fibre direction. Then, according to Puck and Schürmann [131]: "These three stresses $\sigma_n, \tau_{nt}, \tau_{n1}$ must necessarily have a common stress action plane and, consequently, must be compared to the fracture resistances R^{A5} of their action plane, and not just to some strength which might belong to any other fracture plane. Consequently, equation 3.3 can be written in a more general form:

$$\left(\frac{\sigma_n}{R_\perp^{(+)A}}\right)^2 + \left(\frac{\tau_{nl}}{R_{\perp\perp}^A}\right)^2 + \left(\frac{\tau_{nt}}{R_{\perp\parallel}^A}\right)^2 = 1 \qquad \text{for } \sigma_n \geq 0 \tag{3.7}$$

With this equation as starting point, Puck and Schürmann [131] and distinguishing between traction and compression developed the well-known Puck's criterion, which for an UD lamina and $\theta_{fp} = 0^o$ can be written:

$$\sqrt{\left(\frac{\sigma_{21}}{S_{21}}\right)^2 + \left(1 - p_{\perp\parallel}^{(+)}\frac{Y_T}{S_{21}}\right)^2\left(\frac{\sigma_{22}}{Y_T}\right)^2} + p_{\perp\parallel}^{(+)}\frac{\sigma_{22}}{S_{21}} = 1 \qquad \text{for } \sigma_{22} \geq 0 \tag{3.8}$$

$$\frac{1}{S_{21}}\left(\sqrt{\sigma_{21}^2 + (p_{\perp\parallel}^{(-)}\sigma_{22})^2} + p_{\perp\parallel}^{(-)}\sigma_{22}\right) = 1 \qquad \text{for } \sigma_{22} < 0 \tag{3.9}$$

where:

$$p_{\perp\parallel}^{(+)} = -\left(\frac{\mathrm{d}\sigma_{21}}{\mathrm{d}\sigma_{22}}\right)_{\sigma_{22}=0} \quad \text{of } (\sigma_{21}, \sigma_{22}) \text{ curve }, \sigma_{22} \geq 0$$
$$p_{\perp\parallel}^{(-)} = -\left(\frac{\mathrm{d}\sigma_{21}}{\mathrm{d}\sigma_{22}}\right)_{\sigma_{22}=0} \quad \text{of } (\sigma_{21}, \sigma_{22}) \text{ curve }, \sigma_{22} \leq 0$$

Usual values for this derivative terms are given by Puck et al [130]: $p_{\perp\parallel}^{(+)} = 0.3$ and $p_{\perp\parallel}^{(-)} = 0.2$. The graphical interpretation of IFF Puck's criterion is given in Figure 3.3.

The criteria reviewed so far are macroscopical design criteria and they do not take into account local phenomena which take place in the matrix, and which may be responsible of failure. Instead of this, they use stresses associated to a plane. Paris et al [126] proved experimentally that *to associate the failure of the matrix at a plane to a certain interaction between the components of the stress vector associated to the plane does not, generally speaking, appear to be a physically based hypothesis.* In this direction Dávila and Camanho [42] have recently developed, under the name of LaRC, a group of failure criteria which take into account *in situ* effects.

[5] Where "A" denotes action plane

Since the present work is based on microscopical observation and tries to relate the failure behavior , in the following sections local phenomena and failure criteria are reviewed. First, it is convenient to present a short description of the matrix stress state in the transverse direction of a composite.

3.3 Stress state in the matrix of composites loaded transversely

One of the most common materials which are used for matrixes in long fibre reinforced composites are epoxies, and, more generally, polymers. These materials are plastics, or equivalently, they yield when an stress greater than certain constant value is applied to them. As was said in the introduction, although these materials are plastics the transverse failure of composites is normally brittle. Some researchers have analyzed these phenomena.

Driven by some studies [55, 43] which suggested that the triaxial matrix stress state could be important for initiation of transverse failure in the matrix at low strains, Asp and co-workers analyzed the stress state in the matrix of long fiber reinforced composites [12]. They performed Finite Element analysis to determine the stress state in a transversely loaded composite. They used a unit cell containing a single fiber and used periodicity conditions to model a square array of fibers.

From the FE results, they observed that a triaxial stress state acts in the matrix of the composite. The ratio of the stress component magnitudes is approximately 1: 1: 2 (x :y : z), where Z, the largest stress component, is in the loading direction. This ratio varies with position in the composite.

Since a triaxial stress state appears in the matrix of transverse loaded composites the poker-chip test, which has been used widely for rubbers, was proposed like a convenient test to determine the properties of the matrix of the composite. In this test a disk-shaped specimen is subjected to a traction force, in a way that the central part of the specimen is submitted to a nearly uniform state of triaxial tension [75]. The test and the specimen are schematized in Figure 3.4.

Using the governing equations of the poker-chip test they obtained a stress state relation close to 1:1:2 (x:y:z) that is, similar to the stress state in the matrix of a composite loaded in the transverse direction.

Asp and co-workers [12] performed tests for four different resin systems and compared the results of the obtained strength and strain to failure with those obtained with uniaxial tests. The notation used for the names of the epoxy systems is epoxy component/curing agent, where the name of each epoxy component and curing agent can be found on the *List of symbols* section of this work. A good description of each resin and curing agent can be found in the chapter of *Comprehensive Composite Materials* by Nairn [112]

The results they obtained are shown in Table 3.3, where it can be seen that the strength

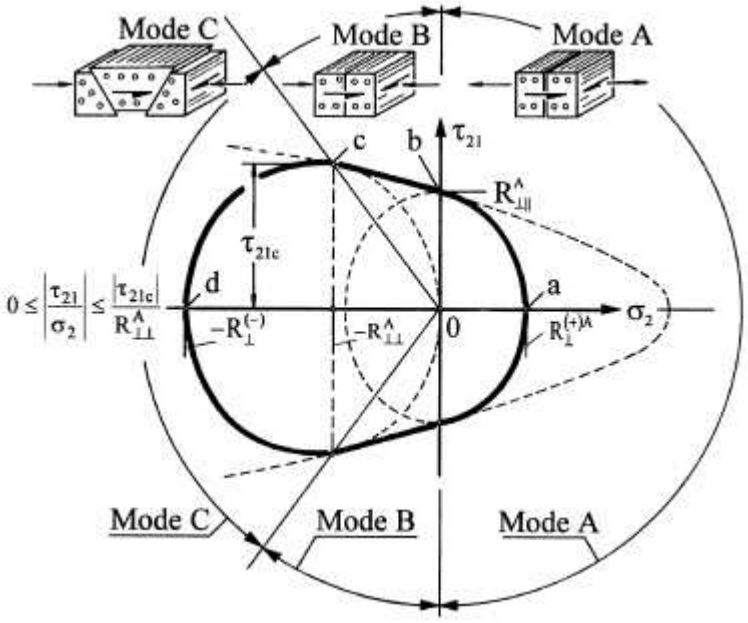

Figure 3.3: Graphical interpretation of Puck's criterion for $\sigma_{22} - \sigma 21$ plane

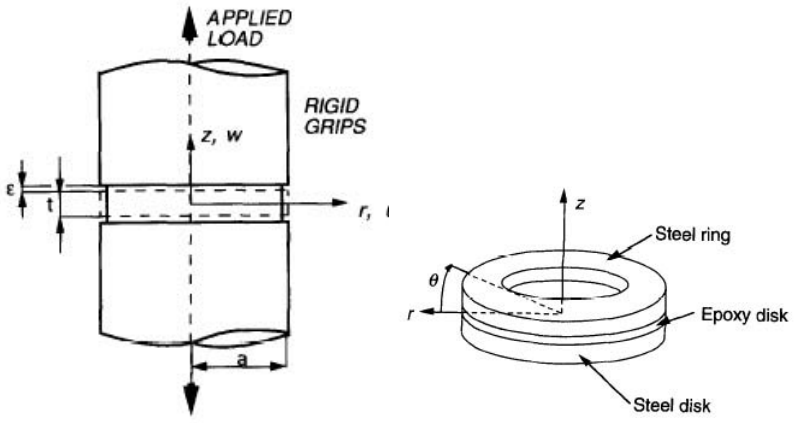

Figure 3.4: Illustration of the poker chip test (left) and typical poker-chip specimen (right). Source: Asp et al.

Resin system	Uniaxial strength (MPa)	Poker-chip strength (MPa)	Uniaxial strain to failure (%)	Poker-chip strain to failure (%)
DGEBA/DETA	69.0 ± 5.4	29.1 ± 4.5	7.00 ± 1.5	0.85 ± 0.1
DGEBA/MHPA	85.9 ± 3.8	26.9 ± 5.7	6.5 ± 1.0	0.57 ± 0.2
DGEBA/APTA	73.1 ± 1.2	32.0 ± 2.2	6.14 ± 0.5	0.79 ± 0.1
TGDDM/DDS	59.9 ± 12	26.6 ± 7.7	1.77 ± 0.4	0.55 ± 0.2

Table 3.1: Fracture data and standard deviations from triaxial and uniaxial tests. Source: Asp et al. [12]

of the matrix under triaxial state can be reduced from a 55% to a 70% with respect to the strength under uniaxial stress state and the strain to failure can be reduced between 70% and 91%. Moreover, the obtained values of the strain to failure with the poker-chip test are much more similar to the typical values obtained with glass fiber/epoxies composites than those obtained with the uniaxial test.

Another important conclusion of the research is that epoxies cured with aliphalitic curing agents (DGEBA/DETA and DGEBA/APTA) show similar stress/strain behavior with strains to failure around 0.8% and epoxies cured with aromatic and cyclo-aliphatic curing agents (DGEBA/MHPA and TGDD/DDS) also showed almost identical stress/strain behavior and failed at strains of 0.5%.

Finally, as a conclusion, they pointed out that debonding, pre-existing material flaws and non-uniform fiber distribution are likely to reduce initiation values of transverse strain failure.

3.4 Criteria for matrix crack initiation

As observed by Asp and co-workers [13], classical approaches in the modelling of matrix crack initiation observed mainly yielding[6] as the first cause and several criteria were proposed. But these criteria usually predicted the effect of hydrostatic compression on the yield stress satisfactorily but were not accurate when hydrostatic tension was applied.

Asp and co-workers [13] tested three epoxy systems and computed the yield criteria modified to account the effect of hydrostatic stress. The comparison of the tests data and the prediction showed that that criterion did not predict the behavior in stress states close to purely hydrostatic tension. Asp and co-workers proposed that under stress states resembling those in matrix constrained between fibers, e.g. equibiaxial and equitriaxial tension (as seen in their former work [12]), yielding is suppressed while brittle failure, presumably caused by crack growth from cavitation, occurs. Consequently, they proposed a criterion for this mode of failure based on the critical dilatational strain energy density.

[6] Yielding is a commonly known phenomenon, associated to plasticity, which produces large increment of strains for small increments of stress when the effective stress (See definition in Section A.2.3) reaches certain value usually called yield stress and denoted σ_y.

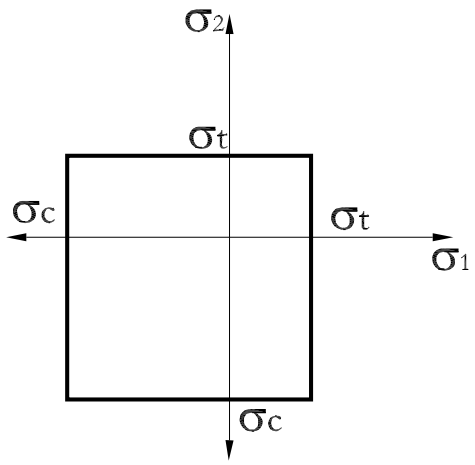

Figure 3.5: Maximum stress criterion

For the experimental validation of the proposed criteria Asp and co-workers performed uniaxial compression and biaxial tension tests using three different epoxy systems. In the following of this section, common yielding criteria are reviewed and the criteria proposed by Asp and co-workers (the dilatational energy density criteria) is summarized.

3.4.1 Brittle failure: Mohr's criterion

The maximum stress criteria is often employed to predict the failure of brittle materials. This criteria states that failure occurs when the maximum principal stress reaches the uniaxial tension strength (X_t) or the uniaxial compression strength (X_t). In a plain stress state, this criteria can be seen as a square defined by X_t and $-X_c$. The criteria is satisfied if the principal stresses σ_1, and σ_2 lie within this square, as shown in Figure 3.5.

A more advanced approach was proposed by Mohr [107], which affirmed that any plane stress situation could be expressed in terms of a normal stress σ_n and a shear stress τ_n. From this created his well-known Mohr's circle, shown in Figure 3.6. Mohr's failure criteria or internal-friction theory states that failure occurs when the Mohr circle at a point exceeds the envelope created by the two Mohr's circles for uniaxial tensile strength and uniaxial compression strength. This envelope is also shown in the same Figure, with a dashed line.

This failure criteria can also be expressed in terms of the principal stresses. In this case, if it is plot in the $\sigma_1 - \sigma_2$ plane it coincides with the maximum stress criterion in the first and third quadrants. In the second and fourth quadrants it can be represented as a straight line between $(0, \sigma_t)$ and $(-\sigma_c, 0)$ and a straight line between $(0, -\sigma_c)$ and $(\sigma_t, 0)$, respectively. Figure 3.7 shows Mohr's criterion and maximum stress criterion in the $\sigma_1 - \sigma_2$ plane.

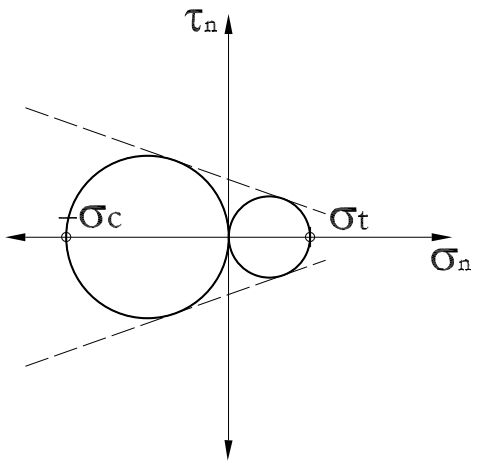

Figure 3.6: Mohr's failure criterion in $\sigma_n - \tau_n$ plane

Mohr's criterion has been classically employed in the mechanics of soils and for concrete. Usually it is also employed for brittle failure of polymers.

3.4.2 Yielding failure: von Mises and Tresca criteria

The von Mises criterion states that failure occurs when the elastic shear strain energy density in the material reaches a critical value. It assumes the yielding to be isotropic. The expression of the yield stress is:

$$\sigma_{VM}^2 = J_2 = \frac{1}{2} s_{ij} s_{ij} \tag{3.10}$$

Where J_2 is the second invariant of the deviatoric part (s_{ij}) of the stress tensor[7].
An equivalent formulation of the criterion is usually:

$$\sigma_{VM}^2 = \frac{(\sigma_1 - \sigma_3)^2 + (\sigma_2 - \sigma_3)^2 + (\sigma_1 - \sigma_2)^2}{6} \tag{3.11}$$

where the principal stresses σ_i follow the convention $\sigma_1 > \sigma_2 > \sigma_3$. In this form, this criteria can be seen graphically as a cylinder whose axis σ_o is located in the intersection of the three planes defined by the principal stresses[8] (that is, $\sigma_1 = \sigma_2 = \sigma_3$).

The Von Mises criterion does not predict differences in yield stress between compression and tension, for this reason Raghava et al.[134] suggested the following modification:

$$\begin{aligned} &2(\sigma_{yc} - \sigma_{yt})(\sigma_1 + \sigma_2 + \sigma_3) + \\ &\quad + [(\sigma_1 - \sigma_2)^2 + (\sigma_2 - \sigma_3)^2 + (\sigma_3 - \sigma_1)^2] = 2\sigma_{yc}\sigma_{yt} \end{aligned} \tag{3.12}$$

[7] See Sections A.2.2 and A.2.3

[8] As defined in Section A.1, the planes on which the shear stresses vanish are called the principal planes and the normal stresses on those planes are called the principal stresses

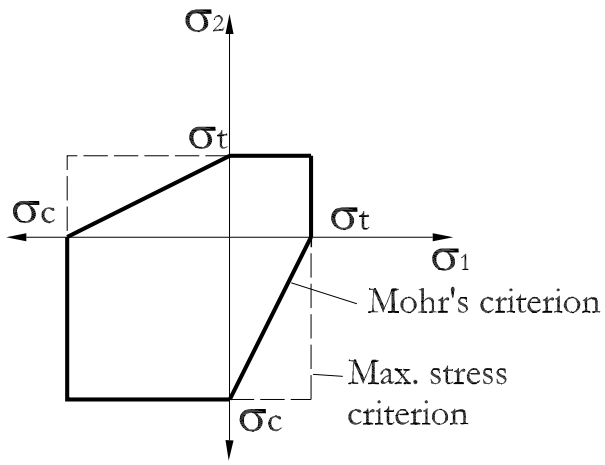

Figure 3.7: Mohr's failure criteria in $\sigma_1 - \sigma_2$ plane

Another well-known approach, the Tresca criterion, proposes that yield will occur when a critical value of the maximum shear stress, σ_s, is reached:

$$\sigma_s = \frac{1}{2}(\sigma_1 - \sigma_3) \tag{3.13}$$

The Tresca criterion can be seen graphically as an hexagon on the $\sigma_1\sigma_2$ plane. This criteria also can be modified to take into account the dependence of hydrostatic pressure:

$$\sigma_s = \sigma_s^0 - \alpha(\sigma_1 + \sigma_2 + \sigma_3) \tag{3.14}$$

where σ_s^0 is the shear yield stress in the absence of any overall hydrostatic pressure and α is a material constant. Both can be found as functions of the compression (σ_{yc}) and tension (σ_{yt}) yield limits, which can be determined experimentally:

$$\sigma_s^0 = \frac{(\sigma_{yc}\sigma_{yt})}{\sigma_{yc} + \sigma_{yt}}, \qquad \alpha = \frac{1}{2}\frac{\sigma_{yc} - \sigma_{yt}}{\sigma_{yc} + \sigma_{yt}} \tag{3.15}$$

Yield criteria are appropriate for ductile materials, like metals or plastics, but reinforced polymers have brittle failure and may not be useful. This fact has been noticed by some authors [131] and will be discussed in section 3.4.4.

3.4.3 Microcavitation: Dilatational energy density criterion

The strain energy of Section 2.4.1 can be expressed s the addition of two components, the dilatational and the distortional energies. The distortional term can be written:

$$U_d = \frac{1}{4G}s_{ij}s_{ij} \tag{3.16}$$

where G is the shear modulus. It can be seen, by comparison of equations 3.10 and 3.16, that the distortional energy density is the physical basis of the Von Mises criterion

Test method	Epoxy system					
	DGEBA/DETA		DGEBA/APTA		TGDDM/DDS	
	U_v	U_d	U_v	U_d	U_v	U_d
Poker chip	0.17	0.00	0.20	0.00	0.13	0.00
Thermally loaded epoxy disk (2D)	0.16	0.33	0.27	0.48	0.12	0.23
Biaxial tension	0.21	0.70	0.34	1.00	0.21	0.61
Uniaxial tension	$-^a$	$-^a$	$-^a$	$-^a$	0.055	0.42

Table 3.2: Dilatational (U_v) and distortional (U_d) energy densities (MPa) at fracture for different test methods (^{a}: Non-linear elastic behavior) Source: Asp et al. [13]

[13].

Under the condition that the distortional energy density at a point is small, much below that required to cause yielding, Asp et al. [13] proposed that microcavitation will occur when the dilatational energy density at a point reaches a critical value. Assuming the material to be linearly elastic, the criterion can be written:

$$U_V = \frac{1-2\nu}{6E}(\sigma_1+\sigma_2+\sigma_3)^2 = U_V^{cri} \tag{3.17}$$

where σ_1, σ_2 and σ_3 are the principal stresses, ν is the Poisson's ratio and E the Young's modulus. When is satisfied micro-cavitation[9] can be considered to start.

3.4.4 Comparison of criteria

Asp et al. [13] carried out some uniaxial, biaxial and multiaxial tests with three different epoxies. With the uniaxial tests the material constants (σ_{yc}, σ_{yt}) are determined and with the biaxial tests a prediction of the yielding is done with each of the formerly described criteria.

Experimental results show a better agreement in the compression region with the Tresca criterion and in the tension region with the von Mises criterion. Since this criteria are three-dimensional it is possible to predict yielding for the composite-like stress state of the poker-chip tests, as decribed in a former work by Asp et al. [12]. Results show that matrix yielding will not cause initiation of failure in glass fiber/epoxy composites loaded transversely and having equitriaxial stress states.

Finally Asp and co-workers [13] compute the dilatational (U_v) and distortional (U_d) energies for each test and epoxy. This computations are shown in Table 3.2.

From results in Table 3.2, some remarks are done by Asp and co-workers [13]:

- The critical value of the dilatational energy density (U_v) is nearly constant for DGEBA/DETA and DGEBA/APTA, and not very different for TGDDM/DDS.

[9] Cavitation is a known phenomena in fluids but here it refers to the apparition of voids or micro-holes.

- The value of U_v is higher for the three epoxies in the biaxial test than in the poker-chip test. This may be caused by the fact that the biaxial test produces unequal principal stresses and, consequently, significant deviatoric stress components which increase the distortional energy density (U_d).

The work of Asp et al. [13] leads to an important conclusion: in evaluating matrix behavior in fiber composites loaded transversely, both yielding and crack initiation from microcavitation must be considered.

3.5 Prediction of transverse failure

From the works by Asp and co-workers it has been seen that matrix in long fiber reinforced composites loaded transversely are submitted to a nearly equitriaxial stress state [12] which cause crack initiation and that the dilatational energy density criterion is a useful indicator of this phenomena in epoxies[13].

From this basis, Asp et al. [15] performed some simulations and tests on glass fiber composites loaded transversely. Three different packing arrangements were simulated: square, hexagonal and square-diagonal each for different volume fractions between 0.2 and 0.8. They assumed two different modes of failure: matrix cracking and yielding. Initiation of matrix cracking is assumed to happen when the dilatational energy density reached a critical value $U_v > U_v^{crit}$, being the critical value U_v^{crit} a parameter of the material which they have already obtained experimentally in a previous work [13]. For the yielding mode they used von Mises criterion.

The results of the FE modelling show how in any case the critical yield stress was reached before the dilatational energy density reached his critical value. That means, the cavitation-induced brittle fracture (matrix-cracking) is the more critical of the two failure modes considered. However, the once the crack initiation has started, it may cause local yielding due to stress concentration in cracked zones. They obtained plots of ultimate strength (σ_{ult}) and ultimate strain (ε_{ult}) versus the fiber content (v_f), as shown in Figure 3.8, where square-diagonal array (square array tilted 45° to the load direction) turns out be the most critical of the three analyzed arrays.

They also compared the results from the square fiber array with the experimental results reported by de Kok [43] and produced plots of ultimate strength (σ_{ult}) and ultimate strain (ε_{ult}) versus the fiber content (v_f), showing predictions using von Mises yield criteria and dilatational energy density criteria, as shown in Figure 3.9. Results show good agreement with experimental data.

3.6 Conclusions

- Macromechanical and micromechanical failure criteria for the transverse section of long fibre reinforced composites have been reviewed.
- From the micromechanical criteria, the dilatational energy density, seems to predict well the failure on carbon fibre and glass fibre reinforced composites.

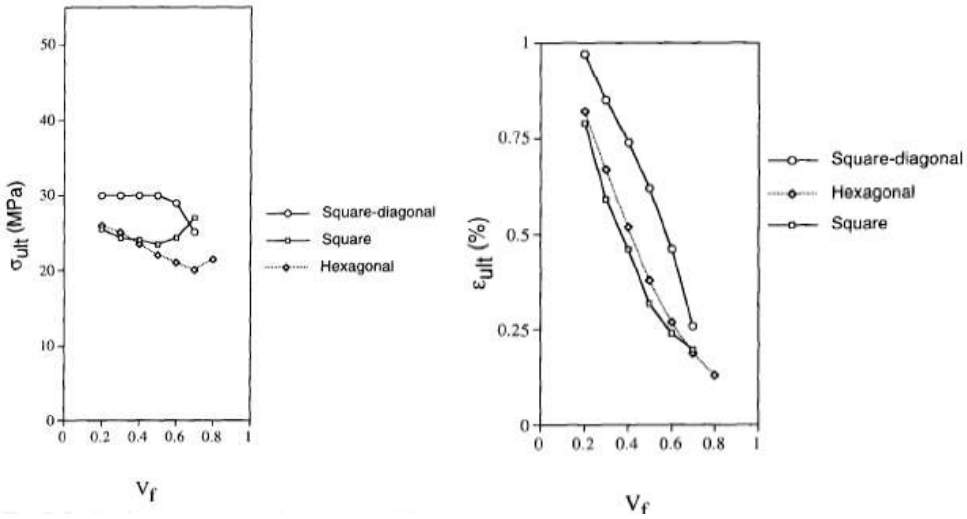

Figure 3.8: Ultimate strength (σ_{ult} and ultimate strain ε_{ult}) versus fiber content (v_f))
Source: Asp et al. [15]

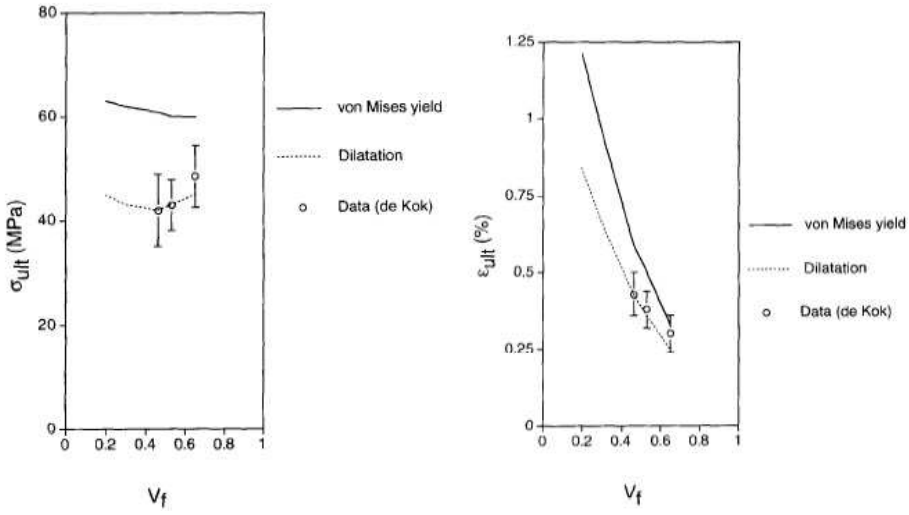

Figure 3.9: Experimental data and Failure predictions (von Mises and Dilatational energy)
Source: Asp et al. [15]

- Works which show the dependency of the results of simulations on the chosen geometry of the unit cell have been reported.

Chapter 4

Models for Random Multi-phase Materials

4.1 Introduction

Traditionally, the study of the micromechanics in composite materials has been performed assuming periodicity or regularity in the distribution of the fibre. Often, a single inclusion model has been used to represent the material [38]. This approach provides simplifications which lead to the possibility of analytical solutions or, in the case of computational methods, reduces the computation time. However, this approach may represent an idealized material which may be useful for computing effective elastic properties but differs from the reality in some important aspects.

It has been experimentally shown that the void and reinforcement distribution have strong effect on the effective properties of materials [19] [100] [33] and on their plastic behaviour [95]. For example, in the work by Lewandowski et al. [96] it is shown how locations with reinforcement clustering are more likely to suffer damage initiation and accumulation. The work of Werwer et al. [157] shows the dependency of hardening mechanisms of metal matrix composites on the inclusion distribution. Recently, the work by Matsuda et al. [102] showed the dependency of micro stress and strain fields in long fibre reinforced laminates on the fibre distribution and pointed out that those distributions should be analyzed in depth for damage prediction.

Some researchers have shown that the computed mechanical behavior depends on the choice of the unit cell geometry which is used in the analysis [98] [160], so the computationally advantageous use of periodic boundary conditions together with deterministic unit cells supposes certain dependency on the discretization or chosen representation of the material. According to Ostoja et al [124] when considering the random distribution of the microstructure of composite materials some questions emerge:

1. what is the effect of randomness of inclusions' arrangements versus (the usually assumed) periodicity on the damage formation and evolution

2. what are such effects, in terms of damage patterns and effective constitutive laws,

for a wide range of material parameters?

3. what are the scale effects on statistics of key parameters, such as the strain-to-failure ratio?

4. what are effective stochastic constitutive laws?

This chapter tries to review the theory and state-of-the-art of the research in this direction. First some definitions about random fields are given. The tools for statistical modelling of composite materials are summarized in Section 4.4. Some models for the simulation of random composite materials are reviewed in Section 4.5. First, in Section 4.2, a review on the main concepts of random fields is given. The basics from multivariable statistics can be found in books such as that written by Johnson [83]. One may consult the book by Chiang [36] for a further knowledge on stochastic processes and the book by Vanmarcke [155] for the concepts on random fields.

4.2 Random fields: properties and definitions

4.2.1 Random fields

When analyzing real materials in a microscopic scale there are many variables which one should consider random, and which depend on their spatial position or depend on the instant in which they are measured. In other words, a random variable, i.e. the concentration of certain pollution element in the water of a river, may be strongly related to the concentration in the points in the nearby and to the concentration in previous time instants. The same could be said of structural loads such as wind or earthquakes in buildings or civil constructions. This correlation can be defined in mathematical terms [40]. Let $\mathbf{x} \in \mathbb{R}^d$ be a spatial location in a d-dimensional space and let us assume $Z(\mathbf{x})$, measured in $\mathbf{x}$, is a random variable. If we let $\mathbf{x}$ vary over an index set $\Omega \subset \mathbb{R}^d$, we can express the multivariable random field $Z(\mathbf{x})$ as:

$$\{Z(\mathbf{x}) : \mathbf{x} \in \Omega\} \tag{4.1}$$

A process which variation is given in space and time is designed:

$$\{Z(\mathbf{x}; t) : \mathbf{x} \in \Omega, t \in T\} \tag{4.2}$$

If $x \in \mathbb{R}$ (that is, the variable is only function of one spatial dimension), the term *random process* is used instead of *random field*.

Usually, the very first assumption which is done when estimating random fields, is the assumption of *ergodicity* of the field. A random field is said to be *ergodic* when any information about it can be obtained from a single realization[1].

[1] A plain definition of *realization* could be "the event for which a random variable obtains a definite and unique value"

4.2.2 Types of Random Fields

Depending on the nature of the domain Ω, four types of random fields are defined [40]:

- *Time series* or *Random series* in which Ω is the temporal dimension. Usually the fatigue behaviour of composite materials [86] [137] and general mechanical engineering materials [24] [45] are modelled using time series.
- *Geostatistical data*. When the spatial index $\mathbf{x}$ varies continuously within a subset of $\mathbb{R}^d$. Most of the physical properties of materials can be seen as geostatistical data. In fact the science of *Geostatistics* has been mainly developed in the study of geology and earth sciences.
- *Lattice data*. When $\mathbf{s}$ is a set of equally-spaced points distributed in $\mathbb{R}^d$ and related in some way. Sometimes, in measuring properties, this properties are computed as mean values. Sometimes, like it happens in finite element meshes, the same value of the property is considered for a subdomain (the element). In these cases we are working with lattice data.
- *Point patterns*. In this case the random variable happens only in some points $\mathbf{s}$. Actually, the random variable being analyzed is the location or the event (and sometimes also some magnitude related to it). The random position of carbon or glass fibres in a fibre reinforced composite is a good example of point pattern [114] [141].

4.2.3 Properties of random fields

A random field $Z(\mathbf{x}) : \mathbf{x} \in \Omega$ is *homogeneous* if its distribution functions remain invariant to translations in the spatial dimensions. This means that the probability functions in this field only depend on the relative position. In one-dimensional fields the term *stationary* is usually employed instead of *homogeneous*.

Since in real applications it is sometimes difficult to obtain data for which the condition of statistic homogeneity stands, some relaxations on this conditions can be applied [120, 121], as is shown in Section 4.2.5.

A random field $Z(\mathbf{x}) : \mathbf{x} \in \Omega$ is second-order stationary if [115]:

- The value of the mean μ does not depend on the position $\mathbf{x}$

$$E[Z(\mathbf{x})] = \mu \qquad \forall \mathbf{x} \in \Omega \tag{4.3}$$

- There exists a function $B(\cdot)$ called stationary variance, and it is defined as:

$$\mathrm{Cov}[Z(\mathbf{x}_i), Z(\mathbf{x}_j)] = B(\mathbf{x}_i, \mathbf{x}_j) = B(\mathbf{x}_i - \mathbf{x}_j) = B(\mathbf{h}) \tag{4.4}$$

where Cov[,] is the covariance, defined in the Appendix B (Equation B.10). If we consider any lineal combination taking m random field values:

$$a_1 Z(\mathbf{x}_1) + \cdots + a_m Z(\mathbf{x}_m) \tag{4.5}$$

with the coefficients $\{a_i\} \neq 0$ and arbitrary locations $\{x_i\}$, the variance of this lineal combination has to be non-negative.

Since the variance is a linear operator [115], this implies:

$$\sum_{i=1}^{m} \sum_{j=1}^{m} a_i a_j B(\mathbf{x}_i, \mathbf{x}_j) > 0 \tag{4.6}$$

A function $B(\mathbf{x}_i, \mathbf{x}_j)$ for which the equation 4.6 stands is called *positive defined*. This is a very desirable property because, when using positive defined functions for constructing the matrices of lineal systems of equations some computationally efficient numerical methods can be used in their resolution.

If besides of being second order stationary, the difference between any two values of the random field is a function of the vector $\mathbf{h}$ which joins their respective positions:

$$\mathrm{Var}[Z(\mathbf{x}_i) - Z(\mathbf{x}_j)] = 2\gamma(\mathbf{x}_i - \mathbf{x}_j) = 2\gamma(\mathbf{h}) \tag{4.7}$$

the random field is *intrinsically stationary*. Then the function $2\gamma(\mathbf{h})$ is called *variogram*. The field of statistics which studies the instrinsically stationary random fields, that is, those in which a variogram can be defined, is called *Spatial Statistics* or *Geostatistics* [40].

A random field is said to be *isotropic* if the density functions keep invariant to rotations in the spatial dimensions. In such a case the statistics of the random field do not depend on the direction, but only in the distance between points of the domain. Therefore, the variogram of an isotropic random field it is only a function of the norm or distance of the vector $\mathbf{h}$:

$$\mathrm{Var}[Z(\mathbf{x}_i) - Z(\mathbf{x}_j)] = 2\gamma(\mathbf{x}_i - \mathbf{x}_j) = 2\gamma(\|\mathbf{h}\|) = 2\gamma(h) \tag{4.8}$$

Usually the variogram (and also the covariance function) of natural processes has a constant values for $h > h_0$. Then h_0 is called the correlation length and it can be interpreted as the minimum length for which the values of a random field in two different locations can be considered uncorrelated.

4.2.4 Fourier series expansion of the covariance function

The theorem of spectral representation or Wiener-Khinchin's theorem of transformation [40, 32, 114] relates the covariance function of a second-order stationary field[2] $B(h)$ with the spectral density function or power spectrum $G(f)$ using the Fourier transform:

[2] That is, the stationary variance.

$$B(h) = \int_{-\infty}^{\infty} G(f) e^{i2\pi fh} df \tag{4.9}$$

and its inverse transformation:

$$G(f) = \int_{-\infty}^{\infty} B(h) e^{-i2\pi fh} dh = 2 \int_{-\infty}^{\infty} B(h) \cos(2\pi fh) dh \tag{4.10}$$

where i is the imaginary unit, $i = \sqrt{-1}$.

The spectral density function has analog properties to those of the covariance [32], like non-negativeness.

The transformation of equation 4.9 converts a problem in the spatial dominium into a problem in the frequency dominium, and consequently, the physical interpretation of it stops being intuitive. In spite of that, this transformation is useful because allows to express a random field using Fourier series:

$$Z(k) = \sum_{j=0}^{n-1} A(j) e^{i2\pi kj/n} \qquad k = 0, \ldots, n-1 \tag{4.11}$$

or in an equivalent way:

$$Z(k) = \sum_{j=0}^{n-1} [a_j \cos(2\pi jk/n) + b_j \sin(2\pi jk/n)] \qquad k = 0, \ldots, n-1 \tag{4.12}$$

The relation between 4.11 and 4.12 is established by means of:

- $A(j) = a_j - ib_j = \|A(j)\| e^{-i\phi(j)}$ A(j) is called the j-th Fourier coefficient.
- $\|A(j)\| = \sqrt{a_j^2 + b_j^2}$ is the amplitude
- $\phi(j) = \tan^{-1}(-b_j/a_j)$ is the phase of the j-th Fourier coefficient.

4.2.5 Definitions for random materials

As seen in section 4.2.3 some type of random fields have properties which simplify dealing with them. But these definitions are made from the theoretical point of view and when working with real random fields some of those properties may not be accomplished in a strict sense. For this reason, Ostoja-Starzewski [120, 121], based on the work perfomed on machine made paper, propose new definitions which can be applied to the random fields related to engineering mechanics materials. These definitions stand on considering the difference between strict-sense stationarity (SSS) and wide-sense stationarity (WSS). The first one corresponds with the stationarity (homogeneity) as defined in section 4.2.3. Recalling this section a random field is stationary or homogeneous if its distribution functions remain invariant to translations in the spatial dimensions. This means that the probability functions in this field depend on the relative position.

If wide-sense stationarity is considered (WSS) only the mean is expected to be invariant with respect to translations and the covariance functions are expected to depend on the interpoint separation only, that is:

- The mean of the field, $E[Z(\mathbf{x})]$, can be considered constant, as seen in equation 4.3
- For any two points $\mathbf{x}_i, \mathbf{x}_j \in R^d$, the covariance

$$\begin{aligned} \mathrm{Cov}[Z(\mathbf{x}_i), Z(\mathbf{x}_j)] &= \langle [Z(\mathbf{x}_i) - \langle Z(\mathbf{x}_i)\rangle] \cdot [Z(\mathbf{x}_j) - \langle Z(\mathbf{x}_j)\rangle]\rangle = \\ & \mathrm{Cov}(Z(\mathbf{x}_i) - Z(\mathbf{x}_j)) = \mathrm{Cov}(\mathbf{h}) \end{aligned} \tag{4.13}$$

Ostoja-Starzewski affirms in [121] that this conditions are sufficient for the Representative Volume Element[3]. It can be seen clearly that these conditions are the same that those established in Section 4.2.3 for a second-order stationary field, but without assuming the existence of a stationary variance.

Let us consider that a random composite material is being analyzed by means of a finite size RVE. The condition for the estimation of any property of a random field is that of *ergodicity*. According to Ostoja-Starzewski, when working with RVEs, the random fields are required to be *quasi-ergodic*. That concept means that the random field should be ergodic in volumes small as compared to the characteristic length scales L_θ of variation of the field statistics.

In such a case, an appropriate model is given by a *strict-sense* (SS) cyclostationary random field, which, for a planar system of square $L \times L$ unit cells, is stated as:

$$F(\mathbf{x}_1 + m\mathbf{L}, \ldots, \mathbf{x}_m + m\mathbf{L}(Z_1, \ldots, Z_m)) = F(\mathbf{x}_1, \ldots, \mathbf{x}_m(Z_1, \ldots, Z_m)) \tag{4.14}$$

where $\mathbf{L}$ is a shift vector (in any combination of directions along the coordinate axes), and m is an integer.

But, according to Ostoja-Starzewski [121], if the microstructure has an imperfectly periodic geometry in addition to possessing some randomness on the level of the unit cell, then one should model it as a *wide-sense* (WS) *cyclostationary* random field, which for a system of square unit cells is stated as

$$< Z(\mathbf{x} + m\mathbf{L}) > = < Z(\mathbf{x}) > \tag{4.15}$$

$$\mathrm{Cov}(\mathbf{x}_i + m\mathbf{L}, \mathbf{x}_j + m\mathbf{L}) = \mathrm{Cov}(\mathbf{x}_i, \mathbf{x}_j) \tag{4.16}$$

The former expressions can be useful in numerical methods such like finite elements or finite differences which discretize the dominium and compute the solutions in the discretization points.

[3]See Section 2.1.3 of Chapter 2 for the definition of RVE

4.3 Models for Spatial Point patterns

As was introduced in Section 4.2.2, the random position of the fibres within a composite material can be modelled as a random point pattern. In this kind of random fields, the location of the point (fibre) is the random variable.

4.3.1 Poisson point field

The usual probabilistic function which is assumed to describe the position of inclusions in a material is the Poisson point field [114] [141]. This model describes complete spatial randomness (CSR) in the distribution of fibres. That means that the probability of finding N fibres in a subdominium of area A is the same for any chosen subdominium. Consequently, this model assumes that clusters of inclusions (fibres) do not take place.

The probability of finding k fibres in a window W of area $A(W)$ is given by:

$$P[N = k] = \frac{(\lambda \cdot A(W))^k}{k!} \cdot e^{-\lambda \cdot A(W)} \qquad k = 0, 1, \ldots \tag{4.17}$$

where λ is the fibre density, that is, the number of fibres per unit area.

The Algorithm 1, of Section 5.2.2, can be used for the simulation of the number of fibres, given the window area $A(W)$ and the fibre density λ.

Nevertheless, the Poisson distribution is physically unattainable due to finite dimension of the inclusions. For this reason, the Poisson distribution is often used for comparison purposes and may serve to distinguish between aggregated and more regular patterns.

4.3.2 Poisson hard-core model

A slight modification in the Poisson point field model is usually taken into account in order to reproduce real situations, in which the inclusions have a finite radius. In this case, the center of two inclusions cannot lay in a distance closer than its diameter. So, this model, which is also known in the literature as Matérn's model, is normally employed to describe the random position of the fibres within the composite.

For the cases in which the radius of the fibre r is much smaller than the sample window, it can be considered that the Poisson hard-core model and the Poisson model are equivalent.

4.4 Statistic description of random composite materials

This section provides some useful functions and formulas for the description of the statistics of the constituent distribution in a composite material.

Let us consider a composite material made of $i = 1, \ldots, n$ homogeneous and perfectly bonded constituents. The volume fraction of the constituent i is denoted by c_i.

4.4.1 The indicator function

Let us define the indicator function $\chi_r(\mathbf{x})$ which is equal to 1 when the location $\mathbf{x}$ lies in phase r and zero otherwise [141] [114] [158] :

$$\chi_r(\mathbf{x}) = \begin{cases} 1 & \mathbf{x} \in r \\ 0 & \text{otherwise} \end{cases} \tag{4.18}$$

4.4.2 Probability functions

Using the indicator function as it has been defined, the probability of the location $\mathbf{x}$ belonging to r ($S_r(\mathbf{x})$) is defined by the ensemble average of the function $\chi_r(\mathbf{x})$:

$$S_r(\mathbf{x}) = \overline{\chi_r(\mathbf{x})} \tag{4.19}$$

The probability of finding the phases r at the point $\mathbf{x}_i$ and the phase s at the point $\mathbf{x}_j$ (in other words, the two-point probability $S_{rs}(\mathbf{x}_i, \mathbf{x}_j)$) can be expressed as:

$$S_{rs}(\mathbf{x}_i, \mathbf{x}_j) = \overline{\chi_r(\mathbf{x}_i)\chi_s(\mathbf{x}_j)} \tag{4.20}$$

The functions described in equations 4.19 and 4.20 are normally difficult to compute. However, if the material can be considered statistically homogeneous and ergodic, the following simplifications can be considered:

$$S_r(\mathbf{x}) = \lim_{\Omega \to \infty} \int_{\Omega} \chi_r(\mathbf{x}) d\mathbf{x} = c_r \tag{4.21}$$

If we sample the dominium Ω with a set of locations $\mathbf{x}_i$ with $i = 1, \ldots, n$, c_r can be estimated easily:

$$\widehat{c_r} = \frac{1}{n} \sum_{i}^{n} S_r(\mathbf{x}_i) \qquad r = f, m \tag{4.22}$$

If the random field can be considered statistically homogeneous, the two-point probability S_{rs} depends only on the distance vector between the two locations:

$$S_{rs}(\mathbf{x}_i, \mathbf{x}_j) = S_{rs}(\mathbf{x}_i - \mathbf{x}_j) \tag{4.23}$$

If, moreover, the material can be considered statistically isotropic, the function S_{rs} depends only on the absolute difference of the locations $\mathbf{x}_i$ and $\mathbf{x}_j$:

$$S_{rs}(\mathbf{x}_i, \mathbf{x}_j) = S_{rs}(|\mathbf{x}_i - \mathbf{x}_j|) \tag{4.24}$$

Ẓeman and Šejnoha [163] describe a procedure for the estimation of S_{rs} .

4.4.3 Second order intensity function

The most informative descriptor of the point distribution is given by the *second order intensity function* $K(h)$ [132], which is usually called Ripley's K-function [111]. This function is defined as the number of further points expected to lie within a radial distance h of an arbitrary point and divided by the number of points per unit area.

Corrections due to edge effects have to be performed in the estimation of $K(h)$ [133][111]. In the research work by Mucharreira [111] some of the approaches for the estimation of $K(h)$ are collected and compared. Ripley's [135] estimator seems to be the more appropriate:

$$K(h) = \frac{A}{N^2} \sum_{k=1}^{N} w_k^{-1} I_k(h) \tag{4.25}$$

where N is the number of points in the observation area A, $I_k(h)$ is the number of points in the circle with center at one of the points and radius h and w_k is the proportion of the circumference contained within the sampling area A to the whole circumference with radius h, as shown in Figure 4.1.

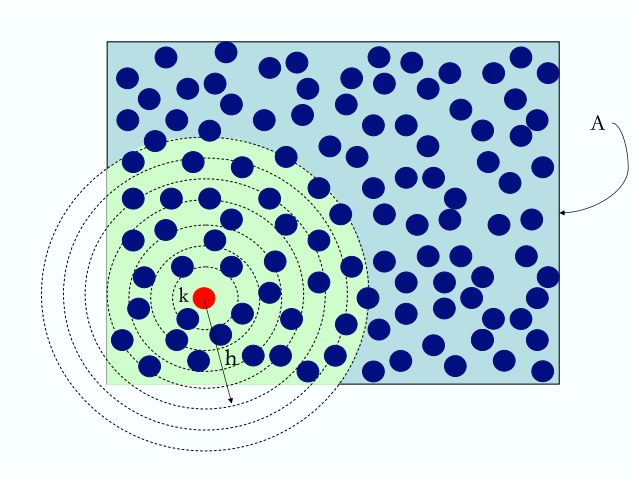

Figure 4.1: .
[Estimation of $K(h)$. ω_k is the fraction of the area of the circle with radius h which is contained by the sampling area A

The second-order intensity function of the Poisson set, $K_P(h)$,in a two dimensional dominium is given by [114] [141]:

$$K_{\mathrm{P}}(h) = \pi h^2 \qquad h > 0 \tag{4.26}$$

and for a Mathérn (hard-core) process with minimum (hard-core) distance d [114] [141]:

$$K_{\mathrm{M}}(h) = \pi (h-d)^2 \qquad h - d > 0 \tag{4.27}$$

For aggregated distributions (that is, distribution showing clusters), $K(h)$ lie above the line corresponding to the Poisson set and tends todiverge from it as the clustering tendency becomes more pronounced. On the other hand, under regular patterns $K(h)$ tends to be below $K_{\mathrm{P}}(h)$ [40].

In Figure 4.2 the second order intensity function of some point distributions is plotted. The deterministic equally-spaced distribution of points (labelled in the figure as *regular*) shows a characteristic form of the second order intensity function, having a "stair" shape. Each "step" in the "stair" indicates a deterministic inter-point distance existing in the distribution. Horizontal fragments of the function represent empty spaces at the corresponding distances, that is those inter-point distances do not take place in the distribution.

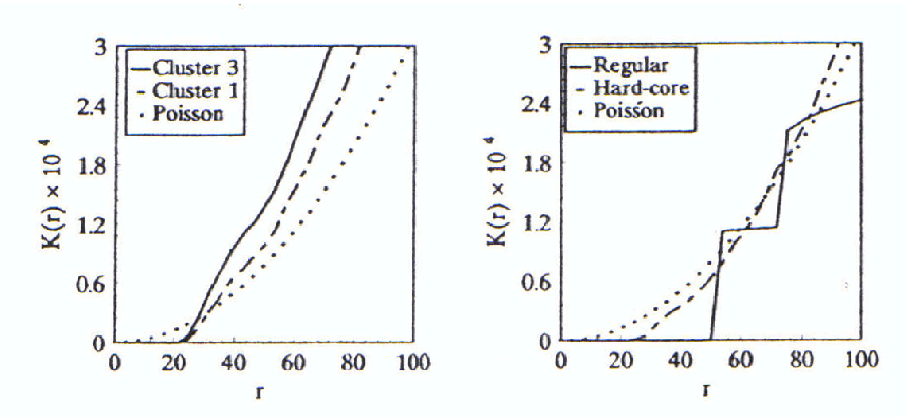

Figure 4.2: Second Order Intensity functions for different fiber arrangements (source: Pyrz [133])

The second-order intensity function $K(h)$ is sensitive to local disturbances and can be useful to distinguish between patterns which look similar [133].

4.4.4 Pair distribution function

The pair distribution function $g(h)$ describes the probability of finding an inclusion whose center lies in an infinitesimal circular region of radius dh about the point h, provided that the coordinate system is located at the center of a second inclusion. Then, recalling the definition of the mathematical expectation B.9, the mean number of inclusions within the circular area with radius h can be written [132]:

$$n(h) = 2\pi\rho \int_0^h \eta g(\eta)\, \mathrm{d}\eta \tag{4.28}$$

where ρ is the number density of inclusions within the observation area A.

This latter function is sometimes called *the integrated pair distribution*. Recalling the definition of $K(h)$, the mean number of inclusions within the circular area with radius h, can also be obtained:

$$n(h) = \rho K(h) \tag{4.29}$$

By differentiating expressions 4.28 and 4.29, the following relation between $g(h)$ and $K(h)$ can be found:

$$g(h) = \frac{1}{2\pi h}\frac{\mathrm{d}K(h)}{\mathrm{d}h} \tag{4.30}$$

Although $g(h)$ and $K(h)$ are related, they provide quite different physical information. As was said in the former section, $K(h)$ can distinguish between different patterns and detect regularities, whereas the pair distribution function $g(h)$ describes the occurrence intensity of inter-inclusion distances. In this function a local maxima indicates the most frequent distances between points and a local minima the least frequent ones in the pattern.

Matsuda et al.[102] use the following discretized definition of the pair distribution function:

$$g(h) = \frac{1}{2\pi h\rho\,\mathrm{d}h}\frac{1}{N}\sum_{i=1}^{N} n_i(h) \tag{4.31}$$

where h is the radial distance from a fibre center, ρ the number of fibres per unit area, N the total number of fibre centers in the region considered, n_i the number of fibre centers which lay within an annulus of radius h and thickness $\mathrm{d}h$, with the same center as the fibre i.

The pair distribution function can be used for the statistic description of a composite sample, instead of the two-point probability function of Eq. 4.20, when the material can be considered ergodic and statistically isotropic.

Figure 4.3 shows the pair distribution function for some fibre distributions. In this figure, it can be seen like the pair distribution function of a Poisson pattern is identically 1. Tsherefore when values of $g(h)$ are greater than 1, the corresponding distances occur more frequently than in a complete random pattern, and conversely for smaller values.

For any homogeneous distribution $g(h)$ tends to 1 for large values of h. Then, we can find a distance h_0 for which $g \approx 1$ for $h > h_0$. This distance h_0 could be seen as a measure of the correlation length[4] of the point field .In the deterministic pattern, $g(h)$ does not tend to a constant value and shows peaks corresponding to the deterministic inter-inclusion distances.

4.4.5 Nearest-neighbor distributions

The second order intensity function, $K(h)$, and the pair distribution function, $g(h)$, are useful in describing long range interactions between points. Another interesting measure of how inclusions or fibers are distributed within the material is given by the *nearest-neighbor distribution* which can be obtained easily as the probability distribution function of the

[4]See Eq. 4.7 and subsequent definition

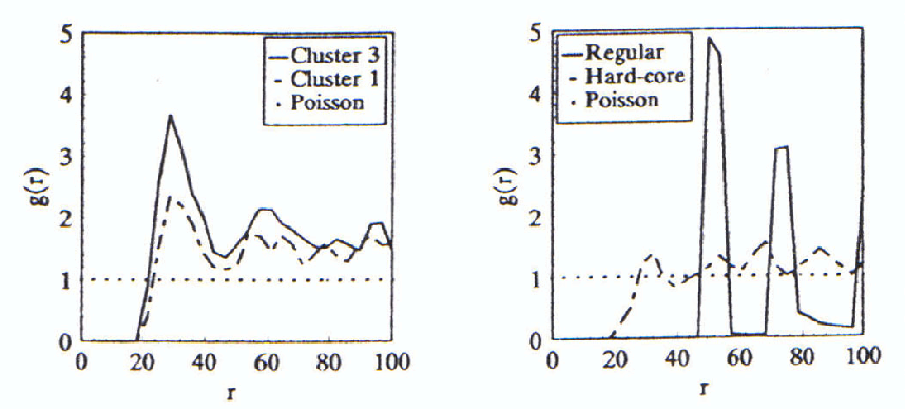

Figure 4.3: Pair distribution functions for different fiber arrangements (source: Pyrz [133])

smallest distance to a fiber for each fiber. Analogously, second or third-nearest-neighbor distributions may be computed. This nearest neighbor functions focus on short-range interactions between points.

For a Poisson point field the nearest-neighbor distribution function $D(h)$ is given by equation [114]:

$$D(h) = 1 - e^{-\lambda\pi h^2} \qquad h \geq 0 \tag{4.32}$$

and the density function $d(h)$ can be easily found by differenciating the former expression:

$$d(h) = \lambda 2\pi h e^{-\lambda\pi h^2} \qquad h \geq 0 \tag{4.33}$$

The mean and the variance of the nearest-neighbor distances are given by [114]:

$$\mu = \frac{1}{2\sqrt{\lambda}} \tag{4.34}$$

$$\sigma^2 = \frac{1/\pi - 1/4}{\lambda} \tag{4.35}$$

The generalized formula for the k-th nearest-neighbor function can also be obtained analytically [114]:

$$\begin{aligned} D^k(h) &= 1 - \sum_{i=0}^{k-1} \frac{1}{i!} \left(\lambda\pi r^2\right)^i e^{-\lambda\pi r^2} \\ &= 1 - \frac{\Gamma(k, \lambda\pi r^2)}{\Gamma(k)}, \qquad r \geq 0, \qquad k = 1, 2, \ldots \end{aligned} \tag{4.36}$$

$$d^k(h) = \frac{2\left(\lambda\pi h^2\right)^k}{h\Gamma(k)} e^{-\lambda\pi h^2}, \qquad h \geq 0, \qquad k = 1, 2, \ldots \tag{4.37}$$

where $\Gamma(x, y)$ is the incomplete gamma function, defined as:

$$\Gamma(x, y) = \int_z^\infty t^{x-1} e^{-t} \, \mathrm{d}t \tag{4.38}$$

And the i-th moments are given by [114]:

$$\tau_i^k = \frac{1}{(\lambda\pi)^{i/2}\,\Gamma(k)} \Gamma\left(k + \frac{i}{2}\right), \qquad k, i = 1, 2, \ldots \tag{4.39}$$

The nearest neighbor probability functions of a complete spatial random (CSR) pattern can be used for interpreting empirical results obtained for other nearest neighbor functions. If the empirical function is larger than the function for a CSR pattern in the small values of r, the empirical point pattern is more clustered than random. Conversely, if the empirical neighbor function is lower than the function for the CSR pattern in the nearest neighbor distances, the pattern possibly shows some regularity. Typically, the neighbor distances for a hard-core pattern show values near zero for some small distance.

4.5 Microstructure Models for Random Composite Materials

In this section a review of some works which deal with different aspects of computational modelling of random composite materials is given.

4.5.1 Statistical Representative Volume Element

As seen in Section 2.1.3 of Chapter 2 the Representative Volume Element (RVE) is a representation of a subdomain of the material which can be used in the analysis of microstructures. In Section **??** of Chapter 2 some mechanical criteria for the determination of the minimal size of the RVE have been reviewed. In this section, some statistical criteria are presented.

Representative Volume Element through Neighbor distances

Shan and Gokhale [140] compared the properties of a large sample of material (1 mm^2) and those of RVEs of increasing size. The mechanical properties were computed using the rule-of-mixtures (Equation 2.13) . The comparison variables were the Young's modulus and the ultimate strength. For the statistical comparison, they took into account the distance to the nearest neighbor, and the distance to the second nearest neighbor. Finally they made use of the distribution of stresses by computing the probability of fracture of a point in the dominium.

They determined the size of an RVE for a ceramic matrix composite (CMC) with fibres of random diameter of mean 14 μm. The resulting RVE was 0.1 mm^2 and contained about 250 fibres.

Optimal Random Periodic RVE

Povirk [129] proposed a method to consider the inherent randomness in heterogeneous material within a usual homogenization technique, which deals with periodic materials. The main idea of this method is to find a periodic RVE with random position of the reinforcement but which is *optimally* representative of the material. The comparison between the real material and the objective RVE is done by computing the power spectral density[5]. Given the length of the RVE and the number of reinforcements contained thereins, an *optimal* RVE is found by solving a minimization problem with an objective function which compares the power spectral density of the material and the one corresponding to the RVE.

The author's argumentation for the use of the power spectral density is that "it can be thought of as a probability density function in the frequency domain. By choosing a periodic structure on the basis of its power spectral density, the structure will have similar spatial distribution of reinforcements, and presumably, similar mechanical behavior, as the actual random structure". However, this similarity in the mechanical behavior is not demonstrated.

The method was applied to an ideal material with $E^{(f)} = 450$ GPa, $E^{(m)} = 72$ GPa, squared reinforcements and 27.5% of reinforcement content. In the cases considered, the reinforcement distribution seemed not to have a strong effect on the elastic behavior. The author argued that the influence in the mechanical behavior would be greater if plasticity were considered in the matrix. According to the author, one of the main interests of this technique could be the study of the initiation and propagation of damage in a two-phase or porous material.

Ẓeman and Šejnoha [163] developed a similar work to the one by Povrik [129]. In this case, an *optimal* for the RVE was found by minimizing the second order intensity function $K(h)$ (Equation 4.25). The authors applied this technique to real composite materials and showed its efficiency in finding effective properties of a graphite tow impregnated by a polymer matrix.

Other approaches

Byström [33] computed the effective conductivity of composites with random inclusions through a homogenization method. In his work, a small size analysis was performed to determine which is the minimum number of inclusions to get a satisfactory random composite. Imposing a volume fraction $v_f = 0.5$ models with $4, 16, 64$ and 144 inclusions were solved. The goodness of the model was evaluated by computing the confidence interval $\mu \pm \sigma$. As a result a random model with 64 inclusions was considered to give a satisfactory result.

4.5.2 Effect of random phase distribution

Knight et al. described in their work [90] a procedure for evaluating the effect of the random distribution of the fibre in the transverse section of a composite material. They

[5] See Section 4.2.4

used the Embedded Cell Approach (described in Section 2.6.2 of Chapter 2), applying a remote unit tensile stress (σ_0) in the y direction, at a sufficient distance from the core such that free surface effects could be neglected.

They performed numerical simulations of embedded cells containing 60 equally sized and randomly distributed fibres. Only full fibres were considered to lay in the core region. The size of this core region was determined by imposing a fibre volume fraction. The size-relations between the core size (L), the embedding region size (H) and the fibre radius (r) were: $H/L = 10.7$ and $r/L = 0.107$. The material properties for the embedding region were computed using Halpin-Tsai relations [6], using $\xi = 2$.

Different volume fraction values were considered (0.2, 0.4 and 0.6). In the simulation of the fibre distribution, fibres were avoided to lie nearer than $1.05d$ (being d the fibre diameter) to avoid numerical problems. In the same reference [90], this hypothesis was shown to not affect the imposed volume fraction of the model.

The effect of different Young's moduli ratio ($E^{(f)}/E^{(m)}$, where f stands for fibre and m for matrix) and Poisson's ratio mismatch ($\nu^{(f)}/\nu^{(m)}$) were also considered. They took into account the case in which fibres are nearly rigid ($E^{(f)}/E^{(m)} = 100$ such as in carbon reinforced polymers), the fibres are compliant ($E^{(f)}/E^{(m)} = 0.1$), and two different cases for Poison's ratio mismatch ($\nu^{(f)} = 0.4$, $\nu^{(m)} = 0.2$ and $\nu^{(f)} = 0.2$, $\nu^{(m)} = 0.4$). In the two first cases the Poisson ratio of both constituents was 0.3 and in the two latter cases the Young's modulus ratio was 10.

In the simulation of the case with $E^{(f)}/E^{(m)} = 100$, the results showed that tensile bands appeared linking fibres which had centers aligned in a direction close to that of the applied load. Within these bands stress concentrations (which were typically twice the applied stress, but could be greater) appeared in the regions of the interface between fibre and matrix. The magnitudes of stress concentrations seem to have strong dependence on the distance between fibre centers and to a lesser extent on the angle which form a vector joining fibre centers relative to the applied load. In the other hand, in the simulation where $E^{(f)}/E^{(m)} = 0.1$ was imposed these stress bands appeared linking fibres which have centers aligned in a direction which is nearly perpendicular to that of the applied load.

Additionally, the simulation results showed that the Poisson ratio mismatch only slightly affects the local stress distributions and their magnitudes.

Finally, a three-parameter Weibull[7] reliability function:

$$R(x) = e^{-\left(\frac{x-\gamma}{\beta}\right)^{\alpha}} \tag{4.40}$$

was used for fitting the stress. In this function α (the shape parameter), β (the scale parameter) and γ (the location parameter) are positive constants to be fitted. This function was found to be well suited for expressing the stress distribution.

[6] See Equations 2.17 and 2.18

[7] Some generalities of the Weibull probability distribution function are given in Section B.5

Matsuda and co-workers [102] have also analyzed the effect of transverse fibre distribution on the mechanical behavior and strain and stress fields of long fibre-reinforced laminates. Three different unit cells were considered: hexagonal periodic , Y-periodic and point-symmetric (in which symmetry of the cell is considered with respect to cell facet centers), as shown in Figure 4.4. As a measure of the randomness degree provided by each kind of unit cell, they use the radial distribution function (Equation 4.31).

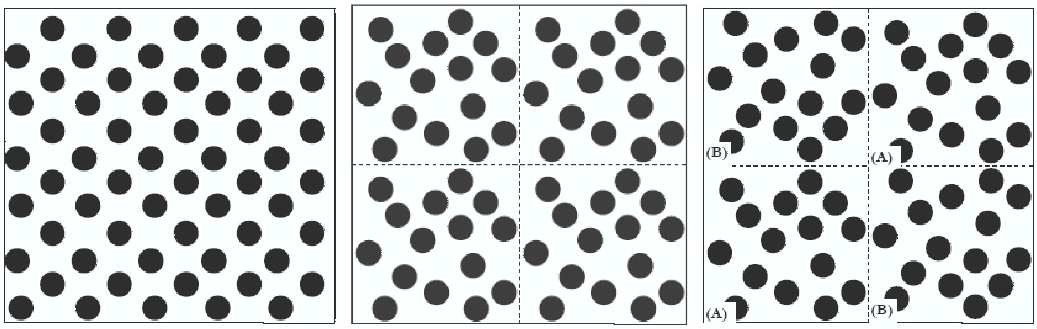

Figure 4.4: Hexagonal periodic, y-periodic and point-periodic unit cells

For the fibre distributions based on the Y-periodic and point-symmetric cell arrangements, $g(h)$ showed some variations around 1. Conversely, the plot of $g(h)$ for the periodic hexagonal arrangement showed very sharp peaks. This means that the fibre distributions based on the Y-periodic and point-symmetric arrangements are, in the words of Matsuda and co-workers, *considerably random*.

As shown in Figure 4.5.2, the plot of this function showed that the point-symmetric cell provides a higher degree of randomness of fibre distribution than the Y-periodic arrangement, due that sharper peaks are found in the plot corresponding to the latter one.

Once the point-symmetric unit cell was chosen, Matsuda et al. [102] implemented a homogenization technique and applied it to a carbon fibre/epoxy laminate in which the fibre content wa 56%, the fibre material was considered elastic and the matrix material was supposed to be elastic-viscoplastic.

By computing the homogenization scheme for both, the point-symmetric and the hexagonal-periodic unit cells and by using a finite element discretization for the in-plane section, they obtained strain-stress relations for uni-directional and cross-ply laminates. Finally, they compared the results with experimental values and the conclusions of their work were the following:

- The point-symmetric cell arrangement can enhance the randomness of the fibre distribution in comparison with the Y-periodic arrangement
- Transverse randomness of fibre distribution has small effect in the macroscopical elastic behavior of composite laminates but strong effect in the microstructural stress

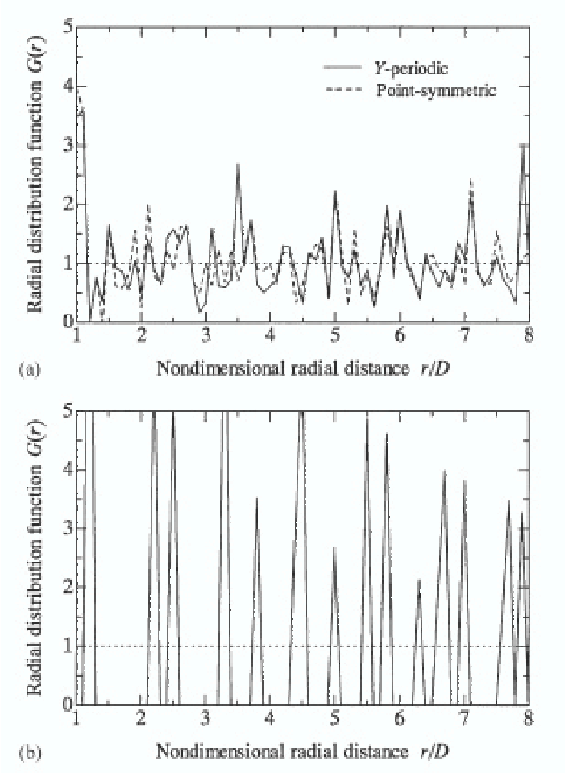

Figure 4.5: Radial distribution function for different fibre arrangements
(a) Y-periodic and point-symmetric and (b) hexagonal (source: Matsuda et al. [102])

distributions. Consequently, it is important to consider the randomness of fibre distribution for studying microscopic problems such as interfacial damage, microscopic failure, etc.

4.5.3 Composite with fibre-rich and fibre-poor regions

Yang and co-workers [159] questioned if the non-periodic (random, as it happens in real materials) distribution of fibres in a composite causes a stress distribution which is different enough from that one caused by a periodic distribution (from the classical models) and so, random microstructure modelling has to be performed.

In their work, they take digital images from a glass ceramic matrix composite with unidirectional aligned SiC fibres. Because of the manufacturing process, the microstructure of this composite shows strips where the reinforcement volume fraction is low. Some other regions show reinforcement clustering.

This microstructure was modeled in a parametrically way, as shown in Figure 4.6, which considers the following parameters:

- $(N_A)_f$: number density of fibre in fibre-rich region
- $(N_A)_p$: number density of fibre in fibre-poor region
- λ_f: width of the fibre-rich region
- λ_p: width of the fibre-poor region

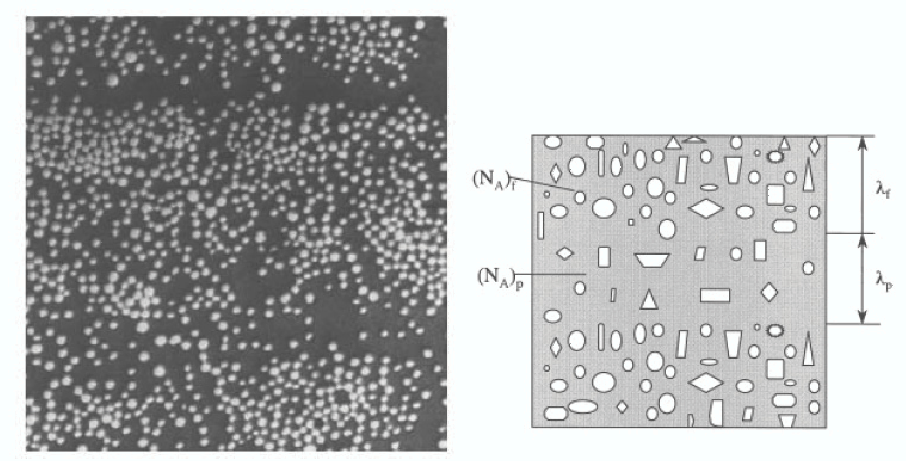

Figure 4.6: Geometrical model for random composite with fibre-rich and fibre-poor regions (source: Yang et al. [159])

Since there are no well-defined boundaries between fibre-rich and fibre-poor regions, these parameters were fitted by an iterative Monte Carlo simulation process. In this process, the set of parameters was randomly changed until some statistical descriptors

(including the pair distribution function of Equation 4.30) were similar to those obtained from digital images.

Once the parameters were fitted, FE computations using the Embedded Cell Approach, (Section 2.6.2) of a typical fibre-rich region, a typical fibre-poor region and an intermediate region were performed. The authors compared then the stress distribution obtained from these three scenarios and found that the third one was the most critic. The stress distribution of this scenario was finally compared with a periodic distribution (one with constant size of the inclusion and another one which considers inclusions having random size) and it turned out to be significantly different, specially in the tail of the cumulative density function, as shown in Figure 4.7 where the random distribution is labelled as *Frame - a*.

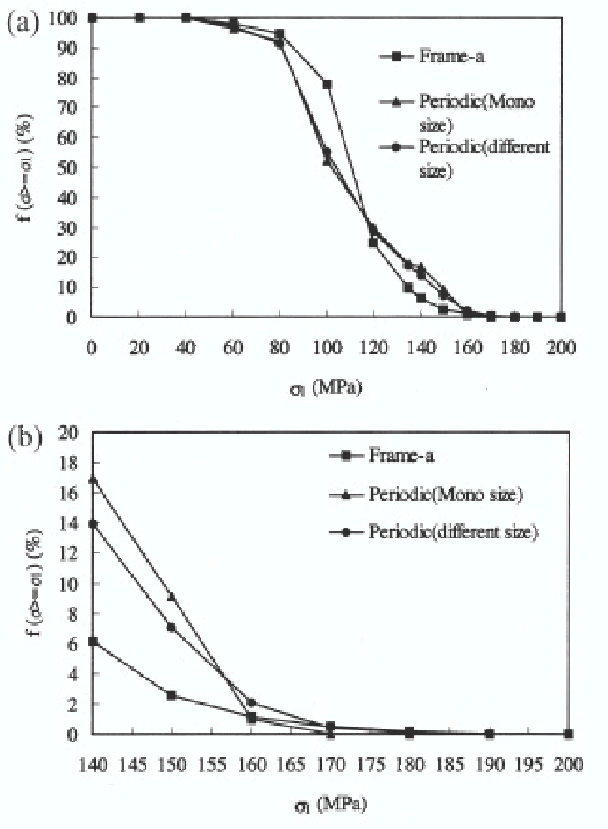

Figure 4.7: Probability distribution function of the principal stress of different fibre arrangements

(source: Yang et al.[159])

4.5.4 Spring networks for random composites

As it was presented in Section 2.6.3, Ostoja et al. [124] used the so-called spring networks for the simulation of microstructures. Here some aspects related to the simulation of random composites are reviewed.

Ostoja and co-workers used a hard-core Poisson point field (See Section 4.3.1) for the modelling of the distribution of the fibres within the transverse section of the composite. Moreover, narrow necks were avoided in the simulation of the fibre location, by requiring the separation between the centers to be greater than the disk diametre d by about $0.1d$.

The dominium was discretized with an equally-spaced grid, which determined the mesoscale size δ. The links joining each grid point represented springs with either fibre or matrix elastic properties, according to their position in the dominium. Fibre centers were forced to lie in the grid points. This way, only re-assigning of matrix or fibre elastic properties to each spring was necessary and there was no need for computationally costful re-meshing. Imposing periodic conditions the stiffness and compliance tensors could be computed. These two tensors were shown to depend on the parameter δ, as seen in Equation 2.76.

Their technique can be used also for obtaining bounds for the elastic response of the composite, by feeding the obtained tensors, separately, into a finite element code. Moreover, by repeating this process for a sufficient number of realizations, in a Monte Carlo simulation procedure, any required moment of the bound can be calculated.

Ostoja et al [124] also proposed an alternative method to decrease computing time. This is based on LU simulation technique [40, 115]. A former simulation using the spring-network which provides the cross-correlations of the random tensor fields has to be performed.

The described methodology was also used by the authors to solve a conductivity problem. In the simulation, the fibre centers were avoided to lie in a distance lower than 1.4 times its diameter. The simulated volume fraction was 20%. Results provided closer bounds than those given by Voigt and Reuss[8] and Hashin[9]. Lower and upper bounds provided by this methodology get closer when δ is increased.

4.6 Modelling of random composites with interface defects

Kaminski and Kleiber [87] considered a periodic random fibre composite in plane strain. The composite was considered random in the following sense:

- Young's moduli in the different phases of the composite were cut-off Gaussian random fields[10] with specified and bounded first two probabilistic moments. These Young's moduli in different regions or phases of the material were uncorrelated.
- In the interface between phases micro-defects were considered. These defects were modelled as random semi-circles with both their radii and frequency of occurrence

[8] See Section 2.4.1 of Chapter 2

[9] See Section 2.4.3 of Chapter 2s

[10] Cut-off Gaussian random fields are Gaussian or normal distributions in which values are greater or lower than certain value. For instance, in the simulation of elastic properties values of the distribution are forced to be positive

being random. The parameters of these defects were assumed to be cut-off Gaussian random variables.

Following these hypotheses Kaminski and Kleiber used homogenization theory to obtain the expected values and variances of the effective elastic properties of the composite material. The results were compared with those obtained using Monte Carlo Simulation.

The main conclusions pointed out that the proposed technique was suitable for many engineering applications and also that, in future studies with the same model, randomness in Young's moduli may be neglected and only randomness of the interphase geometry need to be considered.

4.7 Conclusions

This chapter reviews the foundations of random field theory for fibre reinforced composites and the main functions which can be used for their statistical description such as the second order intensity function and the pair distribution function. The neighbor distances have been shown to be useful for distinguishing between different random materials.

Moreover, the most representative works aiming to model computationally transverse random materials have been reviewed. These works use either statistically arbitrary models or were based on different criteria for the definition of the size of the representative volume element, as shown in Table 4.7. Moreover, the analyzed approaches do not lead to a clear idea about the minimum size of a RVE. For this reason, Chapter 5 of this work will be devoted to the analysis of the minimum required size of a RVE. In this analysis, the statistical functions reviewed here will be also considered.

Finally, the need of the modelling the random distribution of the fibers in the composite appears as a common point in the reviewed works which compare periodic and random models.

Author	$\mathbf{v_f}$	$\mathbf{E^{(f)}/E^{(m)}}$	$\boldsymbol{\delta = L/r}$	**Analysed Statistics**	**Description**
Shan and Gokhale [140]	~ 0.35	~ 2	~ 30	1st and 2nd nearest neighbor, statistical distribution of $\boldsymbol{\sigma}$	FE, ECA, CMC, random diameter
Povirk [129]	0.275	6.25	45 particles[a]	Power Spectral Density	Squared reinforcements. Optimal design of RVE
Zeman and Šejnoha [163]	0.44	70	10 particles[a]	Second order intensity function	Optimal design of RVE
Knight et al. [90]	$0.2, 0.4, 0.6$	$100, 0.1$	~ 19	v_f	ECA, Full fibres, Boundary Element Method
Byström [33]	0.5	10^b	64 particles[a]	Confidence interval $\mu \pm \sigma$	Homogenization

Table 4.1: Summary on the different statistical approaches to determine the RVE size
[a]The size of the RVE is defined through the number of fibres that it contains, for a constant v_f. [b] Thermal analysis, the conductivity ratio is given.

Part II

Analysis and simulation of random fibre reinforced composites

Chapter 5

Development of a Statistical Volume Element

5.1 Introduction

In the Mechanics and Thermodynamics of Solids, the definition of a Representative Volume Element (RVE) is of paramount importance. A review on the evolution of this definition can be found in section 2.1.3 of Chapter 2. As a reminder, it could be said that a Representative Volume Element is a sample of material which is *statistically representative* of the whole material. Although the RVE concept has been used widely in theoretical solid mechanics, for which an infinitessimal RVE is of practical usefulness in the developments of theories and formulae, in Computational Mechanics a finite size RVE has to be used. Then, from the definition of RVE, some criteria which the RVE should satisfy arise.

In Section 2.1.3 of Chapter 2 and Section 4.5.1 of Chapter 4 some mechanical and statistical criteria which a Representative Volume Element should satisfy have been reviewed. The works reviewed in these sections follow either mechanical or statistical criteria but, so far, to the author's knowledge, it has not been published any work which takes into account both groups of criteria in depth: some were only based on the Hill Condition, some others analyzed only the fibre position and none considered the statistics and the distribution functions of the stress and strain fields. Moreover, the works concerned with the size of the RVE consider criterium assuming only the application of the RVE for the simulation of the elastic properties, although some of them use the RVE for damage and fracture [8] simulation.

Another important conclusion when reviewing the works which try to determine the finite size of the RVE is that different criterium lead to different sizes and, since no comparative study for determining which criteria is the most critical has been performed, no clear conclusion about which criteria have to be used is available.

For these reasons, a scale-dependent comparative study of the different criteria which characterize somehow the finite RVE size is performed in this Chapter. Moreover, these criteria are analyzed with the aim of defining a *Statistical Representative Volume Ele-*

ment (SRVE). This SRVE has to reproduce the same statistics related to the stress and strain fields than the whole material and also those statistics related to the fibre distribution. This way, this SRVE will be able to reproduce the random failure behavior of the composite.

5.2 Methodology

For the determination of the finite size of the Statistical Representative Volume Element, models of increasing size are constructed and the evolution of some variables or functions versus the size of the SRVE are analyzed.

First, let us define the dimensionless variable δ, which relates the side length of the SRVE L and the fibre radius r:

$$\delta = \frac{L}{r} \tag{5.1}$$

From the literature review and conclusions of chapters 2 and 4 values of δ between 4 and 100 are chosen. The models are transformed into finite element models to which boundary conditions are applied using the Embedded Cell Approach (ECA), described in section 2.6.2 and then, they are solved for two different loadcases, as it will be seen later.

Some criteria (based on mechanical and statistical variables and functions) which a Representative Volume Element has to satisfy are analyzed. Some of these criterium are found in the literature, but some other aspects are considered. The size above which each criterion is considered to be satisfied can be found by defining an admissible error for which the criterion has to be satisfied.

In the analysis, the following hypotheses are considered:

- A criteria is only satisfied by a RVE candidate when all the bigger RVE candidates satisfy this criteria.
- The biggest RVE candidate is considered to be an RVE, and so to have the same behavior of that of the material.

The considered variables and functions are the following:

1. Fiber content
2. Effective properties
3. Hill Condition
4. Stress and strain fields
5. Probability density functions of stress and strain in the matrix
6. Distance distributions

These will be analyzed as a function of the SRVE size (δ) to determine for which size each of them is satisfied. Consequently, the criterion which is satisfied for a larger δ will also be used to determine the SRVE size.

5.2.1 Material

The present analysis is performed for a typical carbon fibre reinforced polymers (CFRP), whose main data is shown in Table 5.1.

Property	Value
E_f Transverse direction (MPa)	23000
ν_f	0.22
E_m (MPa)	4000
ν_m	0.34
v_f	0.5

Table 5.1: Typical material properties of a CFRP

The material is considered to be ergodic and statistically isotropic when considering the stress and strain fields and the fiber position as random fields. The position of the fibres is assumed to be a Poisson point field. The value of the volume fraction (v_f) which is shown in Table 5.1 is the mean value of a random variable which is dependent of the number and position of the fibers in the model. The number of fibers is drawn from a Poisson distribution and, since complete spatial randomness is assumed, the fiber position is drawn from an homogeneous distribution. The Poisson parameter λ is obtained from a fixed fibre volume v_f, through the following development. Recalling the definition of the parameter λ, we can write:

$$\lambda = \frac{\langle n \rangle}{A} \tag{5.2}$$

where $\langle n \rangle$ is the expected number of fibres which lay in the considered dominium and A the area of that dominium. On the other hand, the fibre volume v_f is the ratio between the total area which is occupied by fibres and the total area of the dominium under consideration:

$$v_f = \frac{A_f}{A} \tag{5.3}$$

taking into account that the volume fraction and the number of fibres are random variables and taking the expectation operator of each side of the equality:

$$\langle v_f \rangle = \frac{\langle A_f \rangle}{A} \tag{5.4}$$

For the computation of the expectation of the total amount of fibre area, let us divide the squared area into three different regions, as shown in Figure 5.1. These regions are chosen because they have different expected fibre area.

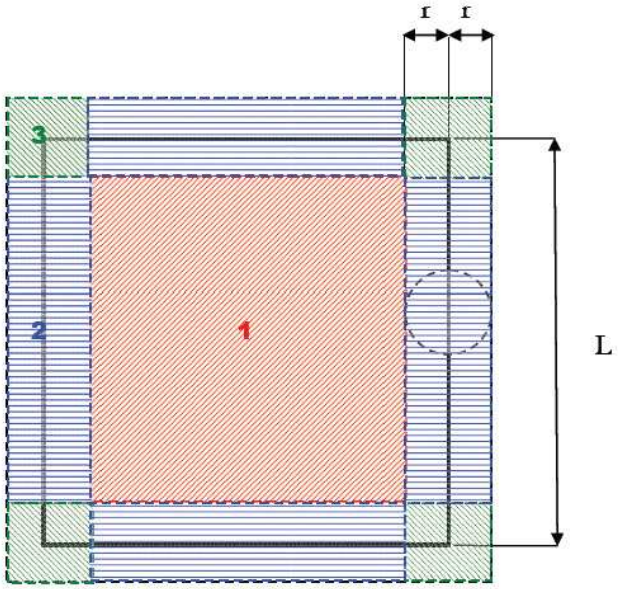

Figure 5.1: Regions associated to the RVE area

The expected number of fibres can be written as a function of the expected number of fibres in each region (n_i) and the area of each region (a_i):

$$\langle n \rangle = \frac{a_1}{a_t} \cdot \langle n_1 \rangle + \frac{a_2}{a_t} \cdot \langle n_2 \rangle + \frac{a_3}{a_t} \cdot \langle n_3 \rangle \tag{5.5}$$

Assuming that the mean volume fraction is constant in any subdominium, the expected number of fibres of each region i can be obtained using the volume fibre and the expected fibre area in that region $\langle a_f^{(i)} \rangle$:

$$\langle n_i \rangle = \frac{v_f \cdot a_i}{\langle a_f^{(i)} \rangle} \tag{5.6}$$

which for the defined regions

$$\langle a_f^{(1)} \rangle = a_f = \pi r^2 \tag{5.7}$$

$$\langle a_f^{(2)} \rangle = a_f/2 \tag{5.8}$$

$$\langle a_f^{(3)} \rangle = a_f/4 \tag{5.9}$$

where a_f denotes the area of a single fibre.

Equation 5.5 can then be rewritten:

$$\langle n \rangle = \frac{\langle v_f \rangle}{a_f} \left\{ \frac{a_1^2}{a_t} + 2\frac{a_2^2}{a_t} + 4\frac{a_3^2}{a_t} \right\} \tag{5.10}$$

Finally the parameter λ of the Poisson distribution can be related with the volume fraction:

$$\lambda = \frac{\langle n \rangle}{A} = \frac{v_f}{a_f \cdot A \cdot a_t} \left[a_1^2 + a_2^2 + a_3^2 \right] \tag{5.11}$$

where the areas of the regions can be easily found:

$$\begin{aligned} a_1 &= (a-d)^2 && (5.12)\\ a_2 &= 4 \cdot (d-\xi) \cdot (a-d) && (5.13)\\ a_3 &= 4 \cdot (d-\xi)^2 && (5.14)\\ a_t &= a_1 + a_2 + a_3 = (a+d-2\xi)^2 && (5.15) \end{aligned}$$

where ξ is a small length set to avoid trouble in the finite element meshing process.

5.2.2 Random Generation of fibre positions

As it was said in the former section, once the Poison parameter, λ, has been obtained, the number of fibers is drawn from a Poisson distribution, as shown in Algorithm 1.

1: $p = 0$
2: $r = \text{RAND}(0,1)$
3: $k = -1$
4: $l = \lambda \cdot A(W)$
5: **while** $p < r$ **do**
6: $\quad k = k + 1$
7: $\quad p = p + \frac{l^k}{k!} \cdot e^{-l}$
8: **end while**

Algorithm 1: Generation of the number of fibres

The random fiber locations are simulated using Algorithm 2, which considers the hard-core Poisson model of Section 4.3.1. An important consideration, due to the finite size of the diameter, is that the generation of the fibre locations must be done within a window of area greater than A(W), to allow fibres not having its centre in W, but laying partly in W. Then, the size E for the simulation window should be $E = L+2r$. Since the model is going to be discretized with a discretization size χ, to avoid discretization problems near the window edges, the size of the simulation window should be $E = L+2(r-\chi)$. Furthermore, to evade discretization problems the minimum allowed distance between centres D will be $D = 2(r+\chi)$. This way fibres laying closer than the discretization size are not allowed in the simulation. A typical algorithm for fibre generation is Algorithm 2.

Using Algorithm 2 models for δ=4, 6, 8, 10, 15, 20, 35, 30, 40, 50, 60, 75 and 100 are generated. The obtained SRVE candidate models are shown in Figures 5.2 to 5.6.

During the testing and execution of this algorithm, it has been observed that it is very time-consuming to obtain volume fractions greater than 0.5. This issue will be considered in Section 8.2 of Chapter 8.

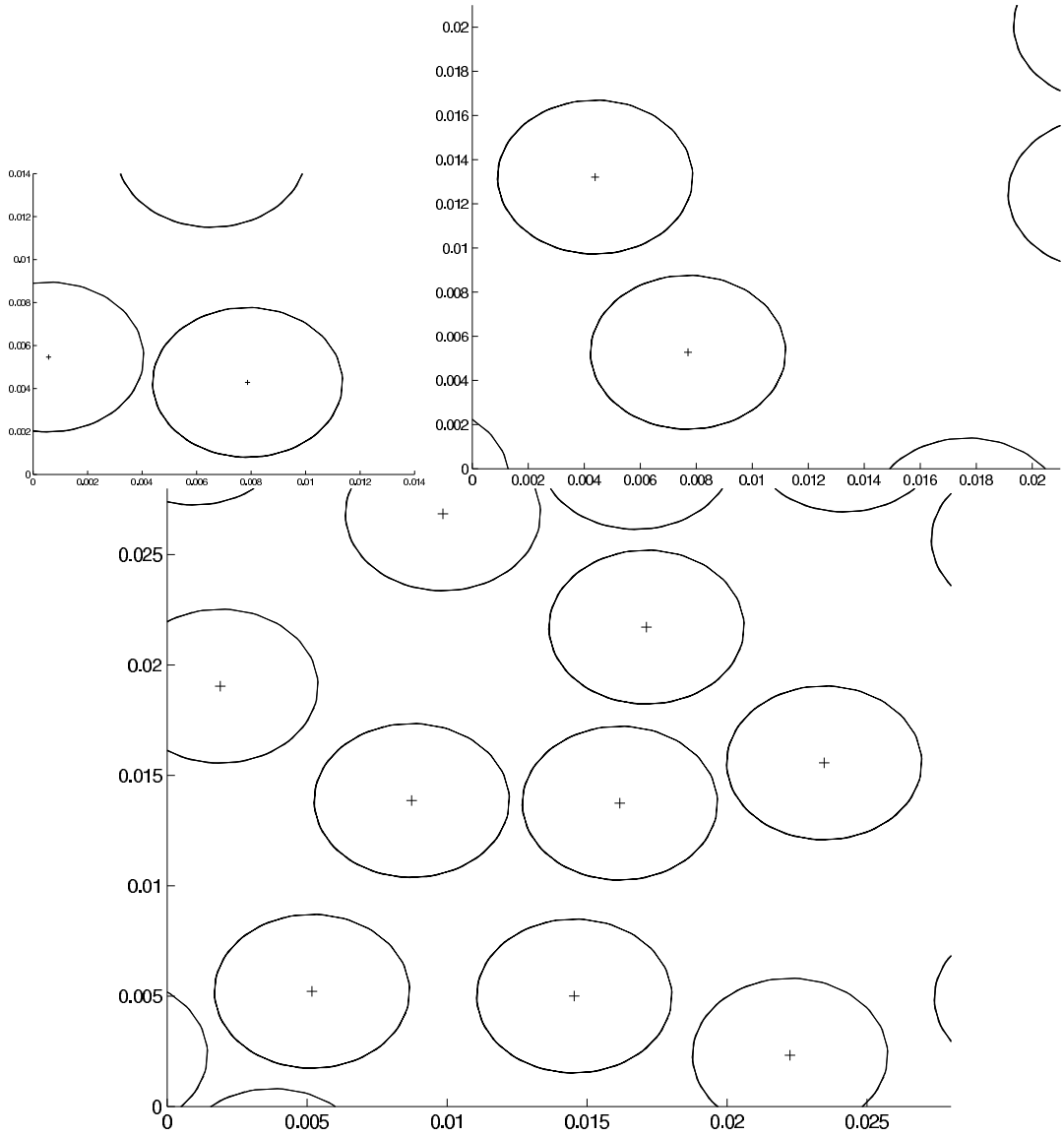

Figure 5.2: Random models for the determination of the SRVE finite size (x4000, Scale in mm)

1: N = number of fibers to be allocated
2: $D = 2(r + \epsilon)$
3: $E = L + 2(r - \epsilon)$
4: **while** $i \leq N$ **do**
5: $\vec{x_i}$ = [RAND(0,E), RAND(0,E)] {RAND(P,Q) is a function which draws a random number between P and Q}
6: $j = 1$
7: **while** $(j < i)\&(d > D)$ **do**
8: d= DIST$(\vec{x_i}, \vec{x_j})$ {The function DIST$(\vec{a}, \vec{b})$ computes the distance between points $\vec{a}$ and $\vec{b}$}
9: $j = j + 1$
10: **end while**
11: **if** $j == i$ **then**
12: $i = i + 1$
13: **end if**
14: **end while**

Algorithm 2: Generation of fibres location

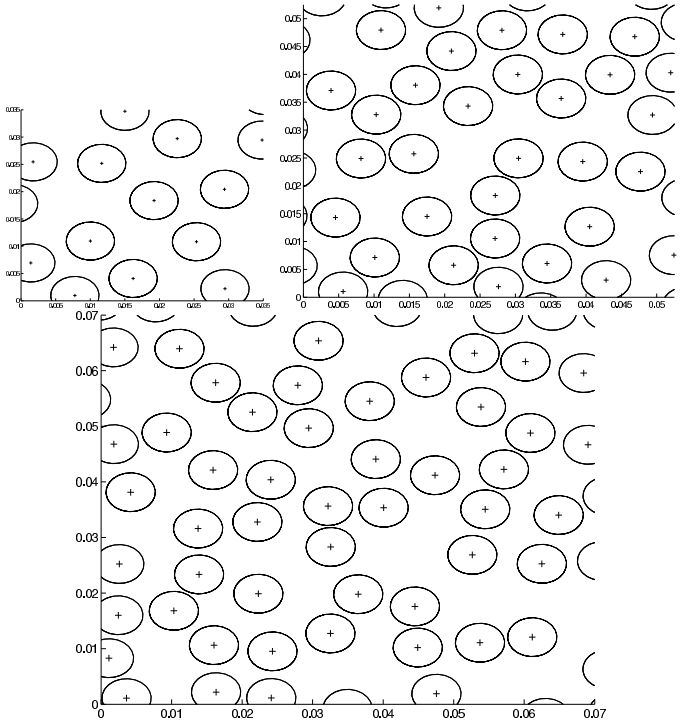

Figure 5.3: Random models for the determination of the SRVE finite size (x2000, Scale in mm)

5.2.3 Finite Element Modelling

Each model is meshed with triangular elements, using MSC MARC's three-node plain strain element type ♯6, as shown in Figure 5.7.

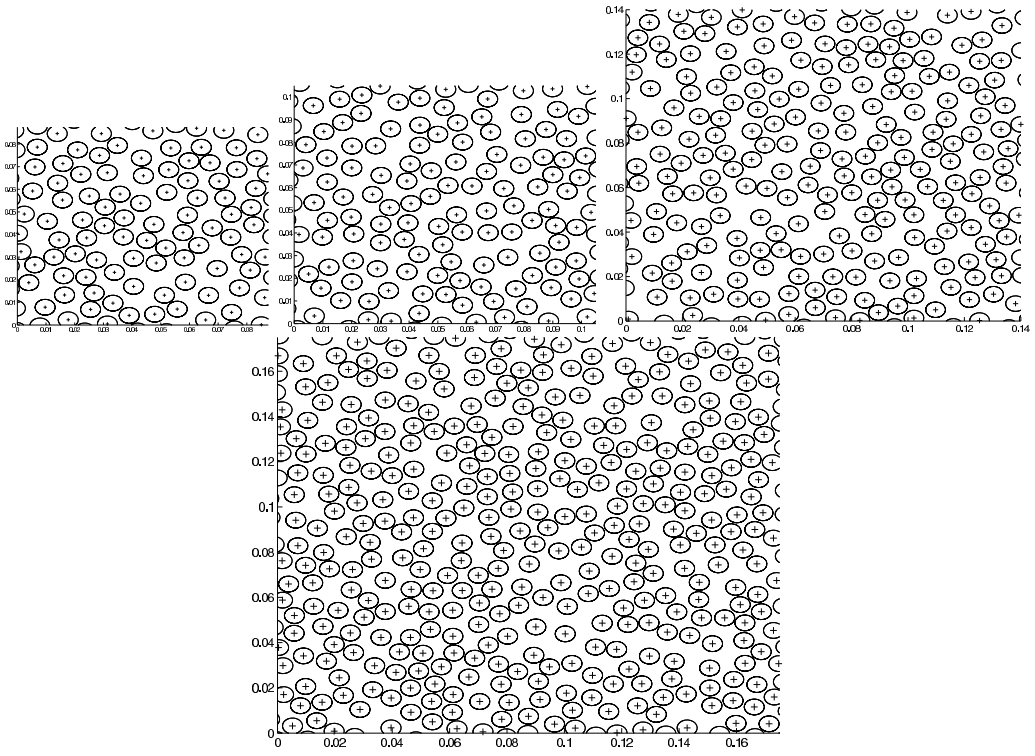

Figure 5.4: Random models for the determination of the SRVE finite size (x400) (Scale in mm)

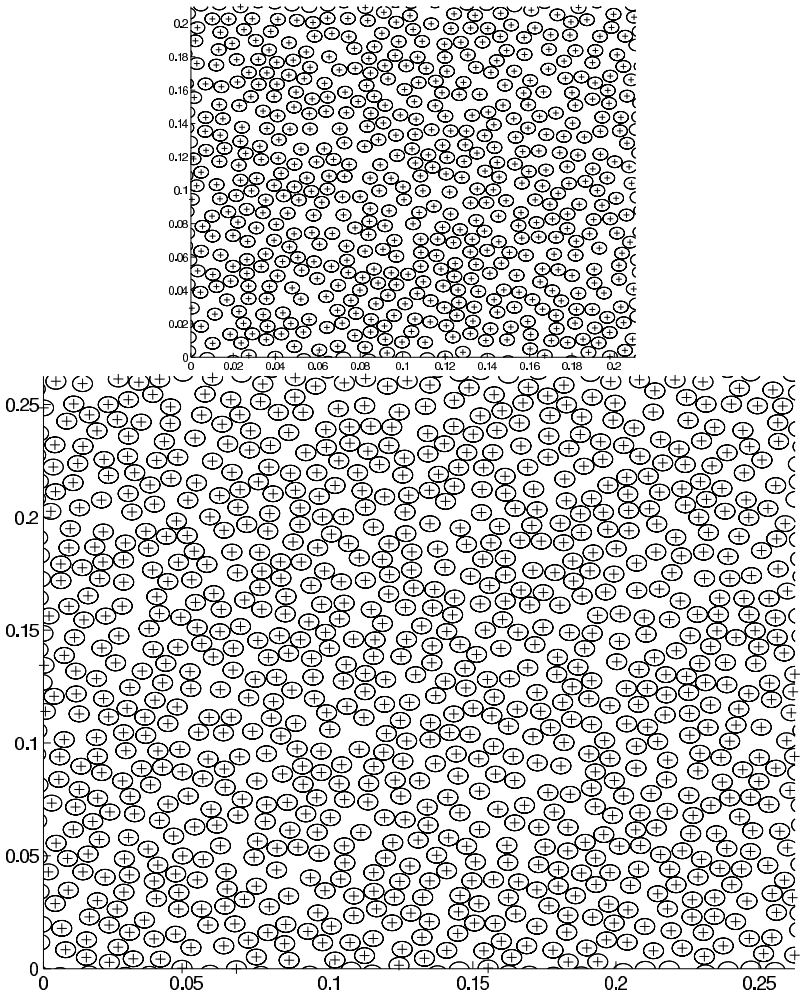

Figure 5.5: Random models for the determination of the SRVE finite size (x366) (Scale in mm)

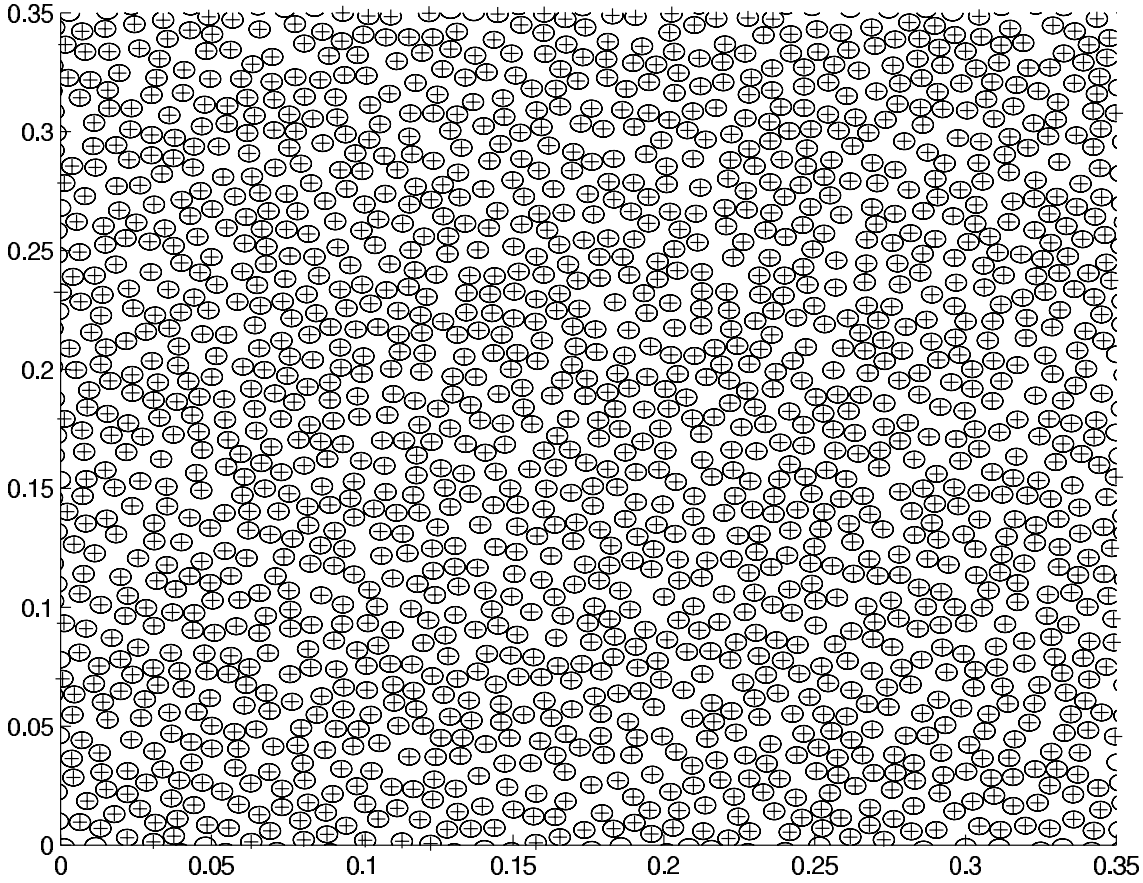

Figure 5.6: Random models for the determination of the SRVE finite size (x375) (Scale in mm)

The embedded cell approach is applied by surrounding the RVE cell by an homogeneous material whose elastic constants are computed through the Halpin-Tsai equations [1], as seen in Figure 5.8. The boundary conditions are then applied to the boundary of this homogeneous material. Since an important requirement for the RVE is the equivalency of boundary conditions[2], two load cases -one with constant forces and one with constants displacements- are applied, in the way shown in Figure 5.9.

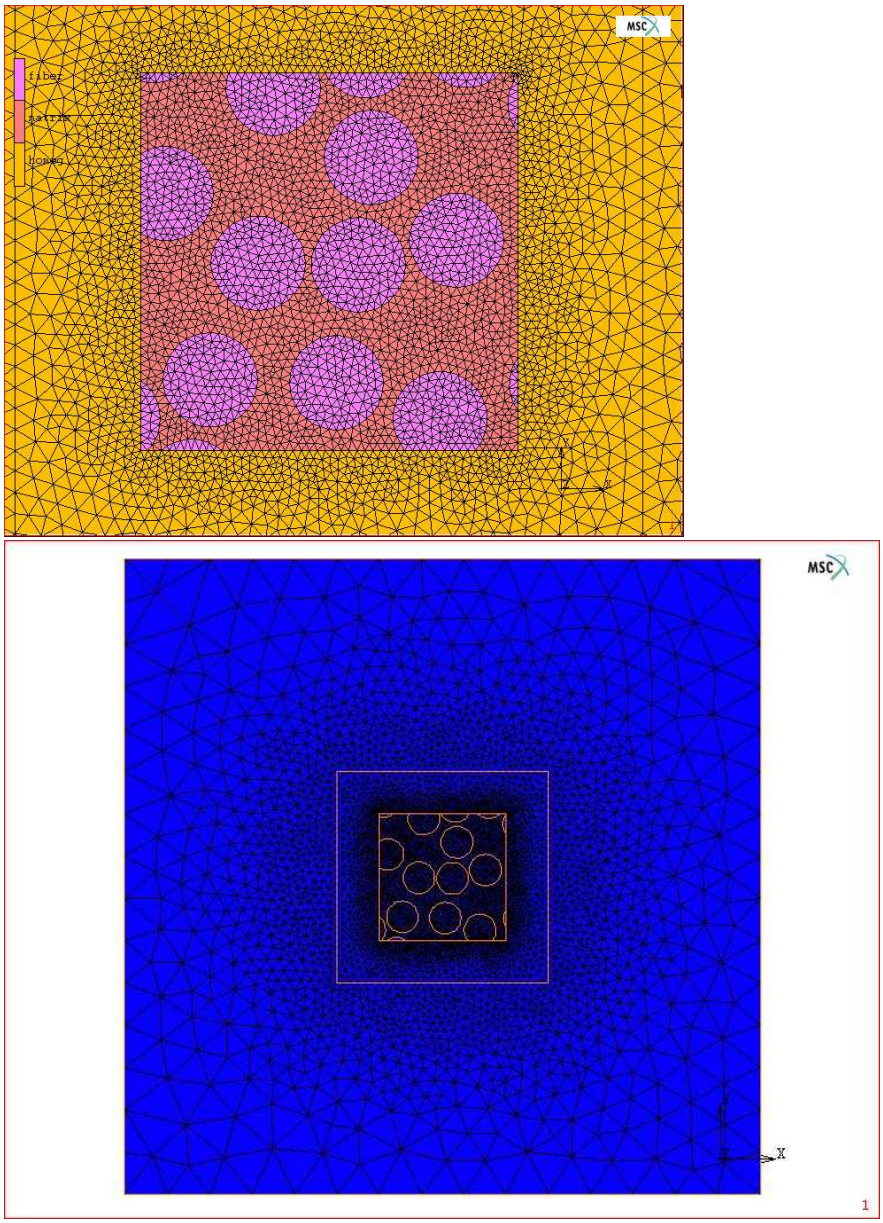

Figure 5.7: FE Mesh in the RVE candidate models

[1] See Equation 2.17, in section 2.4.3
[2] See Section 2.1.3

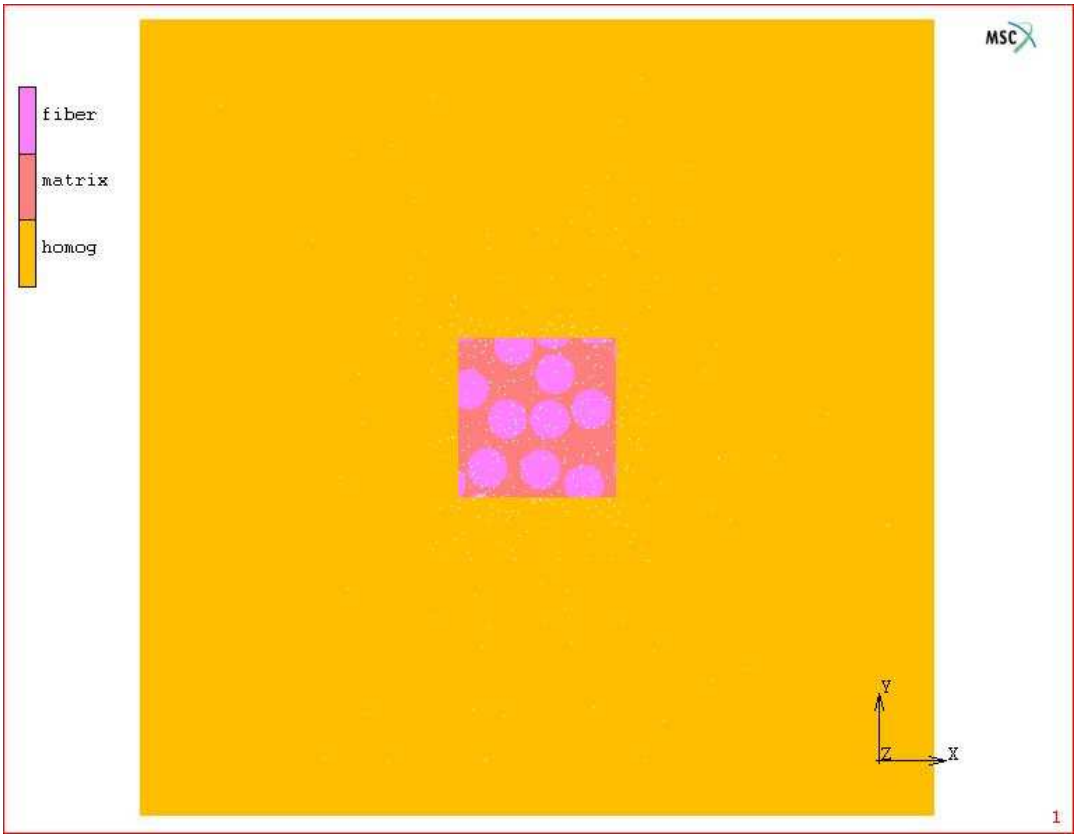

Figure 5.8: Illustration of the Embedded Cell Approach

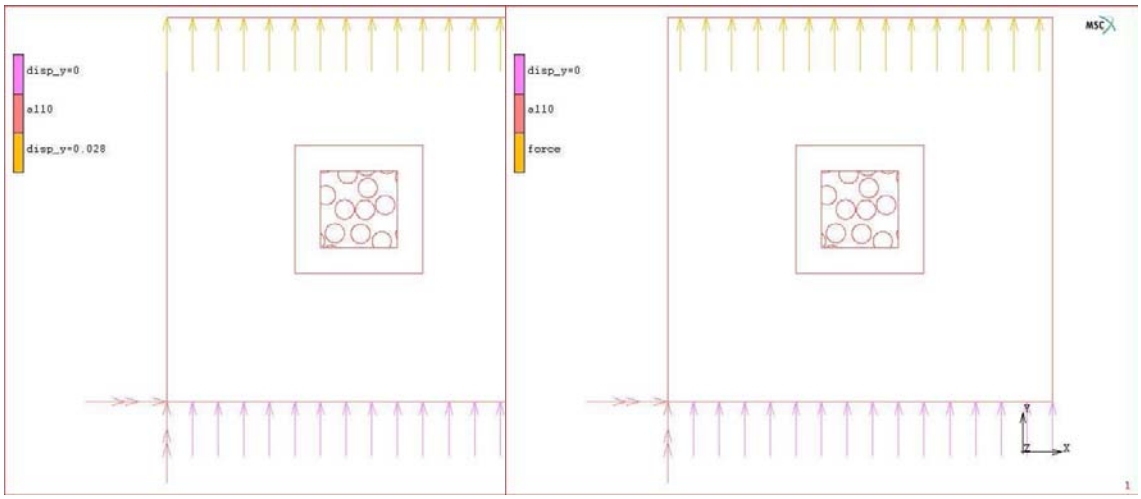

Figure 5.9: Force and displacement boundary conditions in the RVE candidate models

The main data relative to the finite element models is given in Table 5.2. Figure 5.10 shows that the number of nodes (and the number of elements) is a power function of δ with exponent greater than 1. This is reflected by a linear dependency on δ when using a logarithmic-logarithmic plot. This fact shows the importance of defining the minimal usable size of the SRVE.

delta	Absolute size (mm)	Number of fibres	Nodes	Elements
4	0.0140	3	1358	2594
6	0.0210	6	2513	4904
8	0.0280	16	4094	8066
10	0.0350	15	5835	11548
15	0.0525	47	12571	25020
20	0.0700	64	21201	42280
25	0.0875	114	33181	65016
30	0.1050	147	46056	91990
40	0.1400	249	80231	160340
50	0.1750	406	125250	247928
60	0.2100	566	176158	352254
75	0.2625	948	271566	543070
100	0.3500	1604	470305	940548

Table 5.2: FE main data of the SRVE candidates

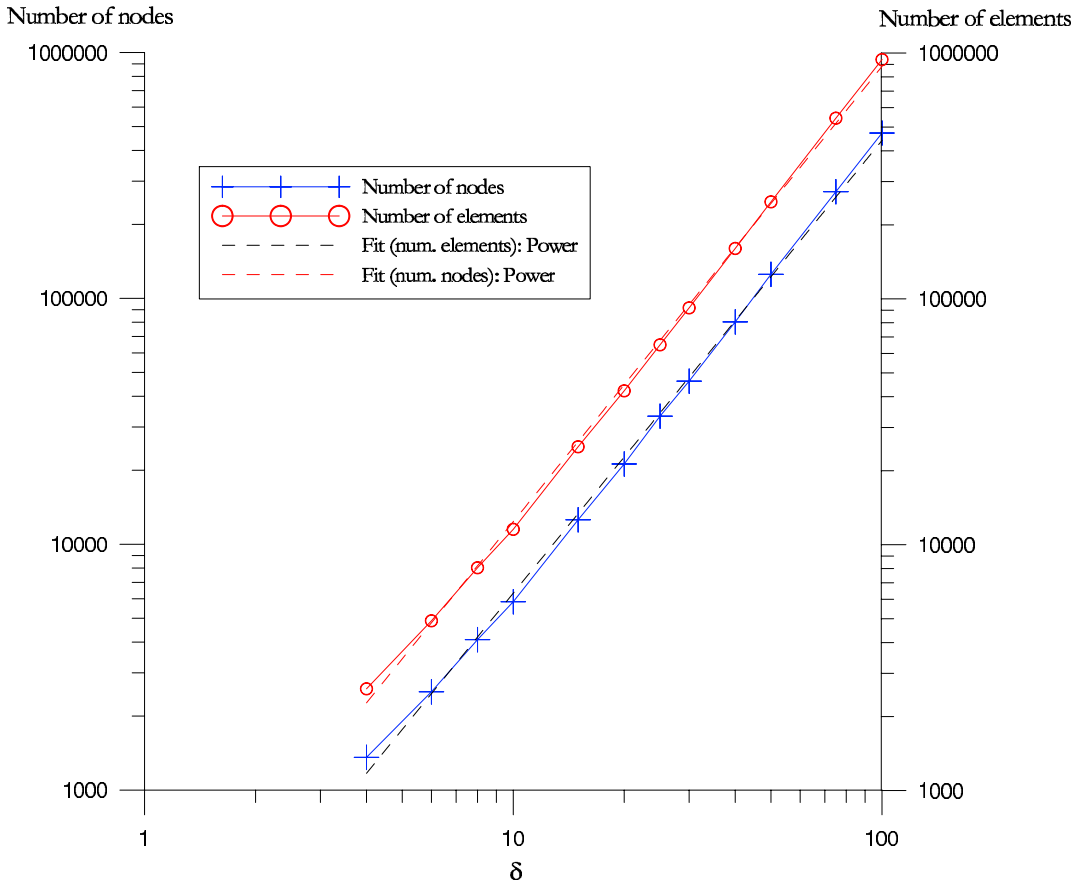

Figure 5.10: Number of nodes and number of elements of the SRVE candidates

5.3 Convergence of fiber content

In handbooks and manuals [44] [106], a 10% of variation for the value of the fiber content is assumed as usual in unidirectional lamina. Consequently, it will be considered that a SRVE candidate has the same fiber content that the model with $\delta = 100$ if the percentual difference is smaller than 10%.

For the computation of the fiber content of the RVE candidates an algorithm based on Monte Carlo integration [136] is used. The total amount of fiber area (A_f) is based on the following conditions:

- If the fiber lays completely within the dominium, $A_f = A_f + \pi r^2$
- If it does not lay completely within the dominium, the area of the fiber which lays within the dominium is computed through a Monte Carlo integration procedure.

Algorithm 3 allows to compute the fiber content with simple computations and a high accuracy. With this algorithm the fiber content for each SRVE candidate is computed. Results are given in Table 5.3 and plotted in Figure 5.11. In the same table, the variation with respect to the immediately smaller SRVE candidate is computed. Also, the percentual difference with respect to the model with $\delta = 100$ is given in the column labelled as *error*. From these values and the plot, it can be observed that variations of the volume fraction are lower than 10% when $\delta \geq 30$. In this figure, the mean and the weighted mean of the fiber content (using the area of the SRVE candidate as the weighting factor) are shown. The weighted mean gives a value much closer to the real value than the simple mean.

δ	v_f	variation (%)	error (%)
4	0.3778	-	20.59%
6	0.2042	59.669%	57.09%
8	0.4431	73.834%	6.86%
10	0.3708	17.762%	22.05%
15	0.4441	17.982%	6.65%
20	0.3963	11.376%	16.70%
25	0.4646	15.859%	2.35%
30	0.4322	7.216%	9.15%
40	0.4242	1.858%	10.83%
50	0.4565	7.326%	4.05%
60	0.4464	2.238%	6.17%
75	0.4759	4.164%	0.04%
100	0.4757	0.036%	-

Table 5.3: Volume fraction of the RVE candidates

```
a: RVE side length
coord(n,2): array containing locations of fiber centres
n: number of fibers
area: total fiber area
a_f = πr^2: area of a single fiber
for i = 1 to n do
   x=coord(i,1)
   y=coord(i,2)
   if x ≥ r AND x ≤ (a − r) AND y ≥ r AND y ≤ (a − r) then
      area = area + a_f
   else
      sum=0
      for i == 1 to npoint do
         θ = rand(1)·2 · π
         {rand(1) is a function which gives a random value between 0 and 1}
         ρ = rand(1) · r
         xp = x + ρ · cos(θ)
         yp = y + ρ · sin(θ)
         if (x ≥ 0) AND (x <= a) AND (y >= 0) AND (y <= a) then
            sum = sum +1
         end if
         w = sum/npoint
      end for
      area = area +w ·a_f
   end if
end for
v_f = area/(a·a)
```

Algorithm 3: Computation of fiber content

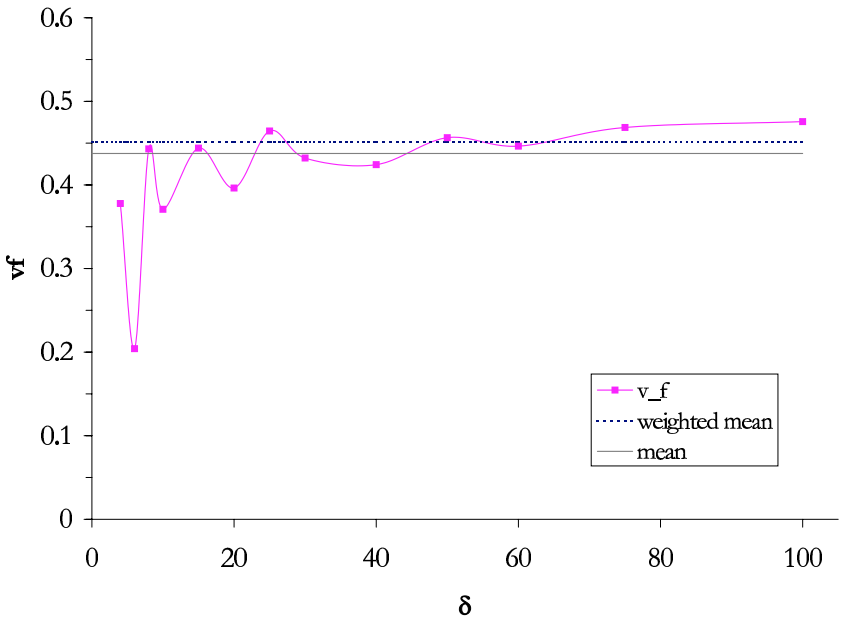

Figure 5.11: Volume fraction of the RVE candidates

5.4 Convergence of effective properties

Following Hill's very first definition of the RVE, a valid RVE has to be typical of the whole material in average. That means that the volume fraction and the effective properties of the RVE are the same of those of the material. In the former section, the fiber content has been analyzed. Although the elastic properties of a unidirectional lamina can be modelled as a linear function of the fiber content[3], in a microscopic scale, due to edge effects and the assumption of constant v_f which is made in the relation between λ and v_f, they can show some deviation from the linear one. Consequently, an analysis of scale-dependency of the elastic properties is performed in this section. Moreover, a comparison of the computed elastic properties for each SRVE candidate is compared with the expressions reviewed in Section 2.2. This comparison will be used as a validity test for the modelling.

The elastic constants are computed for each SRVE candidate, using both type of boundary conditions: displacements and forces. Results, which are nearly proportional to those of volume fraction, are given in Table 5.4 and plotted in Figure 5.12. In this Figure, also a tendency computed by a moving mean model is plotted. It can be observed that small variations of the elastic constant are obtained for $\delta > 30$. The variation with respect to the immediately smaller SRVE candidate is computed and shown in Table 5.4 and the same conclusion is obtained: from $\delta = 30$ variations lower than 10% are obtained when applying displacements and forces.

The values obtained for E_{22} can also be compared with the estimations of different

[3]See Chapter 2

δ	displacement	variation (%)	error (%)	force	variation (%)	error (%)
4	9288.12		21.93%	9303.71		22.00%
6	7173.48	29.48%	39.71%	7174.66	29.67%	39.85%
8	10956.13	34.53%	7.91%	10980.26	34.66%	7.95%
10	8729.33	25.51%	26.63%	8741.19	25.62%	26.72%
15	10817.84	19.31%	9.08%	10842.49	19.38%	9.10%
20	9962.92	8.58%	16.26%	9982.40	8.62%	16.31%
25	11451.12	13.00%	3.75%	11479.23	13.04%	3.77%
30	10611.34	7.91%	10.81%	10634.07	7.95%	10.85%
40	10409.25	1.94%	12.51%	10430.92	1.95%	12.55%
50	11322.54	8.07%	4.84%	11350.03	8.10%	4.85%
60	10989.00	3.04%	7.64%	11014.56	3.05%	7.66%
75	12030.93	8.66%	1.12%	12062.40	8.69%	1.12%
100	11897.83	1.12%	0.00%	11928.53	1.12%	-

Table 5.4: Computed E_{22} in MPa with displacements and force boundary conditions

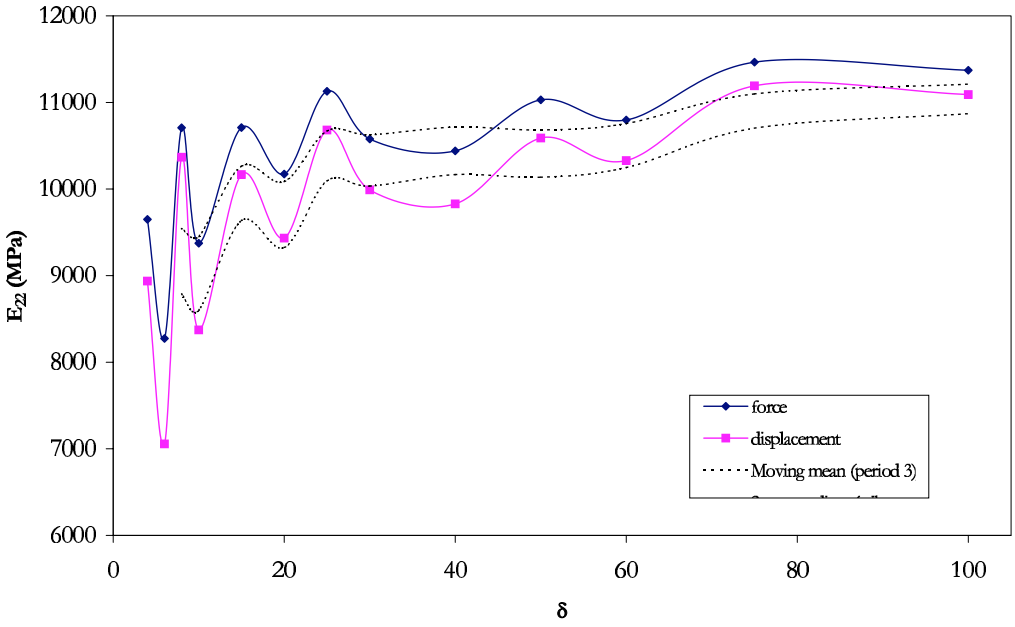

Figure 5.12: Computed E_{22} with displacements and force boundary conditions

formulae reviewed in Section 2.2, like the rule of mixtures and the Halpin-Tsai expressions. The results of this comparison are shown in Figure 5.13. As a verification of the modelling and computational tasks, it can be observed that the computed effective modulus lies between the lower and upper limits and it is close to the Halpin-Tsai equations.

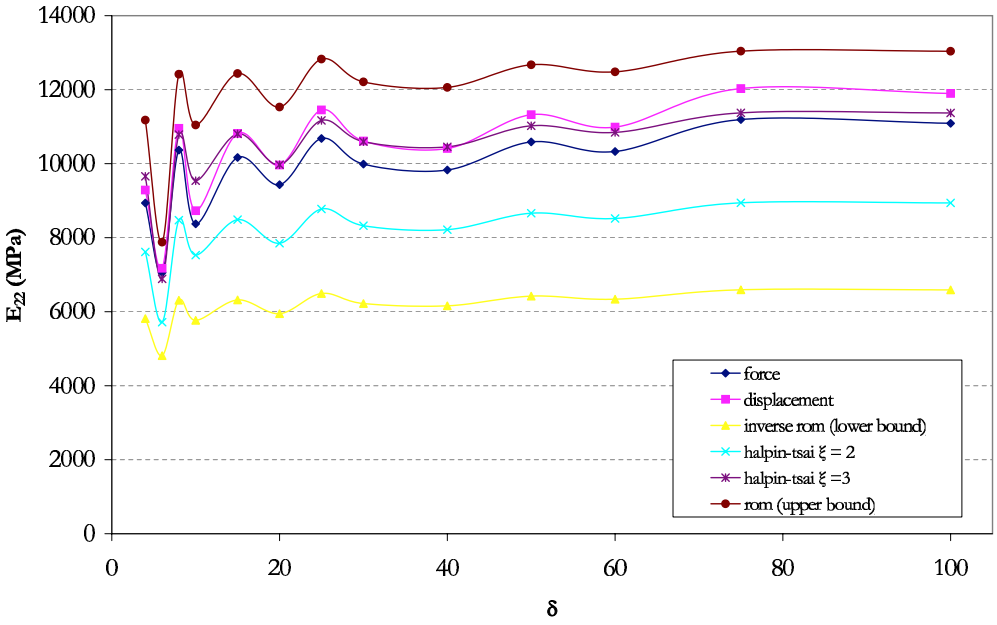

Figure 5.13: Comparison of computed E_{22} with theoretical formulae

5.5 Hill Condition

As reviewed in section 2.1.4, the so-called Hill Condition should be satisfied by any Representative Volume Element [70]:

$$\langle \boldsymbol{\sigma} : \boldsymbol{\varepsilon} \rangle = \langle \boldsymbol{\sigma} \rangle : \langle \boldsymbol{\varepsilon} \rangle \tag{5.16}$$

Both sides of equality 5.16 have been computed for each RVE candidate. Results are shown in Figure 5.14.

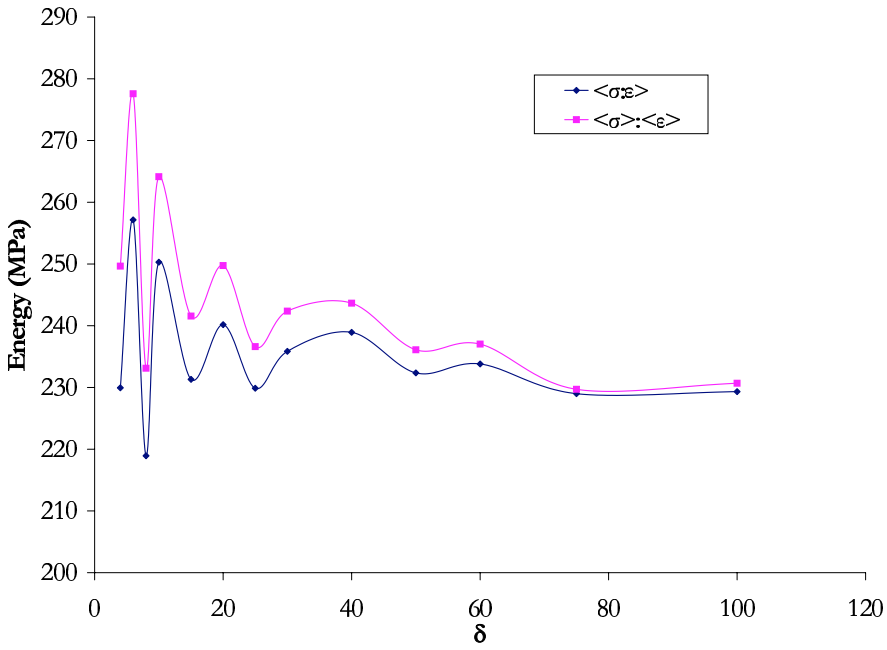

Figure 5.14: Energy bounds for the RVE candidates

The bigger the RVE size, the closer are the measures of the energy, as shown in Figure 5.15, where the relative difference between energy bounds is plotted. In the Figure, a tendency line with a regression exponential fit is shown and it can be verified that for $\delta > 15$ the relative difference is lower than 5%, which can be considered a small enough difference.

5.6 Convergence of stress and strain fields

In some of the works reviewed in Chapter 2 [124, 120] the importance of obtaining the same effective results using the different types of boundary conditions is pointed out. In this section the convergence of the mean, the variance and the coefficient of variation of the stress and strain fields is analyzed for both cases of boundary conditions, displacements and forces, and a comparison to assess their equivalency is performed.

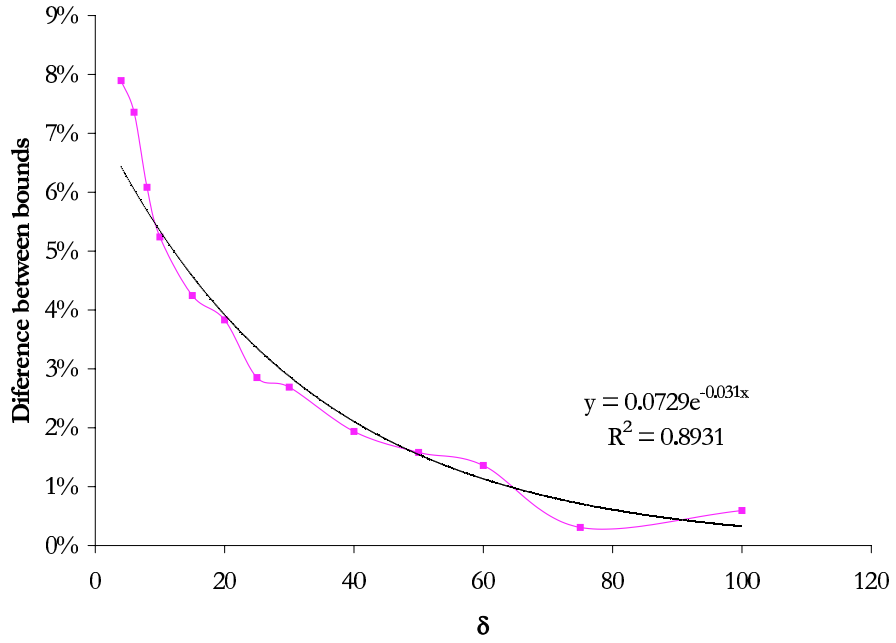

Figure 5.15: Difference between energy bounds for the RVE candidates

5.6.1 Mean of stress and strain fields

Figures 5.16 and 5.17 show the evolution of the mean strain and the mean stress in each constituent and in the composite when the size of the SRVE increases. Since the fibre content in each candidate is a random variable, these plots have to be seen as variations around a tendency. Moreover, since the volume fraction is not constant within the SRVE candidates, the mean strain may tend to converge slowly. Nevertheless, this is a normal situation, since the SRVE has to take into account the fibre content variation, which causes variation in the elastic constants.

Since the SRVE model with $\delta = 100$ is considered to have the same statistics than the bulk material, the following hypotheses can be tested[4]:

$$\begin{aligned} H_0 : \mu(\varepsilon_{22}^{(\delta)}) &= \mu(\varepsilon_{22}^{(100)}) \\ H_1 : \mu(\varepsilon_{22}^{(\delta)}) &\neq \mu(\varepsilon_{22}^{(100)}) \end{aligned} \tag{5.17}$$

where the superscripts 100 δ stand for the mean in the model $\delta = 100$ and any other model, respectively. Thee hypothesis test is used here for detecting when the mean obtained from a SRVE candidate model can be considered to be equal to the mean of the whole composite (computed through the model with $\delta = 100$).

A hypothesis test with $\alpha = 1\%$[5] has been performed for $\mu(\varepsilon_{22})$ in the composite, in

[4]See Section B.7 in Appendix B for test description

[5]When performing a hypotheses test α is the error of rejecting the null hypothesis when it is true

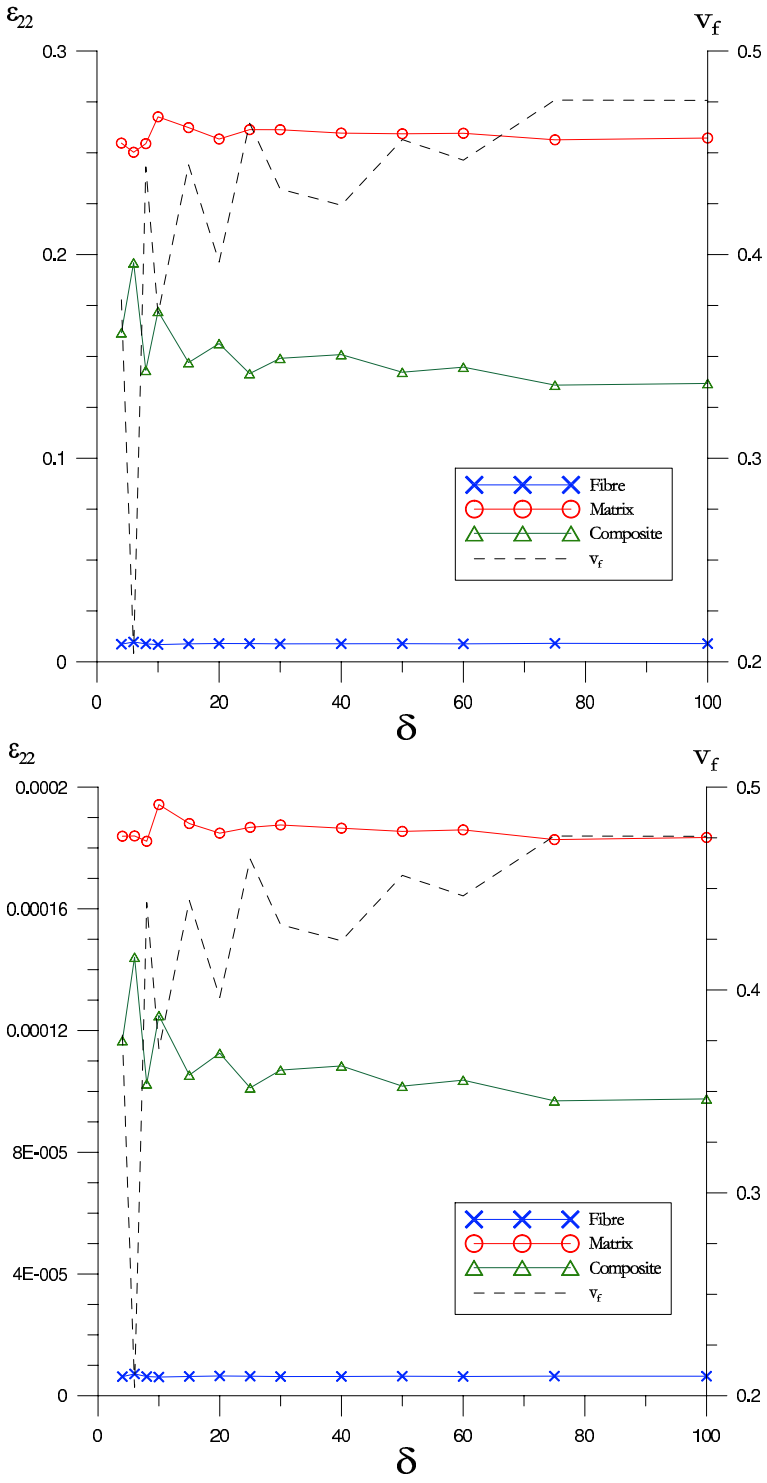

Figure 5.16: Mean strain in the composite and in each constituent for each loadcase: displacement (up) and force (down)

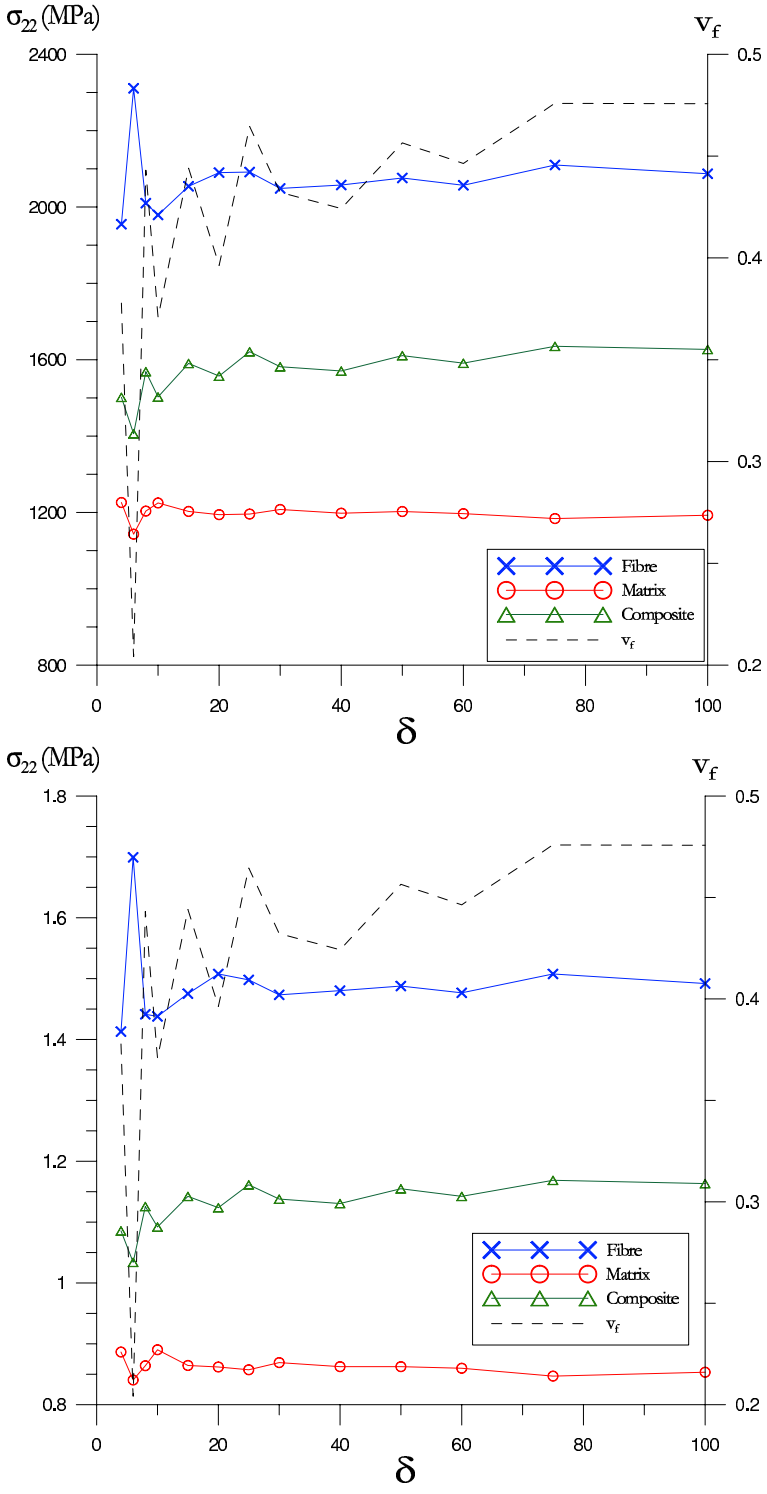

Figure 5.17: Mean stress in the composite and in each constituent for each loadcase: displacement (up) and force (down)

the fiber and in the matrix. Figure 5.18 shows the results of this test for each δ. These results show how the null hypothesis can be accepted for $\delta \geq 15$, since from this value and for all the considered cases $|z_0| - z > 0$ and, consequently, H_0 is accepted for $\delta \geq 15$.

Analogously, the following hypothesis related to the mean of σ_{22} 5.19 can be tested:

$$\begin{array}{lll} H_0 : \mu(\sigma_{22}^{(\delta)}) & = & \mu(\sigma_{22}^{(100)}) \\ H_1 : \mu(\sigma_{22}^{(\delta)}) & \neq \mu(\sigma_{22}^{(100)}) & \end{array} \tag{5.18}$$

with the superscripts having the same meaning than in the former test. Again, the hypothesis test for $\mu(\sigma_{22})$ in the composite, in the matrix and in the fiber has been performed and results plotted in Figure 5.19. Following the same criteria that was used for $\mu(\varepsilon_{22})$, in this case H_0 can be accepted for $\delta \geq 10$.

5.6.2 Variance of stress and strain fields

Figures 5.20 and 5.21 show the evolution of the variances of ε_{22} and σ_{22}.

The variance is a useful statistic to determine if two samples come from the same population [108]. That means, the variance of each SRVE candidate and the variance of the precedent SRVE candidate can be compared using an appropriate hypotheses test:

$$\begin{array}{lll} H_0 : \sigma^2(\varepsilon_{22}^{(\delta)}) & = & \sigma^2(\varepsilon_{22}^{(100)}) \\ H_1 : \sigma^2(\varepsilon_{22}^{(\delta)}) & \neq & \sigma^2(\varepsilon_{22}^{(100)}) \end{array} \tag{5.19}$$

The analogous hypothesis regarding the variance of $_{22}$ can also be written:

$$\begin{array}{lll} H_0 : \sigma^2(\sigma_{22}^{(\delta)}) & = & \sigma^2(\sigma_{22}^{(100)}) \\ H_1 : \sigma^2(\sigma_{22}^{(\delta)}) & \neq & \sigma^2(\sigma_{22}^{(100)}) \end{array} \tag{5.20}$$

In Figures 5.22 and 5.23 it has been plotted the results of the test for the variance of ε_{22} and σ_{22}, respectively, for a significance of 99 %. These figures show that H_0 can be accepted for $\delta \geq 25$, since from this SRVE size a positive value of $F_0 - F$ is obtained.

5.6.3 Coefficient of variation of stress and strain fields

Another useful statistic to analyze he variation within a sample is the coefficient of variation ρ, defined as:

$$\rho = \frac{\sigma}{\mu} \tag{5.21}$$

Since the mean value of the stress and strain is allowed to have some variation, the coefficient of variation can be used to analyze the standard deviation independently of the

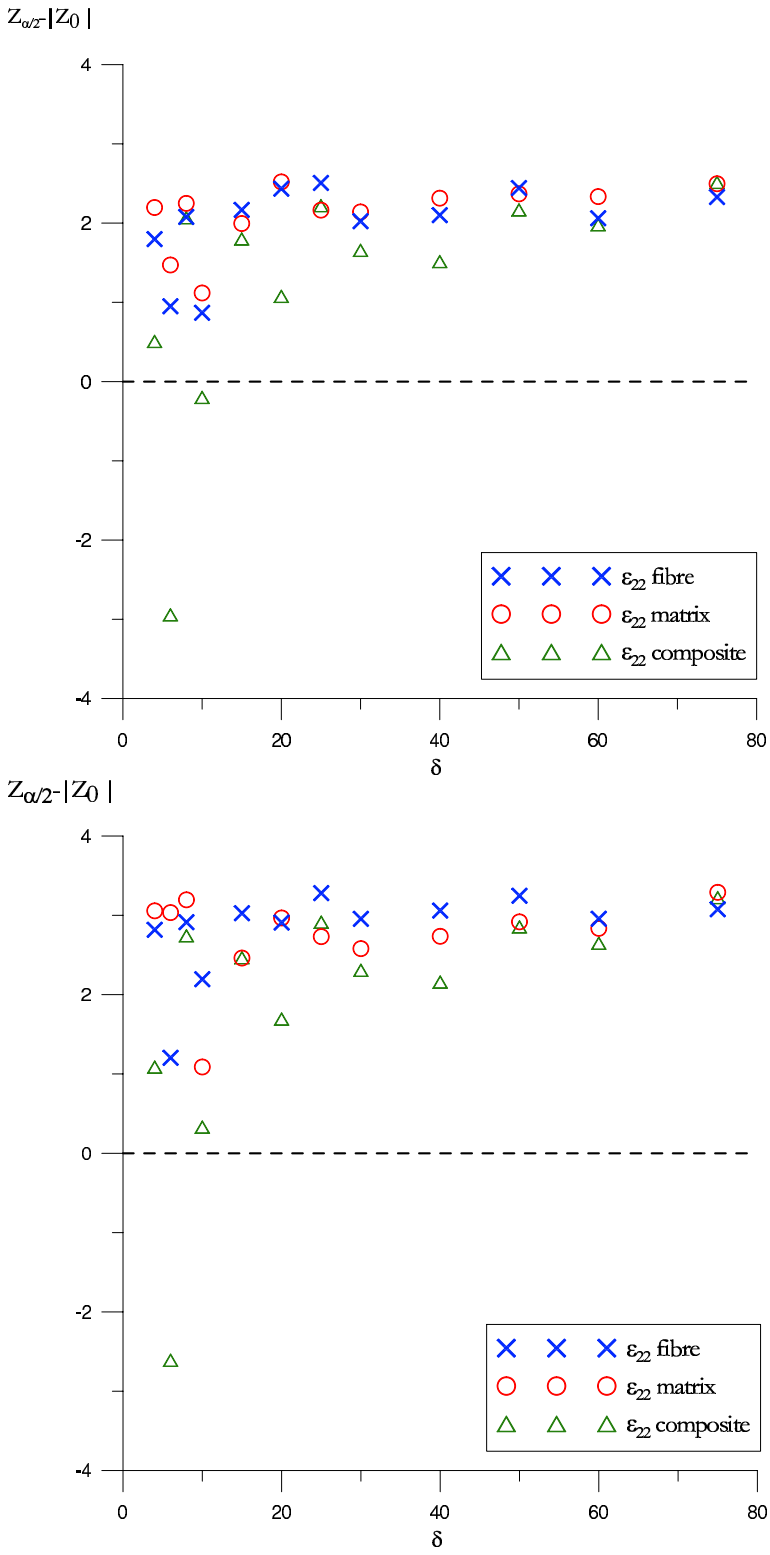

Figure 5.18: Mean ε_{22} hypothesis test for both loadcases: displacements (up) and forces (down)

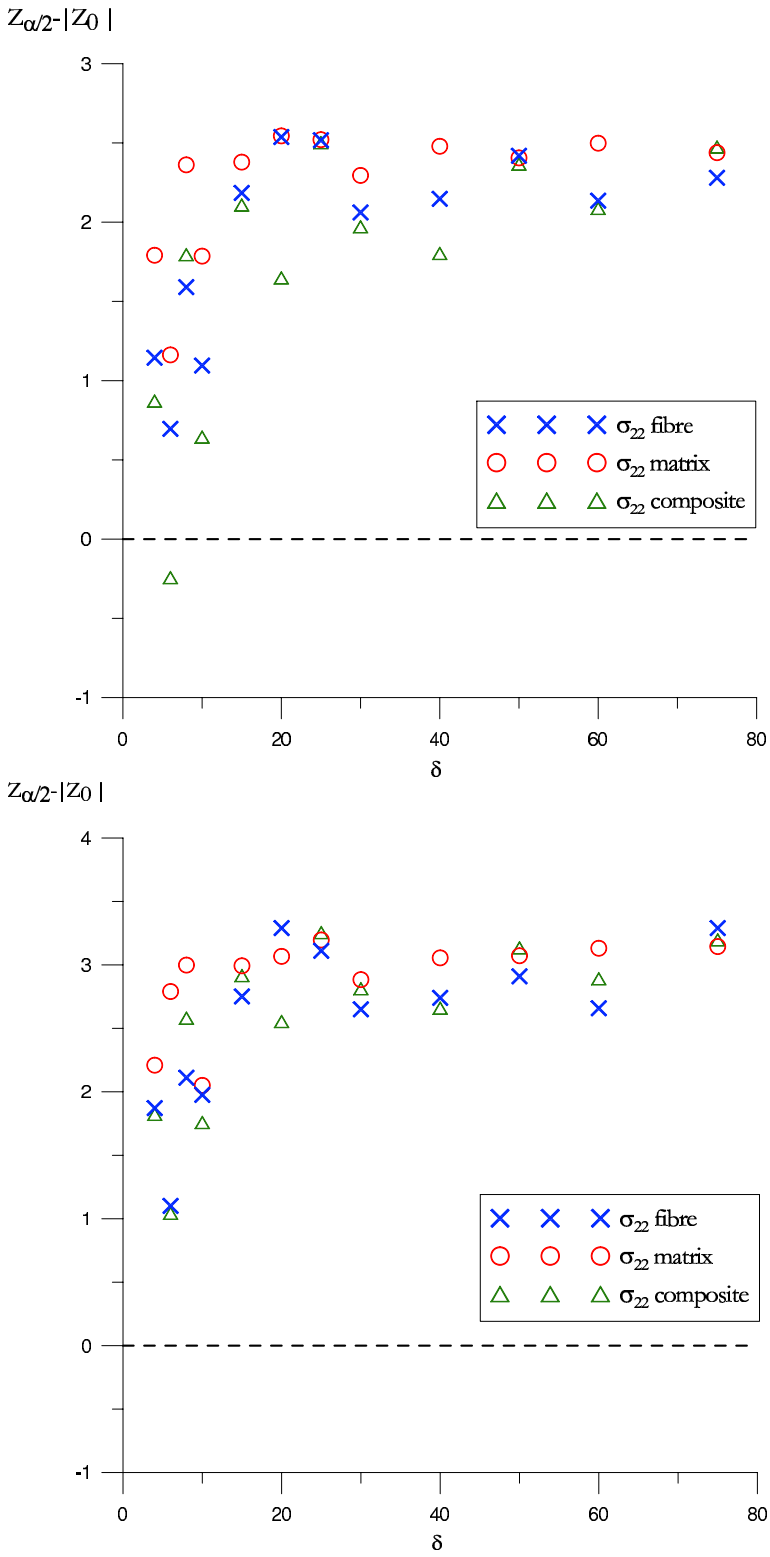

Figure 5.19: Mean σ_{22} hypothesis test for both loadcases: displacements (up) and forces (down)

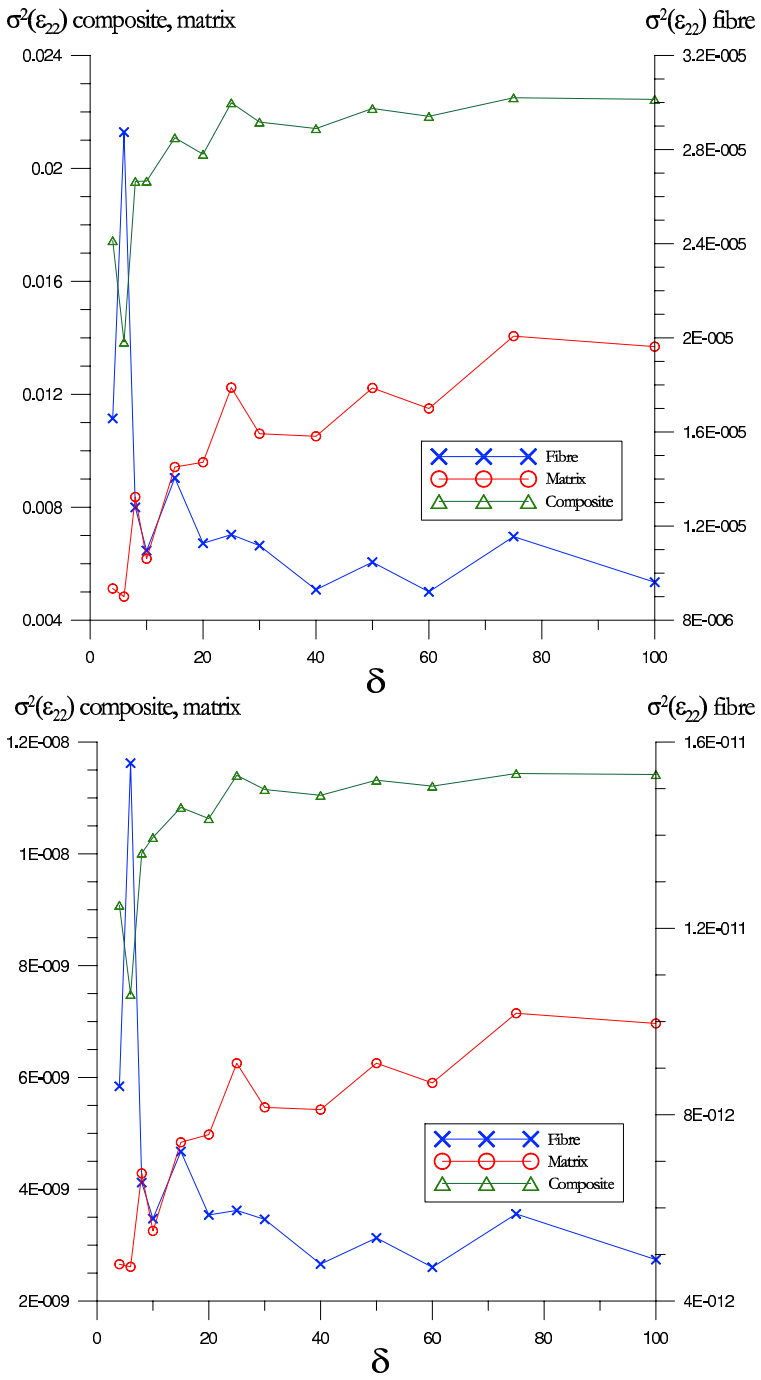

Figure 5.20: Variance of the strain in the composite and in each constituent for each loadcase: displacement (up) and force (down)

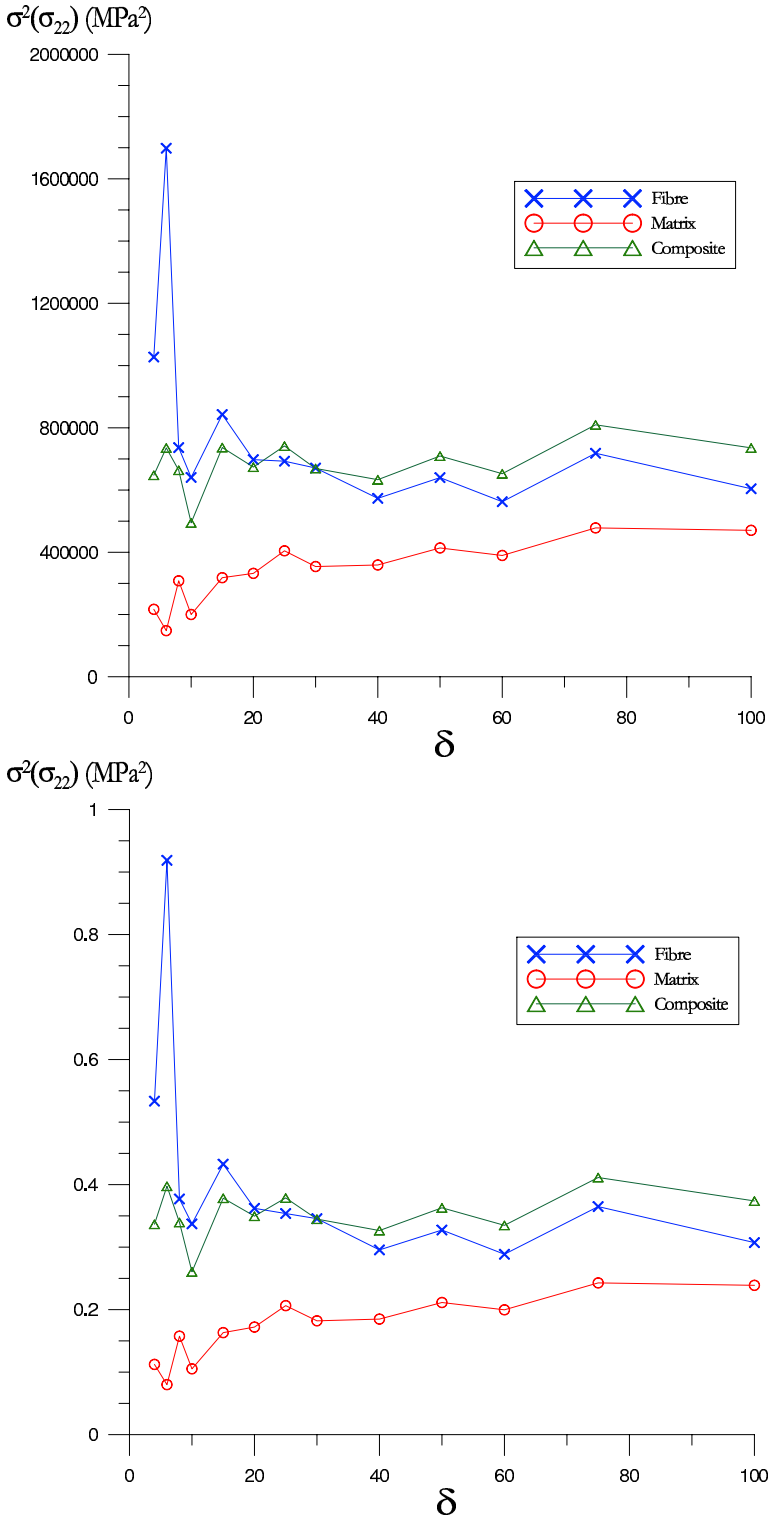

Figure 5.21: Variance of the stress in the composite and in each constituent for each loadcase: displacement (up) and force (down)

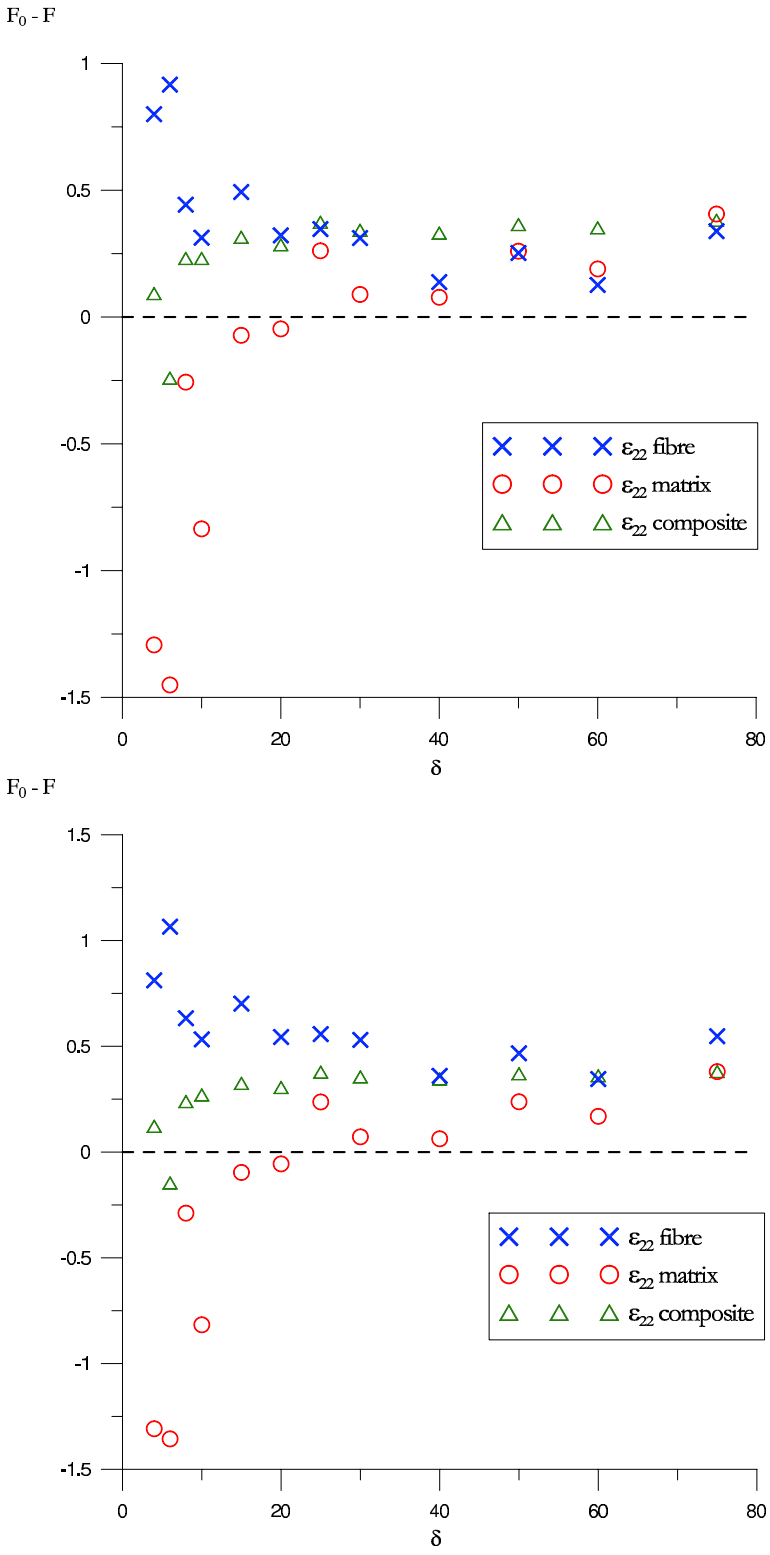

Figure 5.22: $\sigma^2(\varepsilon_{22})$ hypothesis test for both loadcases: displacements (up) and forces (down)

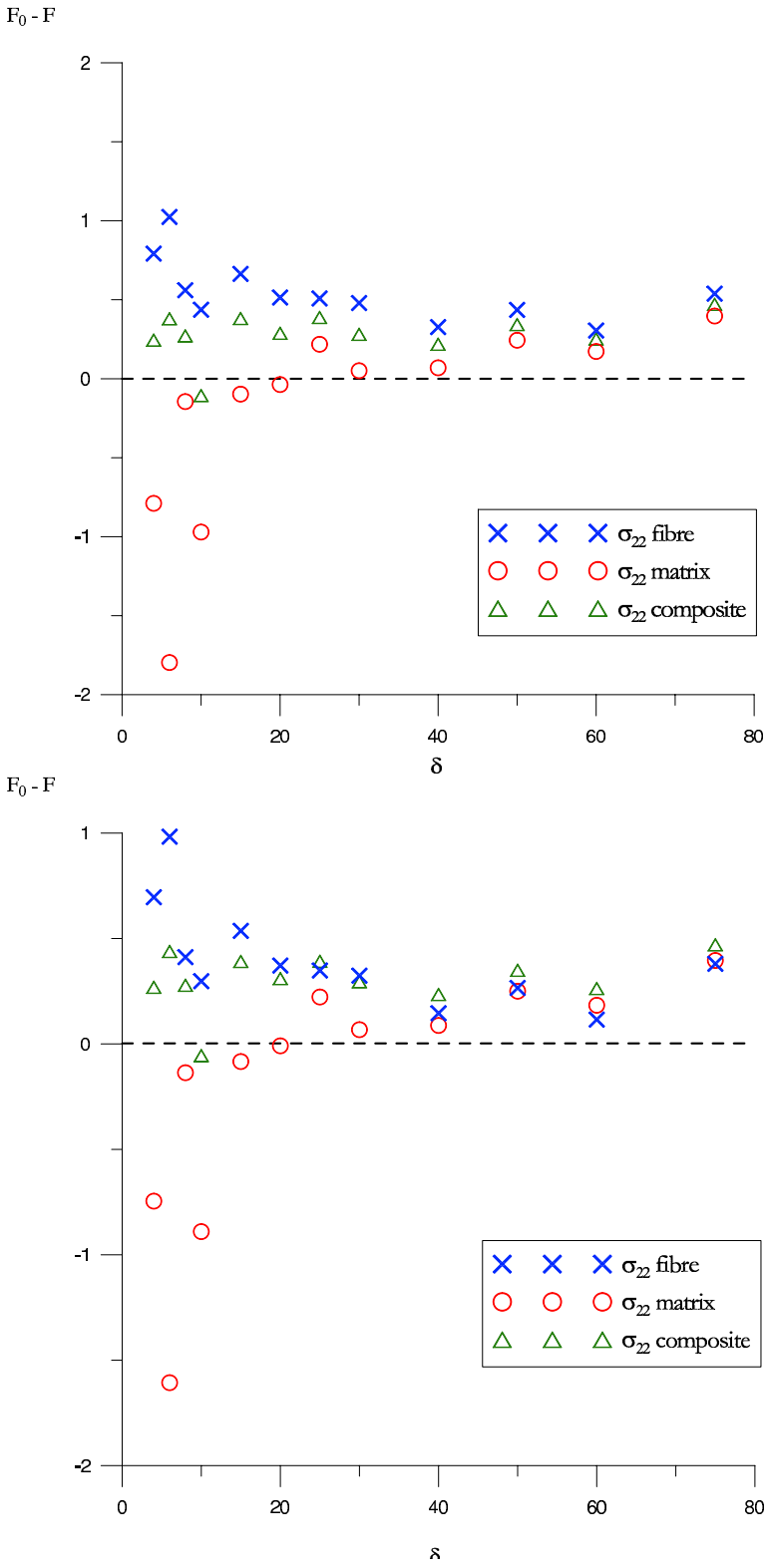

Figure 5.23: $\sigma^2(\sigma_{22})$ hypothesis test for both loadcases: displacements (up) and forces (down)

mean. The plots of the coefficient of variation of σ_{22} and ε_{22} for the fibre, the matrix and the composite for each SRVE candidate are shown in Figures 5.24 and 5.25, respectively.

If the biggest SRVE candidate ($\delta = 100$) is considered to have the same statistics of the whole population, the error can be computed with respect to the value obtained for this SRVE. In Tables 5.5, 5.6 and 5.7 the percentual relative difference between the coefficient of variation of the SRVE of size $\delta = 100$ and that of each SRVE candidate has been computed for the fibre, the matrix and the composite, respectively. Results show that the relative error is lower than 10% for $\delta \geq 50$.

δ	$\mu(\sigma_{22})$	$\sigma(\sigma_{22})$	$\rho(\sigma_{22})$	error	$\mu(\varepsilon_{22})$	$\sigma(\varepsilon_{22})$	$\rho(\varepsilon_{22})$	error
4	1955	1027192	0.5185	39.236%	$8.67{\cdot}10^{-3}$	$1.66{\cdot}10^{-5}$	0.4696	35.70%
6	2311	1698239	0.5639	51.441%	$9.76{\cdot}10^{-3}$	$2.87{\cdot}10^{-5}$	0.5495	58.81%
8	2010	736460	0.4269	14.659%	$8.80{\cdot}10^{-3}$	$1.28{\cdot}10^{-5}$	0.4065	17.48%
10	1979	640302	0.4043	8.582%	$8.44{\cdot}10^{-3}$	$1.10{\cdot}10^{-5}$	0.3920	13.28%
15	2055	842589	0.4468	19.987%	$8.82{\cdot}10^{-3}$	$1.40{\cdot}10^{-5}$	0.4249	22.79%
20	2090	697556	0.3996	7.307%	$9.00{\cdot}10^{-3}$	$1.13{\cdot}10^{-5}$	0.3728	7.74%
25	2092	692598	0.3979	6.849%	$8.94{\cdot}10^{-3}$	$1.16{\cdot}10^{-5}$	0.3817	10.29%
30	2049	670816	0.3998	7.357%	$8.79{\cdot}10^{-3}$	$1.12{\cdot}10^{-5}$	0.3801	9.84%
40	2058	573395	0.3680	1.169%	$8.83{\cdot}10^{-3}$	$9.30{\cdot}10^{-6}$	0.3454	0.18%
50	2076	639954	0.3854	3.493%	$8.92{\cdot}10^{-3}$	$1.05{\cdot}10^{-5}$	0.3626	4.80%
60	2057	562227	0.3645	2.115%	$8.82{\cdot}10^{-3}$	$9.20{\cdot}10^{-6}$	0.3441	0.57%
75	2110	718188	0.4016	7.853%	$9.04{\cdot}10^{-3}$	$1.16{\cdot}10^{-5}$	0.3761	8.69%
100	2087	604079	0.3724	0.000%	$8.96{\cdot}10^{-3}$	$9.61{\cdot}10^{-6}$	0.3460	-

Table 5.5: Coefficient of variation (ρ) of σ_{22} and ε_{22} in the fibre

δ	$\mu(\sigma_{22})$	$\sigma(\sigma_{22})$	$\rho(\sigma_{22})$	error	$\mu(\varepsilon_{22})$	$\sigma(\varepsilon_{22})$	$\rho(\varepsilon_{22})$	error
4	1226	216796	0.3798	33.95%	0.2548	0.005119761	0.2809	38.25%
6	1143	148033	0.3367	41.46%	0.2502	0.004834539	0.2779	38.90%
8	1203	308436	0.4615	19.75%	0.2545	0.008362426	0.3593	21.00%
10	1225	200041	0.3652	36.50%	0.2677	0.00617799	0.2936	35.44%
15	1203	318370	0.4692	18.41%	0.2624	0.009424998	0.3700	18.65%
20	1194	332011	0.4825	16.09%	0.2567	0.009593754	0.3815	16.12%
25	1196	404664	0.5320	7.49%	0.2614	0.01223629	0.4232	6.96%
30	1208	353844	0.4925	14.35%	0.2613	0.010604754	0.3941	13.36%
40	1198	358870	0.5001	13.03%	0.2597	0.01051337	0.3948	13.18%
50	1202	413772	0.5349	6.98%	0.2593	0.01222206	0.4263	6.27%
60	1197	389583	0.5215	9.32%	0.2596	0.01149625	0.4130	9.19%
75	1184	478369	0.5842	1.59%	0.2564	0.014059263	0.4625	1.68%
100	1193	470275	0.5751	0.00%	0.2572	0.01368741	0.4548	-

Table 5.6: Coefficient of variation (ρ) of σ_{22} and ε_{22} in the matrix

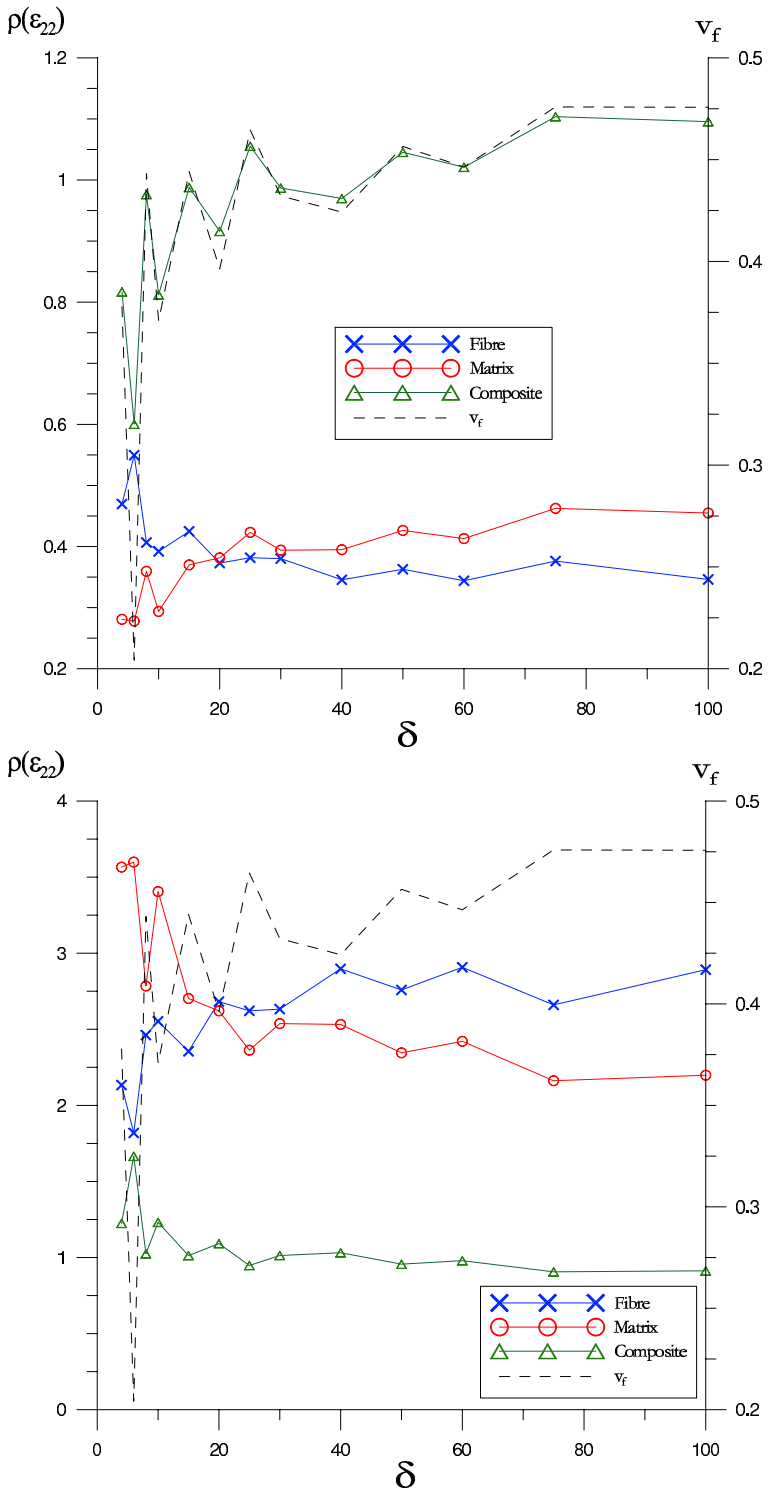

Figure 5.24: Coefficient of variation of the strain in the composite and in each constituent for each loadcase: displacements (up) and force (down)

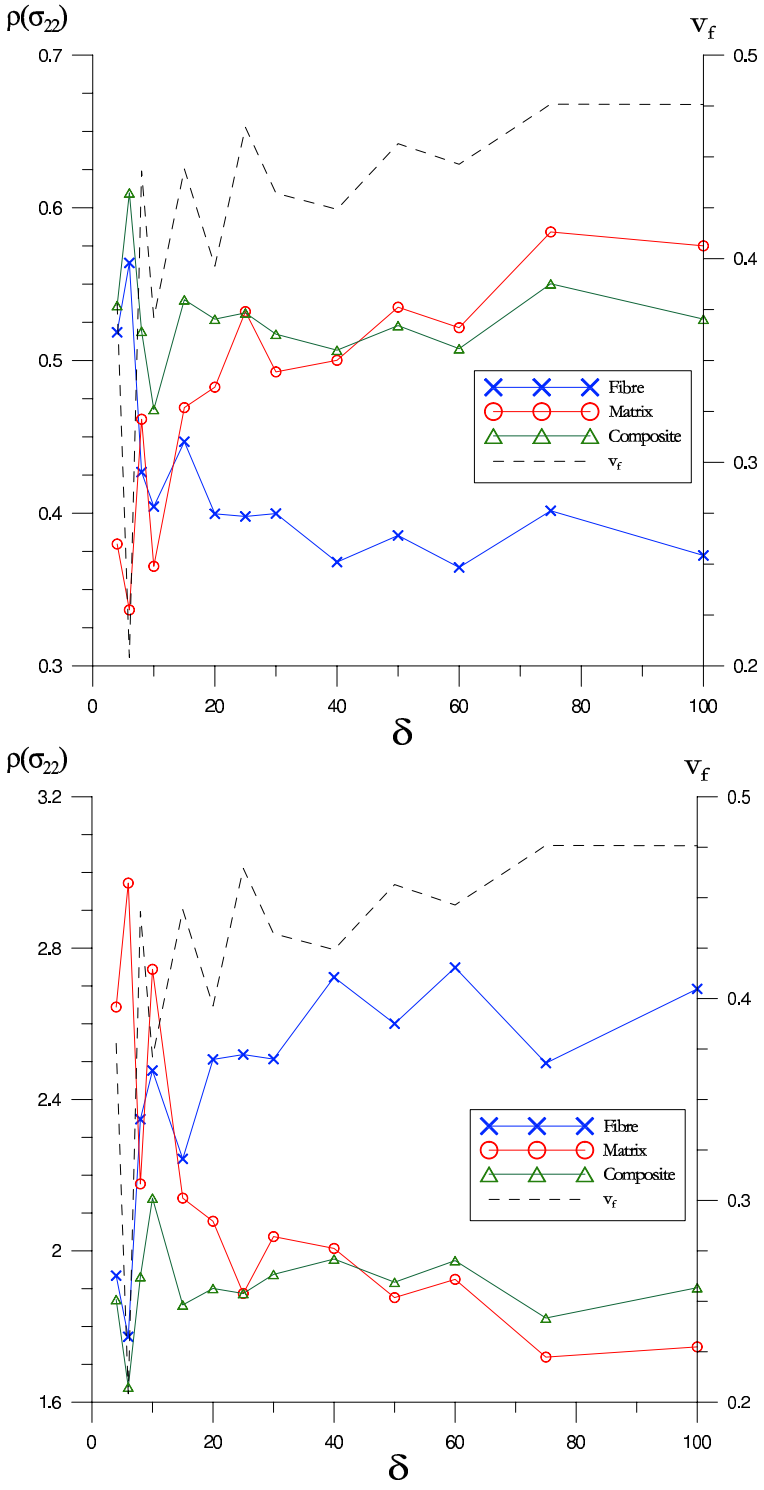

Figure 5.25: Coefficient of variation of the stress in the composite and in each constituent for each loadcase: displacements (up) and force (down)

δ	$\mu(\sigma_{22})$	$\sigma(\sigma_{22})$	$\rho(\sigma_{22})$	error	$\mu(\varepsilon_{22})$	$\sigma(\varepsilon_{22})$	$\rho(\varepsilon_{22})$	error
4	1502	647788	0.5360	1.69%	0.1617	0.0174	0.8169	25.44%
6	1406	735228	0.6098	15.69%	0.1960	0.0139	0.6004	45.21%
8	1569	663505	0.5192	1.49%	0.1432	0.0195	0.9763	10.90%
10	1503	494658	0.4680	11.20%	0.1722	0.0195	0.8122	25.88%
15	1590	736831	0.5398	2.41%	0.1470	0.0211	0.9878	9.85%
20	1557	673720	0.5270	0.01%	0.1563	0.0205	0.9160	16.40%
25	1621	741517	0.5312	0.79%	0.1416	0.0223	1.0555	3.67%
30	1582	669427	0.5173	1.86%	0.1491	0.0216	0.9870	9.92%
40	1571	633480	0.5067	3.86%	0.1509	0.0214	0.9698	11.49%
50	1611	709402	0.5229	0.79%	0.1423	0.0221	1.0455	4.58%
60	1591	652344	0.5077	3.67%	0.1448	0.0218	1.0210	6.82%
75	1635	809564	0.5503	4.41%	0.1359	0.0225	1.1038	0.73%
100	1627	735198	0.5271	0.00%	0.1367	0.0224	1.0957	-

Table 5.7: Coefficient of variation (ρ) of σ_{22} and ε_{22} in the composite

5.7 Probability density functions of stress and strain fields in the matrix

Most of the failure criteria for the composite transverse direction consider that the failure is caused by cracks in the matrix (See Chapter 3). One of the objectives of this work is to find probability distribution functions for the failure in the transverse direction. For this reason, when trying to develop a Statistical Representative Volume Element the stress and strain probability distribution functions in the matrix have to be analyzed.

At this point the equivalence of boundary conditions and, consequently, the obtained probability distribution functions, when applying displacements or forces are equivalent (the *shape* of the function is equivalent but with different scale). For this reason, only the probability distribution functions obtained for the displacement boundary condition are shown.

In Figures 5.26, 5.27 and 5.28 the probability distribution function for ε_{22} in the matrix is plotted for the SRVE candidates. Figure 5.26 shows that for small SRVE sizes the distributions seem to be nearly symmetric, but from $\delta = 25$, in Figure 5.27, this tendency disappears and distributions have a right tail longer than the left tail. One should note the importance of well reproducing the distributions tails, since the failure of the composite will be related to the values which are in these tails. It is important to notice, that a random model of the composite will reproduce in a more realistic way these tails than classical periodic models do[6]. This fact provides random models of the availability of determining the failure of the composite more accurately.

Figures 5.29, 5.30 and 5.31 show the probability density function of σ_{22} in the matrix. The similitude between two probability distributions can be observed with a QQ-plot.

[6]This point will be explained with more detail in Chapter 7.

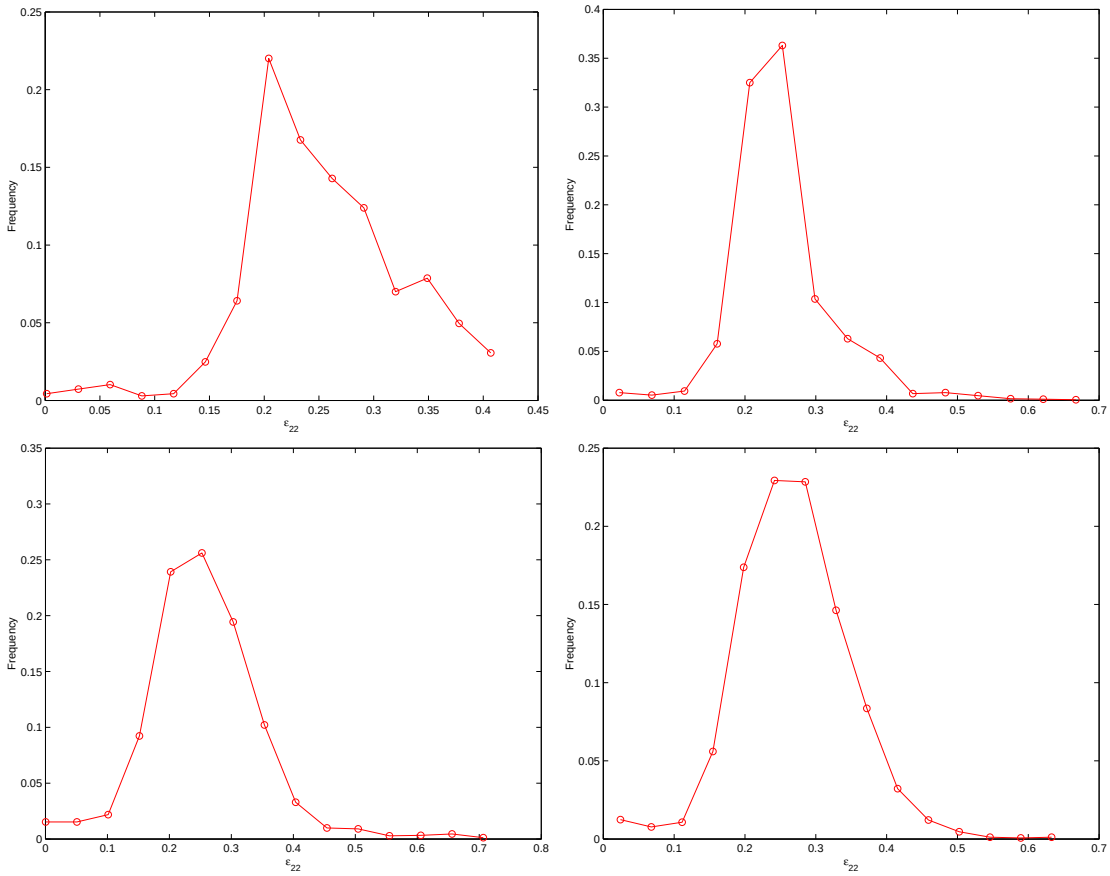

Figure 5.26: ε_{22} in the matrix probability distribution function for δ = 4,6,8,10 (left to right, up to down)

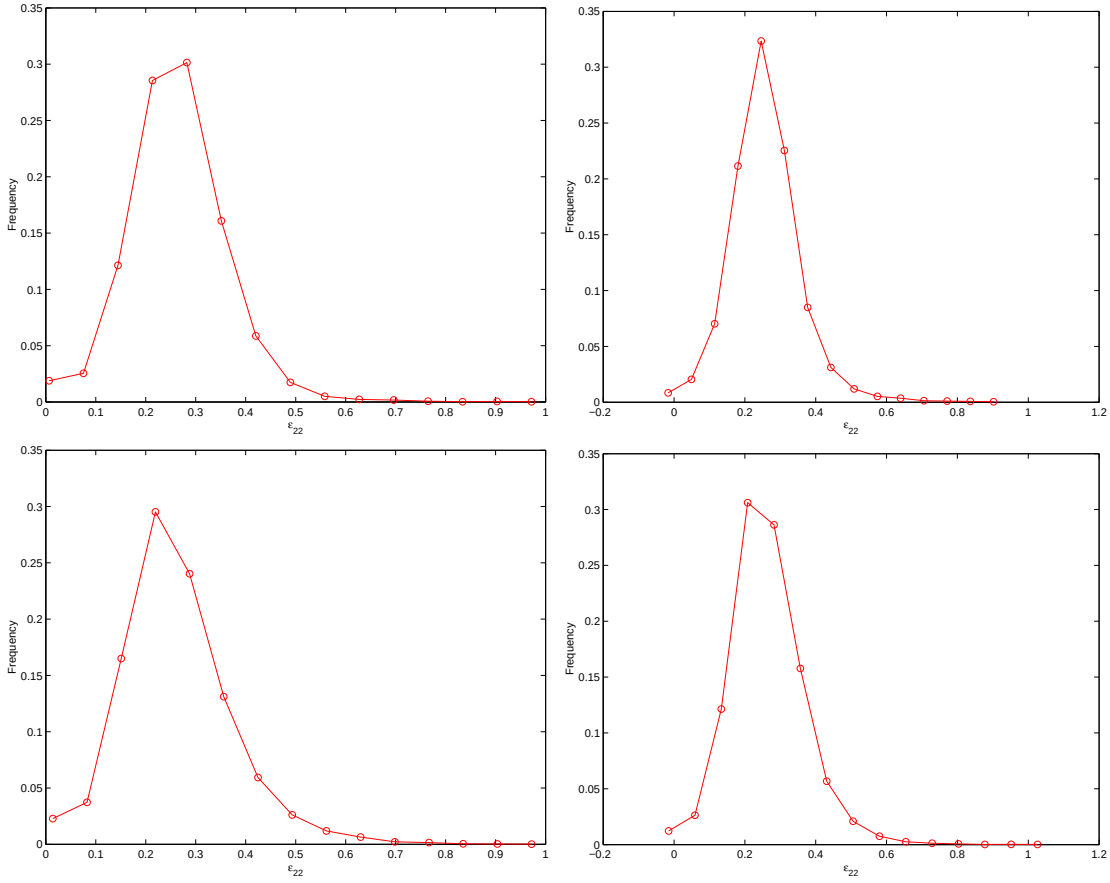

Figure 5.27: ε_{22} in the matrix probability distribution function for $\delta = 15, 20, 25$, and 30 (left to right, up to down)

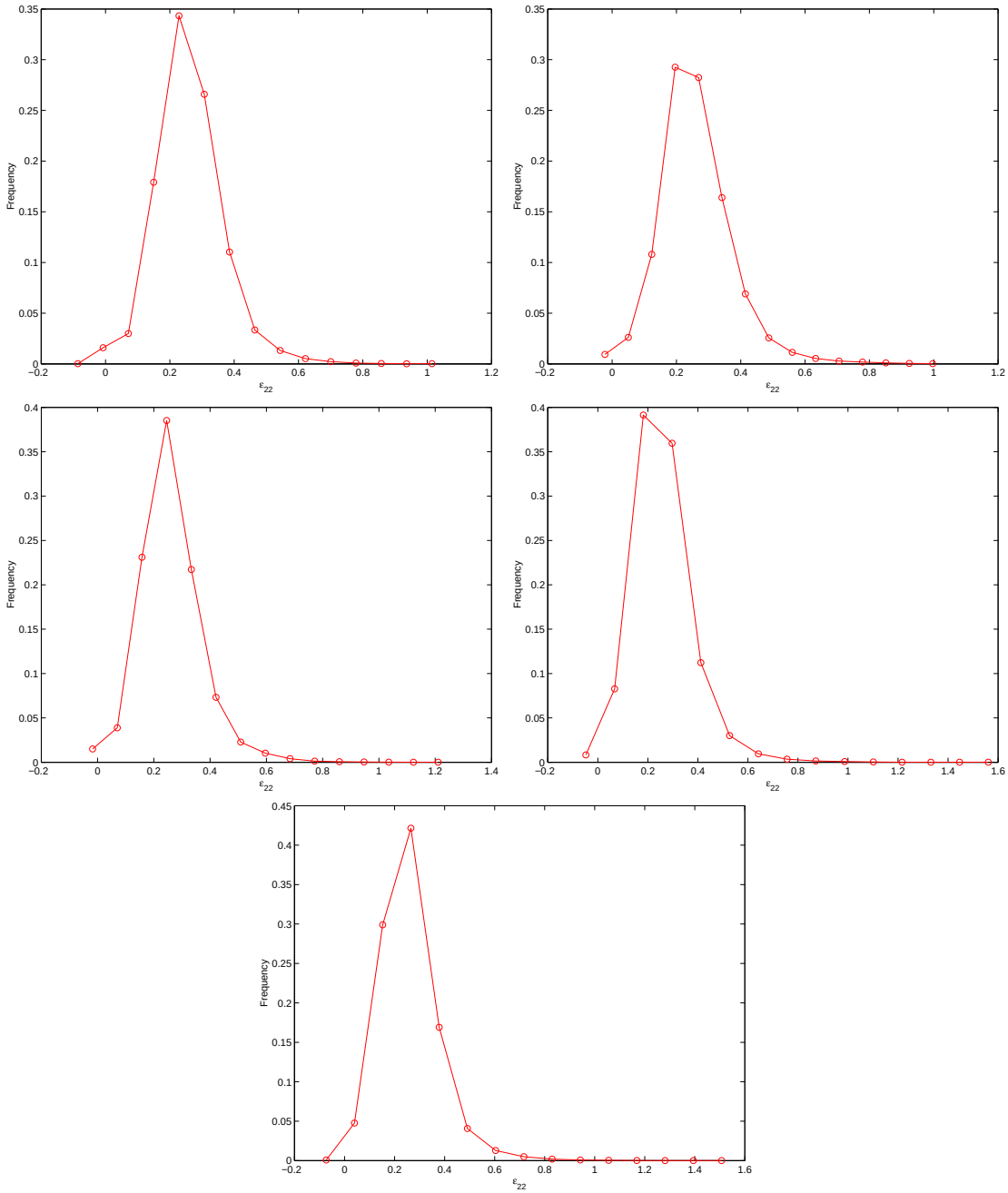

Figure 5.28: ε_{22} in the matrix probability distribution function for $\delta = 40, 50, 60, 75$ and 100

(left to right, up to down)

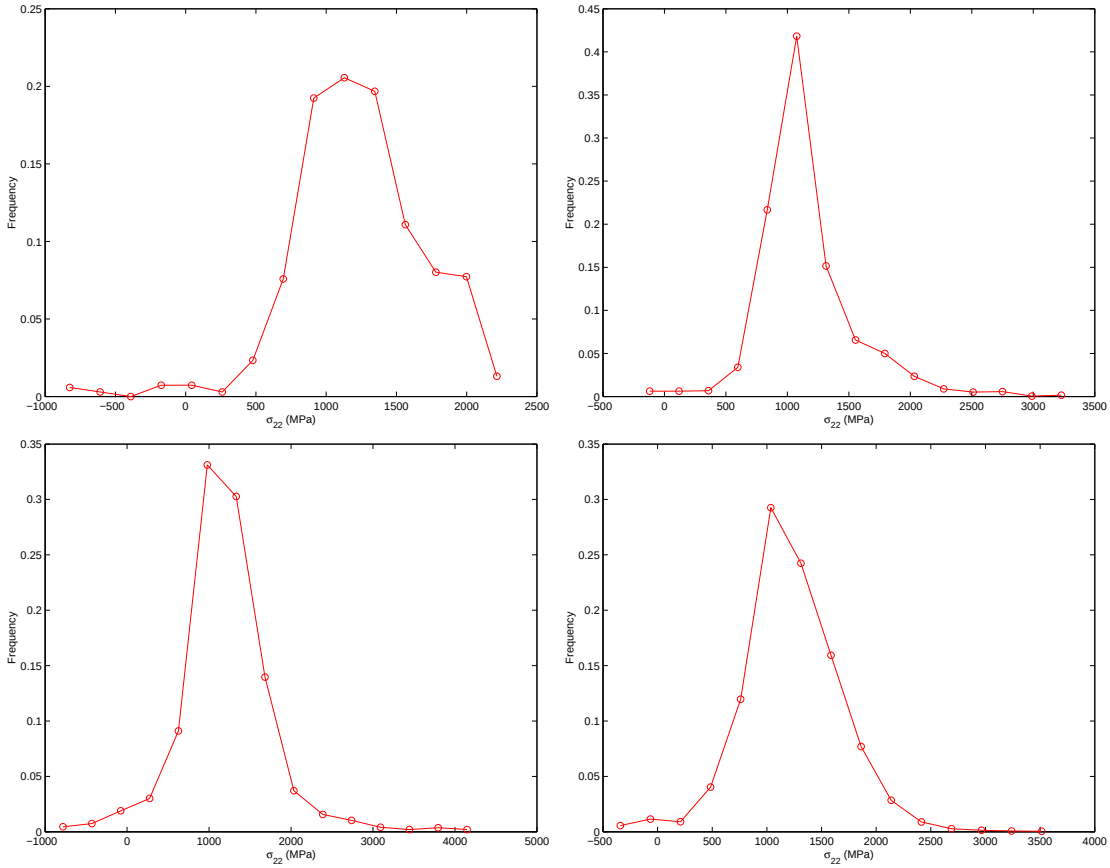

Figure 5.29: σ_{22} in the matrix probability distribution function for $\delta = 4, 6, 8$ and 10 (left to right, up to down)

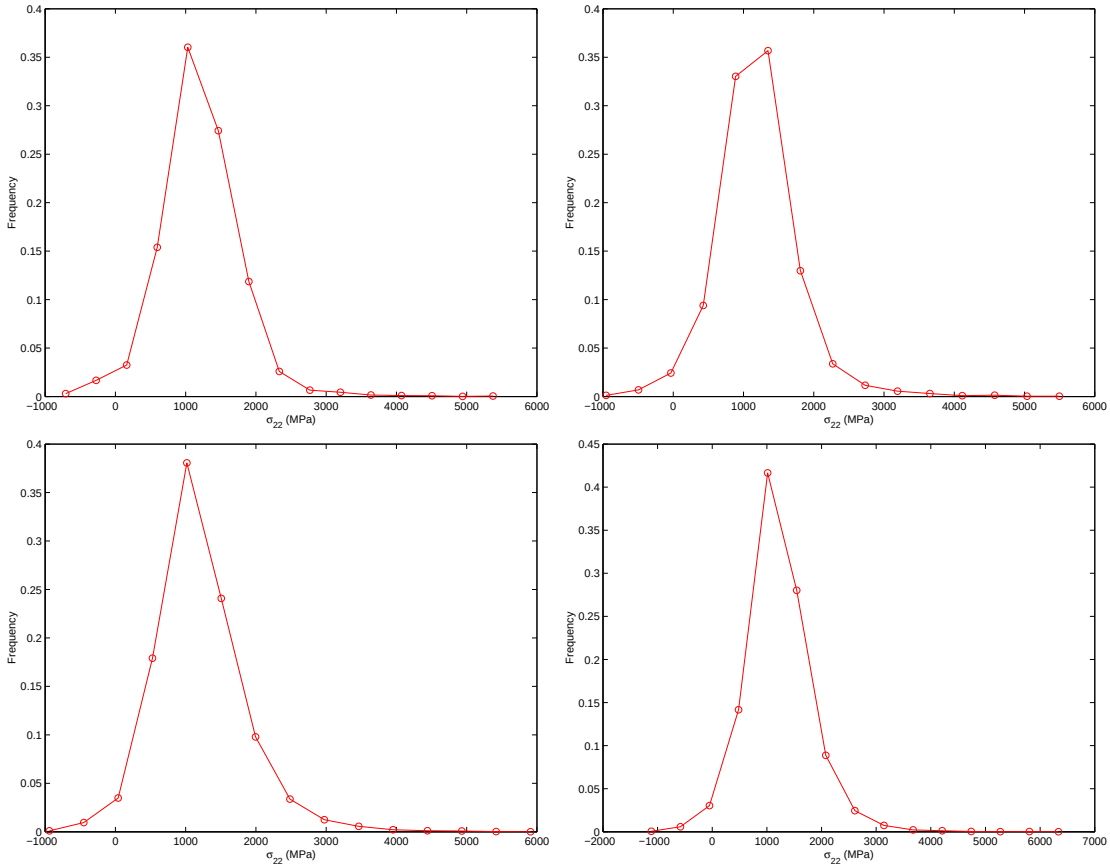

Figure 5.30: σ_{22} in the matrix probability distribution function for δ = 15,20,25 and 30 (left to right, up to down)

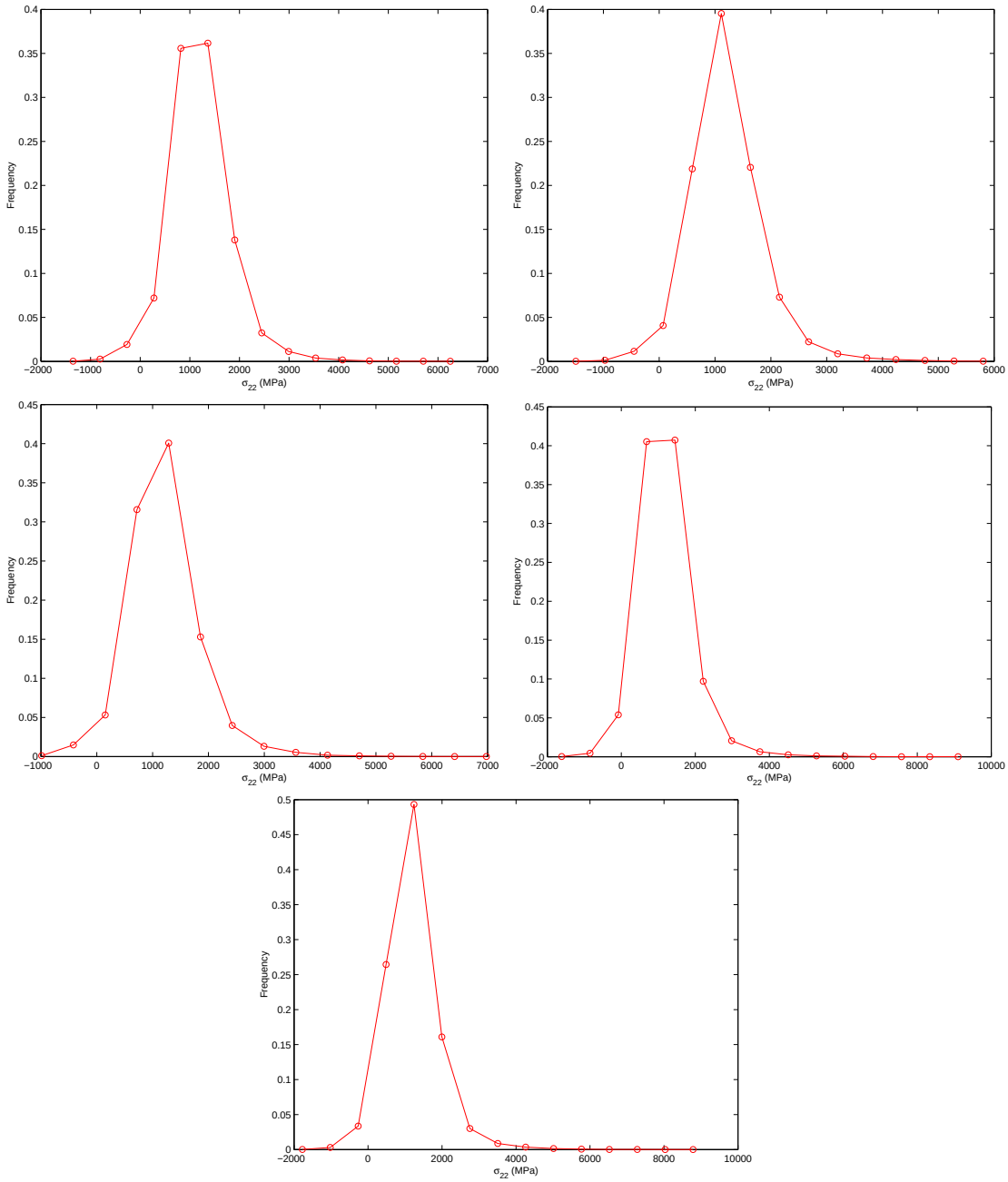

Figure 5.31: σ_{22} in the matrix probability distribution function for δ = 40,50, 60, 75 and 100

(left to right, up to down)

In this plot, if the distributions are equivalent the plot shows a line with slope 1. Figures 5.32 and 5.33 show QQ-plots for ε_{22} in the matrix and Figures 5.34 and 5.34 show QQ-plots for σ_{22} in the matrix. For these figures, the distribution function obtained in each SRVE candidate is compared with the distribution function of the model with $\delta = 100$.

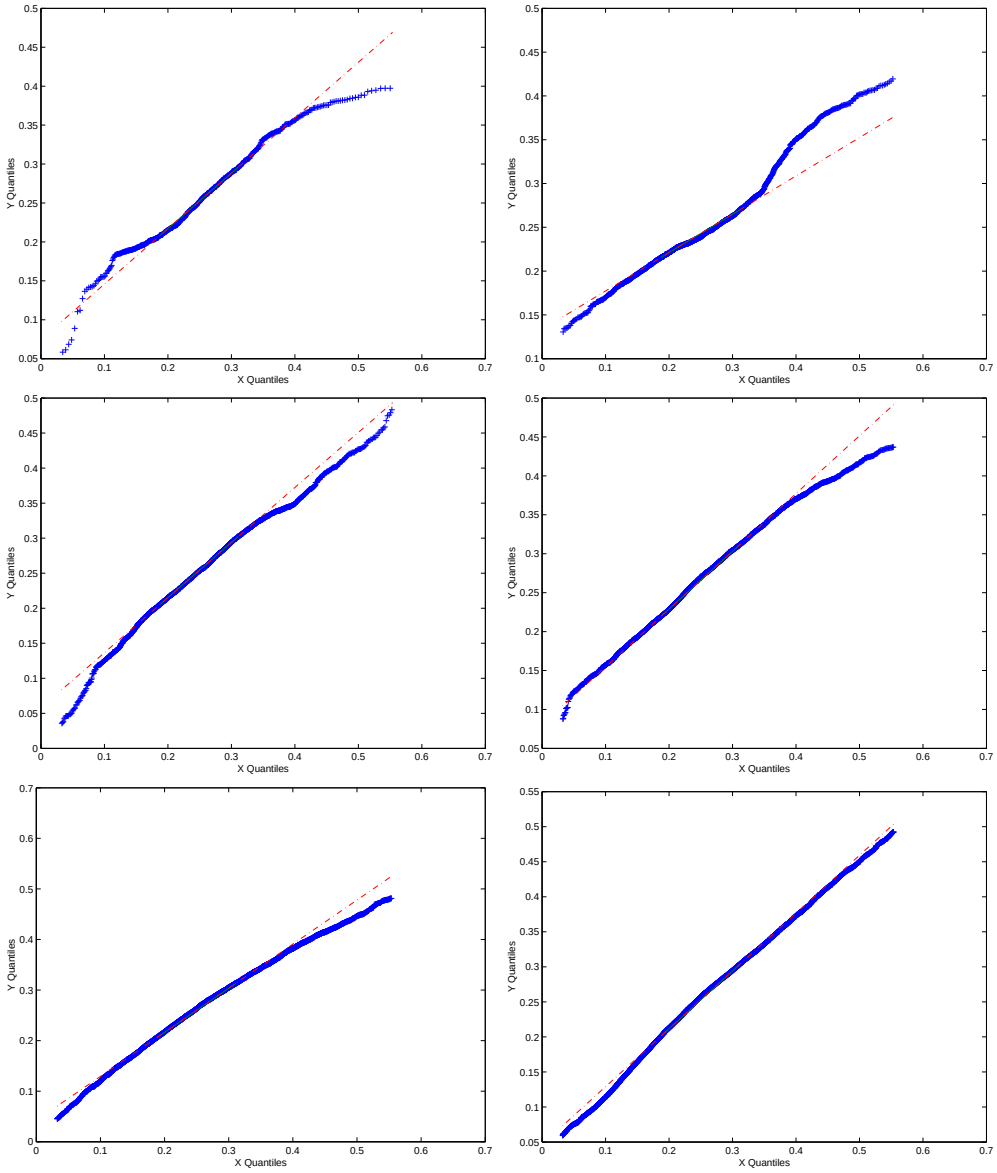

Figure 5.32: QQ-plots of ε_{22} in the matrix for $\delta = 4, 6, 8, 10, 15$ and 20 (left to right, up to down)

From all these plots it can be considered that the probability distribution of ε_{22} in the matrix for the model $\delta = 20$ is equivalent to that corresponding to the model $\delta = 100$. Regarding σ_{22} the analogous conclusion can be derived for $\delta = 25$.

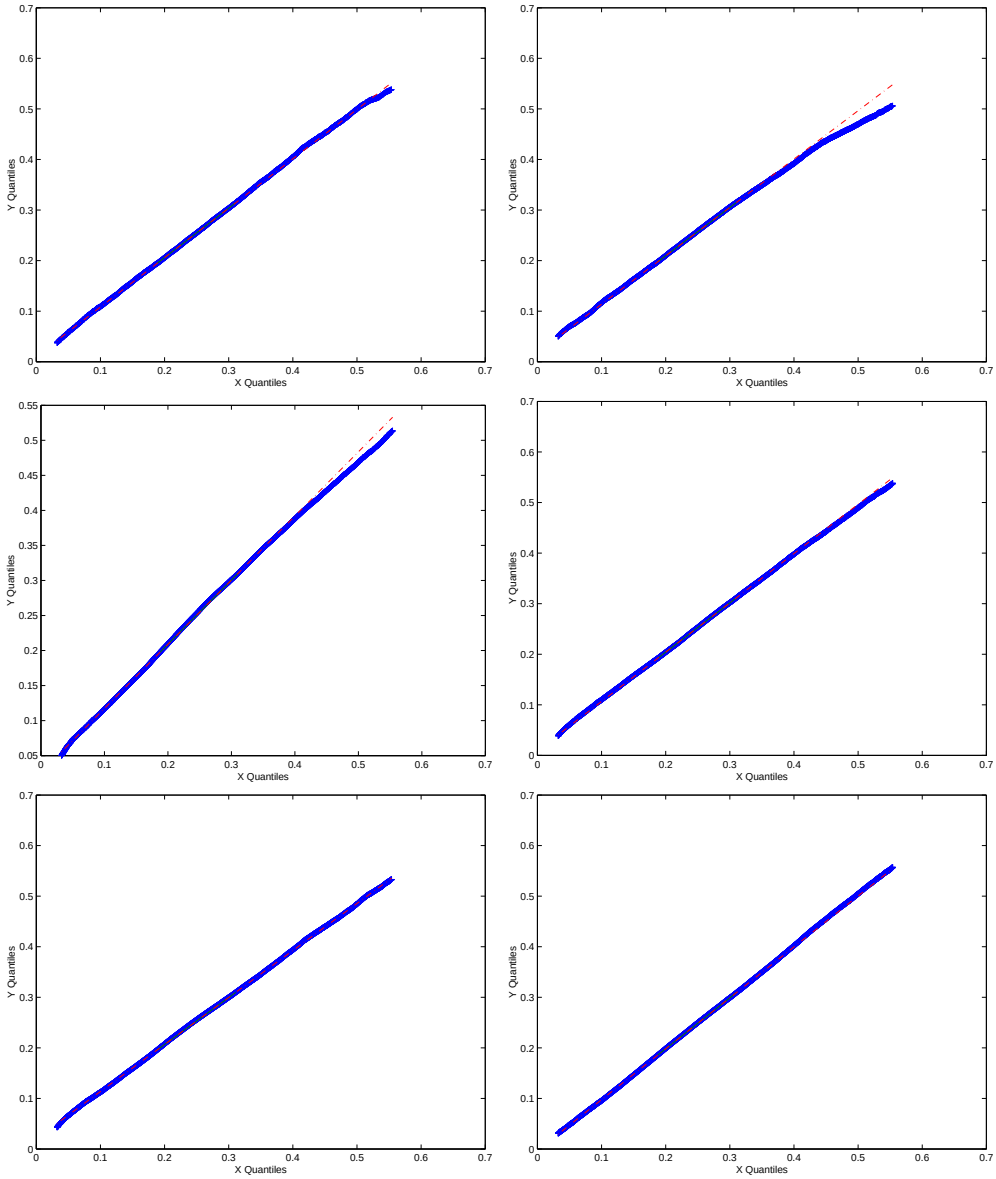

Figure 5.33: QQ-plots of ε_{22} in the matrix for $\delta = 25, 30, 40, 50, 60$ and 75 (left to right, up to down)

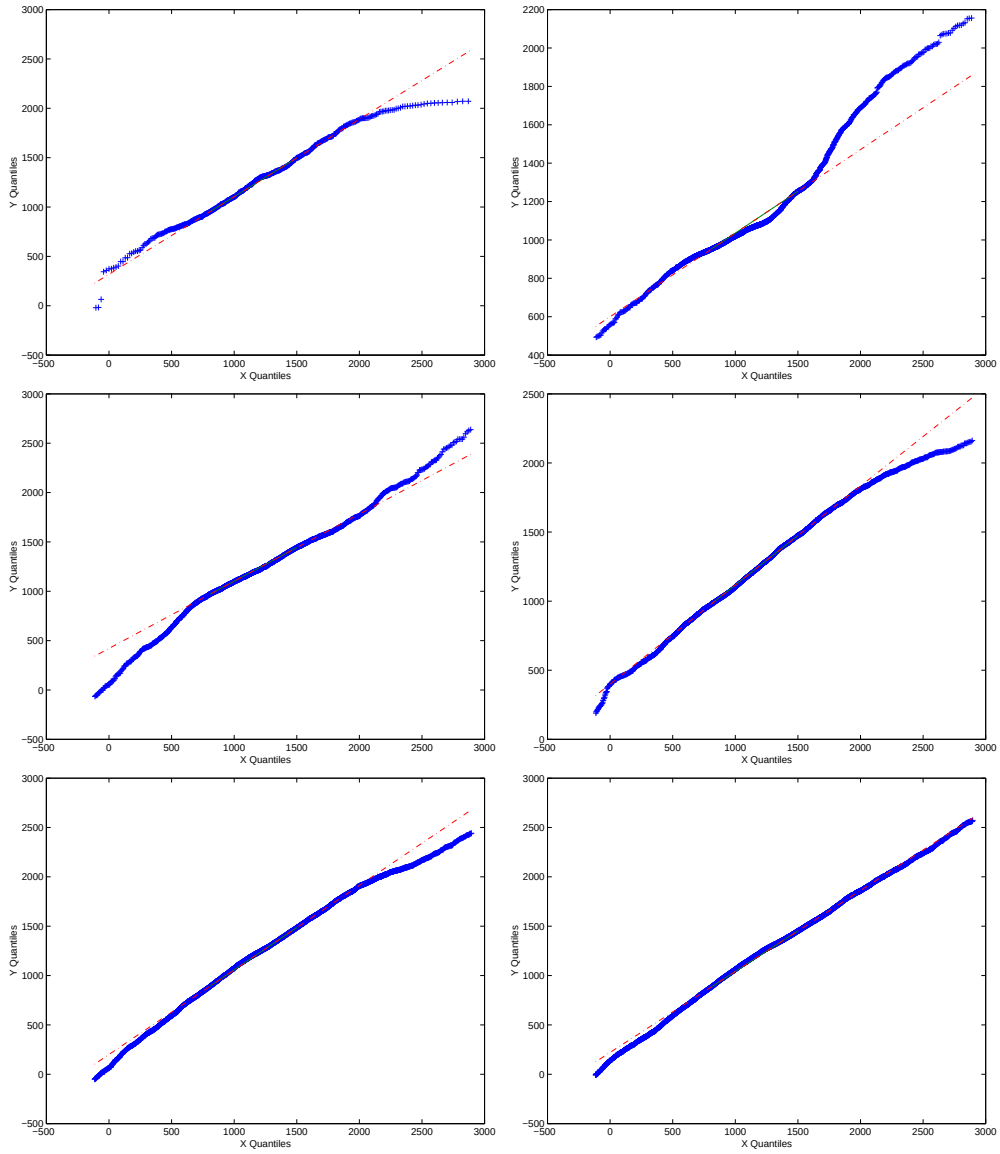

Figure 5.34: QQ-plots of σ_{22} in the matrix for $\delta = 4, 6, 8, 10, 15$ and 20 (left to right, up to down)

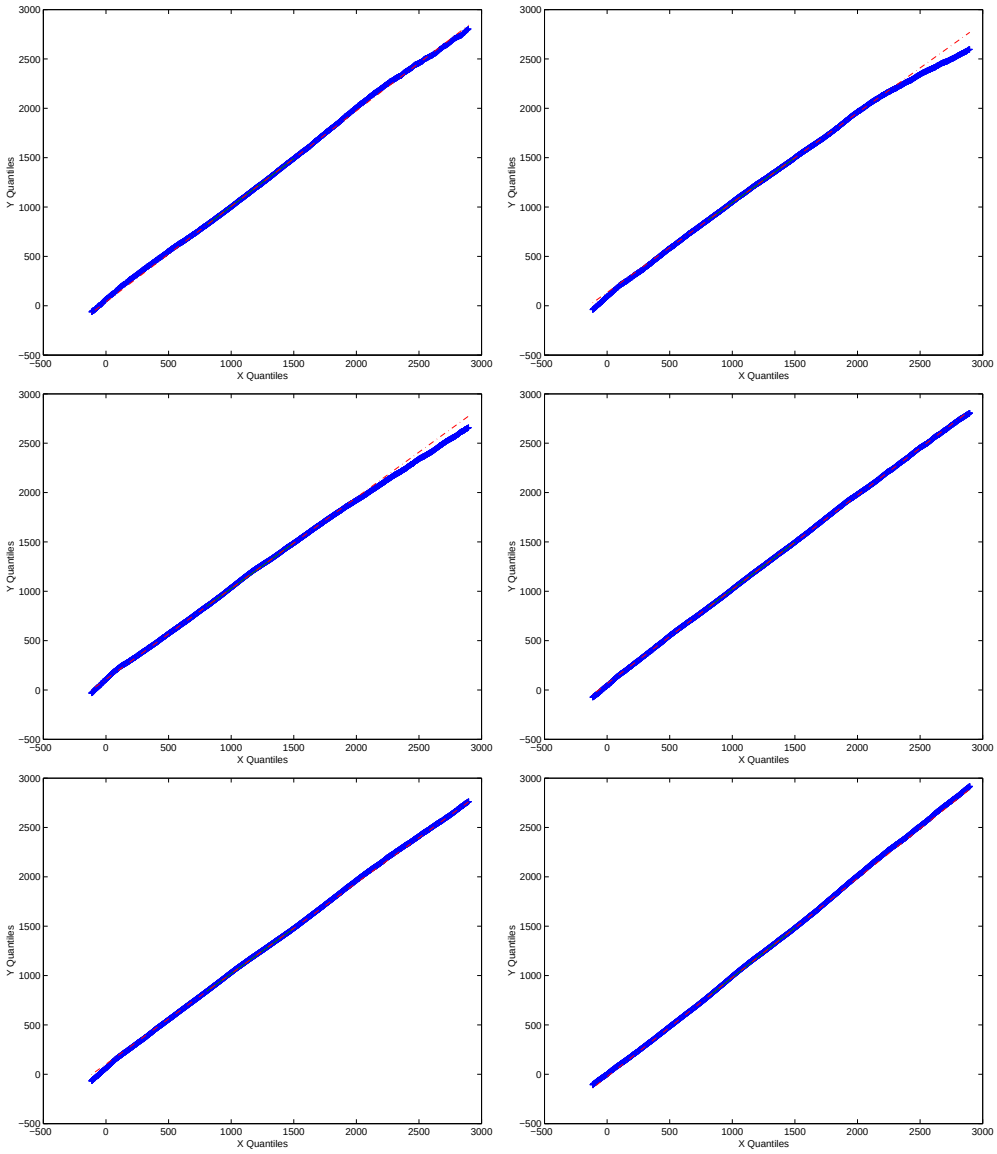

Figure 5.35: QQ-plots of σ_{22} in the matrix for $\delta = 25, 30, 40, 50, 60$ and 75 (left to right, up to down)

5.8 Distance distributions

One of the hypothesis of this work is that the non-uniform distribution of the fibers within a composite affects its failure behavior. For this reason, the SRVE has to represent the statistical distance distribution of the fibers in the bulk material.

As reviewed in Section 4.4 and as can be found in the papers by Pyrz [132, 133] a useful way to analyze inclusions or fibres within a matrix is to use the Second order intensity function and the Pair distribution function. In the following, this functions, together with the nearest neighbor distance functions, for the different SRVE candidates are analyzed.

5.8.1 Second order intensity function

The Second Order intensity function $K(h)$, as defined in equation 4.25 can be seen as the expected number of fibers to be found inside a circle of radius h, divided by the Poisson parameter, λ.

For the SRVE candidates corresponding to $\delta = 4$ to $\delta = 8$, $K(h)$ is not computable with the estimator of equation 4.25. Figure 5.36 shows the second order intensity function for $\delta = 15 - 25$, $\delta = 30 - 50$, and $\delta = 60 - 100$. Besides that, this figure includes a plot of $K(h)$ corresponding to a random pattern (that is, a Poisson process). It can be seen how when δ grows $K(h)$ tends to that of the random process.

It is also important to notice that $K(h)$ tends to be linear. That means, from a certain value of h the expected number of fibres to be found is proportional to the sampling area.

5.8.2 Pair distribution function

Recalling equation 4.30, the pair distribution function is a function of the derivative of $K(h)$, and consequently, can be easily computed can obtained by numerical differentiation:

$$g(h) = \frac{1}{2\pi r}\frac{\mathrm{d}K(h)}{\mathrm{d}h}$$

Figure 5.37 shows the estimated pair distribution function for each SRVE candidate. The plots in Figure 5.37 also show this function for a Poisson process (for which $g(h) = 1$).

The considered estimator of $K(h)$[7] counts the number of fibres which are within a circle of radius h with center in a fibre. Since all the sampling points are fibre centers the derivative of $K(h)$ is overestimated for the lower values of h. For this reason most of the plots show peaks for the lower values of h.

For $\delta = 8$, $\delta = 10$ and $\delta = 15$, $g(h)$ does not converge to any constant value, since the number of fibres in these models is not large enough. For $\delta = 20$ the pair distribution function shows large fluctuations around a constant value. For $\delta = 25$ and $\delta = 30$ g(h), seem to converge but for a higher (in the case of $\delta = 25$) and for a lower value (for $\delta = 30$)

[7] See Equation 4.25

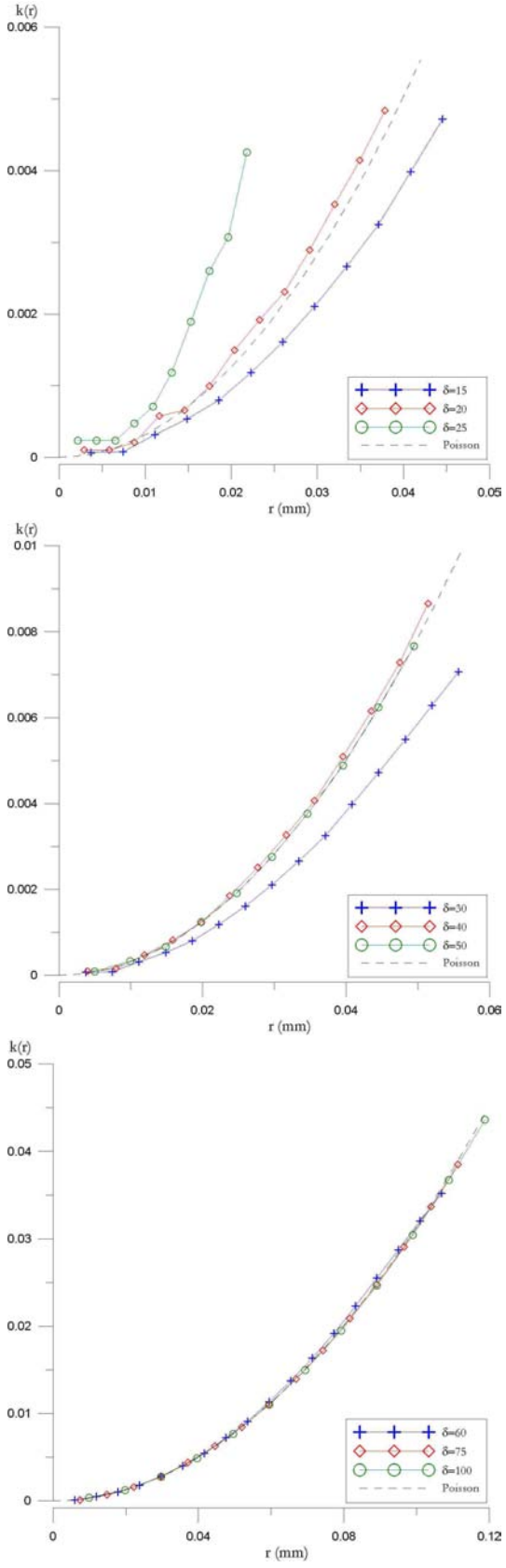

Figure 5.36: Second order intensity function for the SRVE candidates

to that of a CSR pattern. For the SRVE candidates with $\delta \geq 40$ it can be considered that $g(h)$ is equivalent to a Poisson process.

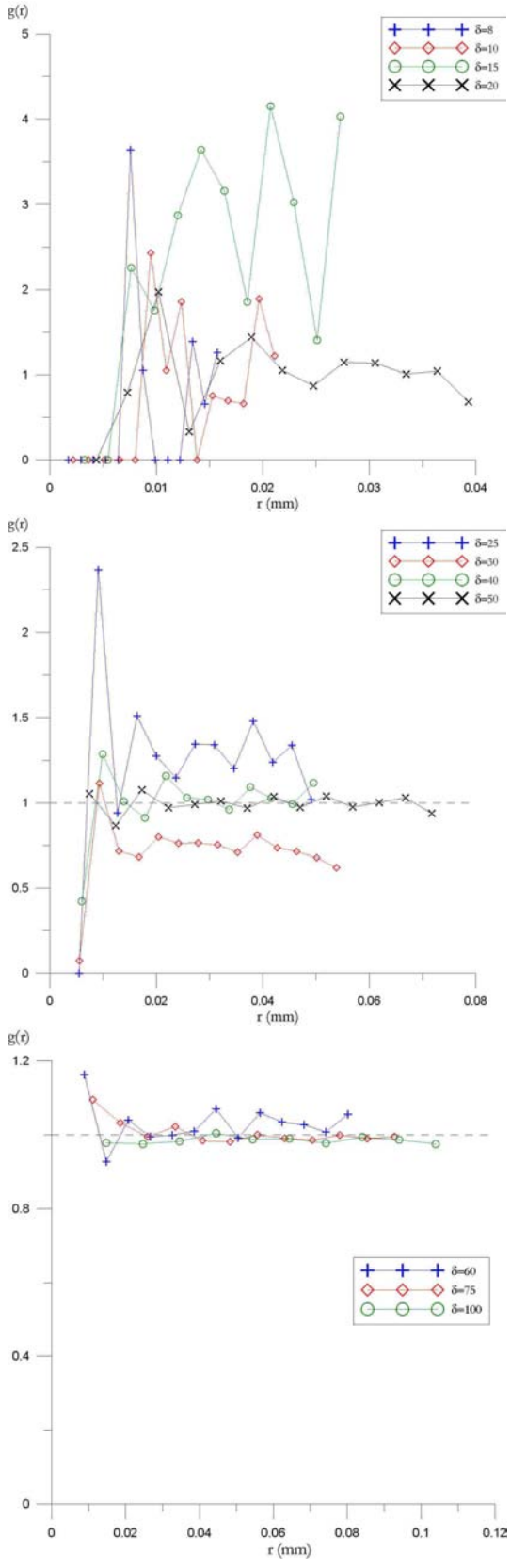

Figure 5.37: Pair distribution function for the SRVE candidates

5.8.3 Neighbor distances

As was described in Section 4.4.5, nearest neighbor distances provide information about the short range interaction between particles. It is important for the SRVE to reproduce the short range interaction between fibers of the bulk composite, because this may have strong influence in the failure properties of the material. In Figures 5.38, 5.39 and 5.40 plots for the first, second and third nearest neighbor probability distribution function are given. Those plots corresponding to small values of δ (δ=4,6,8) show some peaks which may lead to the wrong conclusion of presence of some regularity. However, these peaks are due to the small number of fibres present in those models, more than to regularity. Those plots corresponding to δ =10, 15, 20, 25 and 30 show nearest neighbor distributions which are still not smooth enough. For $\delta \geq 40$ the nearest neighbor functions show typical shapes of random point patterns.

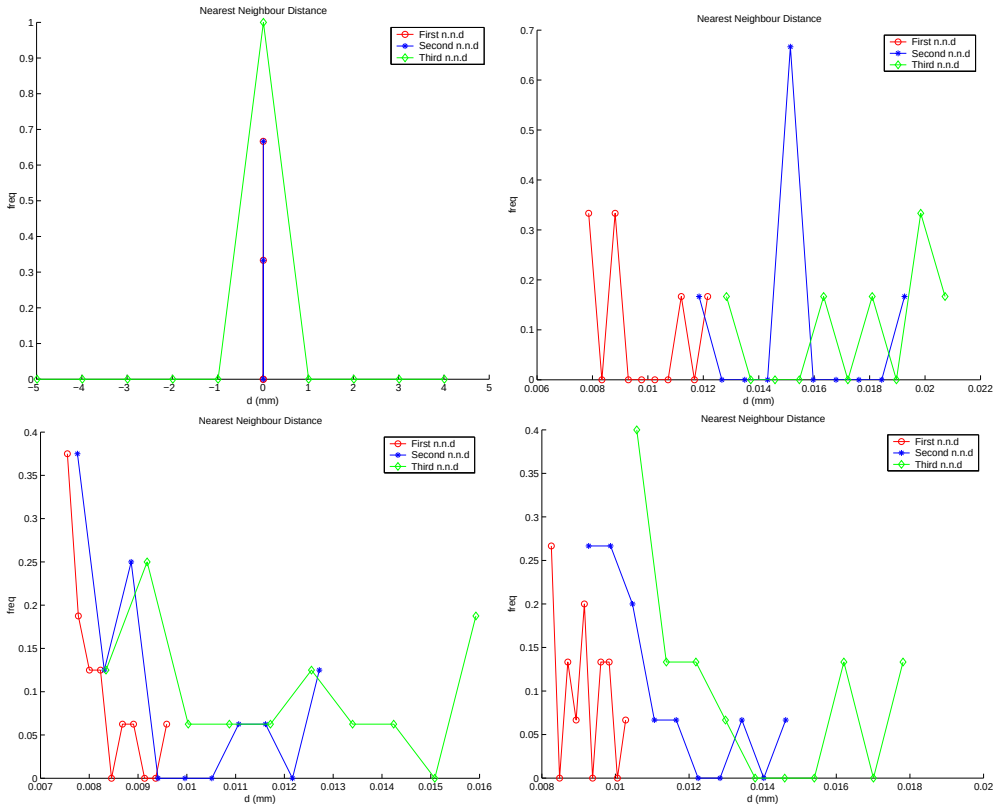

Figure 5.38: Neighbor distance functions for δ = 4, 6, 8, 10, 15, 20

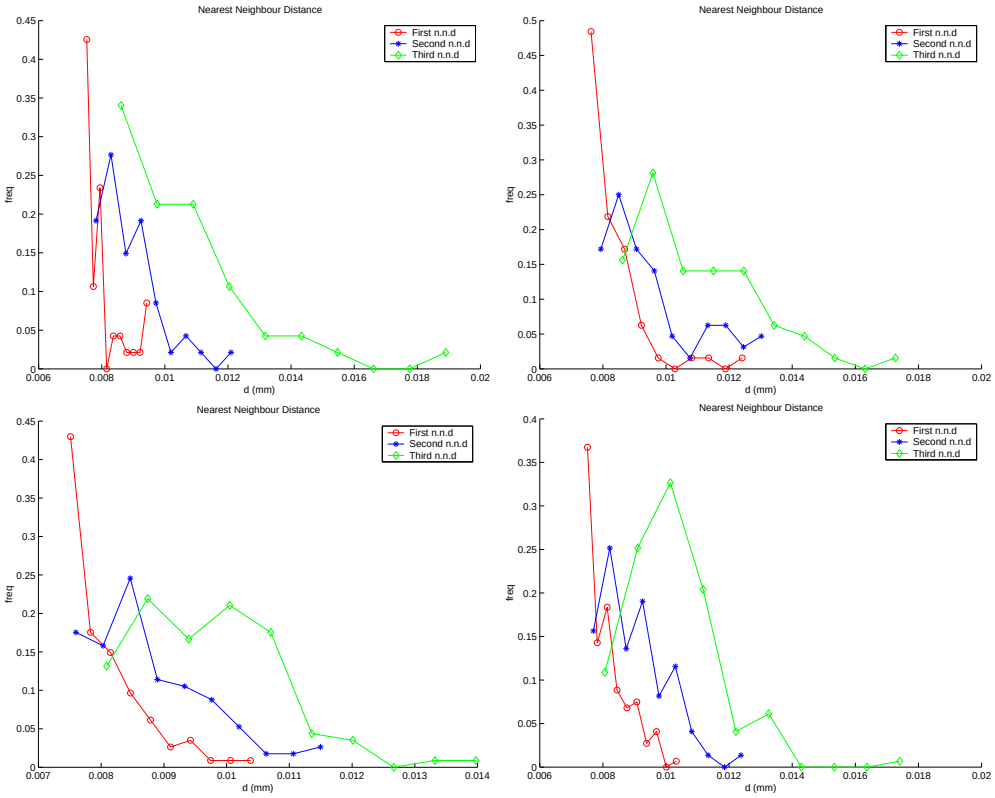

Figure 5.39: Neighbor distance functions for $\delta = 15$, 20 25 and 30

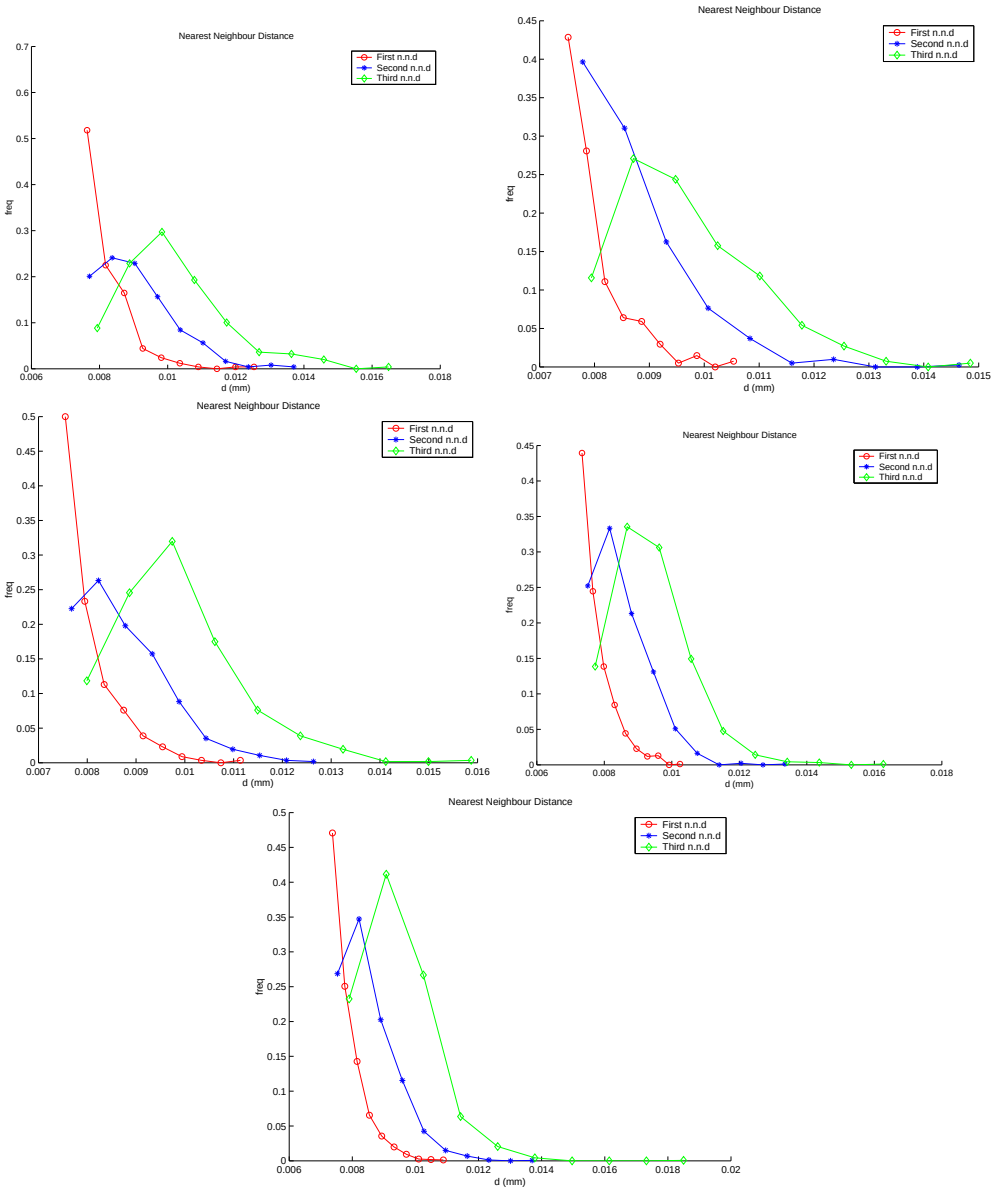

Figure 5.40: Neighbor distance functions for δ = 40, 50, 60 ,75 and 100

5.9 Conclusions

A numerical study to determine the finite size of the Statistical Representative Volume Element has been performed. Finite Element models of different size have been solved and different criteria regarding mechanical and statistical parameters have been analyzed. Each analysis has given a minimum model size (δ) for which it is satisfied. The results are summarized in Table 5.8.

Criteria	**Description**	**Result**
Volume fraction	Percentual difference lower than 10%	$\delta \geq 30$
Effective properties	Percentual difference lower than 10%	$\delta \geq 30$
Hill Condition	Difference between energy bounds lower than	$\delta \geq 15$
Strain field	Hypothesis test for the mean	$\delta \geq 15$
	Hypothesis test for the variance	$\delta \geq 25$
	Coefficient of correlation. Percentual difference	$\delta \geq 50$
Stress field	Hypothesis test for the mean	$\delta \geq 10$
Strain field	Hypothesis test for the variance	$\delta \geq 25$
	Coefficient of correlation. Percentual difference	$\delta \geq 50$
Strain in matrix pdf	Similarity of probability density functions	$\delta \geq 30$
Stress in matrix pdf	Similarity of probability density functions	$\delta \geq 25$
Distance distributions	Comparison with Poisson process	$\delta \geq 50$

Table 5.8: Summary of analyzed criteria

From the analyzed criteria, in the following, it will be considered that the minimum required size of the SRVE model is $\delta = 50$.

Part II

Analysis and simulation of random fibre reinforced composites

Chapter 6

Experimental characterization of the random microstructure of composites

6.1 Introduction

This chapter contains the image analysis of the transverse section of long fibre reinforced composites with the aim to describe statistically the fiber distribution. As shown in figure, this chapter covers the whole experimental process for the acquisition of the necessary data from the composite. First, briefly, the specimen preparation (Section 6.2) is described. Next sections include the steps needed for digital image processing and capturing the position of the fibres of a sample of the material: Mosaicking (Section 6.3.1), Light correction (Section 6.3.3), Segmentation and binarization (Section 6.3.2) and Data acquisition (Section 6.3.4).

After to these descriptive sections, the statistics of the fibre distribution of four different materials will be analyzed. Three of them were produced in the composites group of the Technische Universität Hamburg-Harburg. These three materials are manufactured using the same carbon fibres (HTA5131 HTA 5131 400TEX 6K TO AERO from Tenax) but three different epoxy for the matrix (RTM-6 and 6376 from Hexcel, and 977-2 from Cytec). The fourth analyzed material was produced by the composites group of the Engineering Faculty of the University of Porto (FEUP). This material is made using a IM7/8552 pre-preg from Hexcel.

6.2 Specimen preparation

An interesting introduction report to optical microscopy is that by Davidson and Abramowitz [41] and that by Abramowitz [5]. The reference book by Bousfield [26] can be useful for microscopy specimen preparation. More specialized information can be found in the book edite by Summerscales [143], which covers different methods of microscopy and includes a chapter by Guild and Summerscales devoted to continuous fibre composites. Extensive

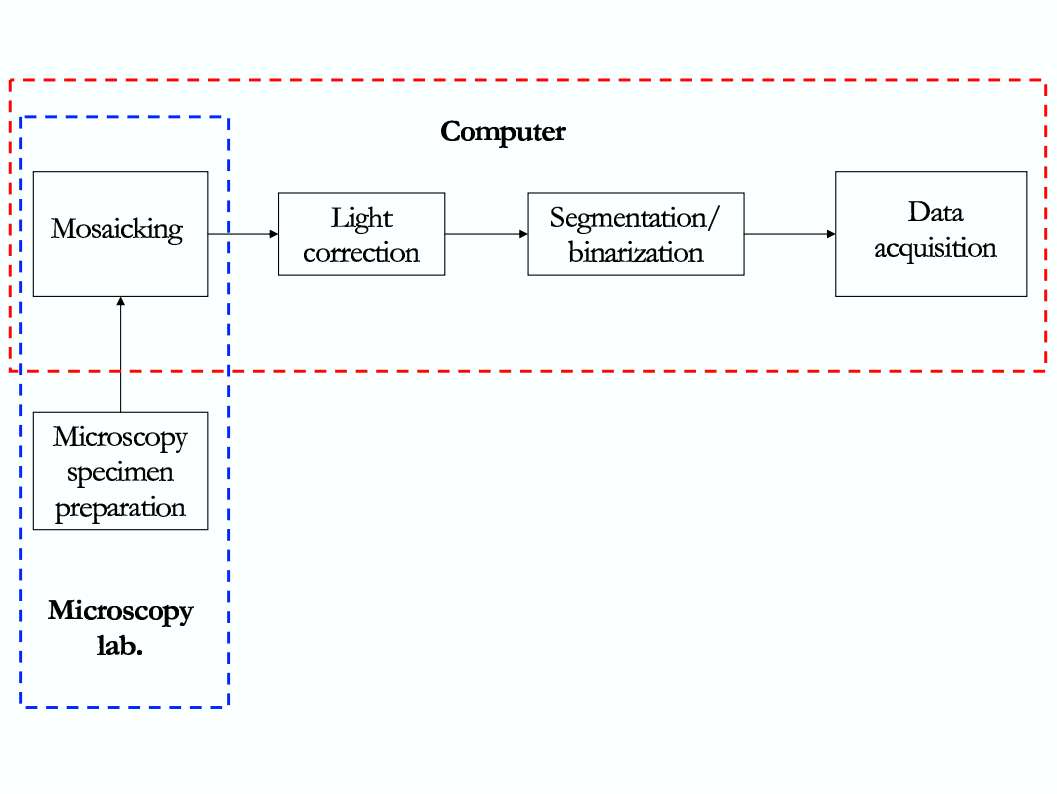

Figure 6.1: Sequence for the obtention of information of the fibre distribution in CFRP

information can also be found in some manufacturers' homepage, for instance Buehler [30].

The usual method for examining composite materials [26] [30] is to embed the sample into a resin and then to polish the observation surface by using abrasives of decreasing size. Resin system (resin plus catalyzer) AXON RSF 816 was employed for embedding the sample. The resin cured under ambient conditions of pressure and temperature during 16 hours. In the polishing process abrasive discs of grading P100, P400, P800 and P1500 were used. After that, a cloth polishing in alumina suspension was performed[1].

Figure 6.2 shows typical microscopy samples. A small piece of laminate of CFRP provided by the University of Porto is embedded in epoxy.

Figure 6.2: Typical FRP microscopy samples: a small piece of laminate is embedded in epoxy.

Obtaining well polished samples of carbon reinforced composites may be a hard task, the carbon dust easily scratches the resin of sample surface and fills possible voids in the material. For this reasons, a good image processing may improve greatly the acquisition results.

6.3 Digital Image Analysis

Image analysis and image processing are mainly used for two different purposes. The first one, to prepare the images for the measurement of geometric features and structures which may be present in the material. And the second, to improve the appearance of images, so they can be easily examined by the researcher.

The tasks involved in this part of the research work were performed in cooperation with Dr. Rafael García from the Computer Vision and Robotics (VICOROB[2]) research group

[1]NOTE: Images from TUHH were obtained from samples produced by their personnel with a similar process, using Struers Epofix epoxy for embedding the sample and polishing with diamond suspension.

[2]http://vicorob.udg.es/

of the *Department of Electronics, Computer Science and Automatics*[3] of the University of Girona, and the students Marc Revenga and Cristina Roura who programmed the computer codes for mosaicking, binarization, light correction and labelling under Prof. García and the author's supervision. The following sections describe briefly these techniques.

6.3.1 Mosaicking

Images bigger than the minimum size of the SRVE, which was determined in Chapter 5, have to be captured . On the other hand a resolution high enough to identify and capture the fibres position is also required. The available system is composed by an optical microscope and a video camera, which sends the images to a computer through a video card. This system does not allow to acquire images with the minimum required size and the minimum required resolution at the same time. If an observation is made with a high magnification, the acquired image will not have a size large enough. On the other hand, if a low magnification lens is used, the acquired image may have a size large enough, but the resolution will not be high enough to capture the fibre position.

To solve this technical disjunctive, the *mosaicking* technique [57] is used. This technique allows to construct big images by joining smaller ones, as is schematized in Figure 6.3. The software developed by the VICOROB group of the University of Girona works in real time, so mosaics can be build up during the observation process.

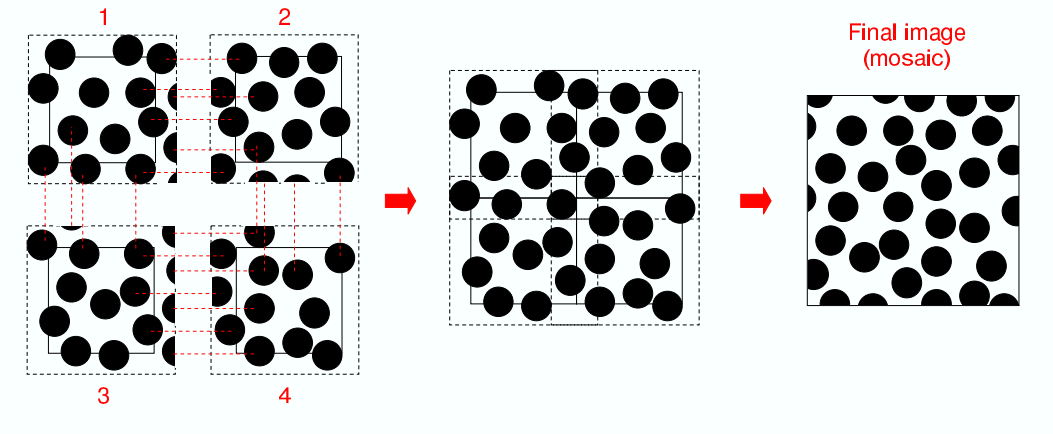

Figure 6.3: Mosaicking technique

As is shown in Figure 6.3, a large image (mosaic) is formed from a matrix of 2×2 smaller images. The observer must fix the microscope in an initial position, acquire image 1 and then, with the help of the real-time capacity of the software and system, to displace horizontally the microscope sample until the *live* observed image seems to match with image 1. Then image 2 is acquired by the observer. Since the window acquired is larger than the window used for building the mosaic, the software can make image 2 match exactly with image 1. Then, the observer should displace the sample vertically until the live image seems to match with image 2, and acquire image 3. Finally, the observer should displace

[3] http://eia.udg.es

the sample horizontally until the live image seems to match with image 1 and image 3.

Some examples of mosaics performed by using this technique can be seen in Figures 6.4, 6.5 and 6.6. Figures 6.4 and 6.6 reproduce typical transverse sections of CFRP. Figure 6.4 shows some vertically aligned matrix-rich regions, possibly produced by the stacking of fibre layers. Figure 6.6 shows some black spots which appear in the sample polishing phase. When holes are present, the carbon dust produced by polishing fills this holes, producing this characteristic holes. The carbon dust can be removed by immersing the sample in an ultrasound tank, but this process does not ensure the complete removal of the black spots, which can be used for easily detecting these holes. This image also shows clearly the presence of matrix vertical regions, produced by the stacking of fibre layers. The heterogeneous distribution of the fibre within the composite, having some fibre-poor regions, is observed clearly in this figure.

Figure 6.5 shows a dark field image of a transverse section of CFRP. This observation technique can also be useful for detecting voids and holes in the matrix, since it provides the observation a *volume* sensation. Holes or voids can be detected because they appear with illuminated contours.

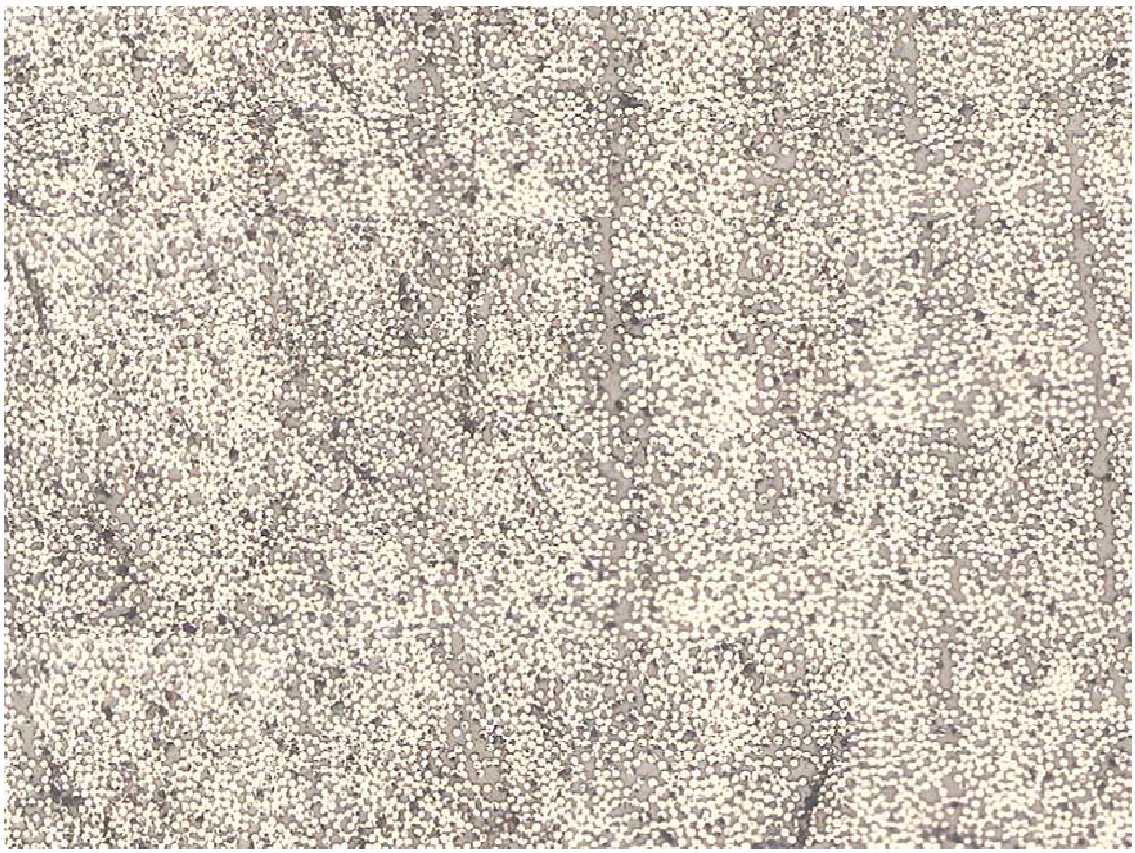

Figure 6.4: Mosaicking technique: CFRP (1). Image formed from 3×5 images

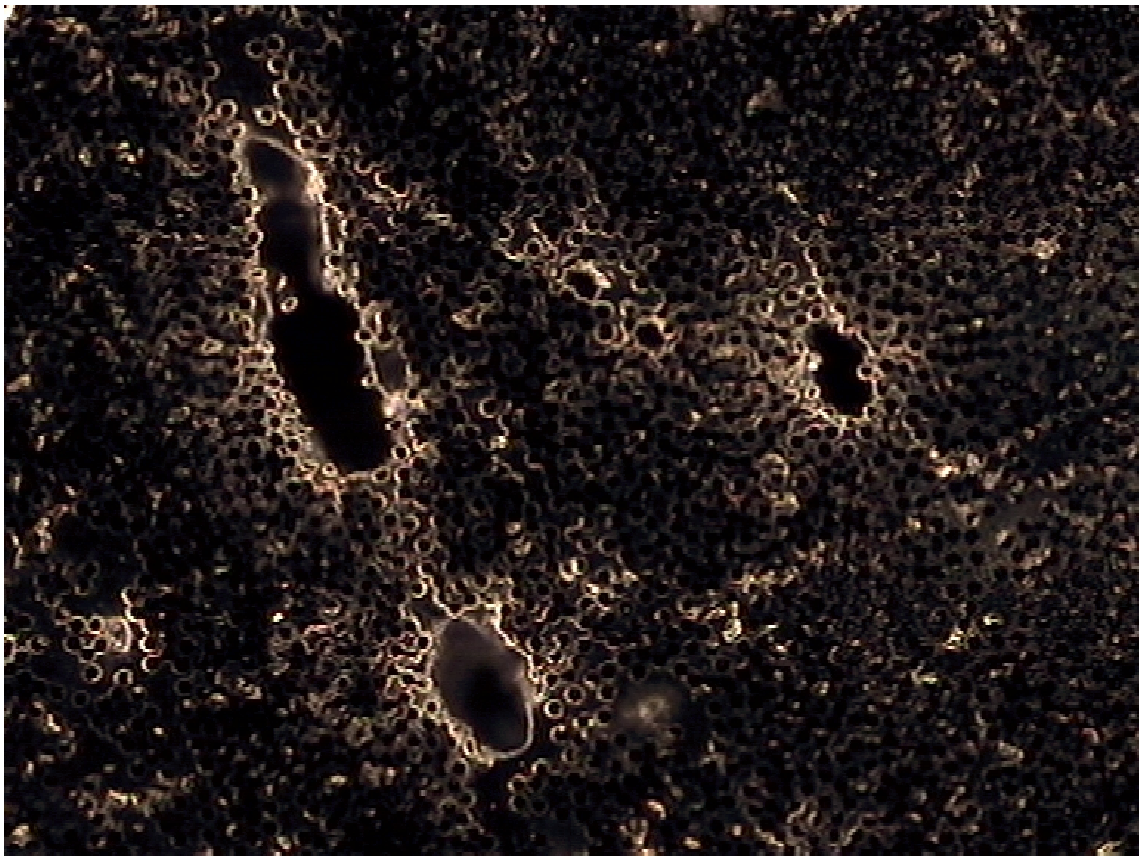

Figure 6.5: Mosaicking technique: Dark field image of a CFRP. Image formed from 3×5 images

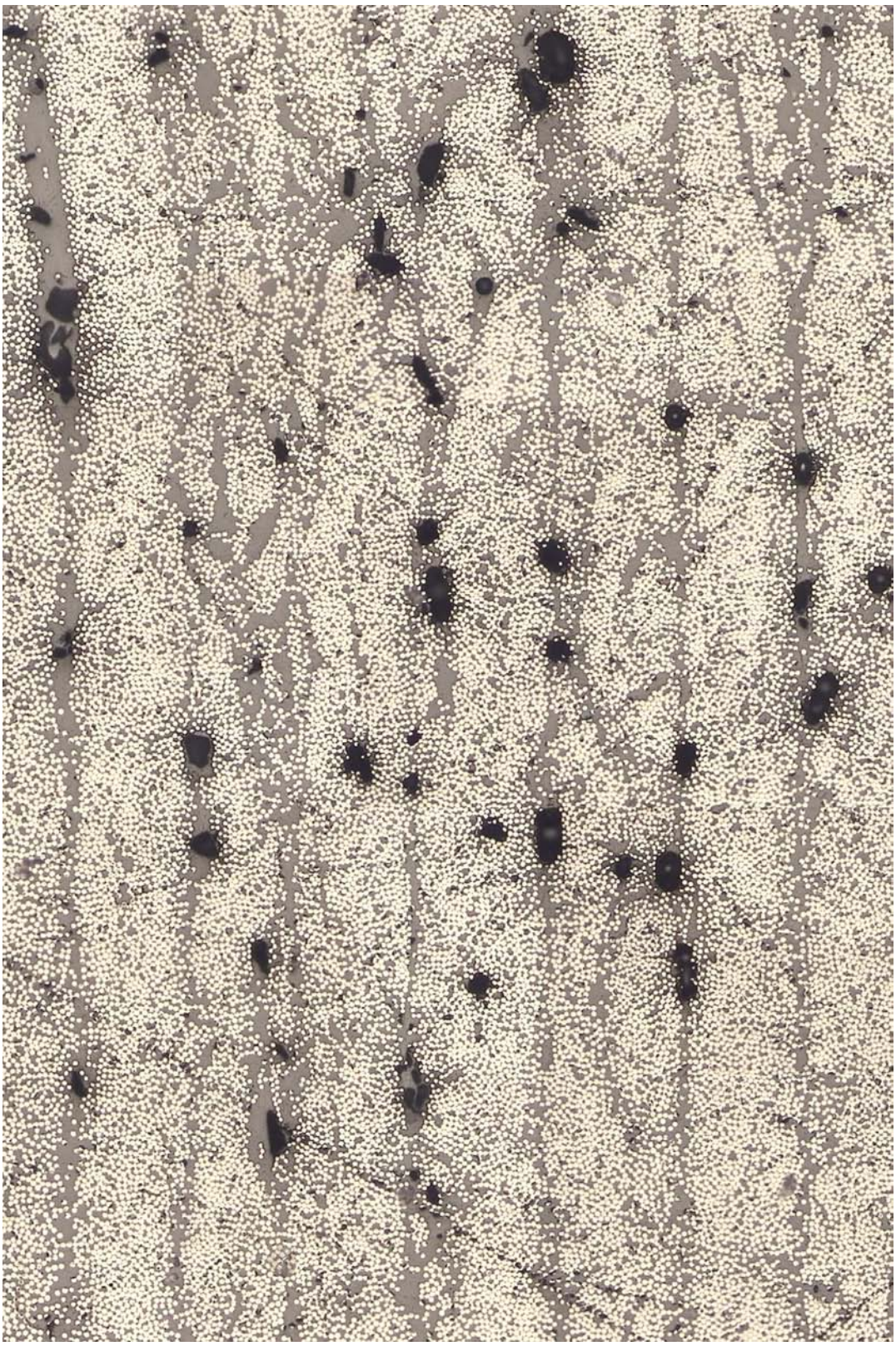

Figure 6.6: Mosaicking technique: CFRP (2). Image formed from 5×10 images

6.3.2 Segmentation

The first step in the digital analysis process is the binarization of the digital image. That means, the color image will be converted in a black and white one, showing in white one constituent (fibre) and in black the other one (matrix). A threshold value from which the color will be converted to white and under which the color will be converted to black, has to be found. This can be easily done by obtaining an histogram (with any image processing like the GNU licensed, GIMP[4]) of the distribution of the gray levels in the figure. From the histogram, a threshold level can be obtained, as shown in Figure 6.7. This Figure shows a gray level histogram of a digital image of a CFRP obtained with GIMP (right) and a sketch of the obtention of the threshold level (left). This process which allows to separate components or objects having similar characteristics is called *segmentation*.

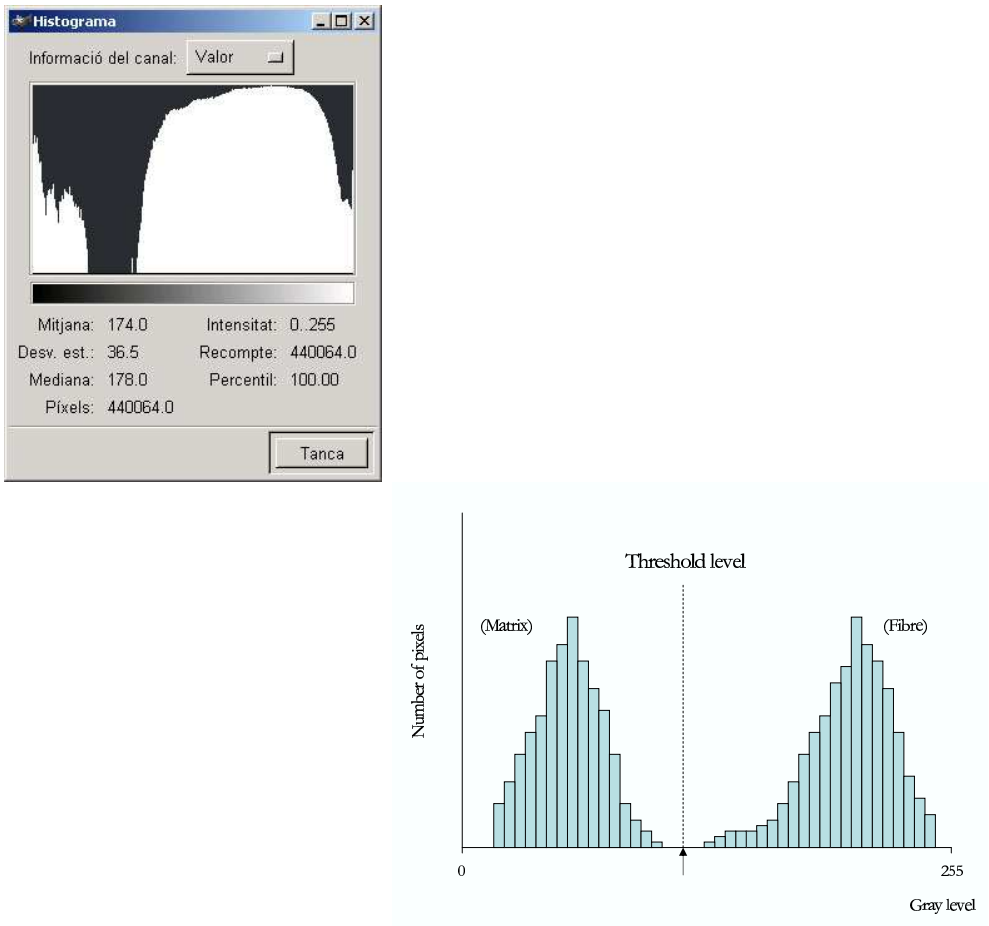

Figure 6.7: Gray level histogram of a digital image (left) and threshold for binarization (right)

Once the threshold has been obtained the image can be converted in a binary image. However, this technique is useful if the light in the image is uniform. As will be seen in

[4]http://www.gimp.org

the next section, non-uniform lighting may lead to an erroneous binarization.

6.3.3 Light correction

Some images obtained by light microscopy may show non-uniform lighting which may cause trouble in the binarization. As it is shown in Figure 6.8: when a high threshold is chosen some area of the image is converted into black; If conversely, a lower threshold is chosen, some area of the image is binarized into white.

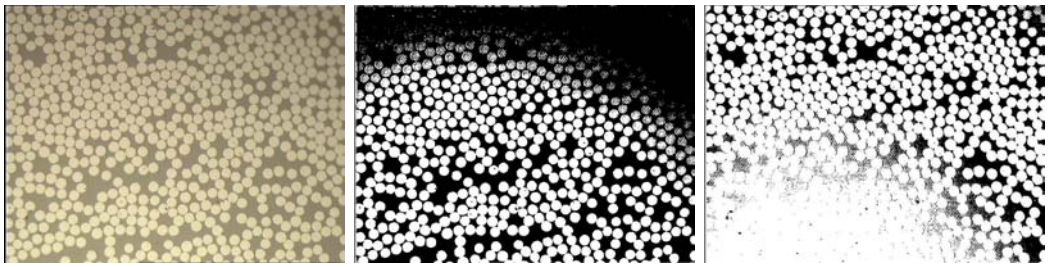

Figure 6.8: Erroneous binarization due to non-uniform lighting

This errors can be avoided by estimating the local light intensity (by computing the intensity in subdominiums or windows) and substracting it from the image. Figure 6.9 shows a 3D plot of the local intensity of the former image. It can be observed that pixels near the corner (0,560) have a local intensity which is about 1.6 times the intensity in the pixels near the corners (0,0) and (0,748).

If this intensity is subtracted from the original image, a correct binarization can be performed, as shown in Figure 6.10.

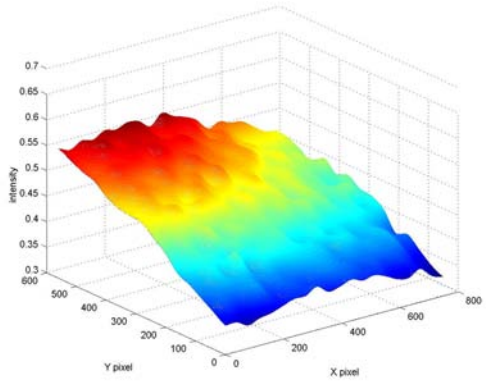

Figure 6.9: Light intensity in an image with non uniform lighting

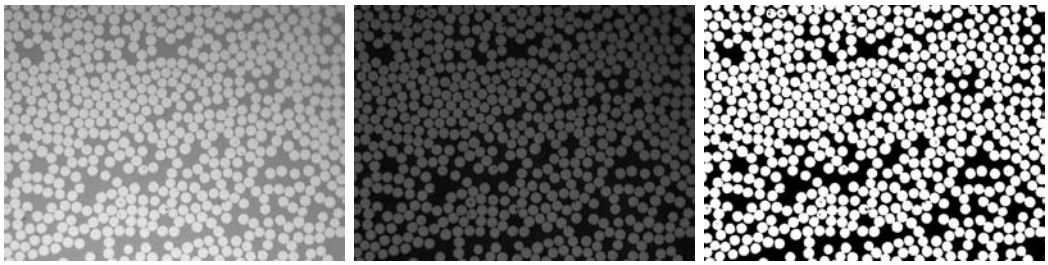

Figure 6.10: Light-corrected binarization
Original image(up), light-corrected image(middle), binarized image (down)

6.3.4 Fibre labelling

The aim of this chapter is to characterize the distribution of the fibre within the composite. This characterization requires the knowledge of the position of each fibres of a sample of the material. This section describes the technique which allows to find them.

A search window of side $2\alpha + 1$ is used. The search window is positioned and the image within the window (I_1) is compared with the pattern image I_2, which has the same size as the window. That is, to identify white fibres[5] of radius r the pattern image I_2 would be a white fibre of radius r. This process is performed point to point, computing the summation of squared differences shown in equation 6.1:

$$SSD(\mathbf{x}, \mathbf{y}) = \sum_{i=-\alpha}^{\alpha} \sum_{j=-\alpha}^{\alpha} (I_1(x_1 + i, y_1 + j) - I_2(x_1 + i, y_1 + j))^2 \tag{6.1}$$

where $\mathbf{x}$ denotes the coordinates of the center of the window and $\mathbf{y}$ the coordinates of the center of the pattern window. This SSD value of equation 6.1 is computed for each pixel in the image and then, in an iterative process which, among other things, avoids that two centers lay in a distance closer than the fibre diameter, those points with lower SSD value are chosen. Figure 6.11 shows the labelling process for one of the TUHH's images. As is also shown in this figure, the fibres which do not lay completely within the image are eliminated in this process. This should have been taken into account because, as was found in Chapter 5, the sample size should not be smaller than 50 times the fibre radius.

6.4 Digital analysis of some CFRP

This section shows results from the image processing of different carbon fibre reinforced composites. The results of the digital image analysis will be used to compute the statistical functions which describe point patterns (and which are described in Section 4.4 of Chapter 4). This analysis will also be used to check if it is possible to distinguish materials from different sources with some of the statistical functions described in Sections 4.4.3 and 4.4.4 of Chapter 4. Also, the obtained statistical information will be analyzed together

[5]As seen in the former section, the image has been binarized and, consequently, fibres appear in white and matrix in black

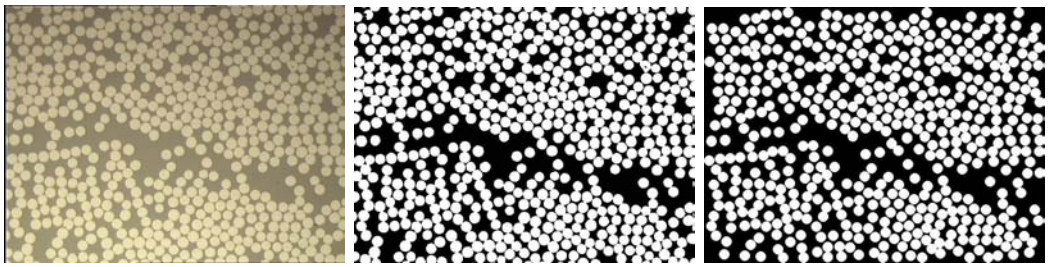

Figure 6.11: Labelling process

statistic / material	$RTM-6$	$977-2$	6376
$\mu(v_f)$	0.5455	0.5410	0.5761
$\sigma^2(v_f)$	0.2069	0.2105	0.0440
$\mu(n_f)$	554.450	549.725	585.450
$\sigma^2(n_f)$	2146.766	2175.845	458.715

Table 6.1: Summary of statistics for three CFRPs microanalysis

with the simulation results of Chapter 8.

6.4.1 Three CFRP from TUHH

Images from three different CFRP produced by the composites group at Technische Universität Hamburg-Harburg have been analyzed. These materials have the same fibre (HTA 5131) but three different epoxy systems for the matrix: RTM-6, 977-2 and 6376. For the human eye, as it is hown in Figure 6.12, the images look very similar and are indistinguishable.

40 microscopy images from each material were analyzed. For each image the position of each fiber was captured and the fiber content was computed. Table 6.1 shows the results for the fibre content and the number of fibres.

The second order intensity function[6] and the pair distribution function[7] of the microstructures have been analyzed. Figures 6.13 and 6.14 show the plot of this function for some specimen from the three considered materials. In each plot, the second order intensity function of a complete random pattern is shown by means of a dashed line, for comparison. The plot of $K(h)$ for the complete sample can be found in Appendix C (Figures C.19-C.24).

Recalling the qualitative interpretation of the second order intensity function given in Section 4.4.3, it can be argued that the laminates made from epoxy RTM6 and 977-2 show some cluster patterns and occasionally (images 04 and 23 in the RTM6 and images images 06 and 14 in 977-2, shown in Figure 6.14) some greatly clusterized patterns. This Figure

[6]Defined in Equation 4.25
[7]Defined in Equation 4.30

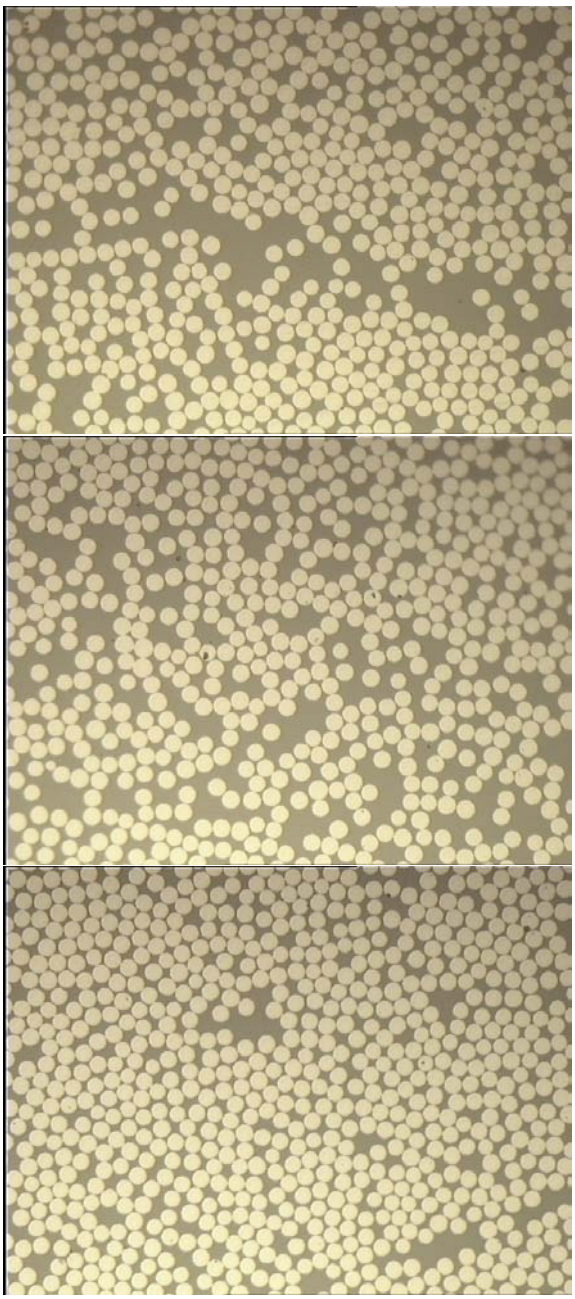

Figure 6.12: Transverse section of three CFRP from TUHH
(HTA 5131/RTM-6 (up), HTA 5131/977-2 (middle) and HTA 5131/6376 (bottom))

also evidences that the dispersion from a CSR pattern is greater in these two materials. This fact is of course related to the greater variance in the volume fraction observed for these materials in Table 6.1.

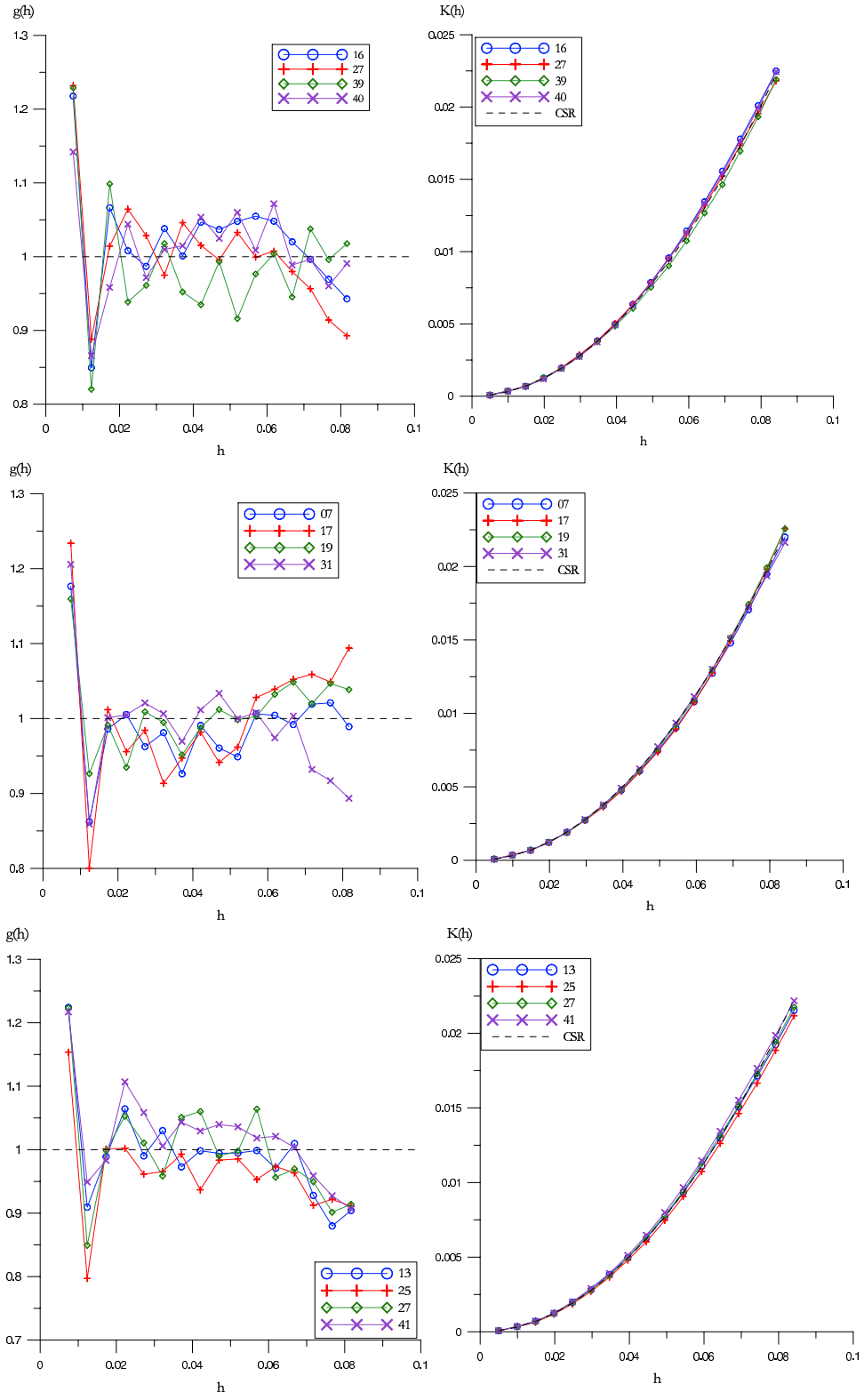

Figure 6.13: Second order intensity and pair distribution functions for RTM-6 (up), 977-2 (middle) and 6376 (bottom). The number in the legend identifies the image from which the function has been obtained.

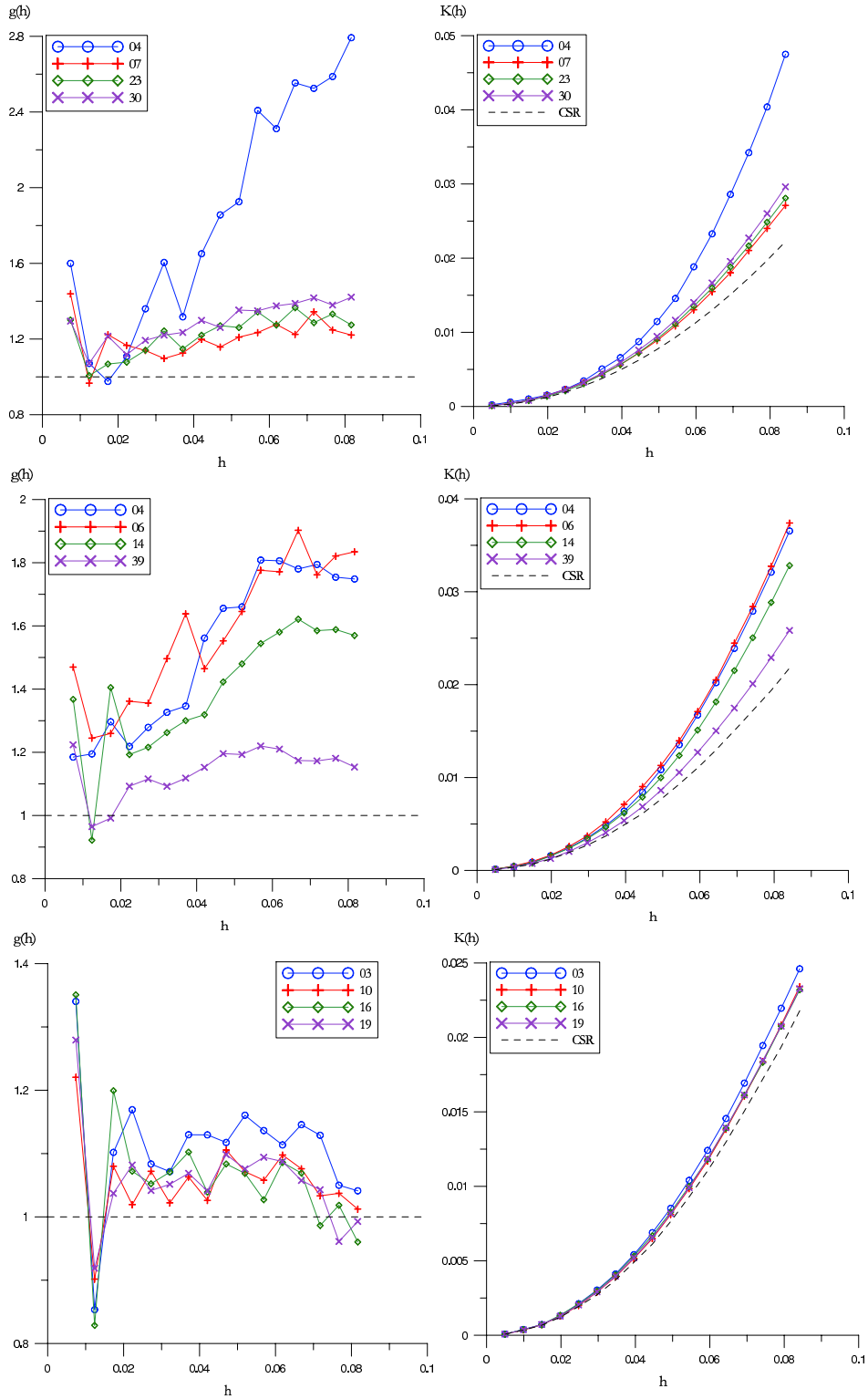

Figure 6.14: Second order intensity and pair distribution functions for RTM-6 (up), 977-2 (middle) and 6376 (bottom). The number in the legend identifies the image from which the function has been obtained.

With the aim to compare the random patterns corresponding to the three analyzed composite materials, the mean squared difference between the functions for the three analyzed materials and a CSR pattern has been computed and plot in Figure 6.15. In this figure it is evidenced that the microstructure of the composite material made using epoxy 6376 can be considered a microscopically complete random material and the composite materials made from epoxies RTM-6 and 977-2 depart considerably from a CSR pattern due to the observed clustering.

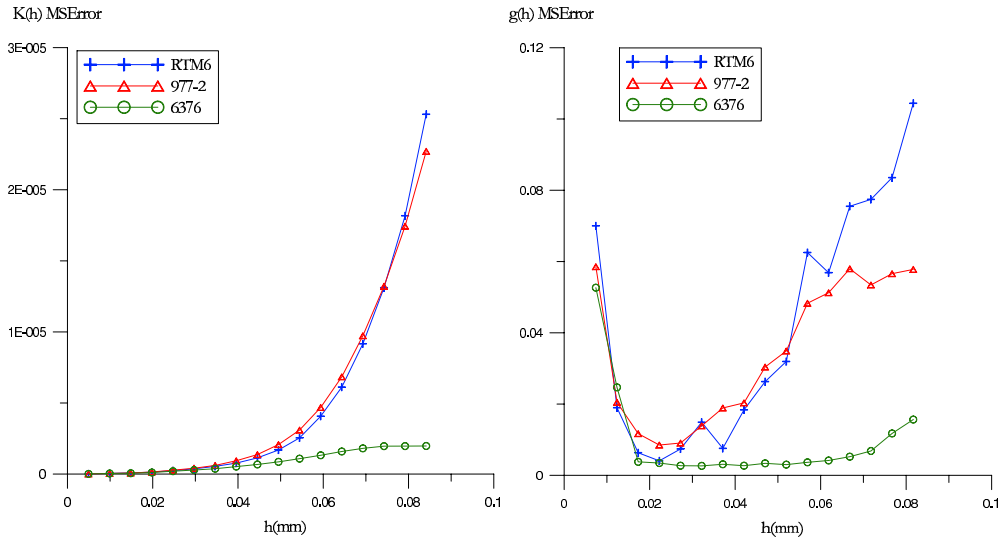

Figure 6.15: Mean squared difference from a CSR pattern

Figure 6.16 shows how functions $K(h)$ and $g(h)$ are useful in detecting cluster patterns. In the micrographs on the left, it can be seen the material microscopic image of two clustered patterns and in the right column the plots for both functions.

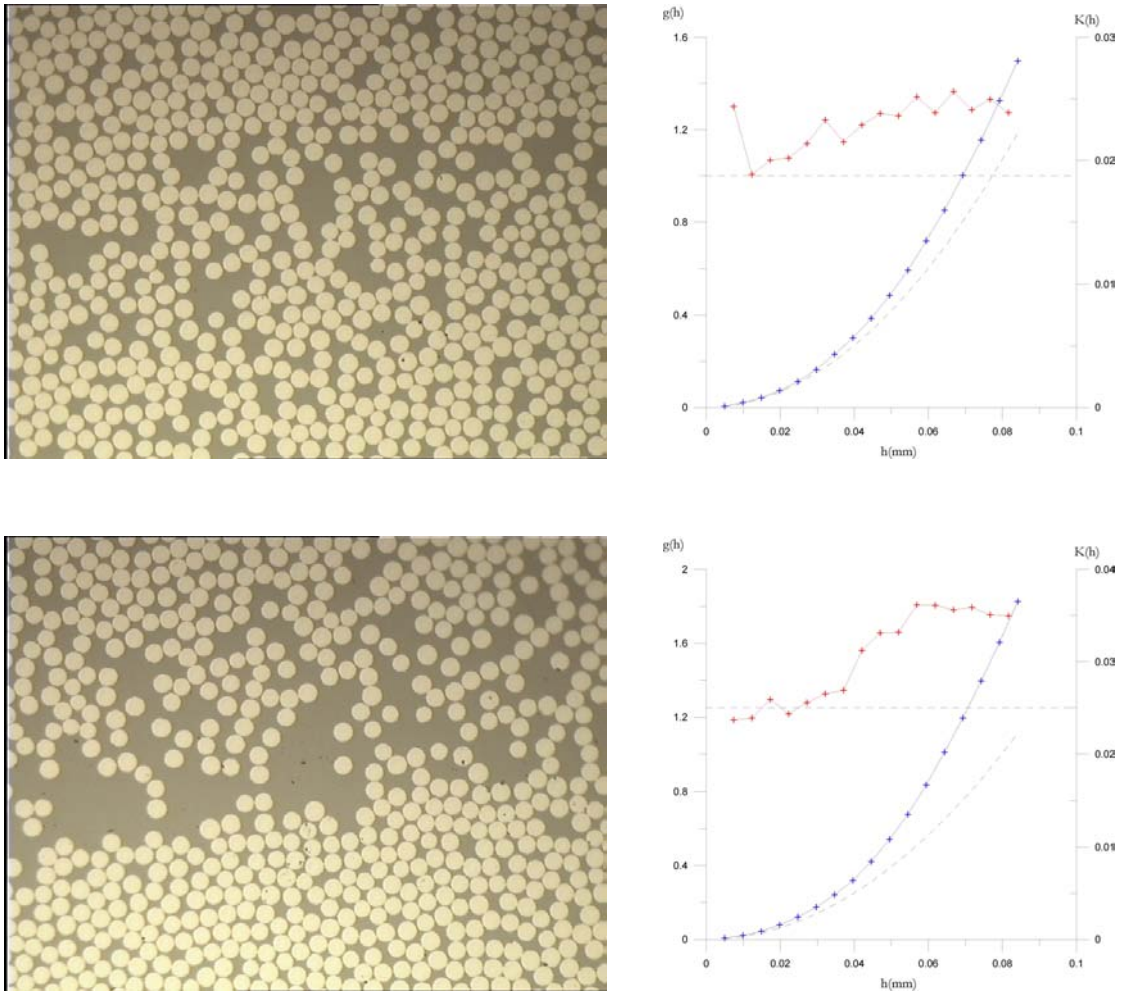

Figure 6.16: Slightly clustered pattern from RTM6 (up) and strongly clustered pattern from 977-2 (down)

All three materials show similar short-range distributions, as shown in Figures 6.17-6.19, which show respectively first, second and third nearest neighbor distributions for some of the images. It can be observed how the short-range distributions reflect typical Mathérn's distribution, showing lower values that a CSR pattern (shown in dashed line in the figures) for distances near to the diameter. Besides this fact, all three materials show reasonably good agreement with a CSR pattern, especially for the third nearest neighbor distance (Figure 6.19). This short range similarity with a CSR pattern is also confirmed by the plots of the mean sum of square-root of squared error (MSSE) which is computed with respect to a CSR pattern and plot in Figure 6.20.

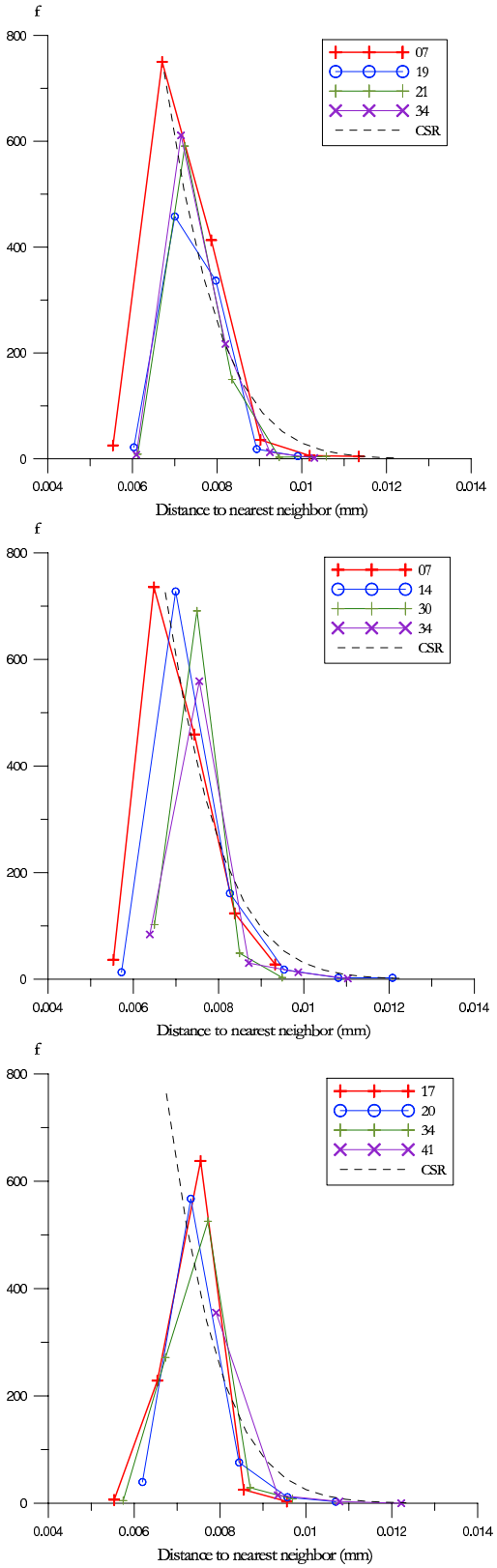

Figure 6.17: Distance to first nearest neighbor distribution in RTM6 (up), 977-2 (middle) and 6376 (bottom). The number in the legend identifies the image from which the function has been obtained.

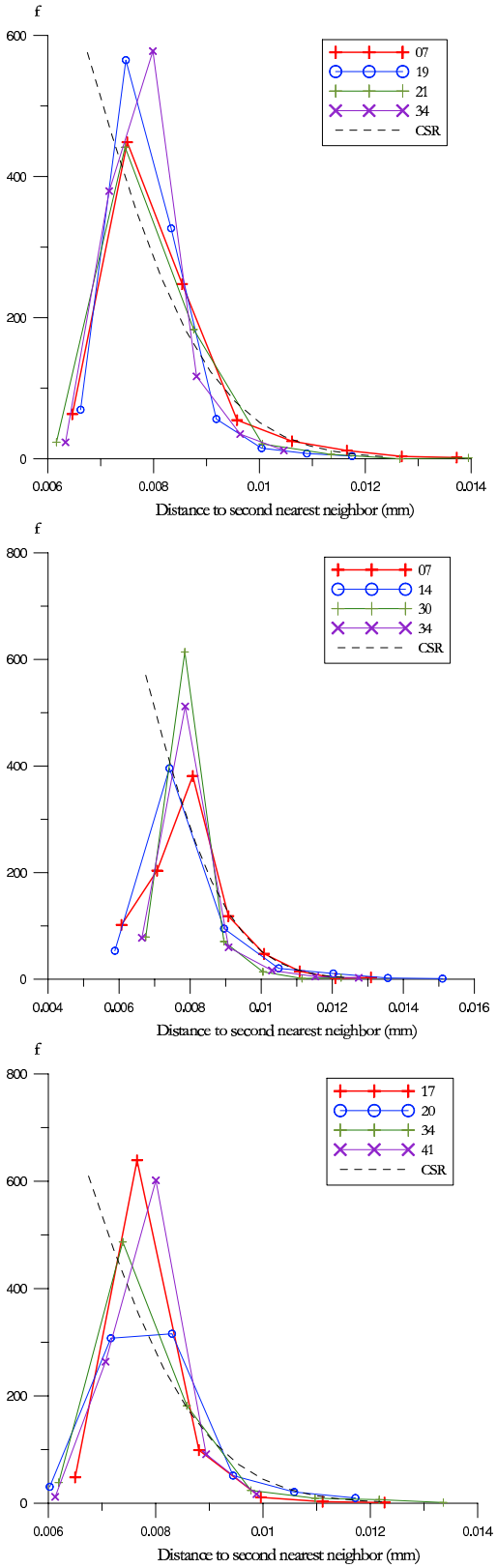

Figure 6.18: Distance to second nearest neighbor distribution in RTM6 (up), 977-2 (middle) and 6376 (bottom). The number in the legend identifies the image from which the function has been obtained.

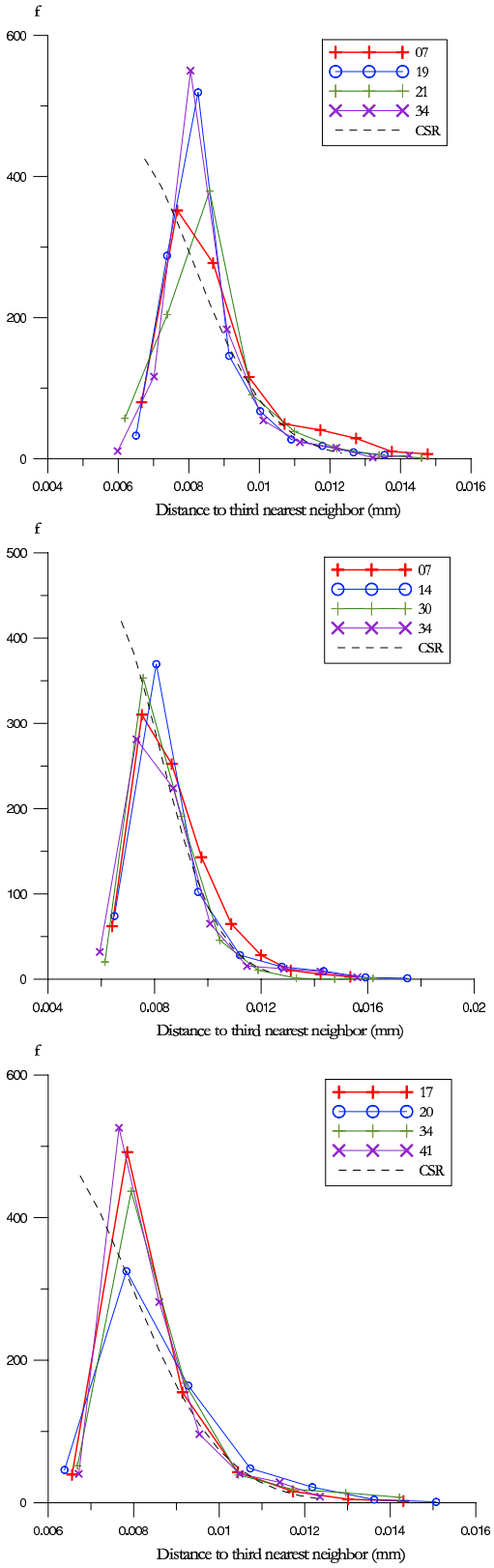

Figure 6.19: Distance to third nearest neighbor distribution in RTM6 (up), 977-2 (middle) and 6376 (bottom). The number in the legend identifies the image from which the function has been obtained.

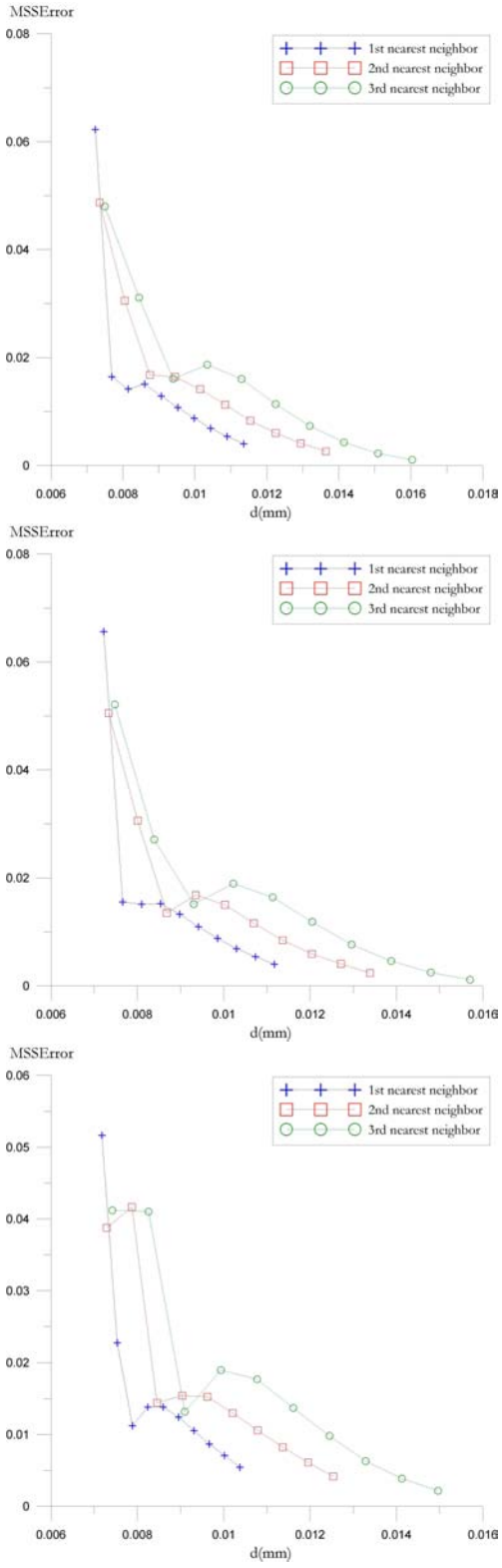

Figure 6.20: MSSError in nearest neighbor distribution with respect to a CSR pattern

6.4.2 CFRP from Porto

A CFRP made from Hexcel IM7/8552 pre-preg by the Engineering Faculty of the University of Porto (FEUP) has been also analyzed. Figure 6.21 shows that the transverse section of this material is apparently similar to those from TUHH. In this case the fibre diameter is 5.2 μm. Seven images have been obtained through the mosaicking technique described in Section 6.3.1. These mosaics where constructed from a set of 3×3 images.

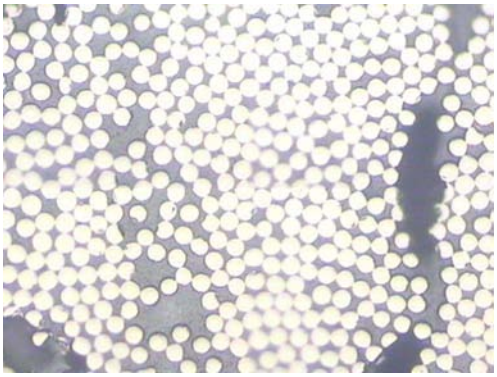

Figure 6.21: Transverse section of a IM7/8552 CFRP produced in FEUP

The second order intensity function K(h) and the pair distribution function g(h) have been estimated for the seven images. These estimations are plotted in Figures 6.22 and 6.23.

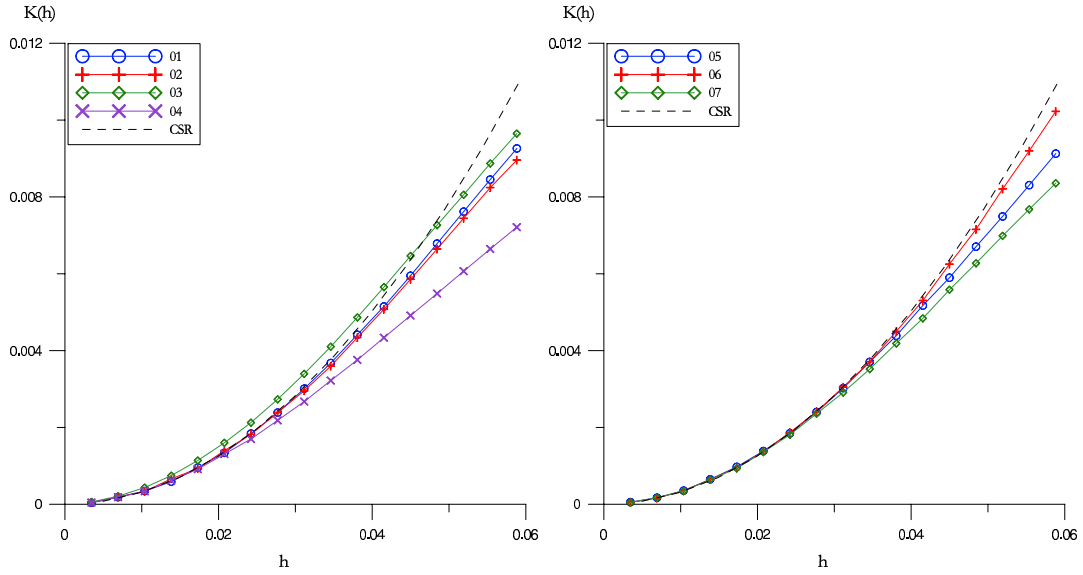

Figure 6.22: Second order intensity function for IM7/8552 CFRP produced in FEUP

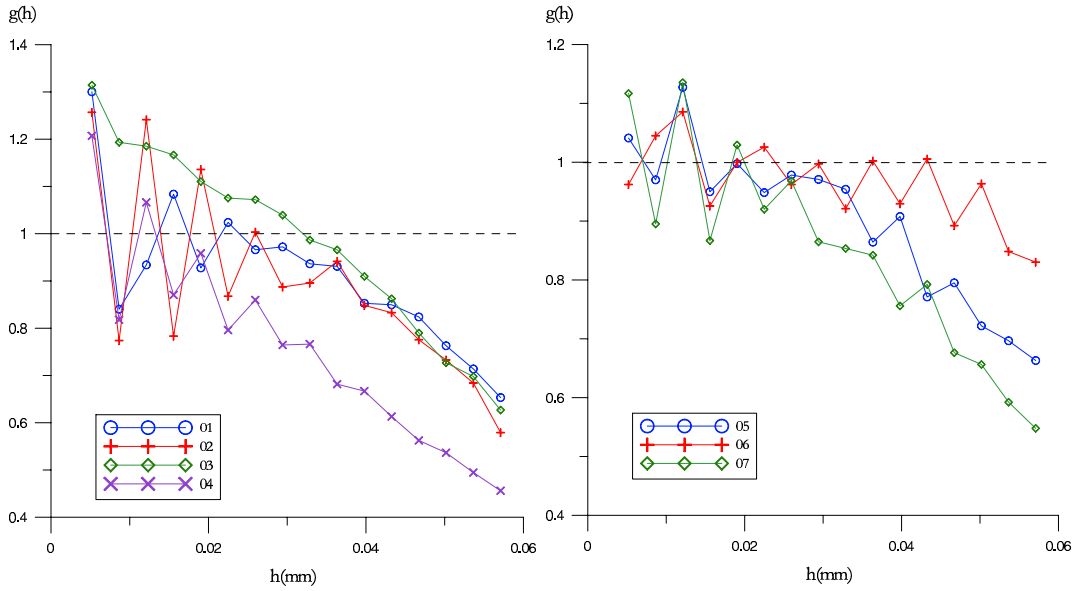

Figure 6.23: Pair distribution function for IM7/8552 CFRP produced in FEUP

The mean squared difference with respect to a CSR pattern has been computed for $K(h)$ and $g(h)$ and given in Figure 6.24, together with that corresponding to the CFRPs analyzed in the former section. Figure shows how the differences are greater for large values of the distance (h) and that none of the patterns of the materials analyzed could be very precisely considered a CSR pattern. In spite of this, Figure 6.24 shows that $K(h)$ and $g(h)$ are very useful for distinguishing materials from different sources.

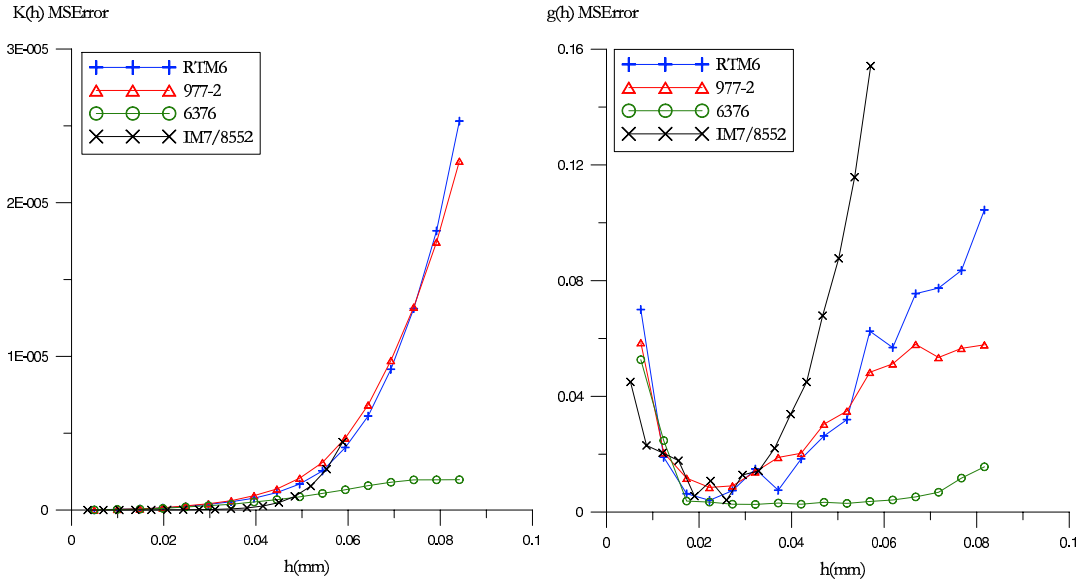

Figure 6.24: MSError difference with a CSR pattern for K(h) and g(h)

The nearest neighbor distances have also been analyzed for the seven images. The plots corresponding to the nearest neighbor functions are shown in Figures 6.25, 6.26 and 6.27.

The error with respect a CSR model has been computed and is shown in the plot of Figure 6.28. This Figure shows how the point pattern of IM7/8552 CFRP has some important differences with a CSR pattern.

6.5 Summary and Conclusions

The long range particle interaction of three different carbon reinforced polymers having the same fibre but different matrix has been analyzed by means of the Second order distribution function ($K(h)$) and the Pair distribution function ($g(h)$). Two of them (those made with epoxy RTM6 and epoxy 977-2) show similar patterns, departing from a complete spatial randomness. The third one (made with epoxy 6376) fits reasonably well in a CSR model.

The same analysis has been performed for a composite material performed with a IM7/8552 pre-preg. The distribution of the fibre in this material can not be considered a complete spatial random pattern.

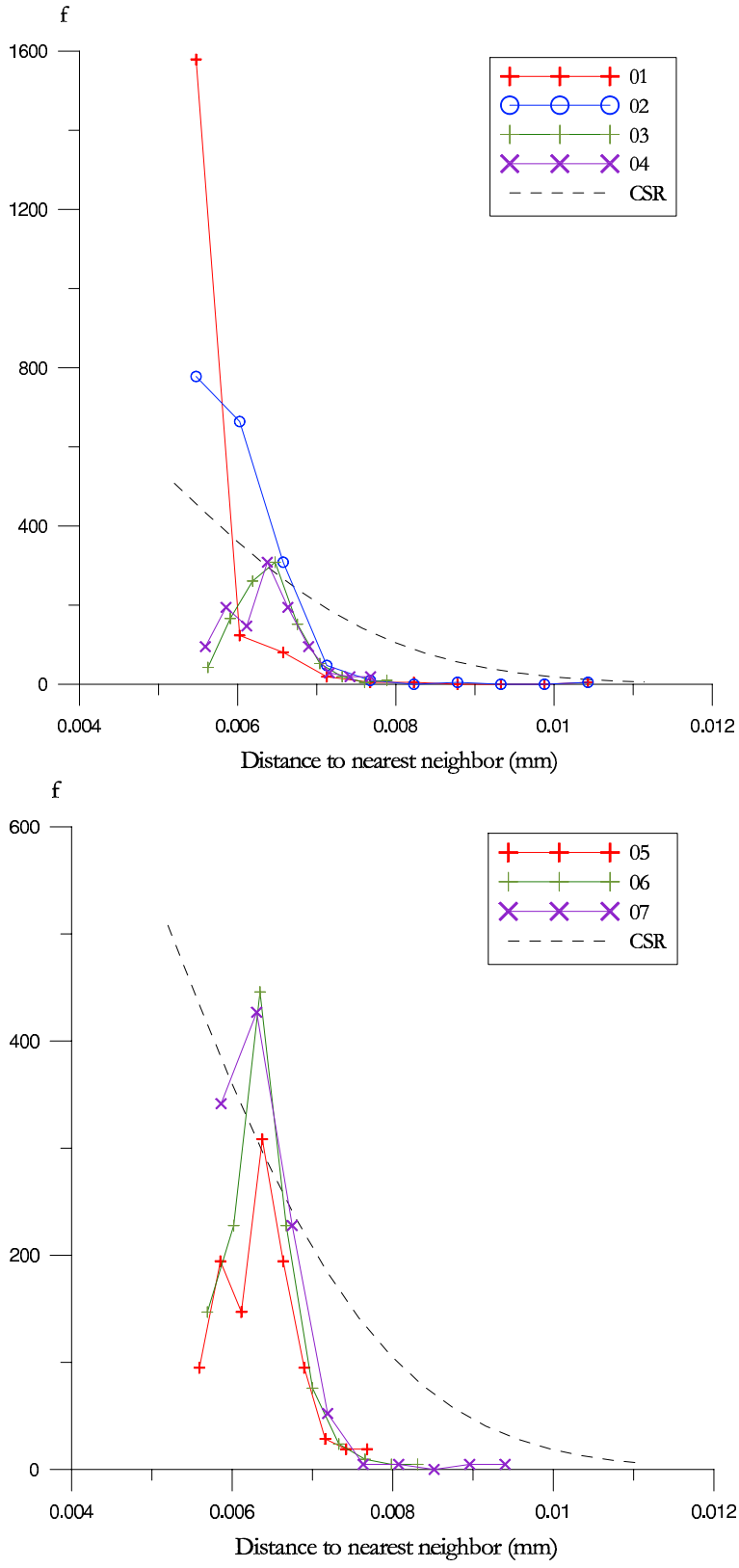

Figure 6.25: Nearest neighbor distance for IM7/8552 CFRP produced in FEUP

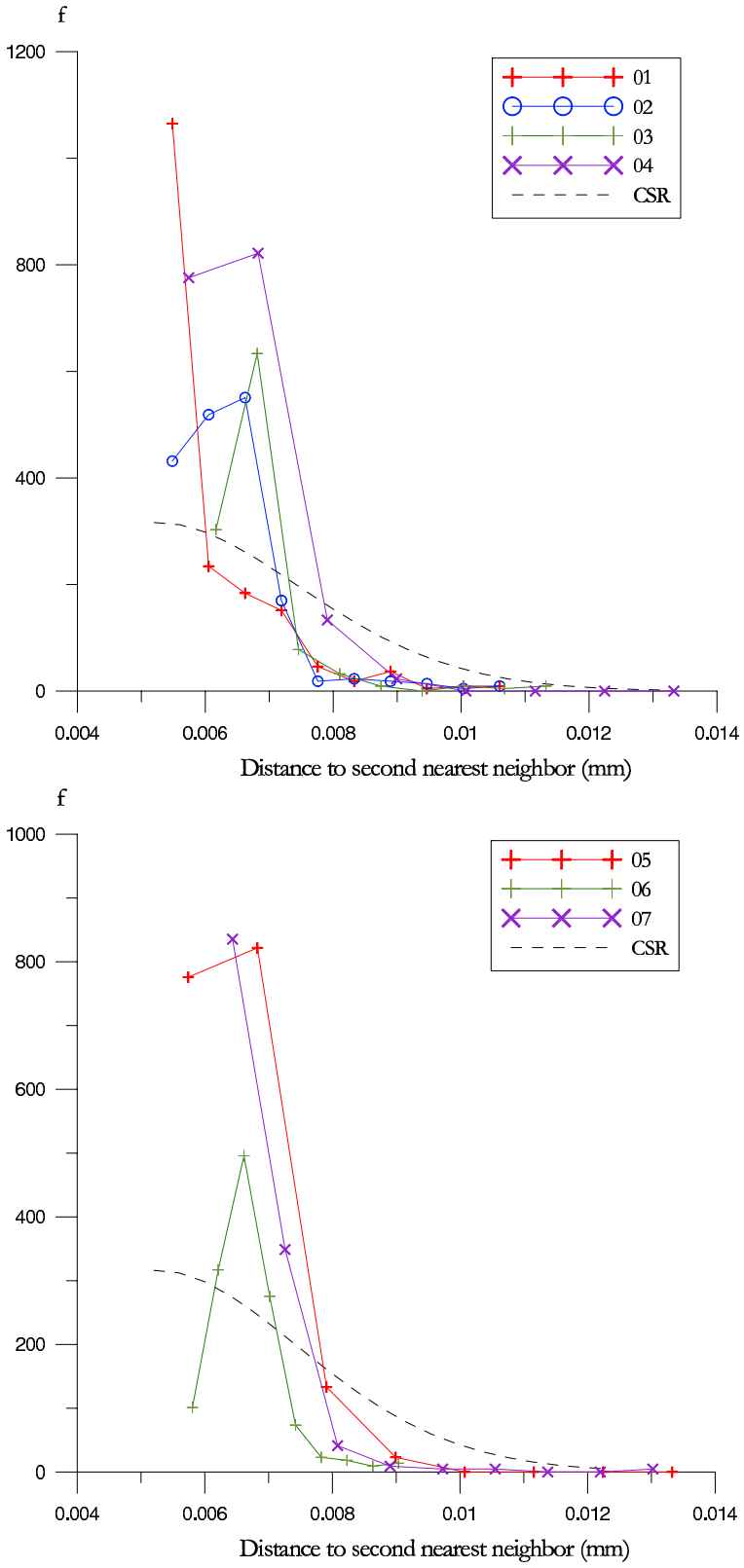

Figure 6.26: Second nearest neighbor distance for IM7/8552 CFRP produced in FEUP

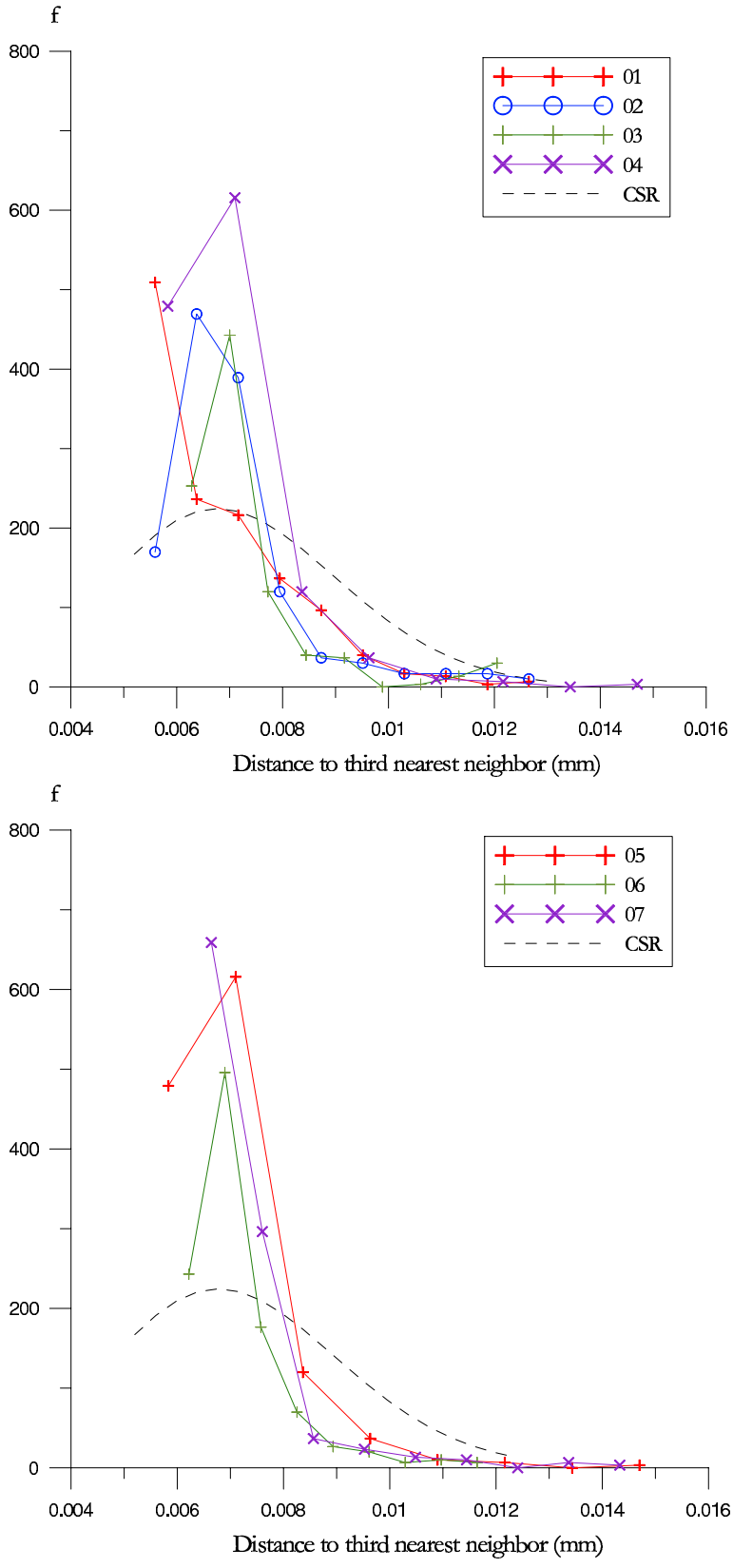

Figure 6.27: Third nearest neighbor distance for IM7/8552 CFRP produced in FEUP

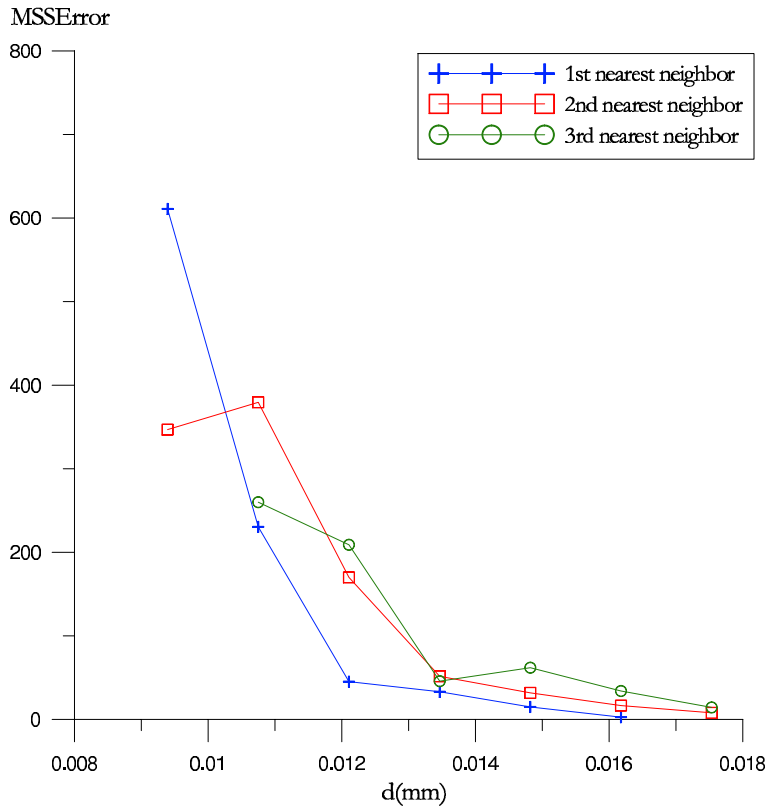

Figure 6.28: MSSError for three first neighbor distances for IM7/8552 CFRP produced in FEUP

Chapter 7

Effects of a Random Fibre Distribution on the stress and strain fields of a composite

7.1 Introduction

In this chapter a comparison between a periodic (deterministic) and a random fibre distribution model for a composite material is performed. Both models have the same volume fraction $v_f = 0.5$ and the same size, that is, the same number of fibres. The deterministic model is produced by repeating a square unit cell along the dominium and the random model is produced in the same way that the SRVE candidates of Chapter 5. In both cases, the Embedded Cell Approach (ECA) which was also described in Section 2.6.2, has been applied in the modelling for the application of equivalent displacement boundary conditions in the y direction to both models. Only this type of boundary conditions are applied because the equivalence of force and displacement in the SRVE was shown in Chapter 5. Since the minimum finite size of the SRVE was found to be $\delta = L/r = 50$[1] the models in the present one fulfill this condition. To ensure that the volume fraction of both models is the same, only full fibres have been considered in both models.

The objective of this analysis is to find out if it is worth to model composite materials as random materials or if periodic models give a solution which is representative enough. This representativeness will be considered correct if the periodic model reproduces the extreme values of some variables. These extreme values are important since they will be the values for which damage and failure mechanisms will initiate. Since fibres are under uniform strain and -as it was seen in Chapter 3- transverse failure in composites is a matrix-dominated phenomena, stress and strain will be only analyzed in the matrix.

[1] See Chapter 5

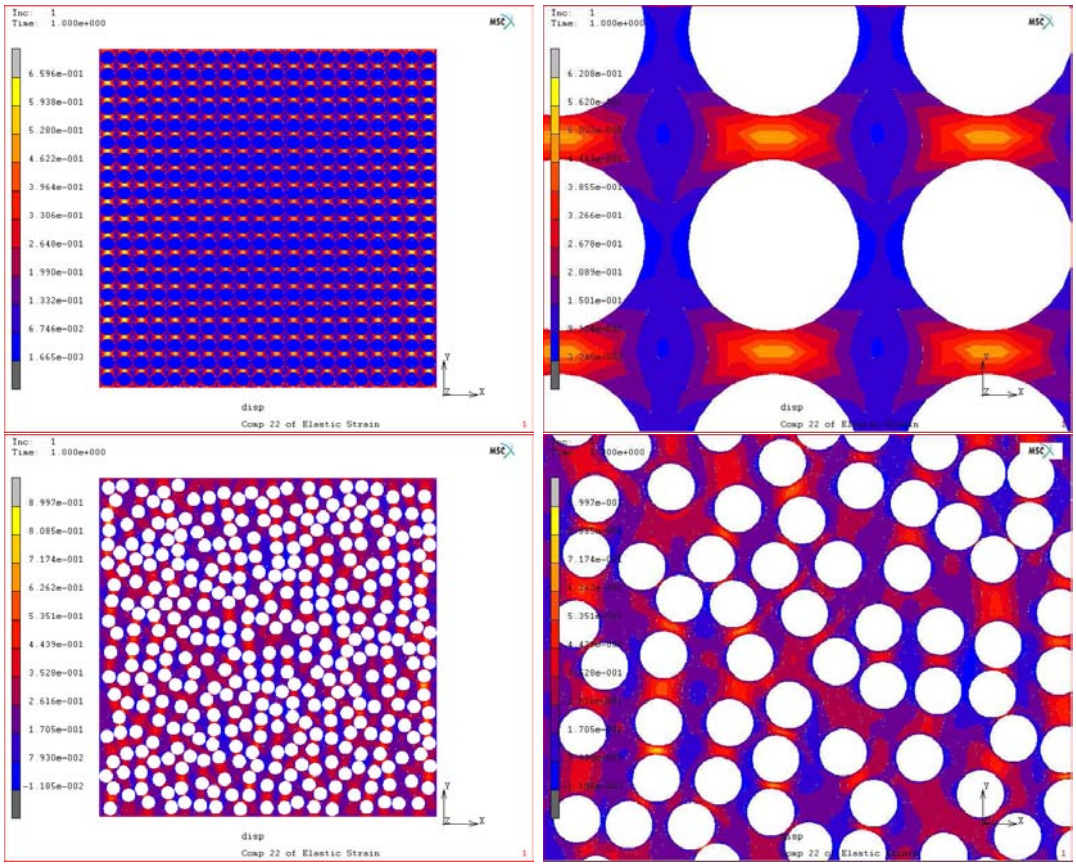

Figure 7.1: ε_{22} in the matrix in the periodic and in the random model. Maximum strain in the random model is about 1.36 the maximum strain in the periodic model.

7.2 Comparison of stress and strain fields in the matrix

Figure 7.1 shows ε_{22} in the periodic and in the random model. It can be seen that the maximum strain is about 36% higher in the random model. These high strains appear between fibers which are very close or between fibers which are aligned in the direction of the load showing high strains and spreading in large matrix areas, with lower strains. Another difference between the models is that some compression areas appear in the random model, while the periodic model only has tractional strains. However these compressive strains have low magnitude.

A quantitative analysis can be carried out by computing the histograms corresponding to ε_{22} in both models. Although to compute an histogram of a non-random field could seem non-sense, the stress and strain in the matrix of periodic models are not constant and an histogram could be a good graphic tool to analyze their (*deterministic*) variation. These histograms (Figure 7.2) show noticeable differences between the models. The results for the periodic model show, as expected, less dispersion: about 40% of sample points have ε_{22} between 0.1 and 0.2 micro-deformations. But the most significant difference appears in the extremes of the histograms: the probability of ε_{22} of being higher than 0.6 and the

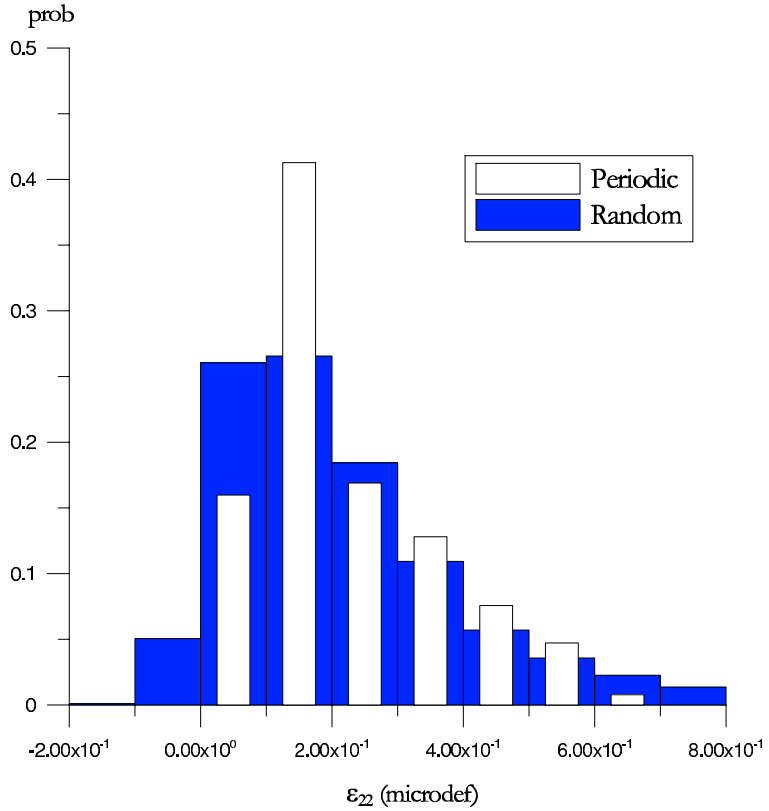

Figure 7.2: Histograms of ε_{22} in the matrix for the periodic and the random model

probability of $\varepsilon_{22} < 0$ (that is, being compressive). This is important because damage initiation in the matrix is likely to start in these highly strained locations. Moreover, from the design point of view, some failure criteria are based on the absolute value of the maximum strain. Compressive strains appear in about the 5% of solution points.

Figure 7.3 shows a histogram for σ_{22} in the periodic and in the random model. This Figure leads to analogous conclusions to those obtained when analyzing ε_{22}. Although there exist some failure criteria based on maximum stress, usually failure criteria involve invariants of the stress tensor. For this reason, some invariant-based quantities are analyzed in Section 7.4

7.3 Principal stresses

For a clearer comparison of the stresses in the periodic and the random models, principal stresses[2] can be analyzed. Figures 7.4, 7.5 and 7.6 show the principal stresses in both models. In the periodic model, the maximum component of the principal stresses σ_1 (plotted in Figure 7.4 right bottom) shows bands between fibers in the direction of the load. In the random model (Figure 7.4 up and bottom left) this stress concentration bands between fibers only appear between those fibers which are located very close, showing high

[2]See Section A.2.1 for a definition of principal stresses

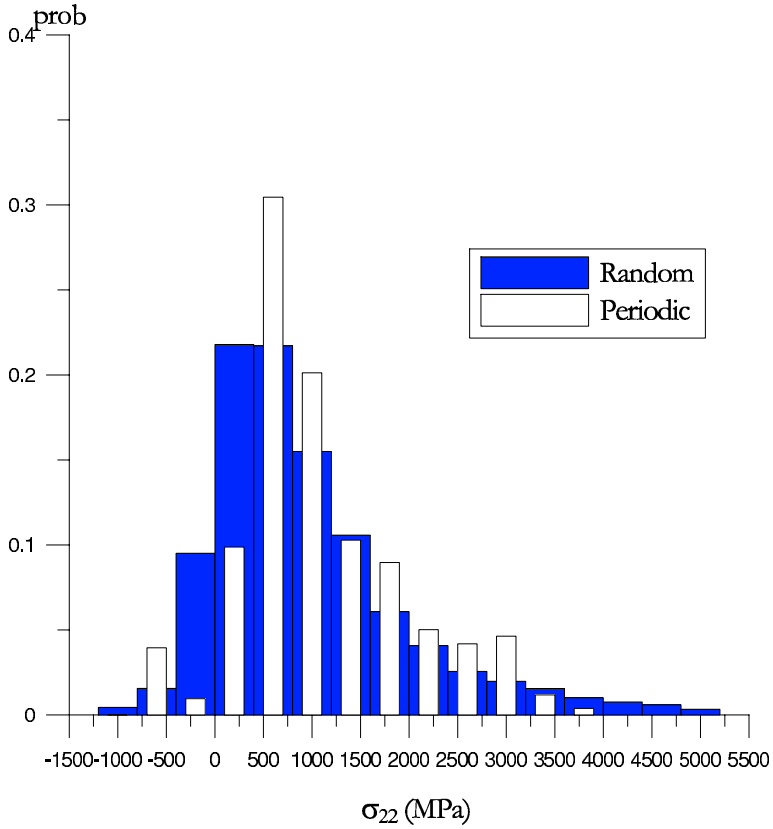

Figure 7.3: Histograms of σ_{22} in the matrix for the periodic and the random model

concentration of stresses which have values around 2 times higher than the concentration stresses of the periodic model. In the random model, low concentration stresses appear in some fibers which are aligned in the load direction. In this case, the concentration stresses remain between $0.9 - 1.1$ times those of the periodic model. Consequently, it seems that the random model takes into account the possibility of concentration of stresses due to close distances which are not described by the periodic model.

In the periodic model (Figure 7.5 right bottom), the intermediate component of the principal stresses (σ_2) shows circular concentration areas which start between fibers aligned in the load direction and which spread along each area of matrix surrounded by four fibers describing a square. In the random model (Figure 7.5 up and left bottom) high stresses appear between fibres which lay very close and spreads in large matrix areas. The ratio between the maximum stresses between fibers in the random model and in the periodic model is about $\sigma_1^{random}/\sigma_1^{periodic} = 1.6$. In the other hand, the ratio of the stresses in large matrix areas is about $\sigma_1^{random}/\sigma_1^{periodic} = 0.76$.

Finally, the minimum component of the principal stresses in the periodic model, shows traction bands which spread in the direction perpendicular to the load. These bands have a maximum value in the region between fibers aligned in the load direction. Also concentration compression bands appear in the direction perpendicular to load showing high values between fibers. These compression stresses are caused by the conservation of volume (or mass) in the elastic analysis which makes that if the material is stretched in one direction, in order to keep the same volume, it reduces its size in the perpendicular direction.

In the random model (Figure 7.6 up and left bottom) high traction values appear in fibers laying very close considering the load direction and high compressive values appear between fibers closely laying in the direction perpendicular to the load. These compressive values are about 1.7 times the value of those in the periodic model.

A comparative analysis of the principal stresses can be performed by plotting a histogram for each component of the principal stresses (Figure 7.7). It can be seen that the three histograms are quantitatively different: the mode[3] differs in all three cases and in all three cases the random model has a greater frequency in the tails.

7.3.1 Equitriaxiality

As seen in Chapter 3, the equitriaxiality or the presence of a nearly hydrostatic stress state is determinant for transverse failure of fiber composites. For the comparison of the equitriaxiality in the random model with the equitriaxiality in the periodic model the coefficients $|\sigma_2/\sigma_1|$ and $|\sigma_3/\sigma_1|$ have been computed for each solution point in the FE model and are shown in Figure 7.8.

The plot of $|\sigma_2/\sigma_1|$ is similar in both models, although it shows a slightly greater dispersion in the random model. In the plot for $|\sigma_3/\sigma_1|$ this greater dispersion in the random model is accentuated and, moreover, the random model seems to have a greater mean.

[3]The mode of a histogram is the interval with higher frequency

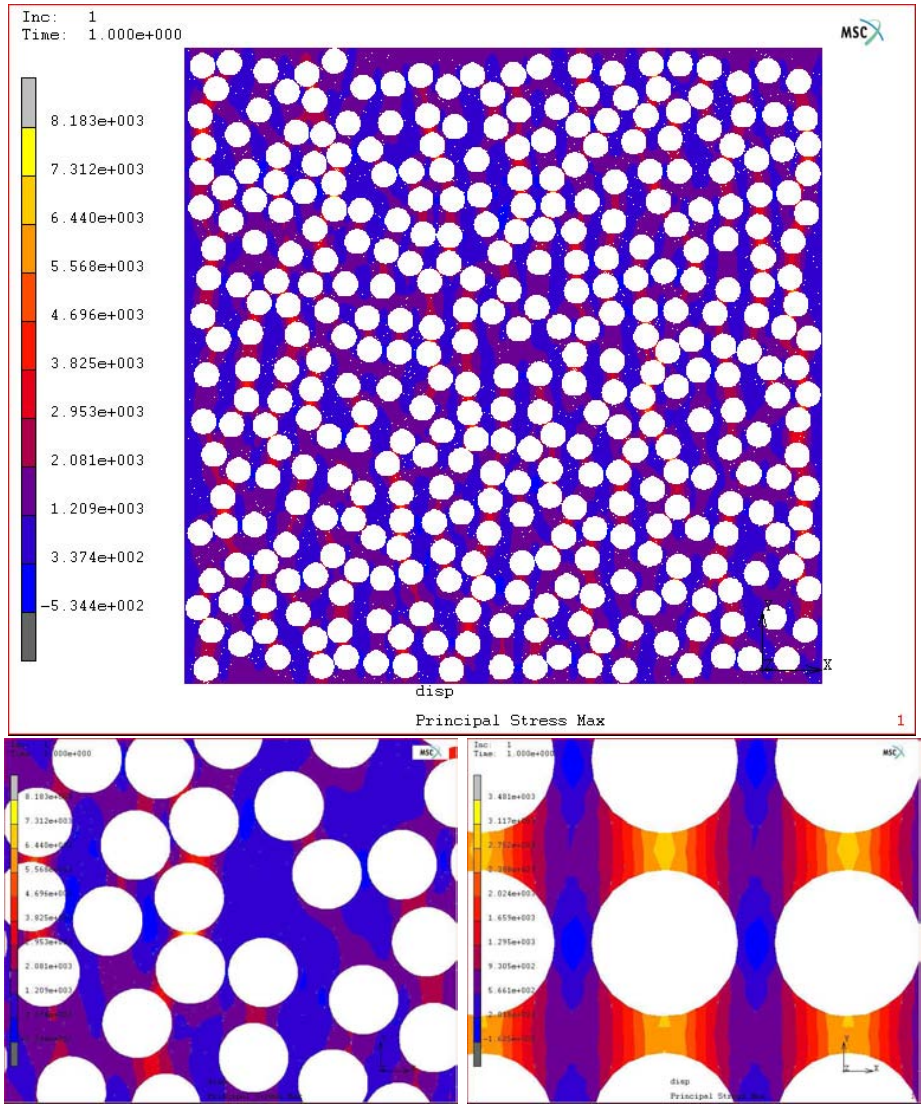

Figure 7.4: σ_1 In the random and periodic models

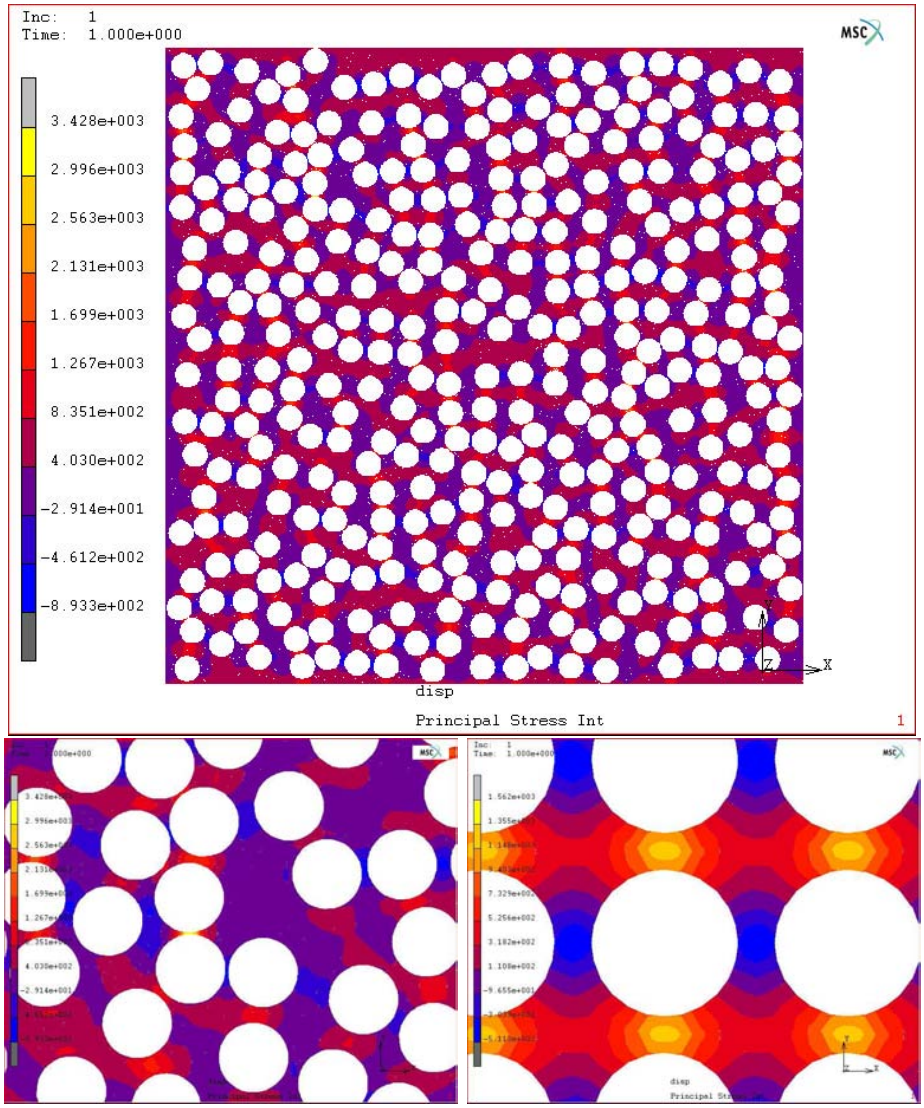

Figure 7.5: σ_2 In the random and periodic models

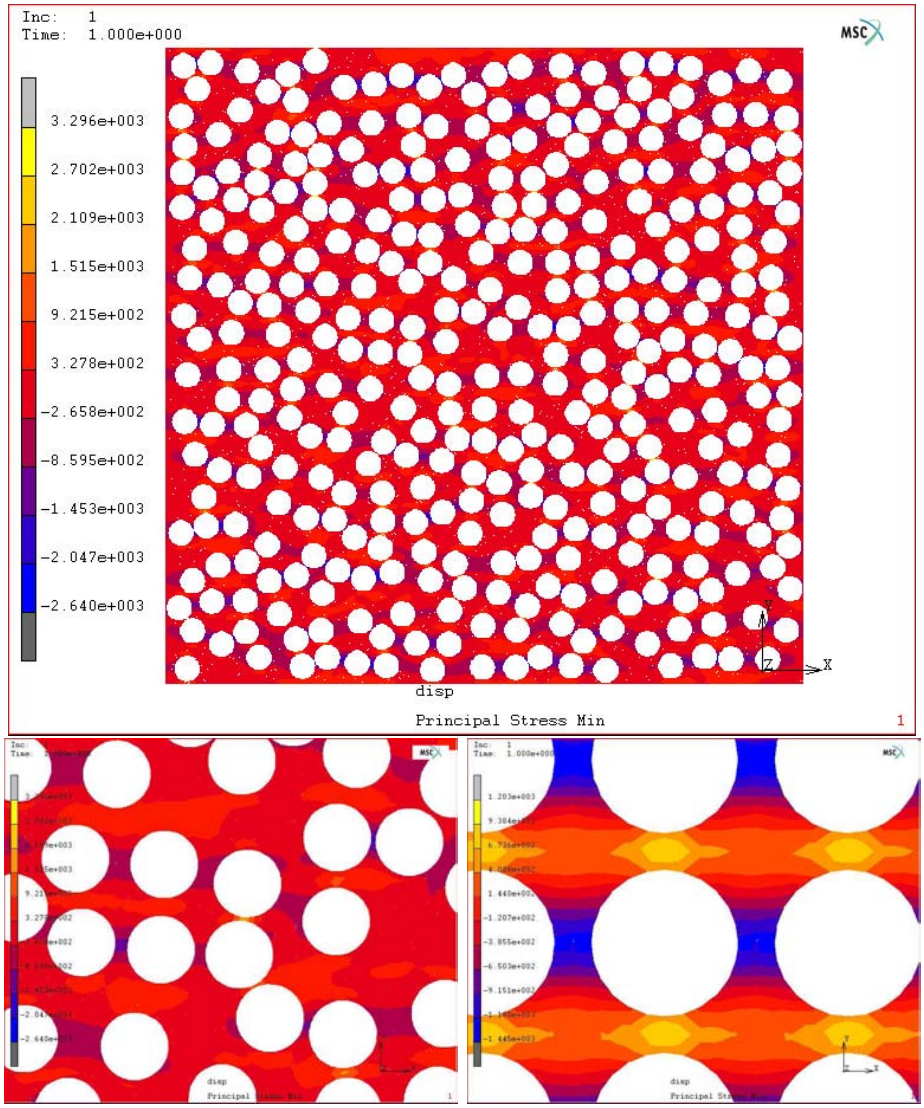

Figure 7.6: σ_3 In the random and periodic models

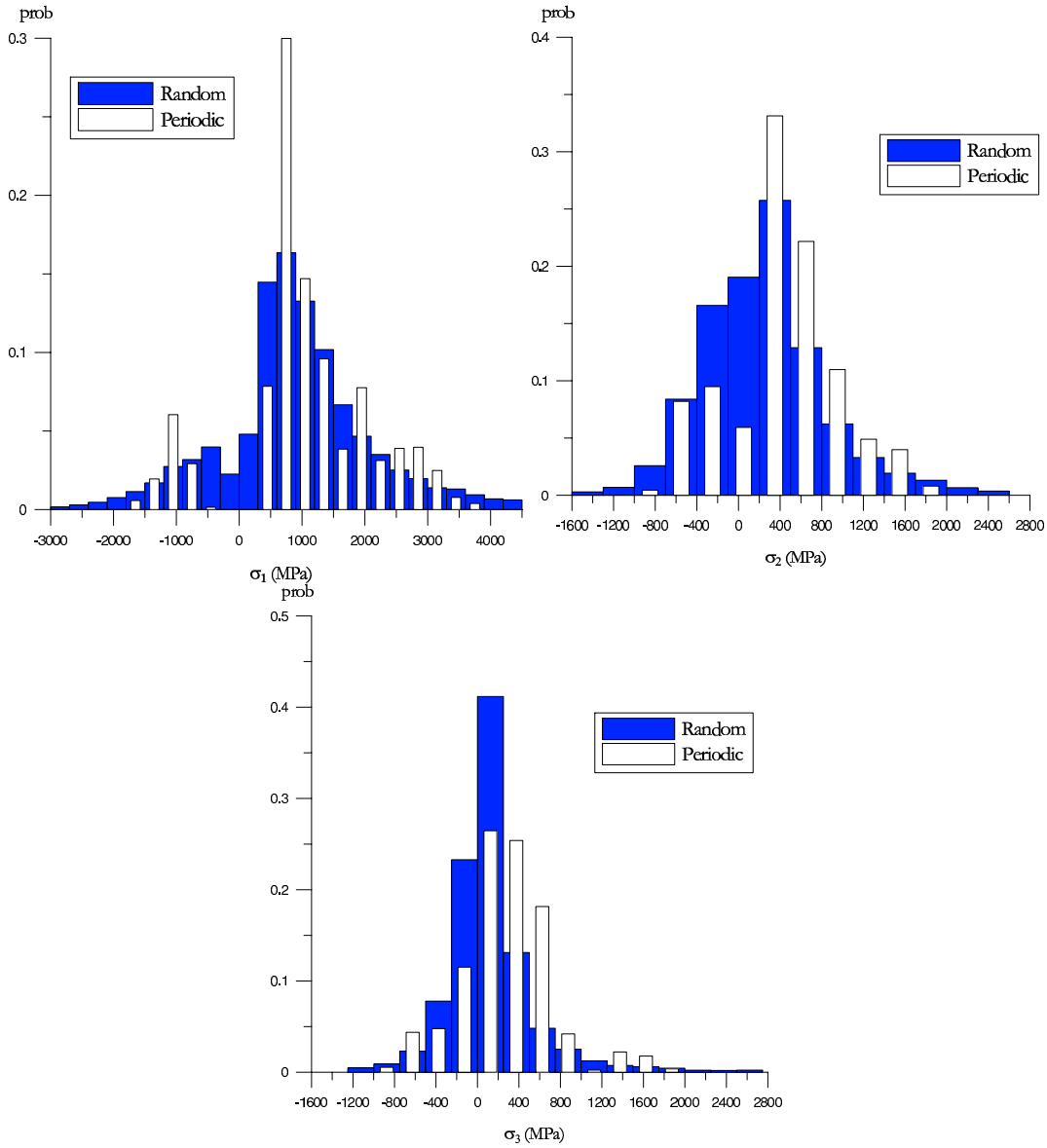

Figure 7.7: Histograms of the principal stresses in the matrix for the periodic and the random model

As it has been seen in the former sections, the histograms of both models show greater differences in the extreme values and consequently, this later plot shows greater differences between the histograms of both models, since it reflects the ratio between the maximum traction values (σ_1) and the maximum compression values (σ_3).

As was reviewed in Chapter 3, Asp and co-workers [12], when they analyzed the stress state in a matrix of a composite loaded transversely, they concluded that there exists a relation 1 : 1 : 2 between the principal stresses and also that this relation could be considered a hydrostatic stress state. From the former analysis, it can be concluded that the relation 1 : 1 : 2 between the principal stresses still remains if a random model is considered. Since the random model is thought to be more realistic than the periodic one, it can be affirmed that the stress state in the matrix of composites loaded transversely can be considered hydrostatic.

7.4 Comparison of invariants

In this section two variables which depend on invariants of the stress tensor will be analyzed: the Von Misses stress and the dilatational energy density (U_V)[4]. As reviewed in Chapter 3, some failure criteria are based in these invariants.

Figure 7.9 shows the Von Misses stress in the random model. Again, the highest values appear between fibers which lay in a closer distance measured in the load direction.

Figure 7.10 shows the Von Misses coefficient in the periodic model, where highest values take place between fibers aligned in the load direction. It can also be observed that the maximum values in the random model are about 1.37 times the maximum values in the periodic model. In the other hand, the minimum value of the Von Misses stress in the random model is about 0.5 times the minimum von Misses stress in the periodic model.

These relations can be observed in the histogram plotted in Figure 7.11. This histogram shows that means[5] are nearly equivalent and that the frequencies in the higher intervals are higher in the random model.

Figure 7.12 shows the dilatational energy density in the matrix for the random model. It can be observed that the value of the dilatational energy density is nearly constant and shows very high peaks between fibers which are located very closely and lay somehow aligned in the load direction. The ratio of the high value divided by the constant value is about 20.

Figure 7.13 shows the dilatational energy density in the periodic model. Concentration areas appear between the fibers in the load direction. The ratio between the value in this concentration areas and the low values is about 11.

[4]See Sections 3.4.2 and 3.4.3 for the definition of the Von Misses stress and the dilatational energy density, respectively

[5]The mean can be seen as the projection of the gravity center of the histogram in the abcisae axis

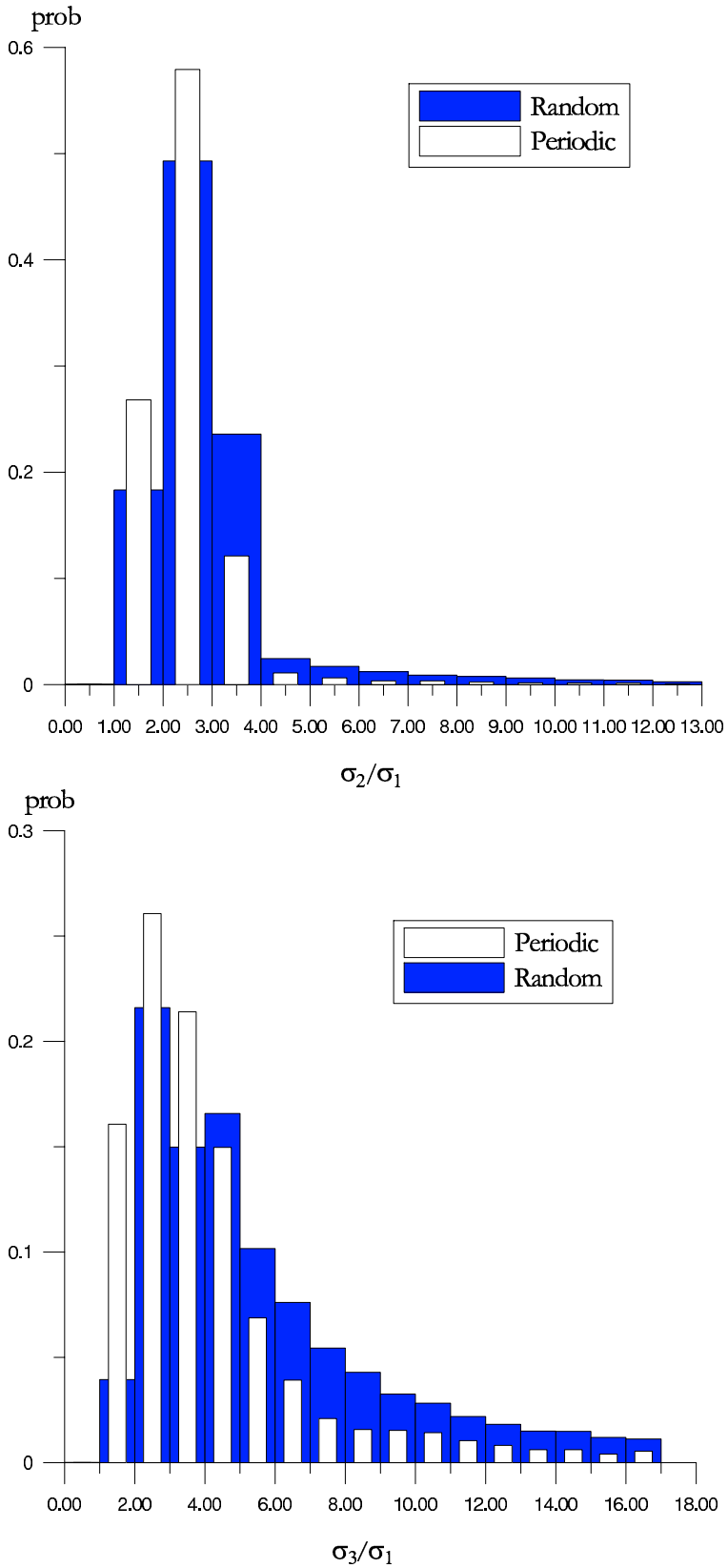

Figure 7.8: Histograms of the equitriaxiality coefficients in the matrix for the periodic and the random model

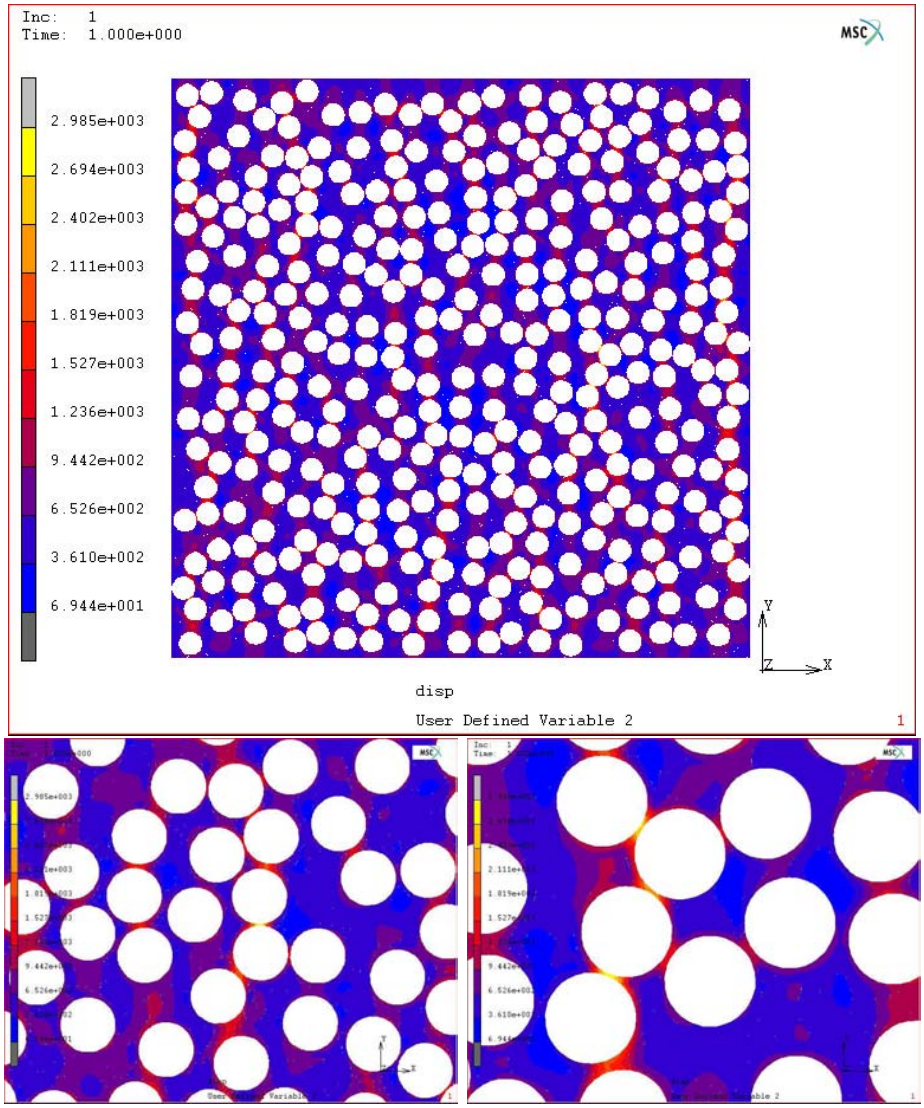

Figure 7.9: Von Misses Stress in the random model

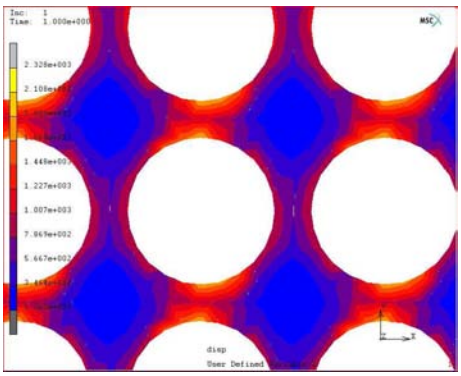

Figure 7.10: Von Misses Stress in the periodic model

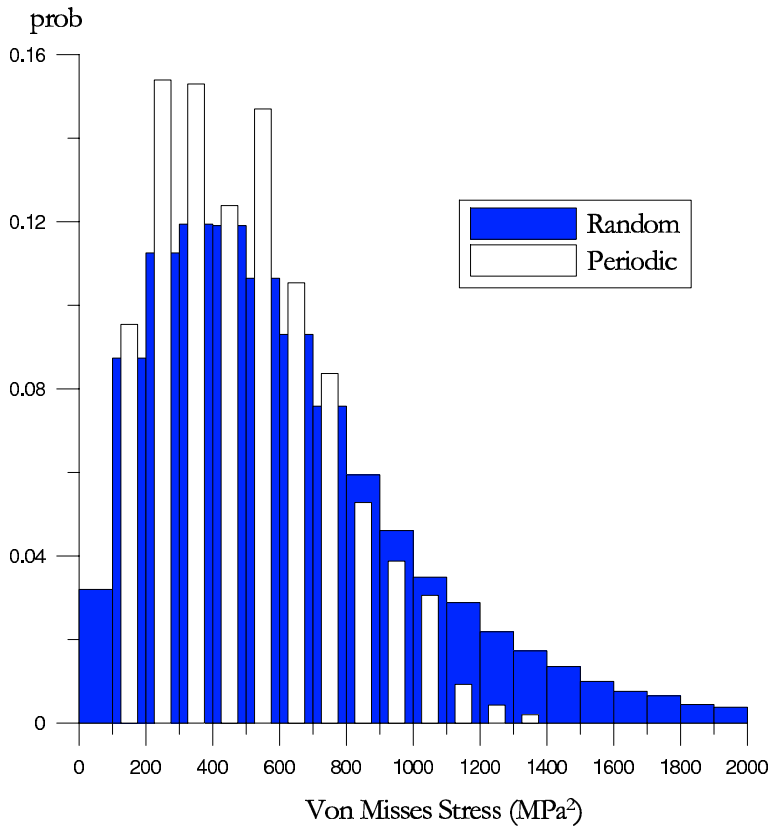

Figure 7.11: Histograms of the von Mises stress in the matrix for the periodic and the random model

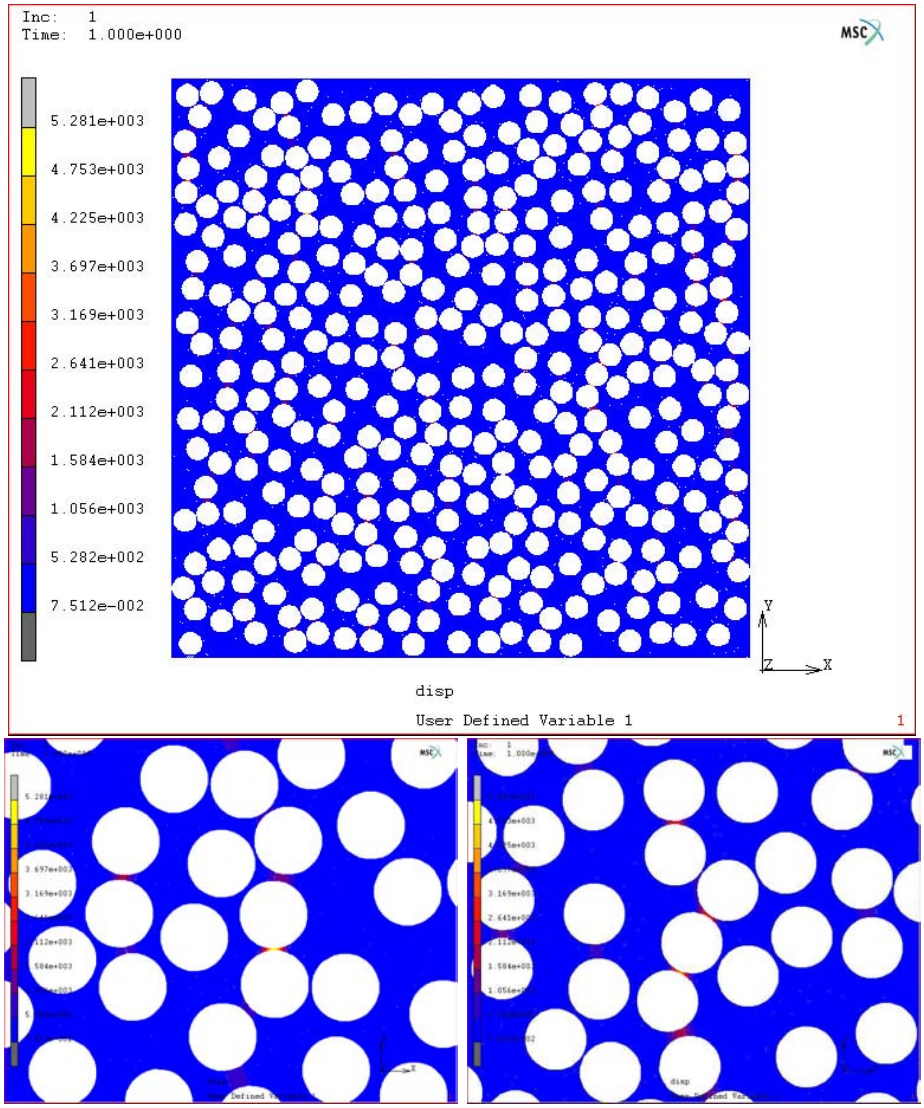

Figure 7.12: Dilatational energy density in the random model

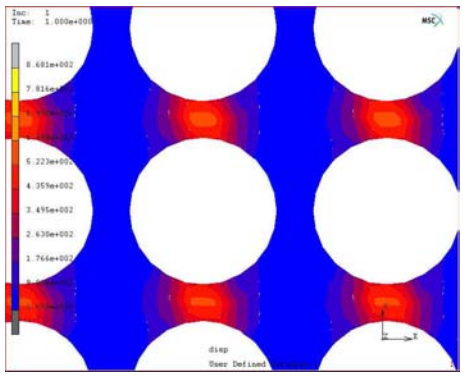

Figure 7.13: Dilatational energy density in the periodic model

Figure 7.14 shows two histograms of the dilatational energy density. The upper histogram covers the complete range of the dilatational energy density. It reflects how the most part of the points in both models are in the same bin (the lower one). In spite of this, it can be seen in the histogram in the bottom of Figure 7.14 that the range of the random model is much larger than the range in the periodic model. This phenomena is very remarkable, since the high values of the dilatational energy density are expected to cause initiation of transverse failure of the composite. It is also important to remark that these high values take place in about 1% in the random model, while are not covered by the periodic model.

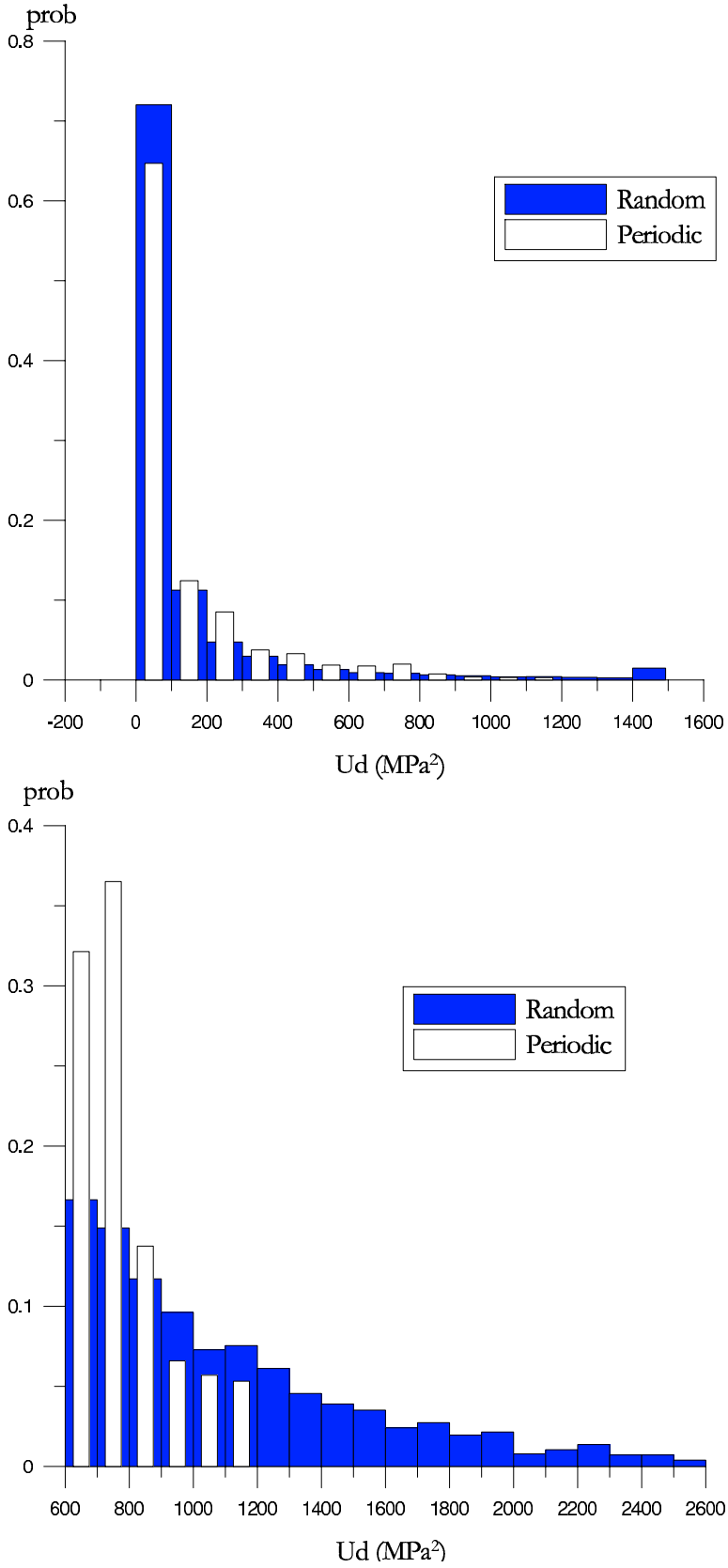

Figure 7.14: Histograms of the dilatational energy density in the matrix for the periodic and the random model

7.5 Conclusions

A comparison between a periodic and a random model for the same long fibre reinforced composite has been performed. The most significant differences are the following:

- The maximum value of ε_{22} is about 40% higher in the random model and the frequency in the right tail is higher in the random model. In the random model appear compressive strains (on the 5% of solution points) which are not considered by the periodic model. Analogous conclusions stand for σ_{22}.
- An analysis of the principal stresses shows that the maximum (in absolute value) stresses for the first and third components in the random model are 2 and 1.7 times those in the periodic model. The histograms show notably different probability distributions in the random and in the periodic model.
- It can be considered that the random model shows the relation $1 : 1 : 2$, present when the periodic distribution of fibers is considered and consequently, the stress state in the matrix can be considered a hydrostatic stress state.
- The Von Misses stress seems to have a similar mean in both models but, again, the random model has a greater probability in the tail of the histogram.
- The dilatational energy density in the random model shows a nearly constant value with some very high peaks in areas between fibers located very close. Observing the histograms both seem equivalent but, again, the random model reflects higher values caused by close distances not considered in the periodic model.

Chapter 8

A two-scale method for transverse random composite materials

8.1 Introduction

This chapter is devoted to the probabilistic simulation of the transverse fracture of long fibre reinforced composites. It was seen in Chapter 7 that a random model reproduces more realistically the stress and strain fields in the composite than a periodic model does, specially in the extreme values of the stress and strain components. Using the information from random models of the microscale, the aim now is to obtain the probability of fracture at any point in a macro-scale dominium.

To construct this micromodels, the information obtained from the analysis of digital images (Chapter 6) will be used. The micromodels will be based on the Statistical Representative Volume Element developed in Chapter 5.

In this Chapter, a two-scale method (schematized in Figure 8.1) for composite materials with random elastic and which exhibit random failure behavior is developed. This method takes into account the random distribution of the fibers at the micro-scale and derives the behavior of the material at the macro-scale. Consequently, the hypothesis that the random failure behavior of the composite material is caused by its random microstructure is made. In the micro-scale the composite material is thought to satisfy:

- All random variables and random fields are ergodic
- All random variables and random fields can be considered second-order stationary
- The position of each fibre is random and it can be modelled with a hard-core model.
- The elastic properties of the constituents (fibre and matrix) are constants.
- The ultimate strength and critical values for failure criteria of the constituents are constants.

In a similar way to that described in Section 2.1.2, and as it is usually done in homogenization theory, the composite material will be seen in the macro-scale as a homogeneous

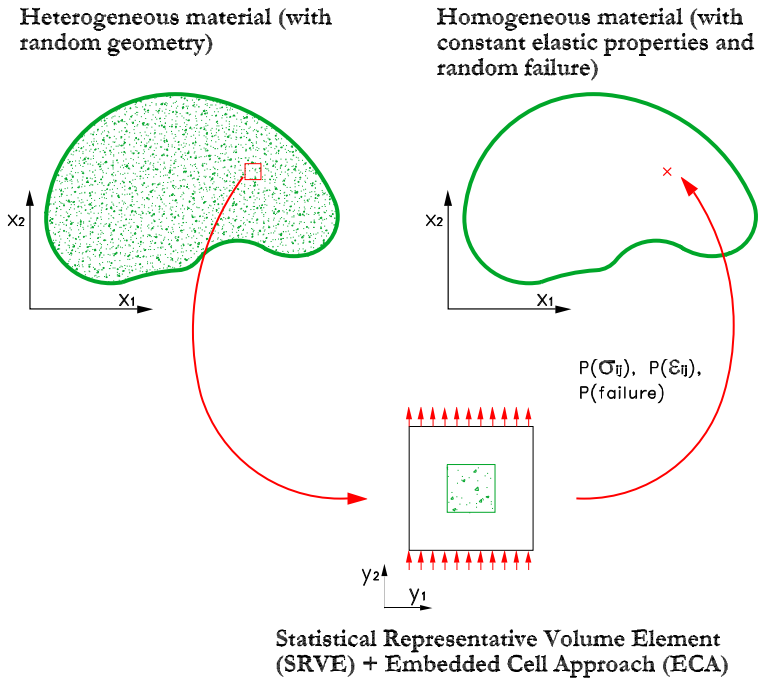

Figure 8.1: Two-scale method for the failure of random transverse composites

material. That means, the equivalent homogeneity hypothesis is thought to be satisfied. The material in the macro-scale is thought to have the following properties:

- All random variables and random fields are ergodic
- All random variables and random fields can be considered second-order stationary
- The elastic properties are known constants. , This information can be provided by the Statistical Volume Element (Chapter 5), or by experimental tests.
- The elastic failure properties are random.
- The elastic and failure properties of two solution points can be considered statistically uncorrelated.

Expressions which relate the macro and the micro-scale will be obtained in Section 8.4. But first, simulations on the micro-scale, which will provide information on the statistical distributions of the stress and strain components, will be performed. This statistical distributions are needed for the macro-micro relations. Section 8.2 is focused on the micro-scale and describe two methods for the simulation of microstructure patterns of fibre reinforced composites. The results of the simulations are analyzed and modelled with statistical distribution functions in Section 8.3.

8.2 Microstructure simulation

8.2.1 Simulation by random generation of fiber positions

As it was experimentally observed in Section 5.2.2 of Chapter 5, usual algorithms for the simulation of Poisson point fields or hard-core point fields are not usable for volume fractions greater than 0.5. For this reason, a new algorithm for the simulation of the fiber position of real fibre reinforced composites has been developed. This algorithm takes some ideas of algorithms used for the simulation of the molecular nature of fluids and of the granular nature of powders and porous materials in which *random close packing* [22] is attained.

Although its mathematical definition has been recently questioned [154], random close packing (RCP) of particles is considered a random distribution of particles touching its nearest neighbor and having the maximum coordination number[1]. Although it is a random distribution of particles it is expected to have a certain stability, caused by field forces. Usually, another state called *random loose packing* is defined as a random distribution of particles touching its nearest neighbor.

The critical packing fraction for the RCP state is defined as:

$$\eta_{RCP} \equiv \min\{\eta | R_{NN}(\eta) = 2r\} \tag{8.1}$$

where R_{NN} is the distance to the nearest neighbor of each particle (fibre). The value of this fraction is not clear but it is generally accepted to fall in the range $\eta_{RCP} \sim 0.82 - 0.89$. This value is not far from the ordered close packing of hard disks: $\eta = \rho\pi r^2 = \pi/\sqrt{(}12) \cong 0.9069$ [22].

Simulation algorithms of random packing are normally based in heuristic rules. They basically, rearrange the particles sequentially in a way that the system gets closer to a RCP state. Some of these heuristic rules are:

- To avoid any bias in the sequence of particle rearrangements, this sequence is randomized after each iteration.

- If particles are overlapped, the new position of particle i is computed as [72, 71]:

$$\mathbf{x}_{ji} = \mathbf{x}_j + (\mathbf{x}_i - \mathbf{x}_j)\frac{2r}{d_{ij}} \tag{8.2}$$

  where $\mathbf{x}_{ji}$ is the displacement vector for the separation of the particle i from particle j, $\mathbf{x}_i$ and $\mathbf{x}_j$ are the locations of the centers of particles i and j respectively, r is the particle radius and d_{ij} is the distance between particles i and j. If particle i is overlapped by n_i particles, its new position can be computed:

[1] The coordination number of a particle i is the number of particles which are in contact with this particle

$$\mathbf{x}_i' = \frac{1}{n_i} \sum_{j=1}^{n_i} \mathbf{x}_{ji} \tag{8.3}$$

This iterative process of separation of particles is usually called *relaxation*.

- A new movement is accepted if the new maximum overlap is less than the maximum overlap among all particles [39]. This way, the growing of the maximum overlap, which could lead to non-convergence, is avoided.
- A particle is vibrated if its coordination number is lower than 4 [72, 71]. That means, it is given a very small random displacement.
- After a certain number of iterations, packing space is expanded [71].

The purpose of this work is to simulate random distribution of fibers in CFRPs. Usual volume fractions for CFRPs are values between 0.55 and 0.65 and the distribution of fibers is not that defined as *random close packing* or *random loose packing*. However, since it is very difficult to simulate distributions with a volume fraction greater than 0.6 with the inhibition process of Algorithm 2[2], some ideas from the algorithms for RCP can be used to construct a new algorithm (Algorithm 4), which allows to simulate random fiber distributions having volume fraction greater than 0.5.

```
1: N: number of fibres (Obtained with Algorithm 1 or from material sample histogram)
2: {Generation of the initial positions: }
3: for i = 1 to N do
4:    coord(i,1) = RAND(0,L)
5:    coord(i,2) = RAND(0,L)
6:    {RAND(0,X) is a function which gives uniformly distributed numbers between 0
      and X:}
7: end for
8: while Overlaps between fibers exist do
9:    for i = 1 to N do
10:      Select those fibers which overlap with fiber i
11:      n_i: Number of fibers which overlap with fiber i
12:      if n_i > 0 then
13:         Compute new position of particle i (Equations 8.2 and 8.3)
14:      else
15:         Particle moves approaching its nearest neighbor k a random distance between
            0 and d_ik
16:      end if
17:      Check if overlaps exist
18:   end for
19: end while
```

Algorithm 4: Simulation of fibre distributions with high volume fraction

[2]See Section 5.2.2

$\overline{v_f}$	Time (min)
0.40	0.52
0.45	1.67
0.48	2.48
0.49	5.82
0.50	7.43
0.51	13.56
0.52	18.32
0.53	22.54
0.54	32.67
0.55	44.86
0.56	60.33
0.57	80.17
0.58	95.72
0.59	127.67

Table 8.1: Simulation times to obtain random distributions for different mean volume fractions, using Algorithm 4

To improve the efficiency of Agorithm 4 it is very important to keep in each iteration an updated database of neighbor fibres, which can be done easily by dividing the dominium in cells of side 2-3 times the fibre radius.

Table 8.1 shows the simulation times of running Algorithm 4 for different volume fractions for SRVE models with $\delta = 50$. These simulations were run on a Intel Pentium-IV 1.4GHz CPU. Simulation times are also plotted in Figure 8.2, where it can be seen that times grow exponentially with the volume fraction and that the simulation of typical volume fractions of carbon reinforced composites (between 0.55 and 0.57) may last between 60 and 90 minutes. This supposes a quite large computational time, considering that afterwards the information on the position of the fibres will be converted in a fine-mesh finite element model (with an unavoidable time consuming meshing process) and finally solved.

8.2.2 Simulation by exact microstructure reproduction

As it was described in Chapter 6 and in opposition to what is normally considered in the theoretical texts [114] [141] some composite materials seem to exhibit random point patterns which cannot be modelled assuming complete spatial randomness. The development of simulation methods for non-uniform random point patterns escapes the scope of this work and, in fact, is a nowadays research field in mathematics and statistics. On the other hand, in the former section it has been observed that the simulation of fibre distributions of real carbon reinforced composites may last between 60 and 90 minutes and that it grows as a exponential function of the volume fraction.

In this section a practical solution, which will be referred as *exact microstructure reproduction* is employed for simulating random composites with non-uniform random

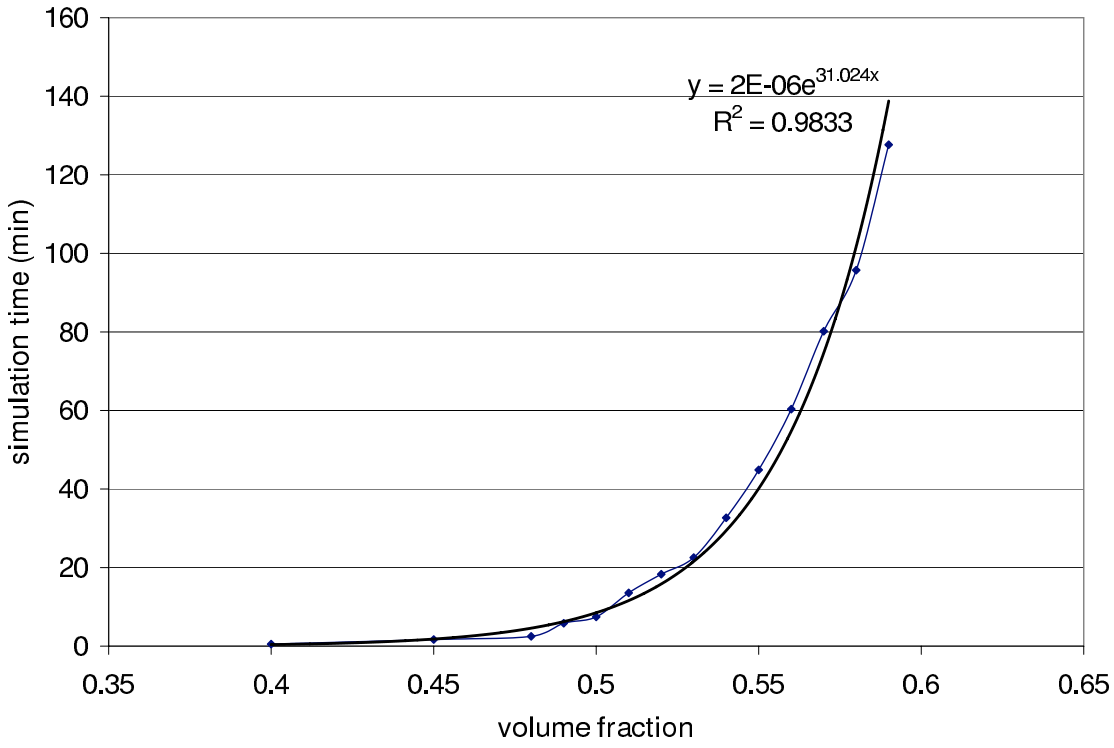

Figure 8.2: Simulation times to obtain random distributions for different mean volume fractions, using Algorithm 4 (Plot of values given in Table 8.1)

distribution. Digital images of the composite microstructure will be converted into Finite Element Models. For this purpose, some conversion subroutines have been developed using *PYTHON* language. This language can be used for batch preprocessing with MSC.Mentat software so, in a three step routine, a Finite Element model of a real transverse section of fibre reinforced composite can be obtained. The procedure includes the following stages:

1. Image acquisition with an optical microscope. To obtain large dominium and high resolution images, a mosaicking software, developed by the Artificial Vision research group of the University of Girona, has been used[3]. This software allows real time acquisition and assembling of contiguous images for the construction of large and high resolution digital images.

2. Process the acquired digital images, using the techniques described in Section 6.3, in order to obtain the position of the center of the fibres.

3. To run a PYTHON routine to convert the information from the image in a meshed finite element model. An ECA model can be obtained within the same routine.

An example of this conversion methodology is given in Figure 8.3, which shows the conversion of one of the images from TUHH.

This process, which includes meshing of multiple narrow necks between fibers [4] and the linear solving, lasts, in mean, 120 minutes from which only 7 come from obtaining the positions of the fibre centers[5]. The meshing and solving time should be added to the times corresponding to the simulation described in the former section, for a better comparison. This would give about 170-200 minutes.

It can be seen that, for this work's purposes, exact microstructure reproduction is much more advantageous than the simulation of the random positions process, not only because the computational times are smaller but also because the process allow to obtain models of microstructure patterns which cannot be considered to have a complete spatial randomness CSR.

8.3 Analysis of results obtained from microstructure simulation

This section presents and analyzes the results of the FEM simulation of the microstructure of the three materials from TUHH. From 40 images from each material, 40 FE models have been obtained using the methodology described in Section 8.2.2. Since the images from TUHH are larger than the minimum size of the SRVE obtained in Chapter 5, the microstructure model is created from a centered window of size $\delta = 50r$ from each digital image.

[3] See Section 6.3.1 of Chapter 6

[4] For a SRVE model with $\delta = 50$ about 290000 triangular elements and about 150000 nodes result from the meshing process

[5] Times using the same Intel Pentium-IV 1.4GHz CPU, that in former section

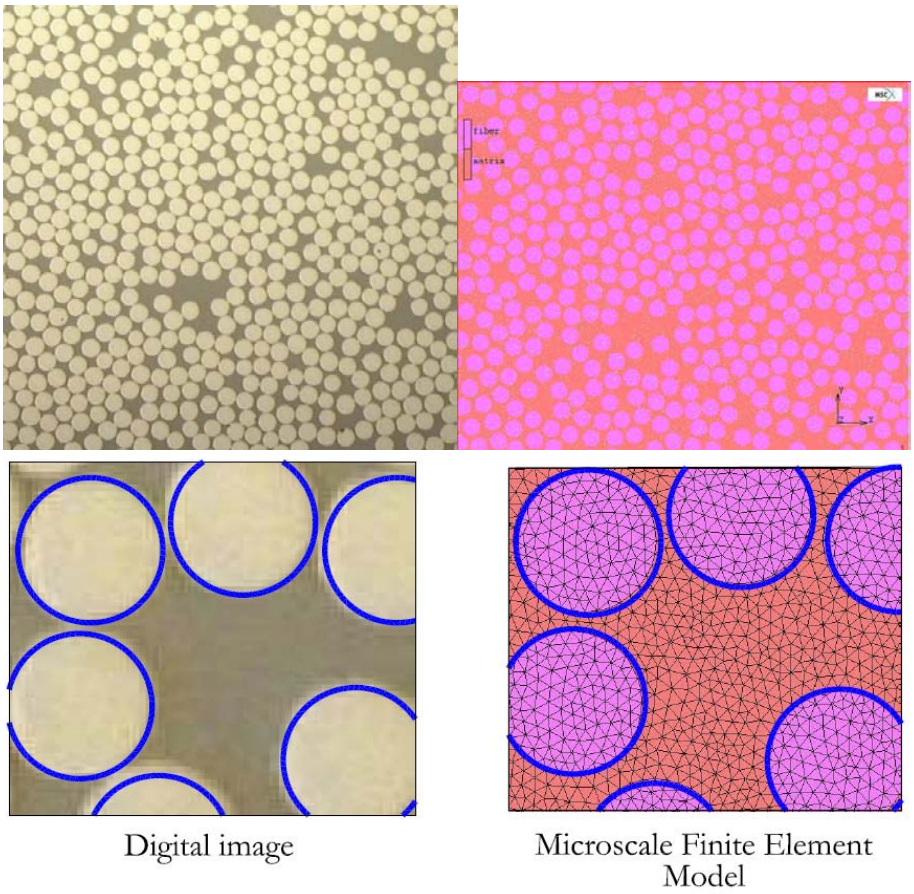

Figure 8.3: The upper images show the conversion a large image from microstructure (left) into a finite element model. The images at the bottom show a detail of this conversion. The fibres have been encircled with a constant radius, for a better appreciation

[hbtp!] heightMaterial	E (MPa)	ν	Fibre diametre (mm)
HTA 5131 (carbon fibre)	28000	0.23	$6 \cdot 10^{-3}$
RTM6 (epoxy resin)	2755	0.34	-
977-2 (epoxy resin)	2730	0.34	-
6376 (epoxy resin)	3630	0.34	-

Table 8.2: Material properties used in FE models

Since each fibre is expected to have nearly uniform stress and strain components, the mesh within each fibre could have been coarser. However, for statistical sampling purposes it can be useful to have uniformly distributed nodes. The material properties obtained from the supplier and from TUHH (shown in Table 8.2) have been used for the FE models.

Arbitrary displacements are applied employing the Embedded Cell Approach. And finally, the models are solved. From each micromodel the following data is stored:

- $\varepsilon_{ij}^{(m)}(k)$: strain components in the matrix for each node k in the mesh, which lays in the matrix region
- $\sigma_{ij}^{(m)}(k)$: stress components in the matrix for each node k in the mesh, which lays in the matrix region
- Mean strain components in the composite:

$$\langle \varepsilon_{ij} \rangle = \int_{\Omega_y} \varepsilon_{ij}(y)\, \mathrm{d}y = \frac{\sum_{k=1}^{N} \varepsilon_{ij}(k)}{N} \tag{8.4}$$

  where Ω_y is the dominium of the SRVE and N is the total number of nodes in the mesh.

- Mean strain components in the composite:

$$\langle \sigma_{ij} \rangle = \int_{\Omega_y} \sigma_{ij}(y)\, \mathrm{d}y = \frac{\sum_{k=1}^{N} \sigma_{ij}(k)}{N} \tag{8.5}$$

  where N is the total number of nodes in the mesh.

From this quantities, the following material constants and quantities can be computed for each model:

- The Young's modulus, which considering that the material is isotropic in the 12-plane, can be obtained as:

$$E = E_{22} = \frac{\langle \sigma_{22} \rangle}{\langle \varepsilon_{22} \rangle} \tag{8.6}$$

- Keeping the assumption of isotropy, Poisson's ratio can be also computed:

$$\nu = \nu_{12} = -\frac{\langle \sigma_{11} \rangle}{\langle \sigma_{22} \rangle} \tag{8.7}$$

- From the stored $\sigma_{ij}^{(m)}$, the dilatational energy density U_V and the Von Misses stress are computed for each node k which lays within the matrix region:

$$U_V(k) = \frac{1-2\nu^{(m)}}{6E^{(m)}}(\sigma_{11}(k)+\sigma_{22}(k)+\sigma_{33}(k))^2 \tag{8.8}$$

  where $E^{(m)}$ is the matrix Young's modulus and $\nu^{(m)}$ the Poisson's ratio of the matrix.

- The contribution of the matrix to the total strain for each model:

$$v_{\varepsilon_{ij}} = \langle \varepsilon_{ij}^{(m)} \rangle / \langle \varepsilon_{ij} \rangle \tag{8.9}$$

  where $\langle \varepsilon_{ij}^{(m)} \rangle$ can be computed:

$$\langle \varepsilon_{ij}^{(m)} \rangle = \int_{\Omega_m} \varepsilon_{ij}(y)\,\mathrm{d}y = \frac{1}{M}\sum_{k=1}^{M} \varepsilon_{ij} \tag{8.10}$$

  where Ω_m is the region of the SRVE occupied by the matrix and M the number of nodes of the FE mesh which lay on Ω_m.

8.3.1 Choice of probability density functions

In this section the probability density functions which more adequately fit the data from the simulations will be chosen.

Usually, the normal distribution is used for modelling stress components in a body. It was seen in Chapter 7 and it can be observed in Figure 8.4 that the histograms of the components of stress are nearly symmetric, so the normal distribution seems to be a good choice.

Both the Von Misses stress and the Dilatational energy density are magnitudes related to stress invariants so they could be modelled with a normal distribution but, since they are non-negative, their histograms (Figure 8.5) show clearly a lack of symmetry. The shape of the histogram suggests a Weibull distribution but also some transformations (squared root or logarithm) can be applied to the data to make some symmetry appear or to try to improve the fit.

Square root and logarithm transformations are applied to U_V and σ_{VM}. Following to these transformations, the maximum likelihood estimators for the parameters of normal and Weibull distributions[6] are obtained and then the χ^2 goodness-of-fit test is computedThe test is described in Section B.7.3 of Appendix B. The result of the test can be interpreted as: the closer to 1 is the value for this test, the better the employed fit. Results for each variable, including the transformations are given in Table 8.3. The table shows in boldface the best result for each variable. In the following subsections, each

[6]See Section B.5 of Annex B for the mathematical expressions which define these functions

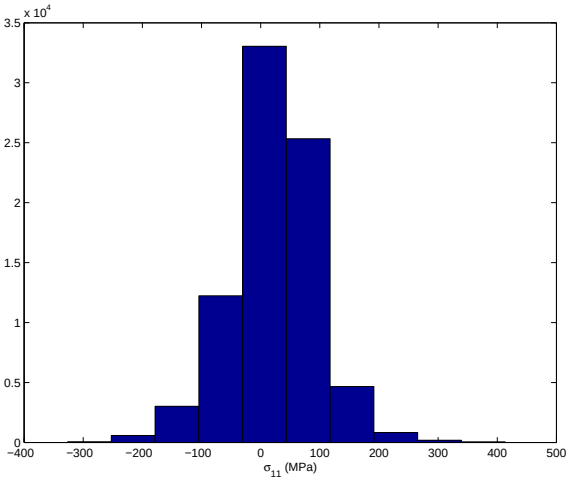
x 10^4
3.5
3
2.5
2
1.5
1
0.5
0
−400
−300
−200
−100
0
100
200
300
400
500
σ11 (MPa)

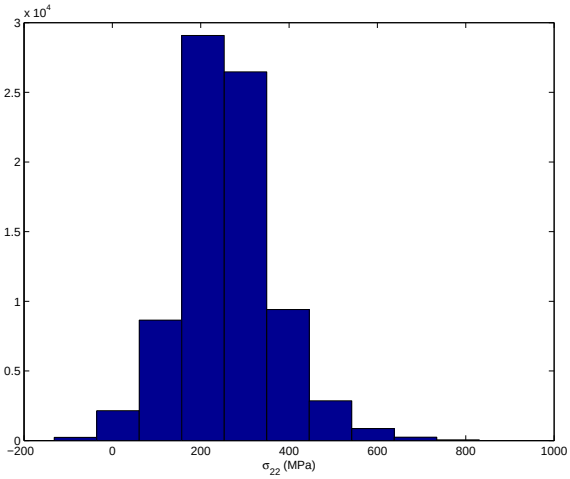
x 10^4
3
2.5
2
1.5
1
0.5
0
−200
0
200
400
600
800
1000
σ22 (MPa)

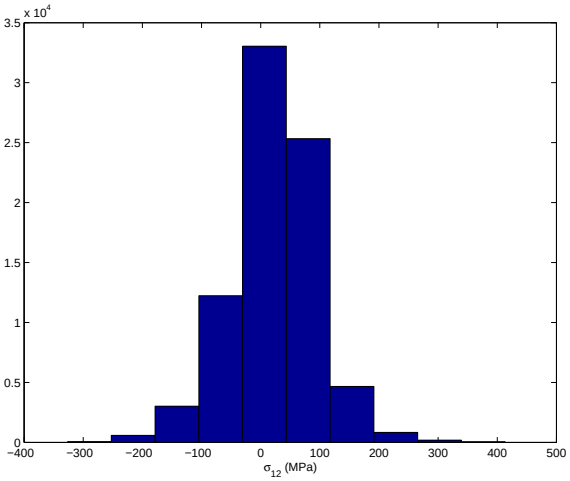
x 10^4
3.5
3
2.5
2
1.5
1
0.5
0
−400
−300
−200
−100
0
100
200
300
400
500
σ12 (MPa)

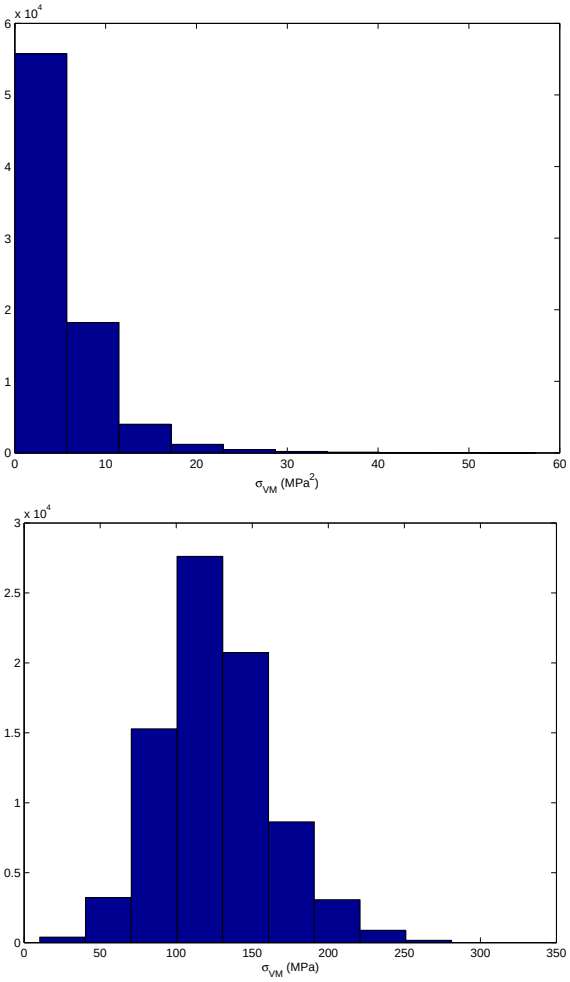

Figure 8.5: Histograms for U_V and σ_{VM}

variable will be fitted using the distribution and transformation which has a larger value in the χ^2 goodness-of-fit-test.

Variable	Weibull	Normal
σ_{11}	-	**0.94770**
σ_{22}	-	**0.94860**
σ_{12}	-	**0.94770**
σ_{VM}	0.94915	0.94747
$\sqrt{\sigma_{VM}}$	**0.94927**	0.94753
$\log 10(1+U_V)$	0.94902	0.94818
U_V	0.94775	0.94499
$\sqrt{U_V}$	**0.94840**	0.94736
$\log 10(1+U_V)$	0.94721	0.94472

Table 8.3: χ^2 goodness-of-fit test for some variables

According to the obtained results in the χ^2 goodness-of-fit test, the stress components will be modelled with a normal distribution, and a square root transformation will be applied to the dilatational energy density (U_V) and the Von Misses stress (σ_{VM}) which then, will be modelled as Weibull distributions.

8.3.2 Probability density function for the stress and strain components

The results from the χ^2-goodness-of-fit shown in Table 8.3 have revealed that normal distribution is a good choice for the stress and strain components. Therefore, maximum likelihood estimators of the mean and the standard deviation are computed for the results of each model.

The good agreement of the data with the normal distribution can be observed in the QQ-plots of Figures 8.6,8.7 and 8.8. This Figure shows the good agrement of the cumulative distribution function of the data from the simulation (labelled as *experimental*) and the fit.

The mean (μ) and the standard deviation (σ) of the three stress components for each analyzed material are given in Table 8.4.

The same conclusions stand for the strain components, whose empirical mean and standard deviation are given in Table 8.5.

8.3.3 Probability density function for the Von Misses stress

The results from the χ^2-goodness-of-fit shown in Table 8.3 have revealed that Weibull distribution is a good choice for the square root of the Von Misses stress. Maximum likelihood estimators for the Weibull shape and scale parameters have been obtained and are shown in Table 8.6. The goodness-of-fit can also be observed in the QQ plots of Figure 8.9.

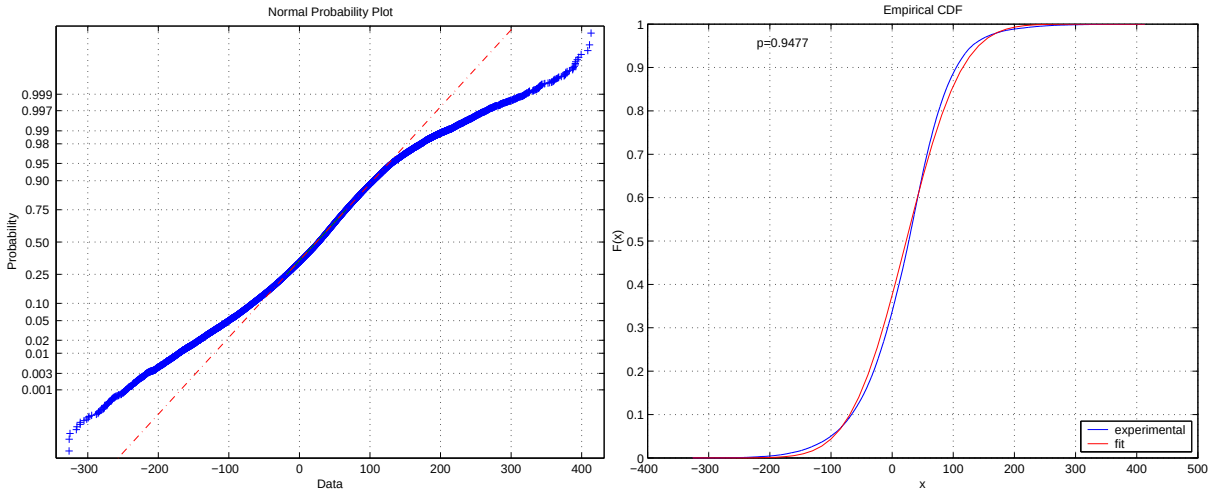

Figure 8.6: Normal plot and CDF plot for σ_{11}

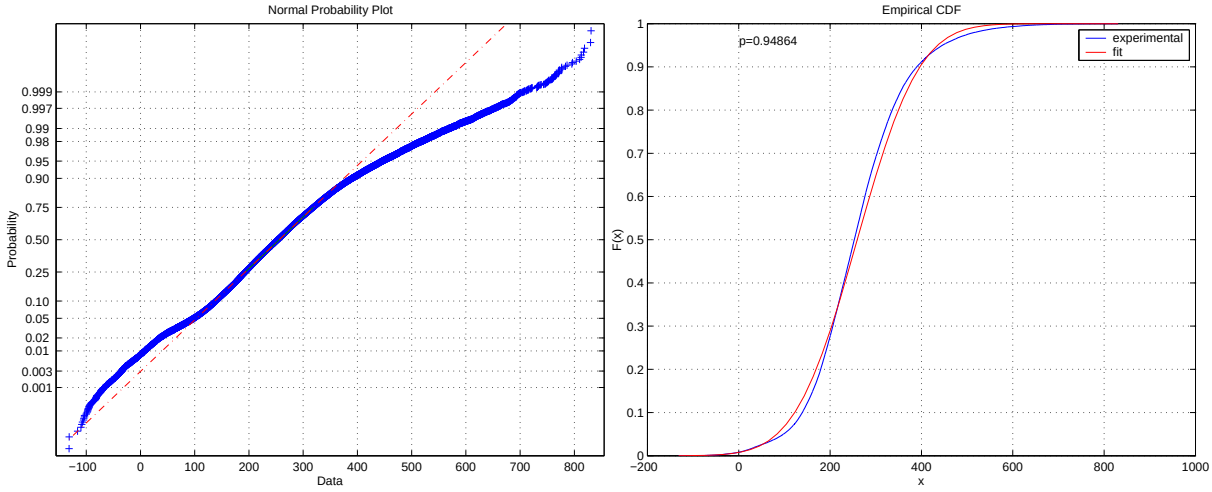

Figure 8.7: Normal plot and CDF plot for σ_{22}

Material	Variable	μ (MPa)	σ (MPa)
RTM6	σ_{11}	22.8182	60.4663
	σ_{22}	248.1615	88.8809
	σ_{12}	22.8182	60.4663
977-2	σ_{11}	23.2556	63.9259
	σ_{22}	250.7342	94.2939
	σ_{12}	23.2556	63.9259
6376	σ_{11}	23.8360	64.3095
	σ_{22}	250.9486	94.4392
	σ_{12}	23.8360	64.3095

Table 8.4: Statistics for the stress components

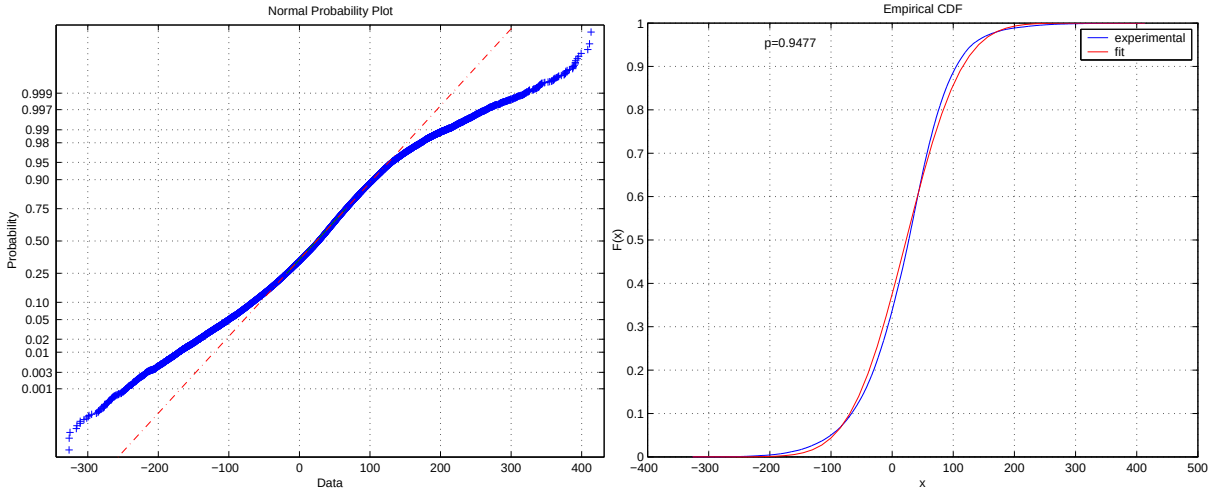

Figure 8.8: Normal plot and CDF plot for σ_{12}

Material	Variable	μ (MPa)	σ (MPa)
RTM6	ε_{11}	-0.0343	0.0142
	ε_{22}	0.0773	0.0239
	ε_{12}	-0.0343	0.0142
977-2	ε_{11}	-0.0343	0.0142
	ε_{22}	0.0773	0.0239
	ε_{12}	-0.0343	0.0142
6376	ε_{11}	-0.0342	0.0142
	ε_{22}	0.0773	0.0239
	ε_{12}	-0.0342	0.0142

Table 8.5: Statistics for the strain components

Material	Variable	α	β	μ	σ^2
RTM6	$\sqrt{\sigma_{VM}}$	$1.5660 \cdot 10^{-7}$	7.7512	9.6270	2.2300
977-2	$\sqrt{\sigma_{VM}}$	11.1506	7.7196	10.8582	2.8019
6376	$\sqrt{\sigma_{VM}}$	8.9507	7.9438	10.8532	2.8039

Table 8.6: Statistics for the Von Misses stress

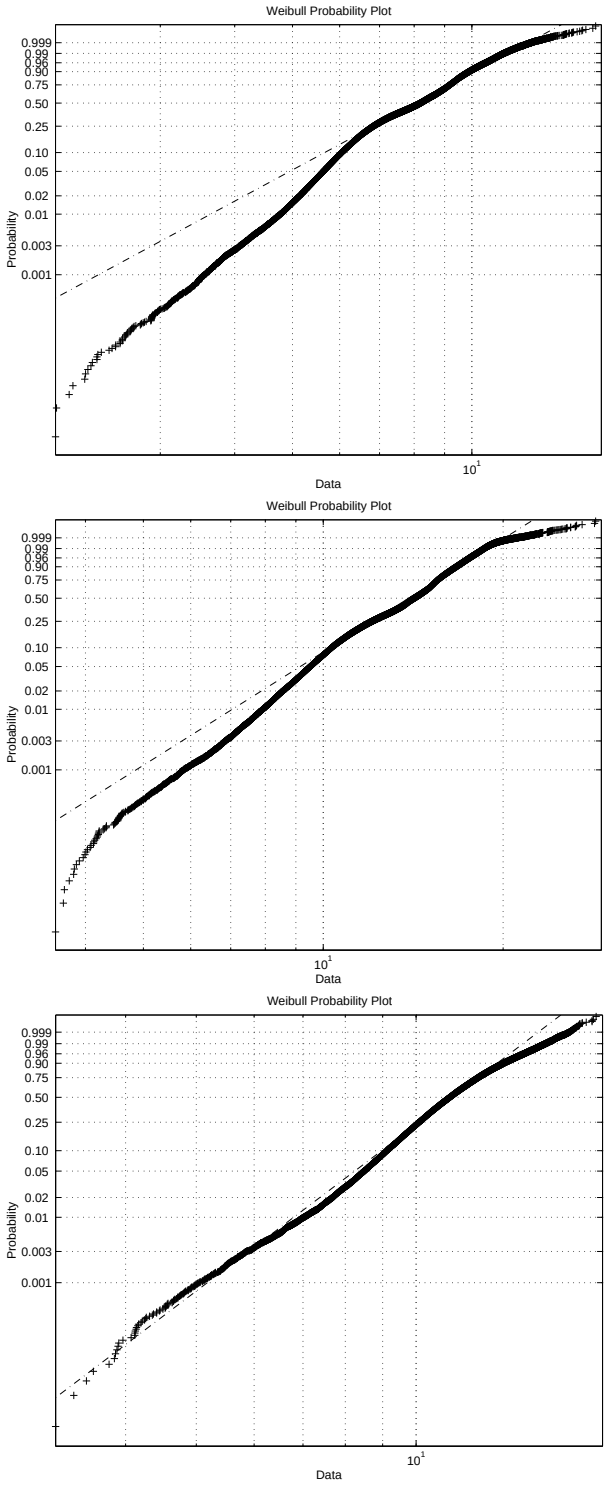

Figure 8.9: Weibull plots for $\sqrt{\sigma_{VM}}$ for RTM6 (up) 977-2 (middle) and 6376 (down)

8.3.4 Probability density function for the dilatational energy density

As it was in the case of the Von Misses stress, the square root transformation was a convenient transformation for the dilatational energy density, which with this transformation fitted correctly with a two-parameter Weibull distribution. Maximum Likelihood estimators for the shape and scale parameters have been obtained and are given in Table 8.7.

Material	Variable	α	β (MPa)	μ (MPa)	σ^2 (MPa)^2
RTM6	$\sqrt{U_V}$	2.5238	2.1371	1.9100	0.6808
977-2	$\sqrt{U_V}$	2.4021	2.1636	1.9326	0.7615
6376	$\sqrt{U_V}$	3.4684	1.7113	1.9374	0.7699

Table 8.7: Parameters and Statistics for the Dilatational energy density

The results for the dilatational energy in the matrix fit very well with a Weibull distribution. This can be seen in Figure 8.10, which shows a QQ plot from a Weibull distribution for the three analyzed materials and denotes that the data from the simulations can be modelled with a Weibull distribution function. The fitting is specially good between probabilities 0.05 and 0.995.

8.4 Macro-micro scale relations

This section derives the expressions which relate the results obtained from the micromodels with the stresses and strains at the macroscale. In the following expressions, the macroscale will be denoted with coordinate x and the microscale with coordinate y. The values of the statistics obtained in the simulations will be denoted with a zero superscript, for instance $\langle I_1^0 \rangle$ will denote the mean of the first invariant of the stress tensor obtained in the micro-scale simulation, by imposing an arbitrary value to the boundary conditions.

Starting from the relations of homogenization and effective medium theory it will be assumed that:

$$\langle \sigma_{ij}^{\mathrm{y}} \rangle = \int_{\Omega_y} \sigma_{ij} \, \mathrm{d}y = \sigma_{ij}^{\mathrm{x}} \tag{8.11}$$

and:

$$\langle \varepsilon_{ij}^{\mathrm{y}} \rangle = \int_{\Omega_y} \varepsilon_{ij} \, \mathrm{d}y = \varepsilon_{ij}^{\mathrm{x}} \tag{8.12}$$

8.4.1 Stress components

For those variables which were fitted using normal distributions (the stress components) the results obtained in the simulations can easily be converted by a simple scaling (See Equations B.11). For any point $\mathbf{x}$ in the macro problem the following relation stands:

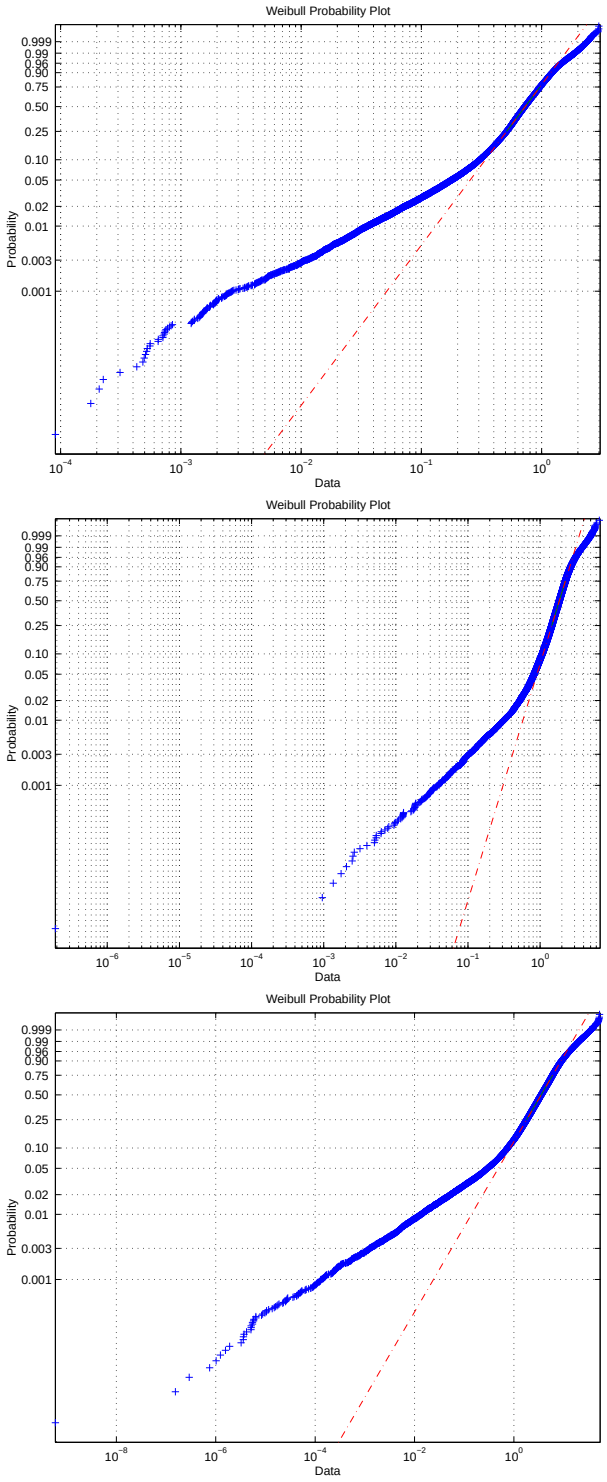

Figure 8.10: Weibull plots for $\sqrt{U_V}$ for RTM6 (up) 977-2 (middle) and 6376 (down)

$$\sigma_{ij}^{\mathrm{x}} = \langle \sigma_{ij}^{\mathrm{y}} \rangle = k_{\sigma_{ij}}(\mathbf{x}) \cdot \langle \sigma_{ij}^{0} \rangle \tag{8.13}$$

where $k_{\sigma_{ij}}(\mathbf{x})$ is a proportionality constant and $\langle \sigma_{ij}^{0} \rangle$ is the mean of the stress component in the micro-scale, as obtained from the FE solution. So, the variance associated the stress at a point of the macro-scale, $\sigma_{ij}^{\mathrm{x}}(\mathbf{x})$, can be expressed:

$$\sigma^2(\sigma_{ij}^{\mathrm{y}}) = k_{\sigma_{ij}}^2(\mathbf{x}) \cdot \hat{\sigma}^2(\sigma_{ij}^{0}) \tag{8.14}$$

Where last equation describes the variance of σ_{ij}^{y} (the stress components in the micro-scale), since the stress components in the macro-scale (σ_{ij}^{x}) are, in fact, deterministic functions of the position (x).

8.4.2 Strain components

Analogously to has been done with the stress components, the following relations can be written for the strain components:

$$\varepsilon_{ij}^{\mathrm{x}} = \langle \varepsilon_{ij}^{\mathrm{y}} \rangle = k_{\varepsilon_{ij}}(\mathbf{x}) \cdot \langle \varepsilon_{ij}^{0} \rangle \tag{8.15}$$

$$\sigma^2(\varepsilon_{ij}^{\mathrm{y}}) = k_{\varepsilon_{ij}}^2(\mathbf{x}) \cdot \hat{\sigma}^2(\varepsilon_{ij}^{0}) \tag{8.16}$$

8.4.3 Dilatational energy density

As it has been seen in Section 8.3.4, the results of the dilatational energy density from the micromodels can be fitted with a Weibull distribution. That is, if U_V^0 is the dilatational energy density at any point in the microscale:

$$p(\sqrt{U_V^0}) = \frac{\alpha^0}{\beta^0} \left(\frac{\sqrt{U_V^0}}{\beta^0} \right)^{(\alpha^0 - 1)} e^{-\left(\frac{\sqrt{U_V^0}}{\beta^0} \right)^{\alpha^0}} \tag{8.17}$$

Let us write down the expression of the stress tensor first invariant at any point in the microscale:

$$I_1^{\mathrm{y}} = \sigma_{11}^{\mathrm{y}} + \sigma_{22}^{\mathrm{y}} + \sigma_{33}^{\mathrm{y}} \tag{8.18}$$

Consequently, the dilatational energy at any point in the micro-scale can be written:

$$U_V^{\mathrm{y}} = \frac{1 - 2\nu^{(m)}}{6E} (\sigma_1^{\mathrm{y}} + \sigma_2^{\mathrm{y}} + \sigma_3^{\mathrm{y}})^2 \tag{8.19}$$

If the mean operator is applied to both sides of the definition of I_1:

$$\langle I_1^{\mathrm{y}} \rangle = \langle \sigma_{11}^{\mathrm{y}} \rangle + \langle \sigma_{22}^{\mathrm{y}} \rangle + \langle \sigma_{33}^{\mathrm{y}} \rangle \tag{8.20}$$

it can be easily seen that if the first invariant of the stress tensor is expressed as:

$$I_1^{\mathrm{x}} = \sigma_{11}^{\mathrm{x}} + \sigma_{22}^{\mathrm{x}} + \sigma_{33}^{\mathrm{x}} \tag{8.21}$$

the following expression stands:

$$\langle I_1^{\mathrm{y}} \rangle = I_1^{\mathrm{x}} \tag{8.22}$$

In order to relate the results from the microstructure simulations to the macroscale, Equation 8.22 will be employed. Let us denote with $\langle I_1^0 \rangle$ the mean of the first invariant of the stress tensor in the micro-scale models, submitted to arbitrary boundary conditions:

$$I_1^0 = \langle I_1^{\mathrm{y}} \rangle = \int_{\Omega_m} I_1(y) dy \tag{8.23}$$

where Ω_m is the region of the SRVE occupied by the matrix. Then, the mean value of the dilatational energy density for the matrix at the micro-scale, obtained with the arbitrary boundary conditions can be written:

$$U_V^0 = \frac{1 - 2\nu^{(m)}}{E^{(m)}} I_1^0 \tag{8.24}$$

At this point the results of the FE simulations with arbitrary values of the boundary conditions can be employed to obtain the results which would be obtained by any other value of the boundary conditions.

Let us assume that knowing the mean strain in the composite at the micro-scale ($\langle \varepsilon_{ij} \rangle$), we could know the mean strain in the matrix at the microscale ($\langle \varepsilon_{ij}^{(m)} \rangle$). Since the elastic properties of the material at the micro-scale are thought to be deterministic, then the components of the stress ($\langle \sigma_{ij}^{(m)} \rangle$) could also be known. From these components, the mean dilatational energy density in the matrix at the micro-scale could be written[7]:

$$\langle U_V^{\mathrm{y}} \rangle = \frac{1 - 2\nu^{(m)}}{E^{(m)}} \left(\langle \sigma_{11}^{(m)} \rangle + \langle \sigma_{22}^{(m)} \rangle + \langle \sigma_{33}^{(m)} \rangle \right)^2 \tag{8.25}$$

$$\langle U_V^{\mathrm{y}} \rangle = \langle U_V^0 \rangle \frac{\langle U_V^{\mathrm{y}} \rangle}{\langle U_V^0 \rangle} = U_V^0 \frac{\langle I_1^{\mathrm{y}} \rangle^2}{\langle I_1^0 \rangle^2} = U_V^0 \frac{(I_1^{\mathrm{x}})^2}{\langle I_1^0 \rangle^2} \tag{8.26}$$

where Equation 8.22 has been applied in the last step. In the last equation the term I_1^{x} means the first invariant of the stress tensor of the matrix component. In fact, according to this work's notation, this term should mean the invariant of the stress tensor for the whole composite but, since the purpose here is to use the dilatational energy density only for a a crack initiation criteria in the matrix, the author has preferred to use this term for simplicity.

If U_V^0 is isolated from equation 8.26 the following expression is obtained:

$$U_V^0 = U_V^y \frac{\langle I_1^0 \rangle^2}{(I_1^x)^2} \tag{8.27}$$

According to this, Equation 8.17 can be re-written to express the probability density function of $\sqrt{U_V}$ at a point x of the macro-scale:

[7] From here the superscripts m (indicating the matrix) for U_V will be dropped, since U_V for the fibre is of no interest here

$$p(\sqrt{U_V}) = \frac{\alpha^0}{\beta^0}\frac{\langle I_1^0\rangle}{I_1^x}\left(\frac{\sqrt{U_V}}{\beta^0}\frac{\langle I_1^0\rangle}{I_1^x}\right)^{(\alpha^0-1)} e^{-\left(\frac{\sqrt{U_V}}{\beta^0}\frac{\langle I_1^0\rangle}{I_1^x}\right)^{\alpha^0}} \tag{8.28}$$

The scale factor β^0 can be re-written:

$$\beta = \beta^0\frac{I_1^x}{\langle I_1^0\rangle} \tag{8.29}$$

and equation 8.28 simplified to:

$$p(\sqrt{U_V}) = \frac{\alpha}{\beta}\left(\frac{\sqrt{U_V}}{\beta}\right)^{(\alpha-1)} e^{-\left(\frac{\sqrt{U_V}}{\beta}\right)^{\alpha}} \tag{8.30}$$

where the relation $\alpha = \alpha^0$ stands since the shape parameter remains invariant to transformation 8.26.

8.5 Applications

By using the results of the microstructure simulation and the microscale-macroscale relations, some applications to derive design maximum strain criteria can be found. These relations allow to define maximum strain related to an imposed probability of fracture. Since transverse composite materials normally exhibit brittle fracture, the term *fracture* will be understood as crack initiation. Consequently, this criteria take into account the random nature of composite materials.

8.5.1 Maximum stress

Equations 8.13 and 8.14 can be used to evaluate the probability of failure at any point of the macro-scale, if the stress $\sigma_{ij}^{\mathrm{X}}(\mathbf{x})$ is compared with a ultimate value σ_{ij}^u:

$$P[\sigma_{ij} > \sigma_{ij}^u] \sim \mathrm{Norm}(k_{\sigma_{ij}}(\mathbf{x})\cdot\langle\sigma_{ij}^0\rangle, k_{\sigma_{ij}}(\mathbf{x})\cdot\hat{\sigma}(\sigma_{ij}^0)) \tag{8.31}$$

where $\mathrm{Norm}(\mu,\sigma)$ is a normal distribution of mean μ and standard deviation σ.

8.5.2 Maximum strain

Analogously, Equations 8.15 and 8.16 can be used to evaluate the probability of failure at any point of the macro-scale, if the strain $\varepsilon_{ij}^{\mathrm{X}}(\mathbf{x})$ is compared with a ultimate value ε_{ij}^u:

$$P[\varepsilon_{ij} > \varepsilon_{ij}^u] \sim \mathrm{Norm}(k_{\varepsilon_{ij}}(\mathbf{x})\cdot\langle\varepsilon_{ij}^0\rangle, k_{\varepsilon_{ij}}(\mathbf{x})\cdot\hat{\sigma}(\varepsilon_{ij}^0)) \tag{8.32}$$

where $\mathrm{Norm}(\mu,\sigma)$ is a normal distribution of mean μ and standard deviation σ.

8.5.3 Probability of fracture at a given strain

Using the stored data from the FE simulations of the micromodels the probability of fracture initiation can be computed following the next steps:

1. Define a critical value for the dilatational energy density (U_V^{crit}), corresponding to one of the analyzed materials.

2. Define a strain ε_{22} to which the composite lamina is expected to be subjected.

3. Compute mean contribution of the matrix to this strain:

$$\langle \varepsilon_{22}^{(m)} \rangle = v_{\varepsilon_{ij}} \langle \varepsilon_{22} \rangle \tag{8.33}$$

4. Make use of the matrix elastic properties and the elasticity relations to compute the mean components $\langle \sigma_{ij}^{(m)} \rangle$:

$$\begin{aligned}
\langle \sigma_{22}^{(m)} \rangle &= E^{(m)} \cdot \langle \varepsilon_{22}^{(m)} \rangle && (8.34)\\
\langle \sigma_{11}^{(m)} \rangle &= \nu^{(m)} \cdot \langle \sigma_{22}^{(m)} \rangle && (8.35)\\
\langle \sigma_{12}^{(m)} \rangle &= \frac{E^{(m)}}{2(1+\nu^{(m)})} \langle \varepsilon_{12}^{(m)} \rangle && (8.36)\\
\langle \sigma_{33}^{(m)} \rangle &= \frac{\nu^{(m)} E^{(m)}}{(1+\nu^{(m)})(1-2\nu^{(m)})} (\langle \sigma_{11}^{(m)} \rangle + \langle \sigma_{22}^{(m)} \rangle) && (8.37)
\end{aligned}$$

5. Make use of the stress components to compute the mean of the first invariant of the stress in the matrix:

$$\langle I_1 \rangle = \langle \sigma_{11}^{(m)} \rangle + \langle \sigma_{22}^{(m)} \rangle + \langle \sigma_{33}^{(m)} \rangle \tag{8.38}$$

6. As seen in Section 8.4.3 the parameters of the Weibull distribution can be related to those obtained for the simulations of the microstructure, in which arbitrary boundary conditions where used:

$$\begin{aligned}
\beta &= \beta^0 \frac{\langle I_1 \rangle}{\langle I_1^0 \rangle} && (8.39)\\
\alpha &= \alpha^0 && (8.40)
\end{aligned}$$

7. The probability of failure initiation due to transverse cracks in the matrix is given by the expression:

$$P[\sqrt{(U_V)} > \sqrt{(U_V^{crit})}] = e^{-\left(\frac{\sqrt{U_V^{crit}}}{\beta}\right)^{\alpha}} \tag{8.41}$$

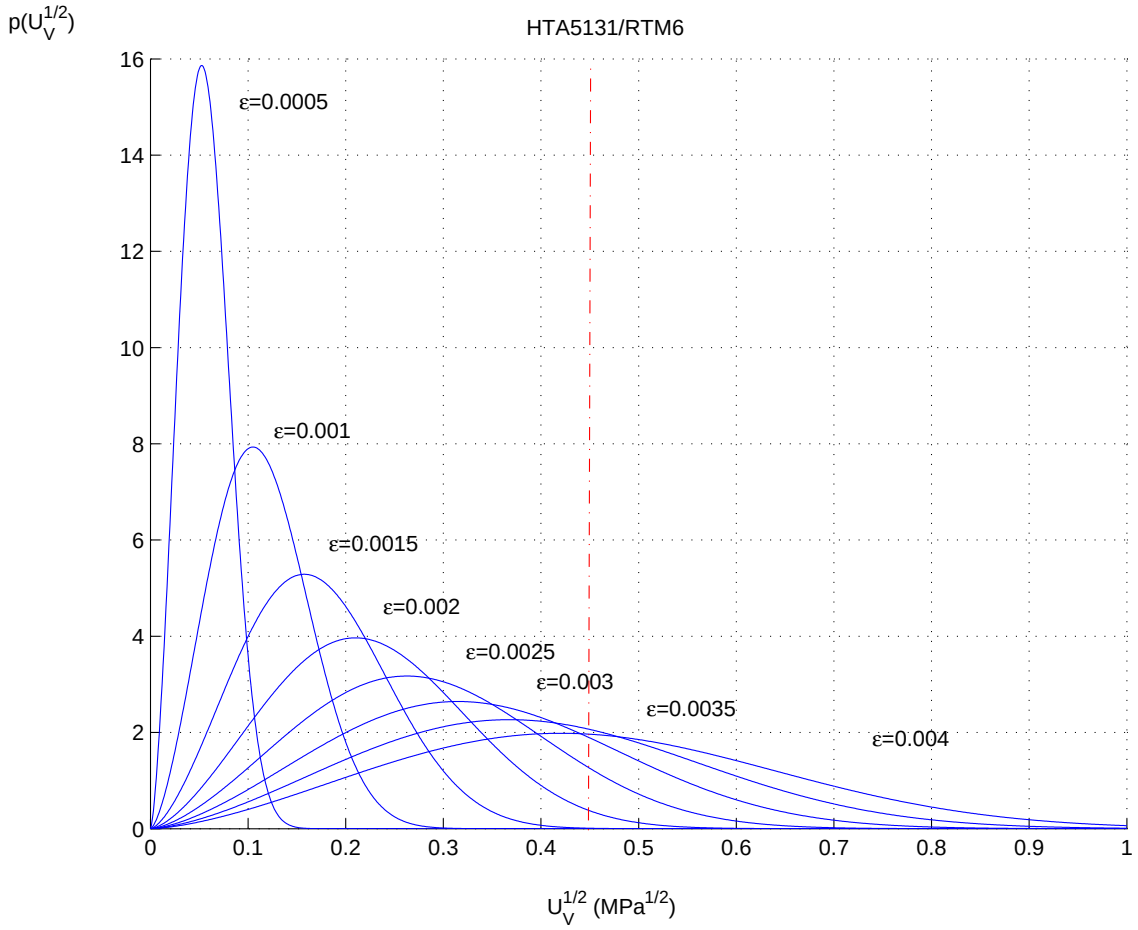

Figure 8.11: Probability of failure initiation for a constant strain for HTA5131/RTM6

Figures 8.11, 8.12 and 8.13 show plots for the Weibull functions obtained for three different materials: HTA5131/RTM6, HTA5131/977-2 and HTA5131/6376, respectively. In each plot a vertical dashed line shows the critical value for U_V (obtained from Asp et al. [13]). Results show how for HTA5131/RTM6 the probability of initiation of failure is nearly null for $\varepsilon \leq 0.002$. For $\varepsilon = 0.0025$ the probability of initiation of failure is small, and this probability grows for greater values of ε. For HTA5131/977-2 the probability of initiation of failure can be considered null for $\varepsilon \leq 0.003$. For $\varepsilon = 0.004$ first cracks are possible with very small probability and this probability grows. The same description is usable for HTA5131/6376.

The values of the failure initiation at each strain increment are given in Table 8.8 where the value of $P[sqrt(U_V) > \sqrt(U_V^{crit})]$ has been computed for each material, using Equation 8.41. These values are plot in Figure 8.14. This Figure could be used to define maximum design strains. For example, if the maximum probability of initiation of matrix failure is required to be lower than 0.0001, for HTA5131/RTM6 the maximum design strain

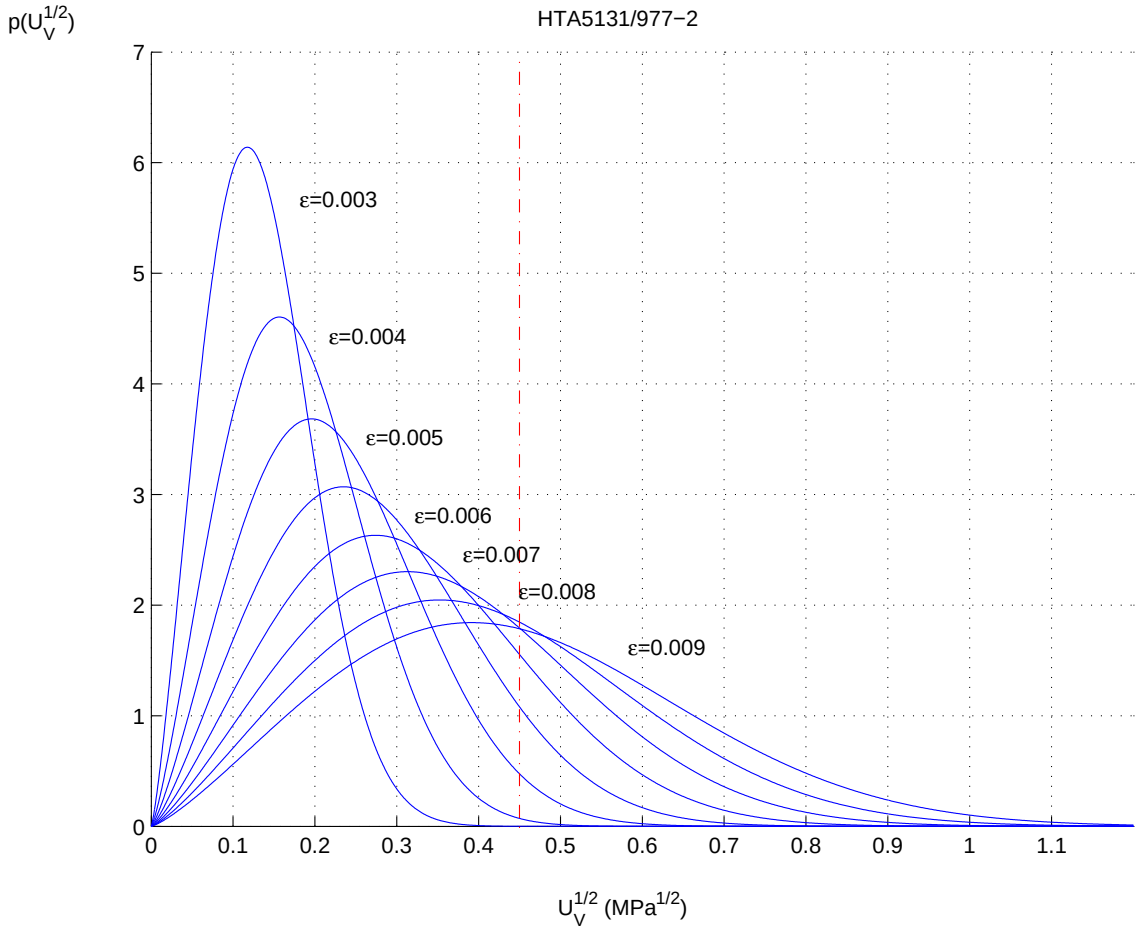

Figure 8.12: Probability of failure initiation for a constant strain for HTA5131/977-2

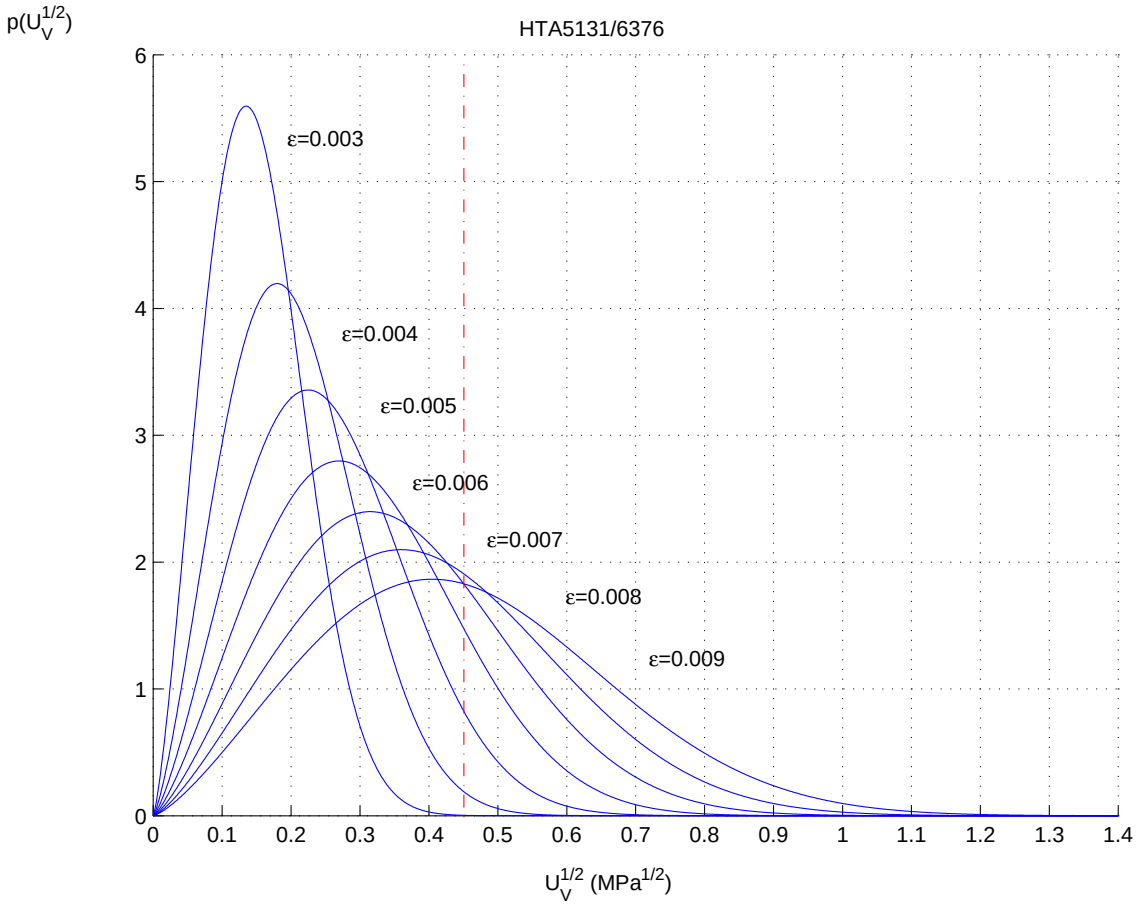

Figure 8.13: Probability of failure initiation for a constant strain for HTA5131/6376

ε_{22}	HTA5131/RTM6	HTA5131/977-2	HTA5131/6376
5.00E-04	1.00E-25	-	-
1.00E-03	6.99E-11	-	-
1.50E-03	2.24E-04	-	-
2.00E-03	1.71E-02	-	-
2.50E-03	9.87E-02	-	-
3.00E-03	2.32E-01	1.09E-05	8.07E-05
3.50E-03	3.71E-01	-	-
4.00E-03	4.93E-01	2.56E-03	8.15E-03
5.00E-03	-	2.72E-02	5.75E-02
6.00E-03	-	9.19E-02	1.55E-01
7.00E-03	-	1.85E-01	2.72E-01
8.00E-03	-	2.88E-01	3.86E-01
9.00E-03	-	3.85E-01	4.86E-01
1.00E-02	-	4.71E-01	5.68E-01

Table 8.8: Probability of failure initiation

Material	$\mu(\varepsilon^u)$	$\sigma(\varepsilon^u)$
HTA5131/RTM6	0.0034	0.0063
HTA5131/977-2	0.0112	0.0099
HTA5131/6376	0.0081	0.0009

Table 8.9: Failure data for three different CFRPs

would be set at 0.0015, for HTA5131/977-2 set at 0.0030 and for HTA5131/6376 at 0.0034.

Figures 8.15, 8.16 and 8.17 show stress-strain curves for the three analyzed materials. Although TUHH performed 7 tests this curves show only the result for a single test. The mean results for these tests are given in Table 8.9.

Figures 8.15, 8.16 and 8.17 also show in an upper horizontal axis the corresponding values of $p[U_V > U_V^{crit}]$ for some values of the strain in the composite ε_{22}. The value of the ultimate strain obtained by TUHH (the mean of the seven tests) is also plotted in these figures by means of a red line. These experimental values are given in Table 8.9. Finally, an extrapolation of the perfect elastic linear behavior of each material is plotted in each figure in a dashed line. This extrapolation is computed using Young's Modulus (E_{22}) obtained by TUHH.

The curve for HTA5131/RTM6 shows a typical brittle fracture. No significant loss of stiffness is shown by the material. Fracture happens a little before $p[U_V > U_V^{crit}]$ reaches the value of 0.37.

The curve for HTA5131/977-2 shows clearly loss of stiffness. The behavior of the material is then far from being linear and the two-scale method employed and, consequently, the results from the simulation will not bes accurate.

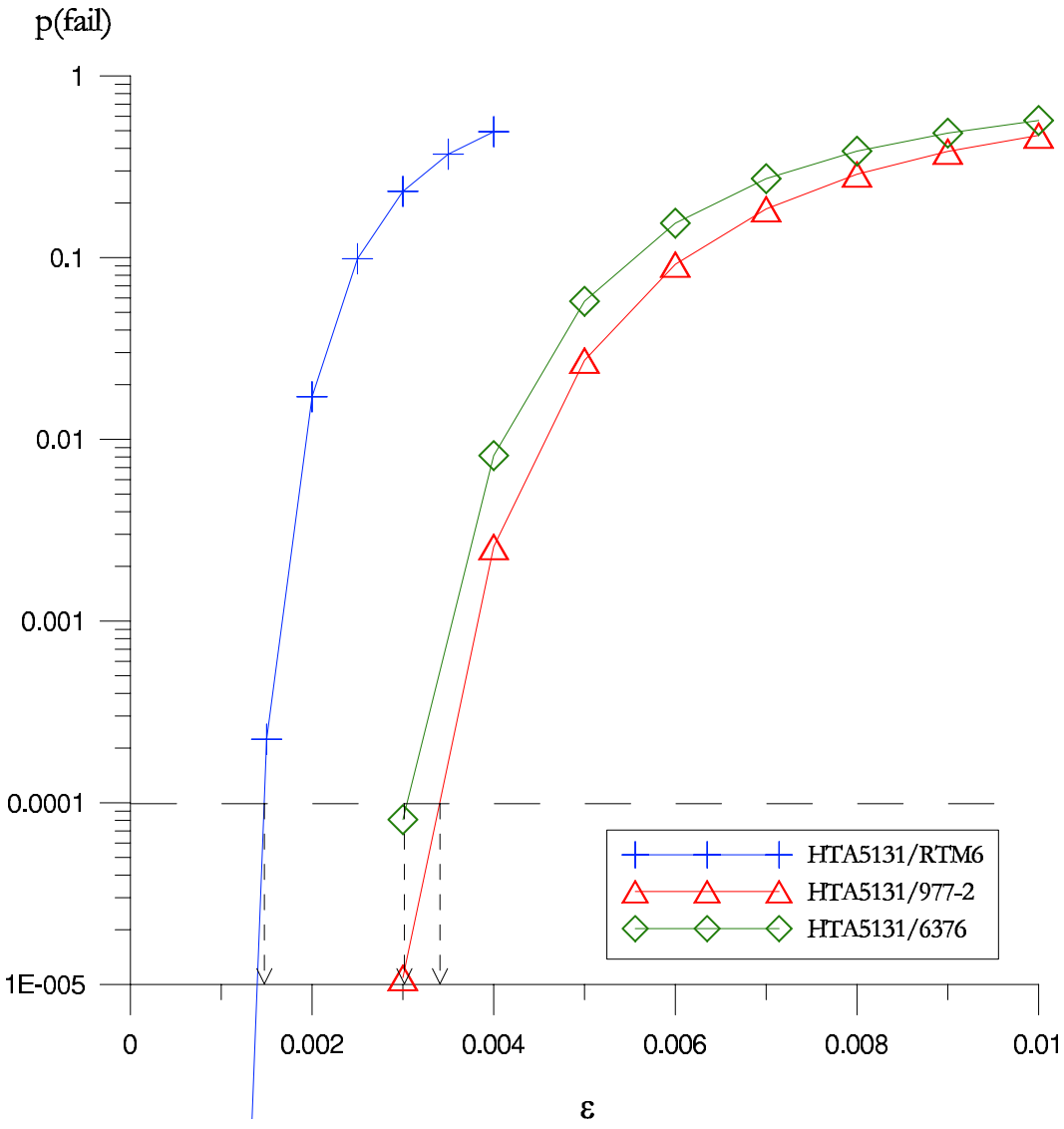

Figure 8.14: Probability of failure initiation

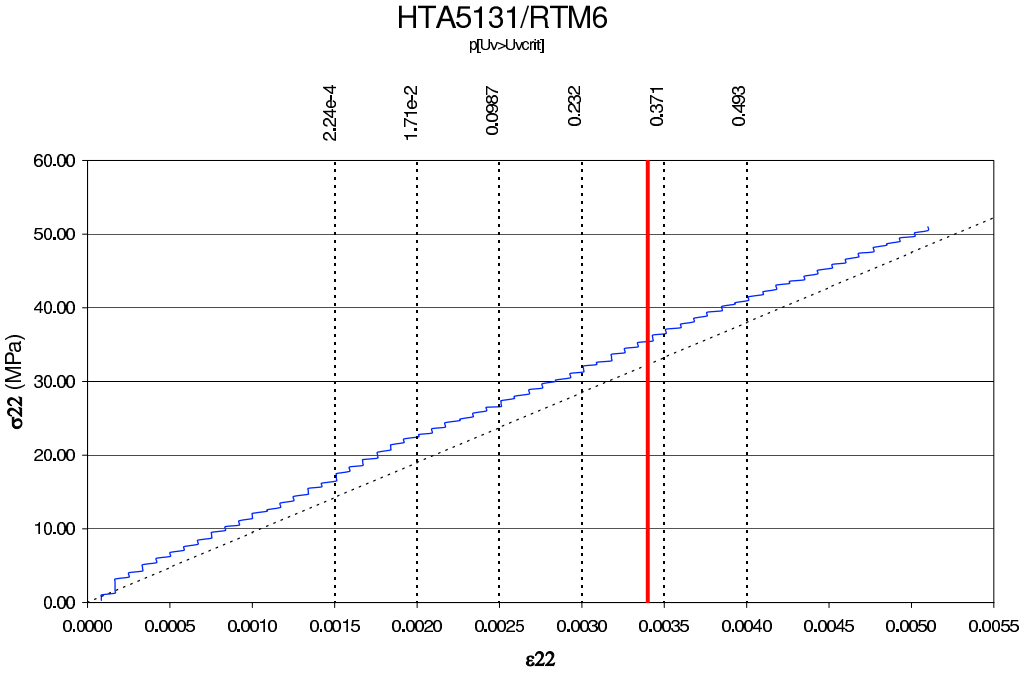

Figure 8.15: $\sigma - \varepsilon$ traction curve for HTA5131/RTM6

Finally, the curve for HTA5131/6376 shows a nearly brittle behavior, since the material fractures before experimenting a small loss of stiffness. The mean ultimate strain obtained by TUHH nearly coincides with a $p\left[U_V > U_V^{crit}\right] = 0.386$.

8.5.4 Simulation of the failure initiation

The obtained data from microstructure simulation can also be used to estimate the failure initiation by using the algorithm shown in Figure 8.18, and described below. Instead of obtaining curves for a single value of the macroscopical strain, as was done in the former section, now a distribution function for the probability of fracture in function of the macroscopical strain will be obtained. To do this a random position in the microstructure will be drawn and the macroscopical strain which causes crack initiation at this point will be found iteratively.

As a very first rough approximation it may be assumed that transverse fracture of CFRPs is brittle. Therefore, it can be considered to happen suddenly after first cracks appear.

1. Stored data $(\langle\varepsilon_{ij}^0\rangle, \alpha, \beta^0)$ from the microstructure simulation is read.
2. Start a loop for the number of simulations (Nsim).
3. Draw p from a uniform distribution between 0 and 1. This value will identify a point in the matrix of the microstructure until the critical value of the macroscopical composite strain which causes crack initiation at this point is obtained.

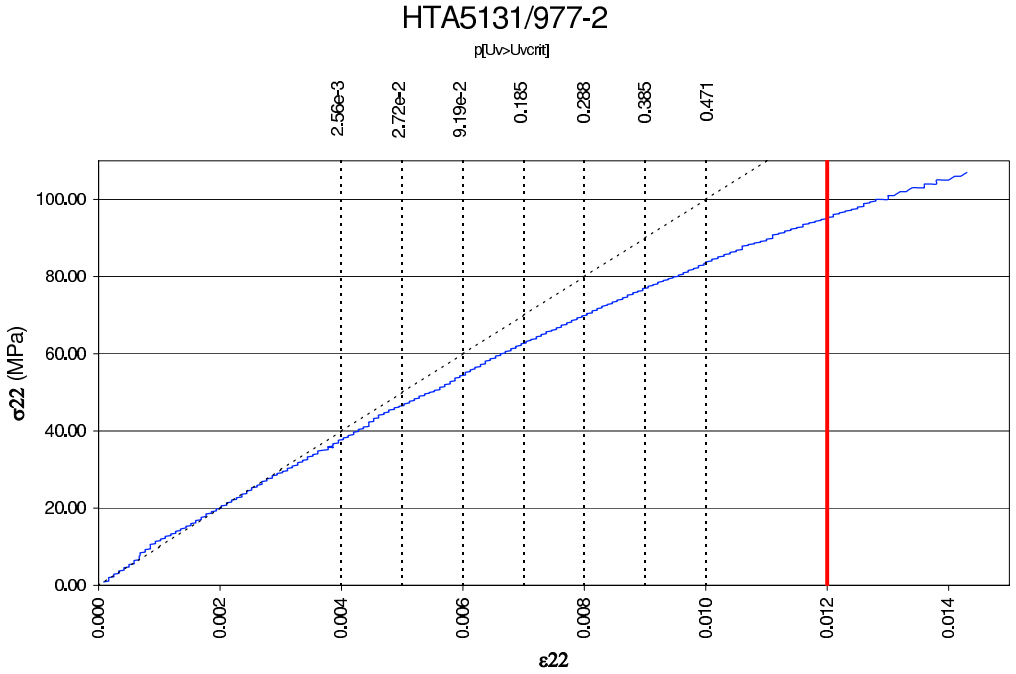

Figure 8.16: $\sigma - \varepsilon$ traction curve HTA5131/977-2

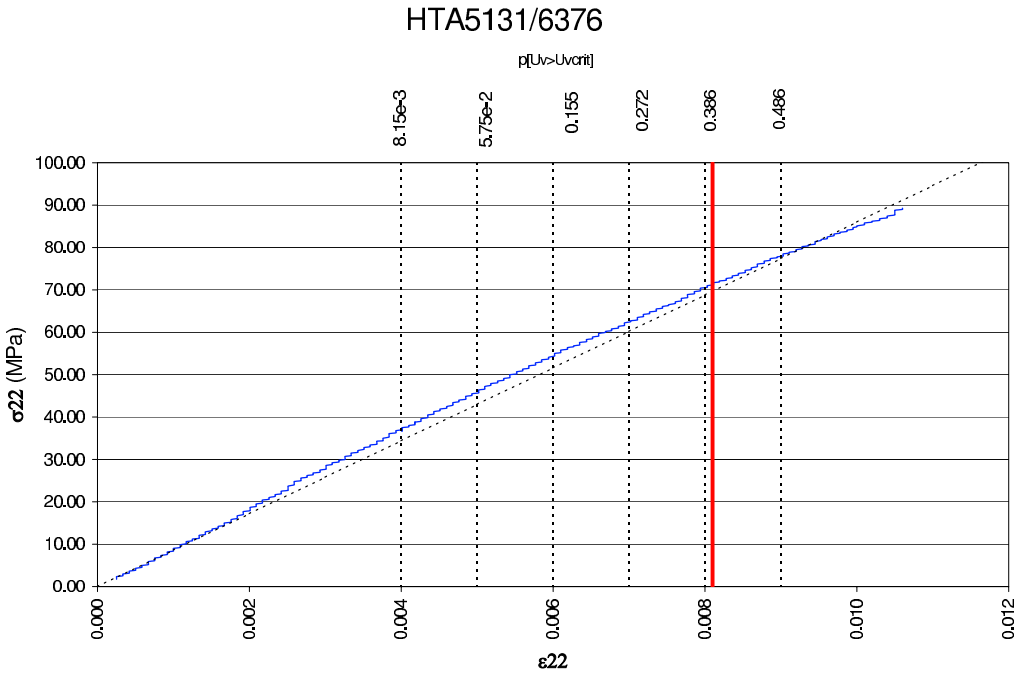

Figure 8.17: $\sigma - \varepsilon$ traction curve HTA5131/6376

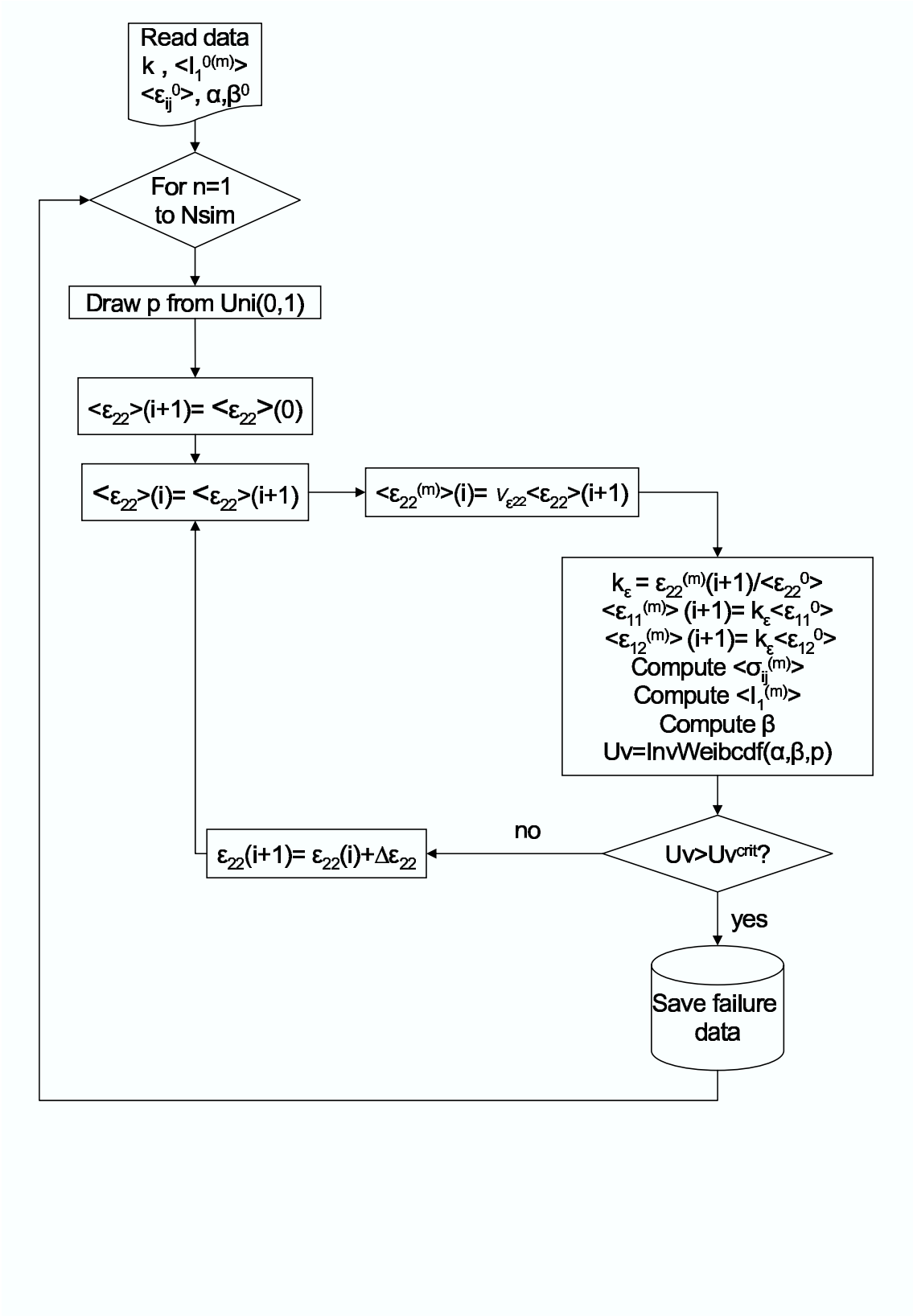

Figure 8.18: Simulation of the macroscopical strain which causes failure initiation

Material	$\hat{\mu}(\varepsilon^u)$	$\mu(\varepsilon^u)$	$\hat{\sigma}(\varepsilon^u)$	$\sigma(\varepsilon^u)$	$\hat{\rho}$	ρ
HTA5131/RTM6	0.0038	0.0034	0.0050	0.0063	1.31	1.85
HTA5131/977-2	0.0072	0.0112	0.0075	0.0099	1.04	0.88
HTA5131/6376	0.0060	0.0081	0.0030	0.0009	0.50	0.11

Table 8.10: Simulation results and failure data for three different CFRPs. the hat over the estimator denotes values from the computer simulations. Estimators without the hat obtained from tests by TUHH

4. Impose an initial value of macroscopical deformation

5. The mean strain in the matrix ($\langle\varepsilon_{22}^{(m)}\rangle$) can be obtained through the macroscopical strain ($\langle\varepsilon_{22}\rangle$) and the factor $\kappa^{(m)}$, obtained from the results of microstructure simulation.

6. By using equations 8.34 the mean stresses in the matrix ($\langle\sigma_{ij}\rangle$) can be computed. From them, the mean first invariant of the stress tensor in the matrix ($I_1^{(m)}$) can also be computed. Then, by applying relations 8.39, the parameters of the Weibull distribution of the dilatational energy density (U_V) can be obtained.

7. Obtain a realization of U_V through the inverse Weibull cumulative density function with parameters α, β. The value p will be used.

8. If $U_V > U_V^{crit}$ a crack will appear in the matrix, at the point represented by p. The value of $\langle\varepsilon_{22}\rangle$ is stored and another point of the microstructure is randomly chosen by drawing a new value of p. If U_V does not reach the critical value U_V^{crit}, $\langle\varepsilon_{22}\rangle$ is incremented.

Figure 8.19 plots the cumulative density function and Table 8.10 shows the main statistics of the results of the simulation for the three analyzed materials with values $U_V^{crit} = 0.055$ and Nsim= 10000. These values are the statistics of the macroscopical strain ε_{22} at which crack initiation takes place. This table also shows the results from seven experimental tests run for each of this three materials by the composites group of Technische Universität Hamburg-Harburg (TUHH). Results from the computer simulation are given in this Table with the symbol ($\hat{}$). Good agreement between experimental and simulation data is obtained, for both mean (μ) results and standard deviations (σ). This agreement could be improved if the number of experimental tests were increased.

8.6 Relation between fibre distribution and failure results

The failure results of the three analyzed materials can be compared with the results of the digital image analysis of Chapter 6. Table 8.11 recalls the statistics obtained for the local volume fraction (v_f) and the number of fibres (n_f) for each material.

The coefficient of variation $\rho = \sigma/\mu$ is useful to compare the variances of populations with different means, for this reason it is given also in Table 8.11. At first sight, it seems to be a clear relation between the variance of v_f and n_f and the variance of the experimental strain to failure, given in Table 8.10: a large variance in the volume fraction seems to cause

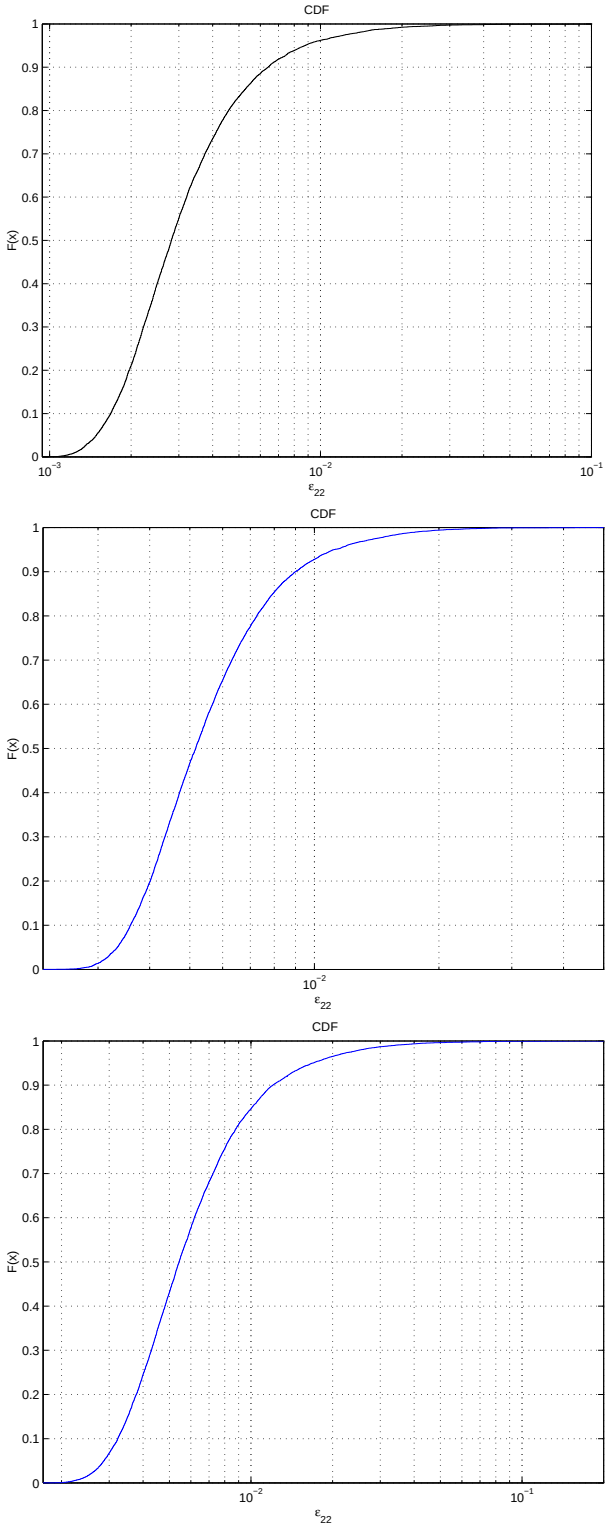

Figure 8.19: CDF of the results of the simulation for HTA5131/RTM6 (up), HTA5131/977-2 (middle) and HTA5131/6376 (bottom)

statistic / material	HTA 5131/RTM-6	HTA 5131/977-2	HTA 5131/6376
$\mu(v_f)$	0.5455	0.5410	0.5761
$\sigma^2(v_f)$	0.2069	0.2105	0.0440
$\rho(v_f)$	0.8338	0.8480	0.3643
$\mu(n_f)$	554.450	549.725	585.450
$\sigma^2(n_f)$	2146.766	2175.845	458.715
$\rho(n_f)$	0.0835	0.0848	0.0365

Table 8.11: Summary of statistics for three CFRPs microanalysis

a large variance in the ultimate strain. This happens for materials HTA 5131/RTM-6 and HTA 5131/977-2. Analogously a small variance of the volume fraction seems to cause a small variance of the ultimate strain, as happens for HTA 5131/6376. Both experimental and simulation results agree with this qualitative conclusion. However, only an Analysis Of VAriance (ANOVA) [27] could confirm this quantitatively.

On the other hand, Figure 8.20 recalls the results from Chapter 6 which revealed that out of the three analyzed materials, only HTA 5131/6376 can be considered to have a complete random distribution of the fibre (CSR).

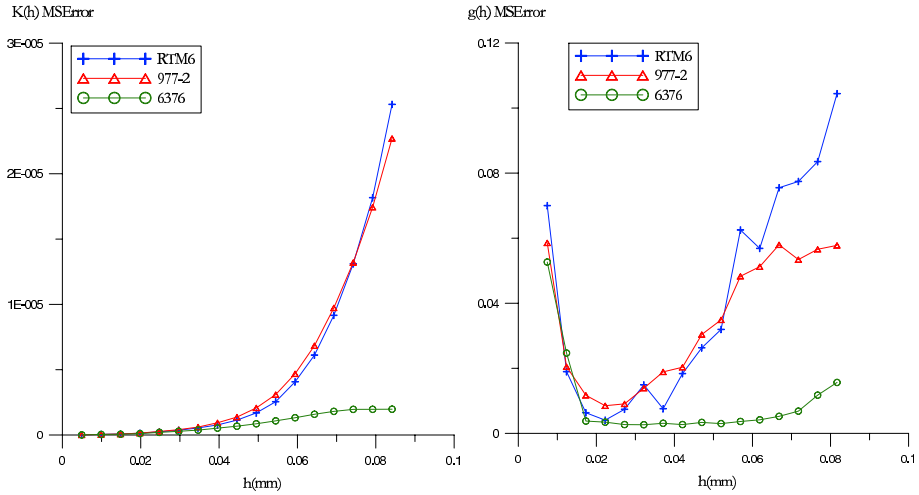

Figure 8.20: Mean squared difference from a CSR pattern

This result also points out that a CSR distribution of the fibre, that is, a random homogeneous *regular* distribution of the fibre within the matrix seems to give a smaller variance of the failure strain.

8.7 Summary and conclusions

Two methods for microstructure pattern simulation have been described. Out of this two methods, *exact microstructure reproduction* has been considered to be useful for the purposes of this work, since it ensures a better pattern reproduction and its computational

cost is lower.

This methodology has been used for the simulation of three different CFRPs laminates. 40 images of each have been converted into FE models and solved for arbitrary value of the boundary conditions. The obtained results could be used for any value of boundary conditions and within a macroscale problem by employing the proposed expressions.

Some applications are also proposed. One of them, the simulation of the probability of failure shows good agreement with experimental data.

Two remarkable facts are observed from the results:

- In the case of brittle fracture, material breaks approximately for $p[U_V > U_V^{crit}]$ between 0.37 and 0.39.
- There is some correlation between the fibre distribution and the variance of the failure strain. When the fibre pattern can be considered CSR the variance of the failure is smaller than for a composite which fibre distribution departs from a CSR pattern.

However, both facts should be verified and quantified with more experimental tests.

Chapter 9

Conclusions

9.1 Summary and conclusions

1. The State-of-the-Art of modelling and simulation of transverse random composites has been reviewed. It has been pointed out that the definition of a finite sized Representative Volume Element, which can be used for the numerical simulation of transverse random composites, is not clear. The different analysis published up to now have considered different criteria which lead to different conclusions. These conclusions cannot be compared since were based on different criteria and different methods and materials were used for its analysis.

2. A review on the available failure criteria for the matrix have been reviewed. From these, the dilatational energy density criteria has been chosen, since it is capable to predict the brittle failure of composites loaded transversely.

3. A numerical scale-dependent analysis has been performed for the determination of the finite size of a Representative Volume Element which can be used for the simulation of transverse random composites. This volume element is expected to have the same mechanical and statistical properties than the bulk material. The following criteria have been taken into account:

   (a) Fibre content
   (b) Effective properties
   (c) Hill Condition
   (d) Stress and strain fields
   (e) Probability density functions of the stress and strain in the matrix
   (f) Distance distributions: $K(h)$, $g(h)$, $n^1(h)$, $n^2(h)$ and $n^3(h)$.

   Since both statistical and mechanical criteria have been considered a Statistical Representative Volume Element has been achieved. The result of this analysis is that a usable SRVE for the analysis of transverse random CFRPs must have a size $\delta = L/r \geq 50$ where L is the length of the size of the SRVE and r the fibre radius. For the correct application of this SRVE, the Embedded Cell Approach has to be

used. This size of the SRVE can also be applied for composite materials with similar contrast to the analyzed material (for which $E^{(f)}/E^{(f)} = 5.75$).

4. The same linear elastic analysis for the transverse plane of a CFRP has been performed using a periodic model and using a random model. Results show how the models are equivalent in mean values but the random models gives much more information about extreme values of stress and strain fields, which are very relevant in terms of the occurrence of damage. The most significant conclusions obtained from this analysis can be summarized as:

   - The value of the maximum strain is 36% in the random model than in the periodic
   - The value of maximum principal stress in the random model may be 60% higher than in the periodic model.
   - In spite of the differences observed between the models, the stress state in the matrix of the random model can still be considered a hydrostatic stress state.

5. The distance functions ($K(h)$, $g(h)$ and nearest neighbor functions) have been used for the analysis of transverse sections of different CFRPs. These functions may be useful for distinguishing materials from different sources. The distribution of the fibre in four different materials has been analyzed. This analysis reveals that from these four materials only one can be considered to have a complete spatial random distribution of the fibres.

6. It has been considered that, nowadays, microstructure reproduction, that is, the conversion of digital images into finite element (or any other computational method) models seems to be a more appropriate approach than simulation by generation of random positions because:

   (a) The simulation of random patterns of high volume fraction fibre reinforced composites needs specific algorithms based upon heuristic approaches and the theory of random close packing. This algorithms can only reproduce complete spatial randomness (CSR) patterns.

   (b) With the algorithms developed so far, a better representativeness of the real material can be achieved than with statistical models which are only capable of reproducing a given $g(h)$. This function, as observed in real composites, may present some dispersion.

7. A two-scale method for the probabilistic analysis of transverse random composites has been proposed. This method is useful for the determination of design ultimate strain which avoid failure initiation. Several applications and capacities of the method have been exposed:

   - If a maximum stress or maximum strain criteria is employed, the proposed method allows the definition of maximum macroscopical stress and strains in function of an imposed probability of failure initiation.

- Obtention of distribution functions of the dilatational energy density, which allow to define allowable macroscopical strain for a critical value of the dilatational energy density.
- Obtention of distribution functions which relate the macroscopical strain with the probability of fracture (understood as crack initiation).

Comparison with experimental data shows that the method is capable to prevent failure initiation but for a full verification of the computed probabilities a statistically significant number of tests should be performed. More precisely, the comparison of the results of the simulation with experimental values reveals that fracture happens for a value of $p[U_V > U_V^{crit}] = 0.37$ - 0.39.

8. Observing both digital image analysis and simulation results, it seems to be a relation between the distribution of the fibre in the composite and the statistics of failure strain: when the distribution of the fibre departs from a CSR pattern, the variance of the failure strain seems to be larger that when the fibre distribution can be considered to be a CSR distribution.

9.2 Future directions

This is an starter work on this field and, consequently, opens a wide range of future directions. Some of them are aspects which remain unsolved after this work and some are new achievements which could be reached by following some of the techniques described in this work. To mention some of them:

1. The CFRPs analyzed show some variation in the diameter. This may affect the results of the simulation somehow. For a better precision of the methodology, the variation of the diameter should be taken into account. The lognormal distribution is usually employed for the modelling of radius of particles [72]:

$$f(r) = \frac{1}{\sqrt{2\pi}\sigma r} e^{-(\ln r - \ln r_0)^2/2\sigma^2} \tag{9.1}$$

where $\ln r_0$ and σ are the mean and the standard deviation of $\ln r$. In CFRP this change could lead to a better knowledge and the description of the micromechanics but results are not expected to vary considerably.

2. The effect of missalligned fibres could be a focus of stress and strain concentration and consequently, a cause of damage. The SRVE could be used for the simulation of layers with orientations different to 90^o. In this case the fibres would appear as ellipses in a transverse section. The image acquisition techniques and software described in Chapter 6 could be easily modified to consider ellipses instead of circles and compute the orientation of each fiber.

3. Three dimensional techniques for the observation of microstructures have already been used for the acquisition of material data [146]. The use of Scanning Acoustic Microscopy (SAM) and Scanning Electron Microscopy (SEM) may improve the

knowledge of the micromechanics and could be used to verify micromodels. The use of embedded optical fiber sensors [145] could also be useful for this purpose.

4. Some researchers deal with matrix cracking as a phenomenon which initiates and is close related to damage evolution [97, 73], fatigue [35] and delamination [113]. Consequently, the SRVE could be used in a statistical modelling approach for obtaining probabilistic results for progressive damage, delamination and fatigue.

5. The composite model which has been used can be improved by taking into account the existence of an interface between fibre and matrix, the strength or the possible defects in this interface [85] and the presence of voids. For this latter option the use of the techniques for the analysis of compositional data [7] may be useful.

6. Although the fracture of CFRPs in the transverse direction is usually elastic, non-linear behavior can take place when layers in different directions are stacked. This random non-linear behavior could be simulated using the same SRVE size. Some further developments in the micro-macro relations should be found.

Part III

Appendixes

Appendix A

Elasticity

A.1 Tensor and index notation

In this section the basics of indicial notation, which is usually employed in the Mechanics y of Continuum are summarized. Further description can be found in the classic text books such as those by Chou and Pagano [37] or by Malvern [101].

Probably, *indicial* notation appears like a way of expressing equations which differ only in subscripts referring to space coordinates in a compact form. For this reason the usual spatial coordinate symbols x, y, z are replaced in indicial notation by x_1, x_2, x_3.

The basic rules of indicial notation are the following:

- Vectors (or first-order tensors) are expressed as a term with and only subscript, such as v_i. Second-order tensors are written as a term with two subscripts (like the strain tensor ε_{ij}) and three-order tensors with three subscripts (such as the elastic tensor C_{ijk}).

- An equation expressed in indicial notation represents usually three or more equations in unabridged notation.

- A subscript which appears repeated in a monomial[1] is called *dummy* index and a non-repeated subscript *free* index.

- A *dummy* index must be understood like a summation over that index where the dummy index takes the values assigned to each spatial coordinate $1, 2, 3$. For instance, the scalar product of two vectors u_i and v_i is expressed in indicial notation as:

$$u_i v_i \equiv \mathbf{u} \cdot \mathbf{v}$$

- A *free* index must be understood as a repetition of the equation for each spatial coordinate. For instance, using the repetition over the dummy index, the next equation:

[1] A monomial is defined in Chou and Pagano [37] as a term in an equation written in indicial notation

$$\frac{\partial \sigma_{ij}}{\partial x_i} = 0$$

expresses, actually the three following equations in unabridged notation:

$$\begin{aligned}
\frac{\partial \sigma_{11}}{\partial x_1} + \frac{\partial \sigma_{21}}{\partial x_2} + \frac{\partial \sigma_{31}}{\partial x_3} = 0 \\
\frac{\partial \sigma_{12}}{\partial x_1} + \frac{\partial \sigma_{22}}{\partial x_2} + \frac{\partial \sigma_{32}}{\partial x_3} = 0 \\
\frac{\partial \sigma_{13}}{\partial x_1} + \frac{\partial \sigma_{23}}{\partial x_2} + \frac{\partial \sigma_{33}}{\partial x_3} = 0
\end{aligned}$$

- In a correctly written equation, a subscript may appear not more than twice in each monomial
- If a subscript appears only once in a monomial, it must appear just once in each other monomial

A.2 The stress tensor

The subscripts of the stress tensor σ_{ij} have to be understood as follows: the first subscript i stands for the plane on which the component acts (defined by its normal vector x_i) and the second subscript indicates the direction of the component (given by x_j). The components of the stress tensor with $i = j$ are called the *normal stresses*, because they act in a perpendicular direction to a surface and the components with $i \neq j$ are called *shear stresses*, since they act in a parallel direction to a surface.

A.2.1 Principal stresses

The planes on which the shear stress vanishes are called the principal planes and the normal stresses on this planes are called the principal stresses. They can be computed easily by writing the characteristic equation of the stress tensor and finding the principal planes. The method can be found in many textbooks such as Chou and Pagano [37] and, basically, reduces to find the eigenvalues of the stress tensor ($\boldsymbol{\sigma}$):

$$|\boldsymbol{\sigma} - \boldsymbol{\lambda}\mathbf{1}| = 0 \tag{A.1}$$

Since $\boldsymbol{\sigma}$ is symmetric, the three possible solutions are real. Once ordered following the convention ($\lambda_1 \equiv \sigma_1, \lambda_2 \equiv \sigma_2, \lambda_3 \equiv \sigma_3$) the eigenvector $\mathbf{v}^(i)$ for each stress σ_i can be found by solving the equation system:

$$[\boldsymbol{\sigma} - \sigma_i \mathbf{1}] \cdot \mathbf{v}^{(i)} = \mathbf{0} \qquad i \in \{1, 2, 3\} \tag{A.2}$$

which produces three orthogonal eigenvectors $\mathbf{v}^{(i)}$ which once normalized define the coordinate system corresponding to the principal directions. The stress state in which

$$\sigma_1 = \sigma_2 = \sigma_3 \tag{A.3}$$

is usually called hydrostatic stress state.

A.2.2 Spherical and deviatoric stresses

The stress tensor can be decomposed as the addition of an spherical part ($\boldsymbol{\sigma}_{esf}$) and a deviatoric part ($\boldsymbol{\sigma}'$):

$$\begin{aligned} \boldsymbol{\sigma} &= \boldsymbol{\sigma}_{esf} + \boldsymbol{\sigma}' && \text{(A.4)} \\ \boldsymbol{\sigma}_{esf} &:= \frac{1}{3}\sigma_{ii}\delta_{ij} && \text{(A.5)} \\ \boldsymbol{\sigma}' &= \boldsymbol{\sigma} - \boldsymbol{\sigma}_{esf} && \text{(A.6)} \\ & && \text{(A.7)} \end{aligned}$$

$\boldsymbol{\sigma}'$ may be seen as a measure of how the stress state differs from a hydrostatic stress state.

A.2.3 Invariants of the stress tensor

Some quantities derived from the stress tensor are of special interest because they remain *invariant* with respect to orthogonal rotations. The invariants of the stress tensor are the following:

$$\begin{aligned} I_1 &= \sigma_i && \text{(A.8)} \\ I_2 &= \frac{1}{2}\left(\boldsymbol{\sigma} : \boldsymbol{\sigma} - I_1^2\right) = -(\sigma_1\sigma_2 + \sigma_1\sigma_3 + \sigma_2\sigma_3) && \text{(A.9)} \\ I_3 &= det(\boldsymbol{\sigma}) && \text{(A.10)} \\ & && \text{(A.11)} \end{aligned}$$

And those of the deviatoric stress are:

$$\begin{aligned} J_1 &= I_2 && \text{(A.12)} \\ J_2 &= \frac{1}{2}\sigma'_{ij}\sigma'_{ji} = \frac{1}{2}(I_1^2 + 2I_2) && \text{(A.13)} \\ J_3 &= \frac{1}{3}\sigma'_{ij}\sigma'_{jk}\sigma'_{ki} = \frac{1}{3}\left(I_1^3 + 3I_1I_2 + 3I_3\right) && \text{(A.14)} \\ & && \text{(A.15)} \end{aligned}$$

Using some invariants, the eigenvalues λ_i of equation A.1 can be found by solving the following characteristic equation:

$$\lambda^3 - I_1\lambda^2 - I_2\lambda - I_3 = 0 \qquad \text{(A.16)}$$

The effective stress or equivalent uniaxial stress is defined as:

$$\bar{\sigma} := \sqrt{3J_2} = \sqrt{\frac{3}{2}\boldsymbol{\sigma}' : \boldsymbol{\sigma}'} \qquad \text{(A.17)}$$

A.3 Static elasticity problem

Let us consider an homogeneous solid located in the region Ω. The local static equilibrium equation for this solid is:

$$\frac{\partial \sigma_{ij}}{\partial x_i} + \rho b_i = 0 \tag{A.18}$$

where b_i is a vector of body forces (such as magnetic forces or gravity) which in the present work will not be considered. So, the static equilibrium equation which will be considered is:

$$\frac{\partial \sigma_{ij}}{\partial x_i} = 0 \tag{A.19}$$

σ_{ij} is the stress tensor, which can be related through a fourth-order tensor with the strain[2]:

$$\boldsymbol{\sigma} = \mathbf{C} : \boldsymbol{\varepsilon} \qquad \text{or, in indicial notation,} \qquad \sigma_{ij} = C_{ijkl} \cdot \varepsilon_{kl} \tag{A.20}$$

Where $\boldsymbol{\varepsilon}$ is the strain tensor defined as:

$$\varepsilon_{ij} = \frac{1}{2}\left(\frac{\partial u_i}{\partial x_j} + \frac{\partial u_j}{\partial x_i}\right) \tag{A.21}$$

In some part of the boundary of Ω some forces and displacements are applied. This boundary conditions are briefly described in the next section.

A.3.1 Boundary conditions

Different conditions may be applied to the boundary $\partial\Omega$ of the domain Ω

- Kinematic uniform boundary conditions (Dirichlet boundary conditions): The displacement u is imposed to a subset $\partial\Omega_u$ of the boundary $\partial\Omega$ such that:

$$u = \bar{u} \in \partial\Omega_u \tag{A.22}$$

- (Neumann boundary conditions): A traction force $\bar{t}$ is applied to a subset $\partial\Omega_t$ of the boundary $\partial\Omega$ such that:

$$\sigma_{ij} \cdot n_i = \bar{t} \in \partial\Omega_f \tag{A.23}$$

  where n_i is the normal vector to the boundary $\partial\Omega_t$

These are the classic boundary conditions of the mechanics of the continuum which are normally treated in the classic texts [101], but in addition to these boundary conditions the hypothesi of periodicity which is required in some approaches such as homogenization leads to the definition of:

[2]The operator : expresses the inner product of two tensors and is implicitly defined in this equation.

- Periodic boundary conditions: the considered dominium is a periodic cell whose geometry is repeated all along the problem dominium, and so do the boundary conditions.

A.4 Lamé constants

In the case of isotropy the stress-strain relations can be written as [37]:

$$\sigma_{ij} = \lambda \varepsilon_{kk} \delta_{ij} + 2\mu \varepsilon_{ij} \tag{A.24}$$

where λ and μ are the Lamé elastic constants and δ_{ij} is the Kronecker's delta. The stress-strain relation can be expressed in the following compact form:

$$\sigma_{kk} = 3k\varepsilon_{kk} \tag{A.25}$$

and

$$s_{ij} = 2\mu e_{ij} \tag{A.26}$$

where s_{ij} and e_{ij} are the deviatoric components of stress and strain, defined as:

$$s_{ij} = \sigma_{ij} - \frac{1}{3}\delta_{ij}\sigma_{kk} \tag{A.27}$$

$$e_{ij} = \varepsilon_{ij} - \frac{1}{3}\delta_{ij}\varepsilon_{kk} \tag{A.28}$$

in these expressions k is the bulk modulus[3] and μ the shear modulus (usually represented by G).

Finally, the bulk and shear modulus can be related with the commonly used Young's modulus (E) and Poisson's ratio (ν) through:

$$\mu = \frac{E}{2(1+\nu)} \tag{A.29}$$

$$\lambda = \frac{\nu E}{(1+\nu)(1-2\nu)} \tag{A.30}$$

$$k = \frac{E}{3(1-2\nu)} \tag{A.31}$$

$$E = \frac{9k\mu}{3k+\mu} \tag{A.32}$$

$$\nu = \frac{3k-2\mu}{2(3k+\mu)} \tag{A.33}$$

[3] From equations A.24 and A.25 it can be seen that $\lambda = 3k$

A.5 Plane strain conditions

In situations where a mechanical component has constant section and infinite length or finite length with fixed ends, the following displacement conditions can be considered:

$$u_2 = u_2(x_2, x_3), \qquad u_3 = u_3(x_2, x_3) \qquad \text{and } u_1 = 0 \tag{A.34}$$

From this conditions, it can be seen that:

$$\varepsilon_{23} = \varepsilon_{31} = 0 \tag{A.35}$$

$$\sigma_{23} = \sigma_{31} = 0 \tag{A.36}$$

And the stress-strain relations can be written:

$$\begin{aligned}
\sigma_{22} &= 2\mu\varepsilon_{22} + \lambda(\varepsilon_{22} + \varepsilon_{33}) && \text{(A.37)}\\
\sigma_{33} &= 2\mu\varepsilon_{33} + \lambda(\varepsilon_{22} + \varepsilon_{33}) && \text{(A.38)}\\
\sigma_{11} &= \lambda(\varepsilon_{22} + \varepsilon_{33}) && \text{(A.39)}\\
\sigma_{12} &= \mu\varepsilon_{12} && \text{(A.40)}\\
& && \text{(A.41)}
\end{aligned}$$

where the following relation may be useful:

These conditions can be used when considering composites in the section which is perpendicular to fibre direction.

A.5.1 Hill's notation

For generalized plain strain conditions, the stress-strain relation can be expressed:

$$\begin{bmatrix} \sigma_{11} \\ \sigma_{22} \\ \sigma_{33} \\ \sigma_{12} \end{bmatrix} = \begin{bmatrix} (k+m) & (k-m) & 0 & 0 \\ (k-m) & (k+m) & 0 & 0 \\ 0 & 0 & n & 0 \\ 0 & 0 & 0 & m \end{bmatrix} \cdot \begin{bmatrix} \varepsilon_{11} \\ \varepsilon_{22} \\ \varepsilon_{33} \\ \varepsilon_{12} \end{bmatrix} \tag{A.42}$$

The constants k, l, m and n are related to the material engineering constants through:

$$\begin{aligned}
k &= \frac{-1}{1/G - 4/E4\nu^2/E} && \text{(A.43)}\\
l &= 2k\nu && \text{(A.44)}\\
m &= G && \text{(A.45)}\\
n &= E + 4k\nu^2 && \text{(A.46)}
\end{aligned}$$

A.6 Transversely isotropic media

An anisotropic material is considered transversely isotropic if it is isotropic in one of its three planes. In a unidirectional long fiber reinforced material the coordinate system is set to have direction x_1 in the fiber direction. Then, plane 23 (that is, the plane which is perpendicular to fiber direction) is isotropic. The constitutive relations for a transverse isotropic material are the following:

$$\begin{bmatrix} \sigma_{11} \\ \sigma_{22} \\ \sigma_{33} \\ \sigma_{12} \\ \sigma_{23} \\ \sigma_{31} \end{bmatrix} = \begin{bmatrix} C_{11} & C_{12} & C_{12} & 0 & 0 & 0 \\ C_{12} & C_{22} & C_{23} & 0 & 0 & 0 \\ C_{12} & C_{22} & C_{23} & 0 & 0 & 0 \\ 0 & 0 & 0 & C_{66} & 0 & 0 \\ 0 & 0 & 0 & 0 & C_{22}-C_{23} & 0 \\ 0 & 0 & 0 & 0 & 0 & C_{66} \end{bmatrix} \cdot \begin{bmatrix} \varepsilon_{11} \\ \varepsilon_{22} \\ \varepsilon_{33} \\ \varepsilon_{12} \\ \varepsilon_{23} \\ \varepsilon_{31} \end{bmatrix} \tag{A.47}$$

With constants:

$$C_{11} = E_{11} + 4\nu_{12}^2 K_{23} \tag{A.48}$$
$$C_{12} = 2K_{23}\nu_{12} \tag{A.49}$$
$$C_{22} = \mu_{23} + K_{23} \tag{A.50}$$
$$C_{23} = -\mu_{23} + K_{23} \tag{A.51}$$
$$C_{66} = \nu_{12} \tag{A.52}$$
$$\tag{A.53}$$

where K_{23} is the plain strain bulk modulus, which under the stress-strain state specified by:

$$\varepsilon_{11} = 0, \qquad \varepsilon_{22} = \varepsilon_{33} = \varepsilon$$

and

$$\sigma_{22} = \sigma_{33} = \sigma$$

can be defined by:

$$\sigma = 2K_{23}\varepsilon \tag{A.54}$$

In such a material only five independent material constants can be defined and the following relations stand:

$$\nu_{12} = -\frac{\varepsilon_{22}}{\varepsilon_{11}} \tag{A.55}$$
$$\nu_{13} = -\frac{\varepsilon_{33}}{\varepsilon_{11}} \tag{A.56}$$
$$\nu_{21} = -\frac{\varepsilon_{11}}{\varepsilon_{22}} \tag{A.57}$$
$$\nu_{23} = -\frac{\varepsilon_{33}}{\varepsilon_{22}} \tag{A.58}$$

$$\nu_{31} = \nu_{21} \tag{A.59}$$

$$\nu_{32} = \nu_{23} \tag{A.60}$$

$$\frac{\nu_{12}}{E_{11}} = \frac{\nu_{21}}{E_{22}} \tag{A.61}$$

The following relations may be useful:

$$E_{22} = \frac{4\mu_{23}K_{23}}{K_{23}+\mu_{23}+4\nu_{12}^2\mu_{23}K_{23}/E_{11}} \tag{A.62}$$

$$\nu_{23} = \frac{K_{23}-\mu_{23}-4\nu_{12}^2\mu_{23}K_{23}/E_{11}}{K_{23}+\mu_{23}+4\nu_{12}^2\mu_{23}K_{23}/E_{11}} \tag{A.63}$$

$$\nu_{21} = \frac{4\nu_{12}^2\mu_{23}K_{23}}{E_{11}(K_{23}+\nu_{23})+4\nu_{12}^2\mu_{23}K_{23}} \tag{A.64}$$

$$\nu_{12}^2 = \left(-\nu_{23}-\frac{1}{4}\frac{E_{22}}{K_{23}}+\frac{1}{4}\frac{E_{22}}{\mu_{23}}\right)\frac{E_{11}}{E_{22}} \tag{A.65}$$

Appendix B

Basic Statistics

B.1 Random variables, distribution functions

A random variable X is a function which is measured in certain sample space S. The probability that certain event A, related to the random variable, happens is denoted by $P[A]$. When working with quantitative real number random variables two different types of them can be discerned: *discrete* random variables and *continuous* random variables.

Discrete random variables

The random variable X is *discrete* if the set of possible values for X is finite. Then

$$P\{X = x_i\} = p_i, \qquad i = 0, 1, \ldots \tag{B.1}$$

The sequence $\{p_i\}$ is called the probability distribution of X and the cumulative probability, defined as:

$$P\{X \leq x_i\} = \sum_{x \leq x_i} p_i = F(x) \qquad -\infty < x < \infty \tag{B.2}$$

is called probability distribution function (PDF) of X.

B.1.1 Continuous random variables

The random variable X is continuous if there exists a non-negative function f, such as, for any $a \leq b$:

$$P[a < X \leq b] = \int_a^b f(x)dx \tag{B.3}$$

The function $f(x)$ is called probability density function or density function, of X . This function has the following property:

$$\int_{-\infty}^{+\infty} f(x)\,\mathrm{d}x = 1 \tag{B.4}$$

The probability distribution function, sometimes called *cumulative density function* of X is:

$$F(x) = P[X \leq a] = \int_{-\infty}^{a} f(x)dx \tag{B.5}$$

Using the former definitions in equations B.4 and B.5 the following expression could be proved :

$$F(x) = P[a < X \leq b] = F(b) - F(a) \tag{B.6}$$

$F(x)$ is monotonically increasing between 0 and 1 whereas the domain of $f(x)$ is $(-\infty$,$+\infty)$.

For continuous random variables, the next equation also stand:

$$f(x) = \frac{dF(x)}{dx} \tag{B.7}$$

B.2 Mathematical expectation

Also called *mean value* or *expected value*, the mathematical expectation ($< \cdot >$ or $E[\cdot]$) is the weighted mean of the possible values of a random variable, using the probability density function as the weight function. For a discrete random variable it can be written:

$$E[X] = \sum_{i=1}^{n} x_i \cdot f(x_i) \tag{B.8}$$

and for a continuous variable:

$$E[X] = \int_{-\infty}^{\infty} x \cdot f(x) \tag{B.9}$$

B.3 Moments, variances and covariances

B.3.1 Statistical Moments

Some expected values of the random variable X are of special interest:

1. The moments $\tau_r = E[X^r] \quad r = 1, 2, ...$
2. The factorial moments $E[X(X-1) \cdot \ldots \cdot (X-r+1)] \quad r = 1, 2, ...$
3. The central moments $E[X - E(X)]^r \quad r = 1, 2, ...$

The first moment, $E[X]$ is called the mean and is usually written as μ_X or $< X >$.

The second central moment is the variance, represented usually by $\mathrm{Var}[X]$ or $\sigma^2[X]$. The variance is a useful measure of the dispersion in a data set. The square root of the variance, $\sigma[X] = \sqrt{\sigma^2[X]}$ is usually called the standard deviation.

A practical measure of the relation between two random variables X and Y is the covariance which is defined as follows:

$$\text{Cov}[X, Y] = E(X \cdot Y) \tag{B.10}$$

The covariance of two variables X and Y is also usually expressed by $\sigma_{X,Y}$.

Like the mean operator, the variance is a linear operator and consequently, the variance of a linear functionof random variables with coefficients c_i can be written:

$$\text{Var}[c_0 + c_1X_1 + \ldots + c_nX_n] = \sum_{i=1}^{n} c_i^2 \cdot \sigma_{X_i}^2 + \underbrace{\sum_{i=1}^{n}\sum_{j=1}^{n} c_i c_j \sigma_{X_i,X_j}}_{i \neq j} \tag{B.11}$$

B.4 Standarized variables and the Correlation Coefficient

The *standarization* of the random variable X is defined as the following transformation:

$$U = \frac{X - E(X)}{\sigma_x} \tag{B.12}$$

where σ_x is the standard deviation. The standarized variable U has null mean and unity standard deviation.

$$E(U) = 0 \qquad \sigma_U = 1 \tag{B.13}$$

Let X and Y be two random variables and U and V their respective standarized variables. The correlation coefficient between X and Y, ρ_{XY}, is defined as the covariance between U and V:

$$\rho_{XY} = \text{Cov}[U, V] = E(UV) = E\left[\frac{X - E(X)}{\sigma_X}\right]\left[\frac{Y - E(Y)}{\sigma_Y}\right] \tag{B.14}$$

or, also:

$$\rho_{XY} = \frac{\text{Cov}[X, Y]}{\sigma_X \sigma_Y} \tag{B.15}$$

When $\rho_{XY} = 0$, it is said that X and Y are independent or uncorrelated variables. The closer to 1 is the value of ρ_{XY} the greater correlation exists between X and Y.

B.4.1 Approximate variance

There is no exact expression for obtaining the variance of a random variable function which is a function of dependent variables. One may use the Taylor series expansion for this purpose,

Let $\phi(X)$ be a random variable function, with variables $X = (x_1, ..., x_n)$. The Taylor series expansion for $\phi(x)$ in the around the expected value $\mu = (\mu_1, ..., \mu_n)$ is:

$$\phi(X) = \phi(\mu) + \sum_{i=1}^{n}(x_i - \mu_i)\phi_i(\mu) \tag{B.16}$$

where $\phi_i = \frac{\partial}{\partial x_i}\phi(x)|_{X=\mu}$.

Applying the property of linearity of the variance operator [115] to B.16, the approximated variance of $\phi(x)$ is obtained:

$$\mathrm{Var}[\phi(x)] = \sum_{i=1}^{n} [\phi_i(\mu)]^2 \, \phi_{x_i}^2 + \underbrace{\sum_{i=1}^{n} \sum_{j=1}^{n}}_{i \neq j} [\phi_i(\mu)] \, [\phi_j(\mu)] \tag{B.17}$$

Some numerical methods [89, 142] use the Taylor series expansion for approximating random fields in which the variables may be correlated.

B.5 Common probability functions

Some of the probability functions which are of interest in engineering mechanics are the Gauss distribution (or Normal distribution) and the Weibull distribution.

The density function of a Normal distribution with mean μ and variance σ^2 is:

$$f(x) = \frac{1}{\sqrt{2\pi} \cdot \sigma} \cdot e^{\frac{-(x-\mu)^2}{2\sigma^2}} \tag{B.18}$$

Generally one tends to work with *standarized* variables, and so to use the *standard* Normal distribution:

$$f(x) = \frac{1}{\sqrt{2\pi}} \cdot e^{-x^2/2} \tag{B.19}$$

The Normal distribution is often used for modelling the elastic properties of materials or thermal expansion coefficients.

From the point of view of mechanic properties of materials, another statistic distribution used frequently is the Weibull function. Since this distribution function is useful in modelling of extreme values it is used mainly for properties related to the mechanic failure of the material, such as the ultimate strength (σ_u) or the yield stress (σ_y). Actually there exist several types of Weibull distributions, depending the number of parameters involved. The most general is the three parameter Weibull, for which:

$$f(x) = \frac{\alpha}{\beta} \left(\frac{x-\gamma}{\beta} \right)^{\alpha-1} e^{-\left(\frac{x-\gamma}{\beta}\right)^{\alpha}} \tag{B.20}$$

$$F(x) = e^{-\left(\frac{x-\gamma}{\beta}\right)^{\alpha}} \tag{B.21}$$

where α is the shape parameter, β the scale parameter, and γ the location parameter. All of them have to be greater than 0. The expression for a two-parameter Weibull distribution can easily obtained by making $\gamma = 0$.

Although Equations B.20 and are quite spread, some modifications are also used. For instance, the Weibull distribution function used in the modelling of ultimate tension of some fibers used in composite materials is [106, 127]:

$$F(\sigma) = 1 - e^{-\beta L \sigma^{\alpha}} \tag{B.22}$$

and its density function:

$$f(\sigma) = L\alpha\beta\sigma^{\alpha-1}e^{-L\beta\sigma^{\alpha}} \tag{B.23}$$

where $\sigma \leq 0$ is the random variable *ultimate strength* of the fiber, $L > 0$ is the fiber length and $\alpha, \beta > 0$ are, respectively, the shape and the scale parameter which have to be experimentally fitted.

B.6 Maximum Likelihood Estimators (MLE)

Let x be a random variable with probability density function:

$$f(x; \theta_1, \theta_2, \ldots, \theta_k) \tag{B.24}$$

where $\theta_1, \theta_2, \ldots, \theta_k$ are a set of constant parameters to be estimated. Let $x_1, x_2, \ldots, x_N$ be a set of N independent experimental results. The likelihood function, L, is defined through the following product:

$$L(x_1, \ldots, x_N|\theta_1, \ldots, \theta_k) = \prod_{i=1}^{N} f(x_i; \theta_1, \theta_2, \ldots, \theta_k) \tag{B.25}$$

The logarithmic likelihood function, Λ, can be written:

$$\Lambda = \ln L(x_1, \ldots, x_N|\theta_1, \ldots, \theta_k) = \sum_{i=1}^{N} \ln f(x_i; \theta_1, \ldots, \theta_k) \tag{B.26}$$

The maximum likelihood estimators (MLE) of the parameters $\theta_1, \ldots, \theta_k$ are obtained by maximizing the function Λ[1]. That is the parameters $\theta_1, \ldots, \theta_k$ are the solution of the set of equations:

$$\frac{\partial \Lambda}{\partial \theta_j} = 0 \qquad j = 1, \ldots, k \tag{B.27}$$

B.7 Hypothesis Testing

A statistical hypothesis is an affirmation or statement on a statistical parameter. The *null hypothesis*, usually noted as H_0, defines the hypotheses which is thought to be true. The alternative hypothesis, which is denoted by H_1, is the statement which is verified if the null hypothesis is not true.

The error of rejecting the null hypotheses when it is true is called the type I error, and the probability of committing it is denoted by α. The value of α is important, since it determines the statistical test, and has to be fixed before analyzing the data. It also exists a so-called *type II error* which is committed when the null hypotheses is not rejected, although it is false. The probability of committing the error of type II is β.

This concepts will be clarified in the following sections where the techniques for testing hypotheses on the mean and the variance of samples are reviewed.

[1] Sometimes the function L is used instead, but *Lambda* is normally easier to work with

Further information can be found in reference books such as those by Montgomery [108], and by Box et al. [27].

B.7.1 Inference about the differences in means

The two populations are assumed to be independent and normally distributed.

$$H_0 : \mu = \mu_0$$
$$H_1 : \mu \neq \mu_0$$

In the case of known variances σ_1^2 and σ_2^2, the statistic Z_0 is used:

$$Z_0 = \frac{\bar{y}_1 - \bar{y}_2}{\sqrt{\frac{\sigma_1^2}{n_1} + \frac{\sigma_2^2}{n_2}}} \tag{B.28}$$

The null hypotheses is rejected if $|Z_0| > Z_{\alpha/2}$

B.7.2 Inference about the variances of normal distributions

In this case, for the comparison of the variances from two different samples the hypothesis can be written:

$$H_0 : \sigma_1^2 = \sigma_2^2$$
$$H_1 : \sigma_1^2 \neq \sigma_2^2$$

The statistic to be used is:

$$F_0 = \frac{S_1^2}{S_2^2} \tag{B.29}$$

where S_1^2 and S_2^2 are the estimators of the variances. The null hypothesis is rejected if $F_0 < F_{1-\alpha/2,n_1-1,n_2-1}$.

B.7.3 χ^2 goodness-of-fit test

This test can be used for testing if a probability distribution function is a good choice for fitting some data, or for checking the assumption of normality of the sample.

$$\chi^2_{N-1} = \sum_{i=1}^{N} \frac{(\hat{P}(x_i) - P(x_i))^2}{P(x_i)} \tag{B.30}$$

where $P(x_i)$ is the cumulative density function which is assumed to be a good fit for the data, $\hat{P}(x_i)$ is the experimental cumulative density function.

Appendix C

Results of microstructure image analysis of composites

C.1 Nearest neighbor distance

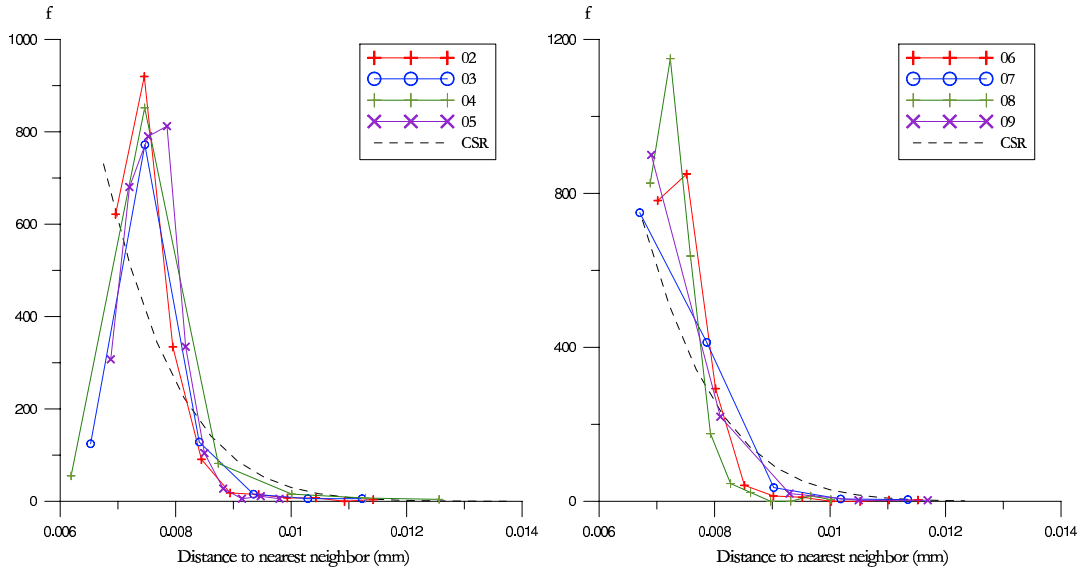

Figure C.1: Nearest neighbor distance RTM6 (I)

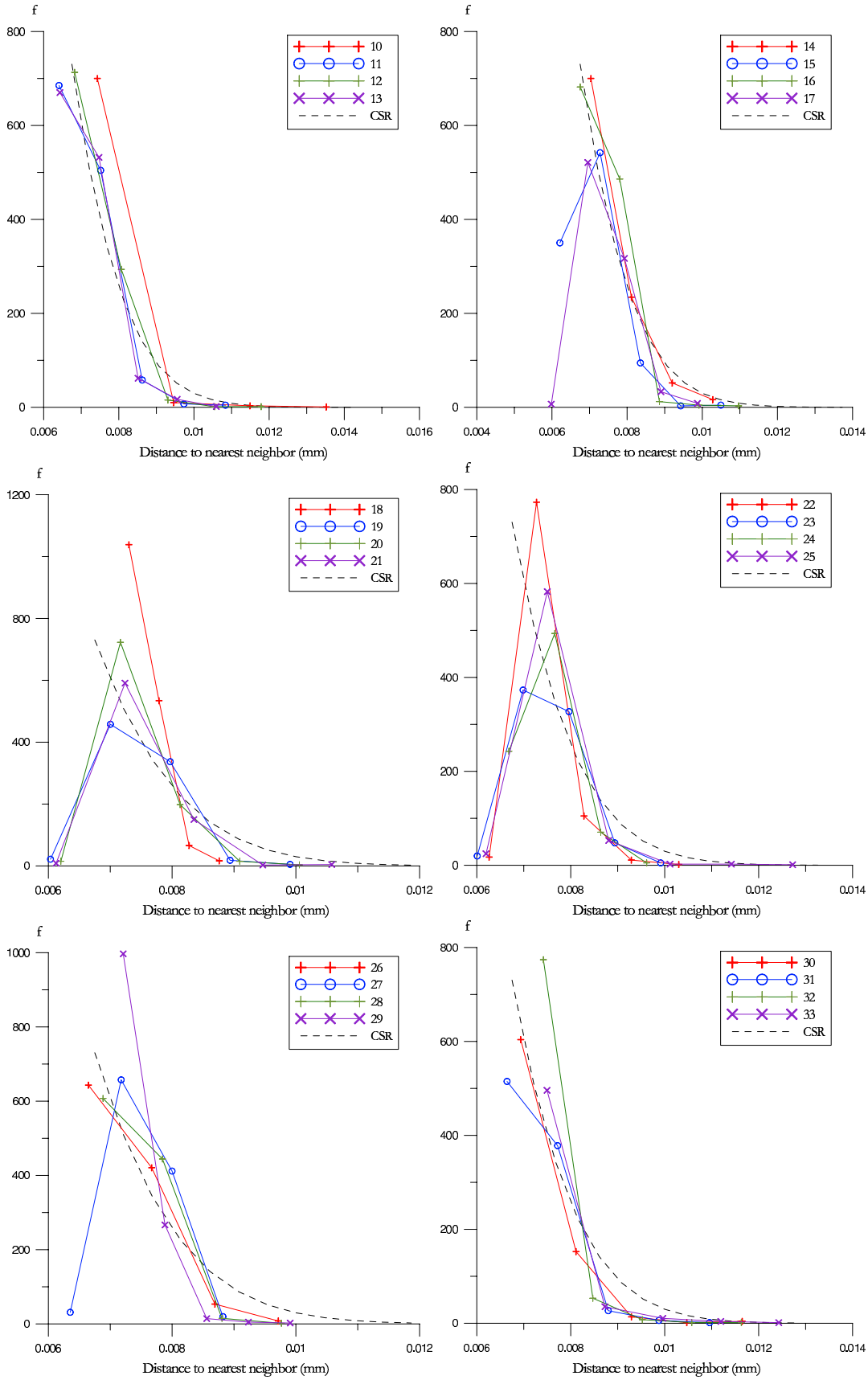

Figure C.2: Nearest neighbor distance RTM6 (II)

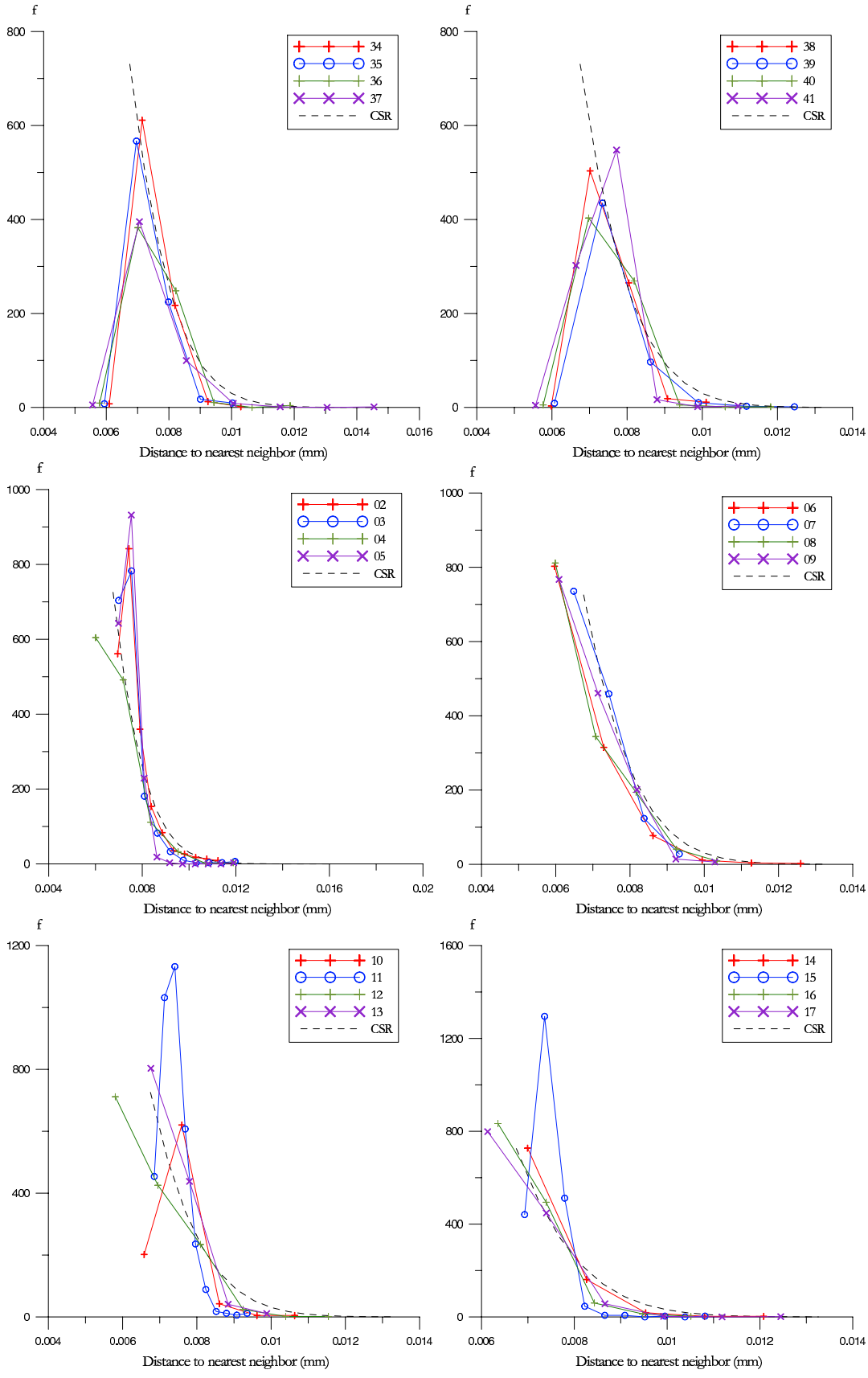

Figure C.3: Nearest neighbor distance 977-2 (I)

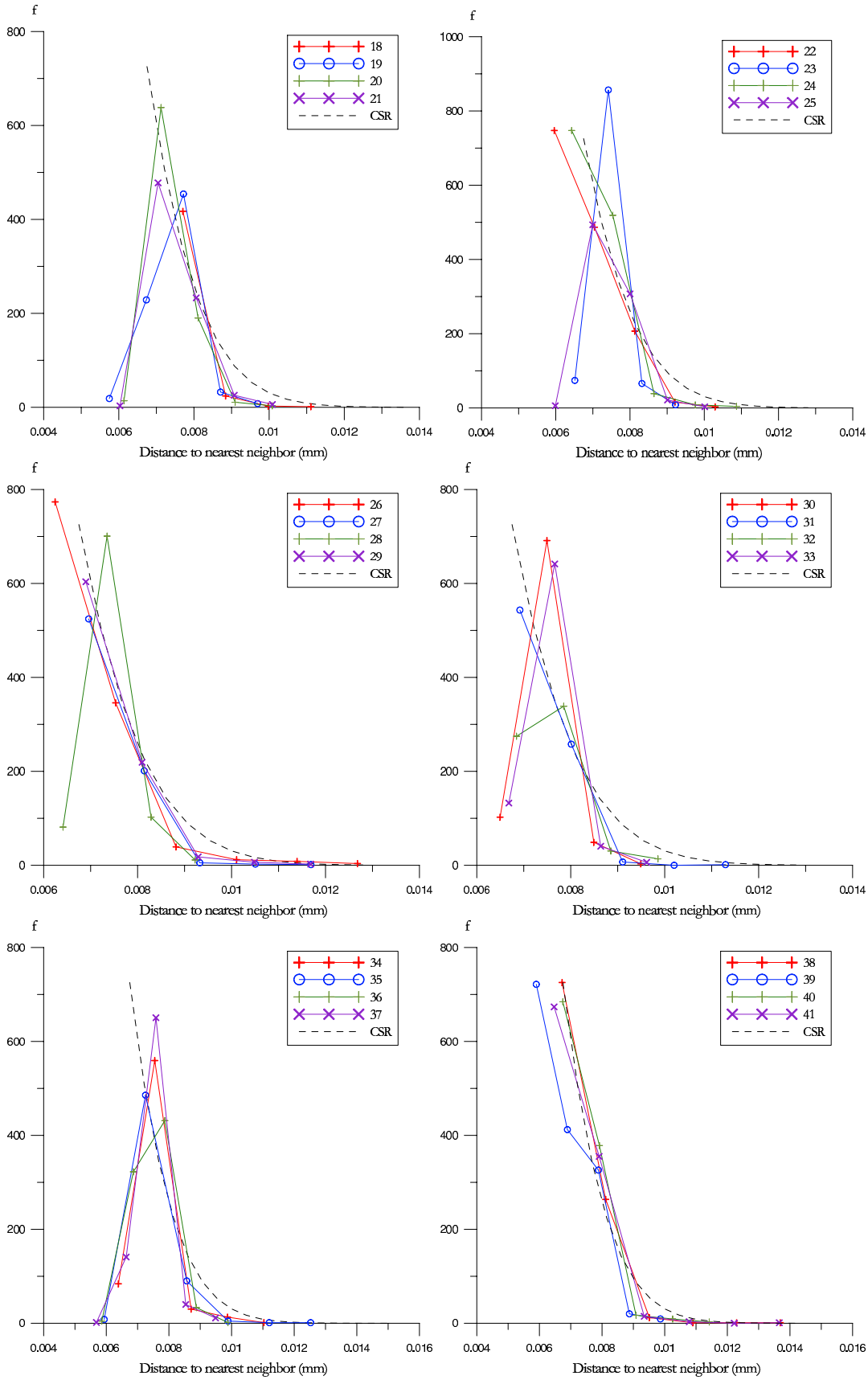

Figure C.4: Nearest neighbor distance 977-2 (II)

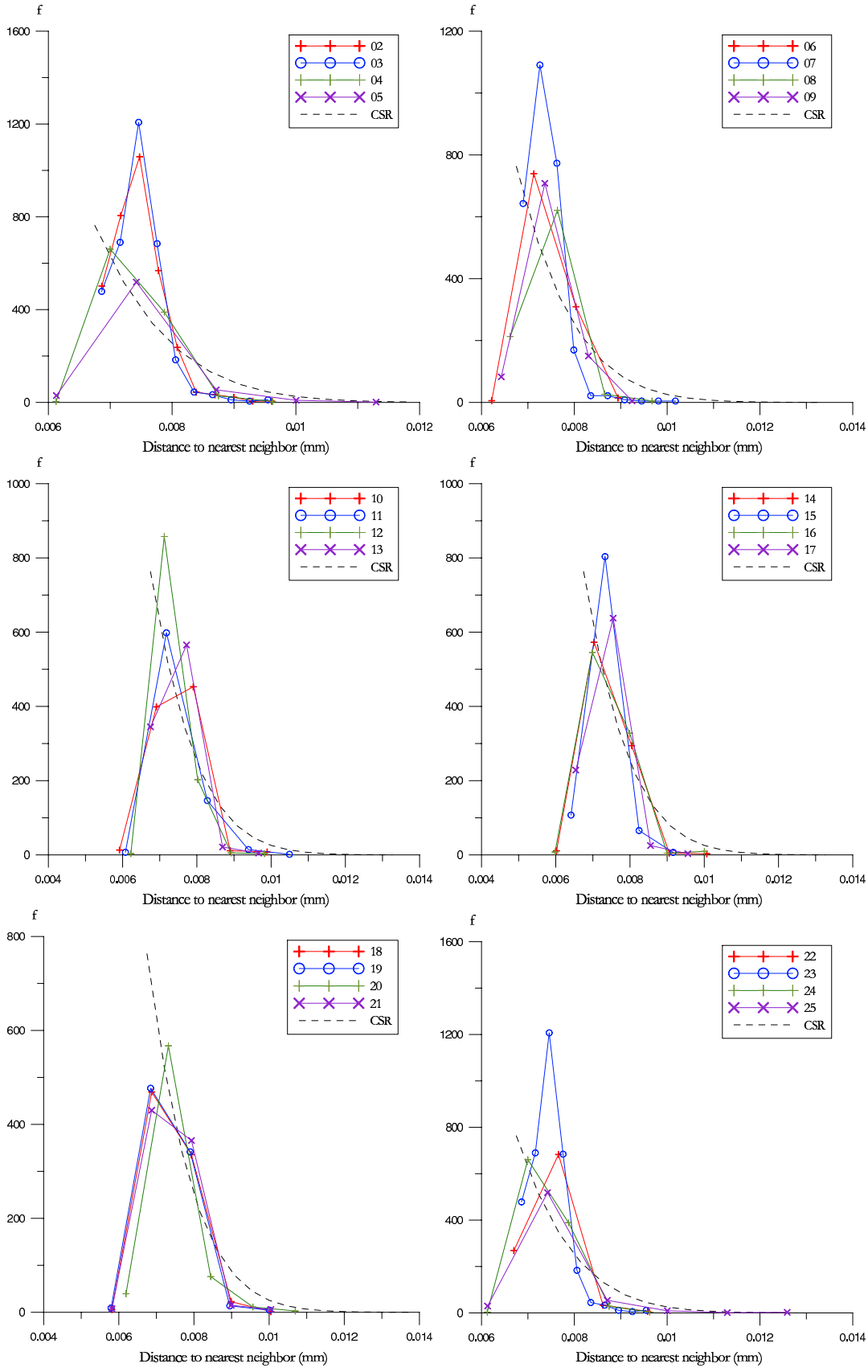

Figure C.5: Nearest neighbor distance 6376 (I)

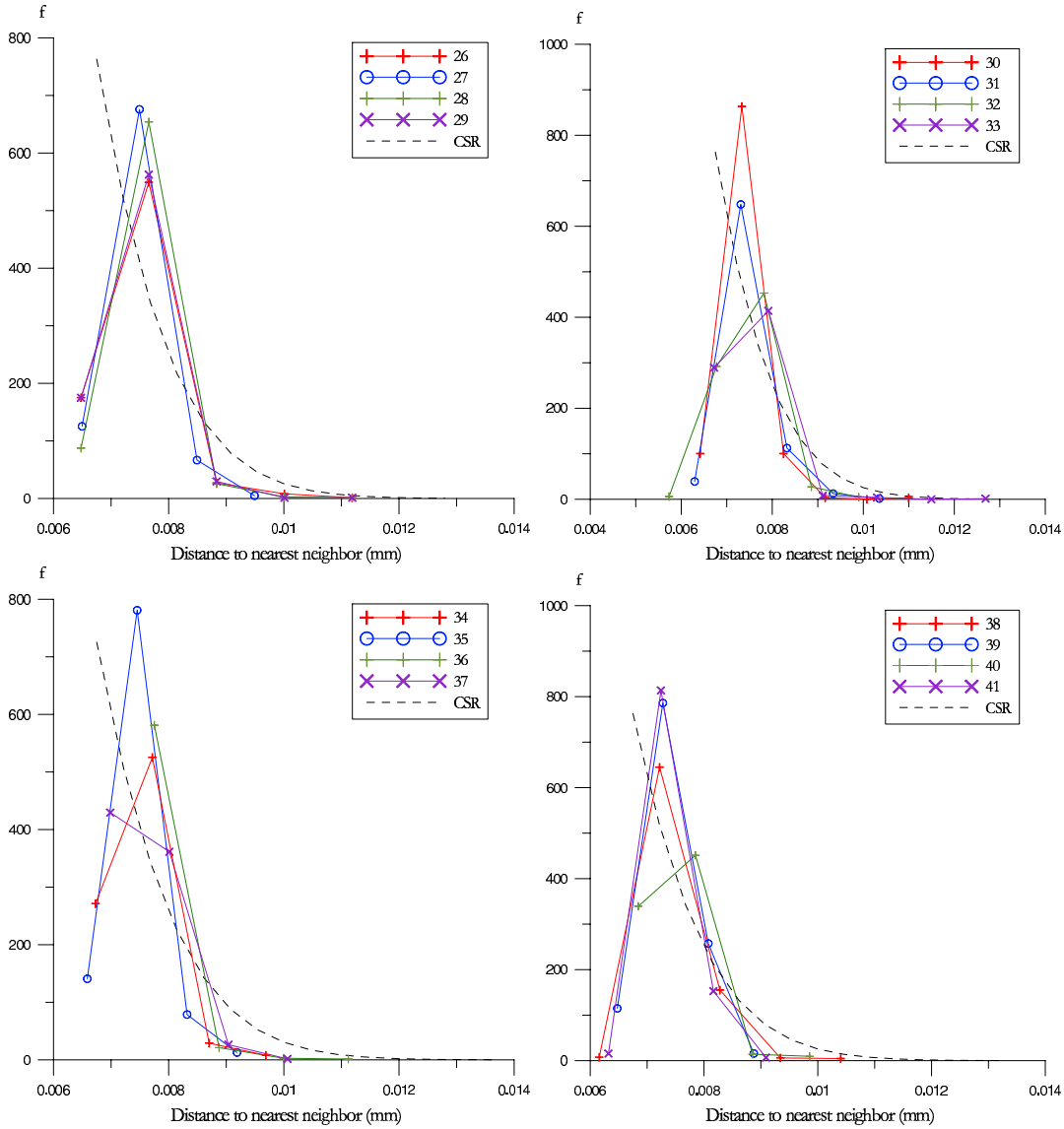

Figure C.6: Nearest neighbor distance 6376 (II)

C.2 Second nearest neighbor distance

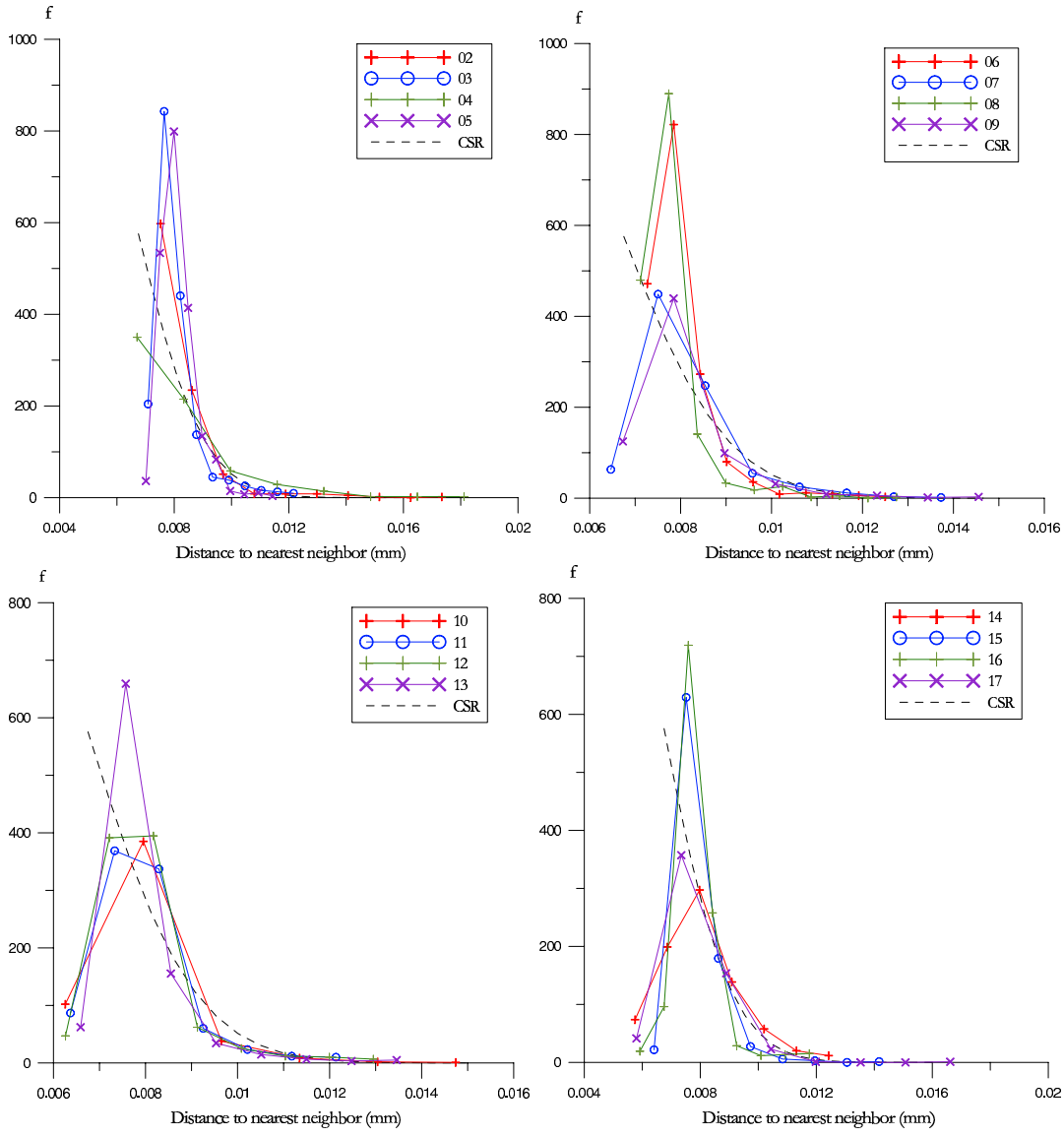

Figure C.7: Second nearest neighbor distance RTM6 (I)

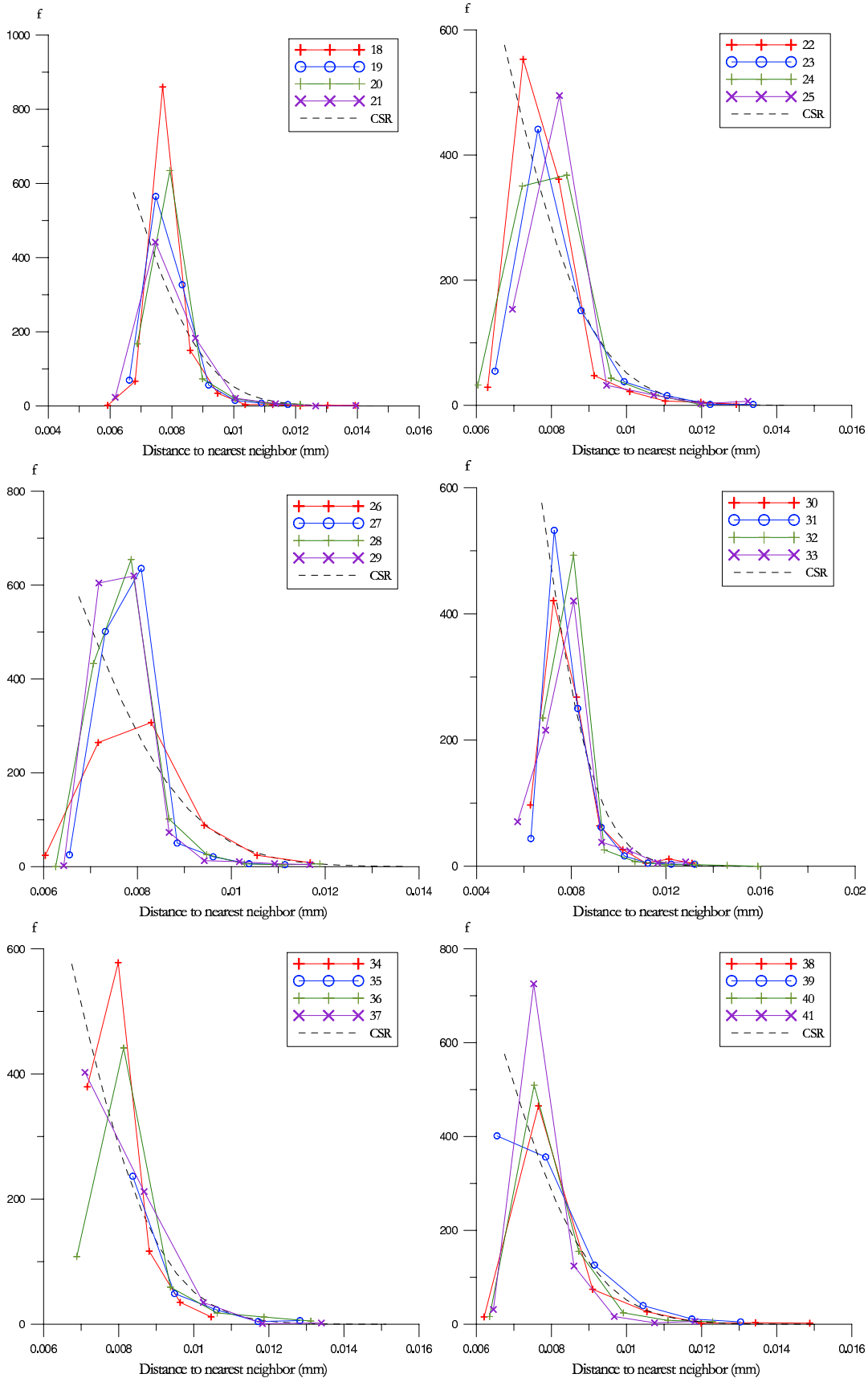

Figure C.8: Second nearest neighbor distance RTM6 (II)

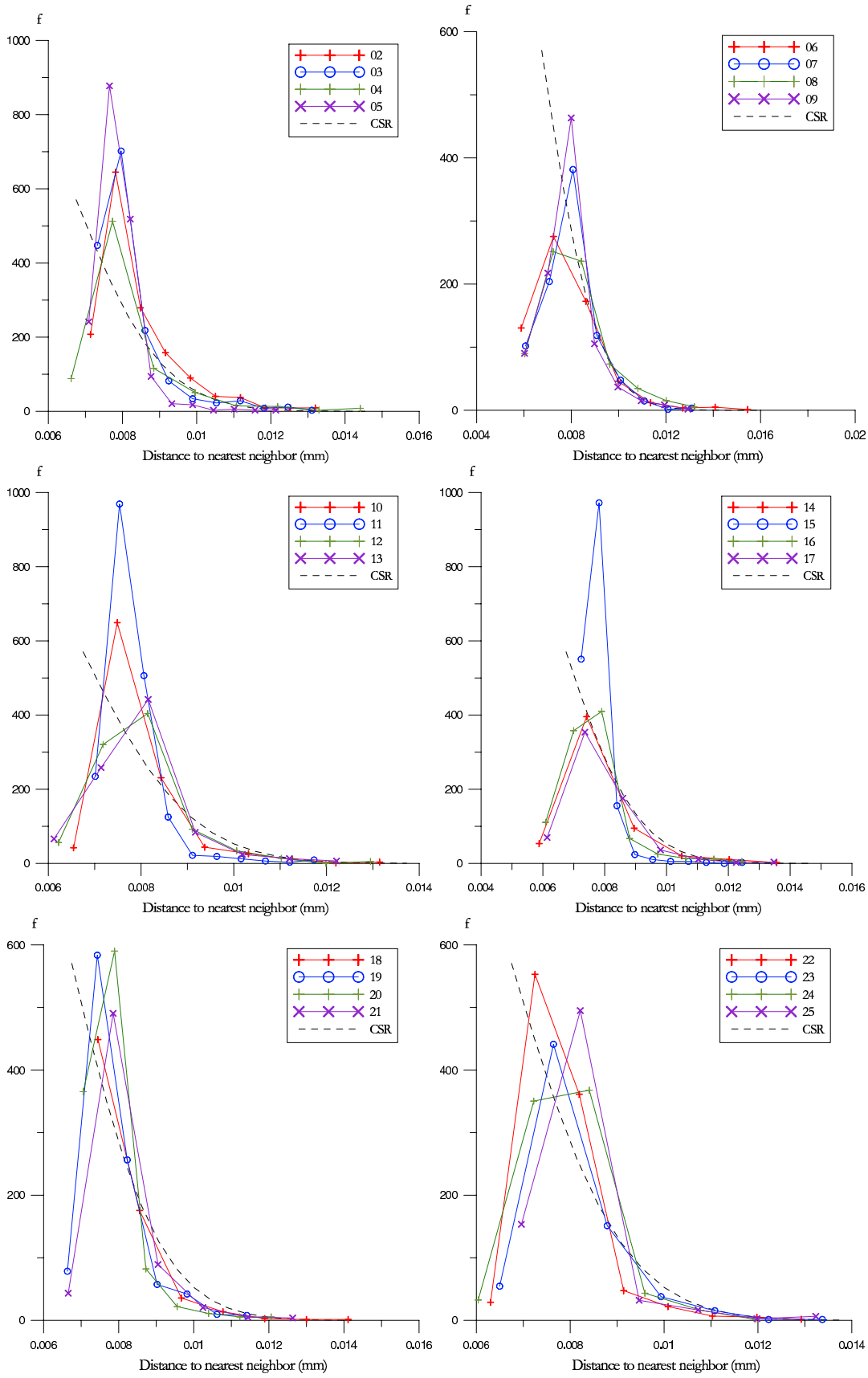

Figure C.9: Second nearest neighbor distance 977-2 (I)

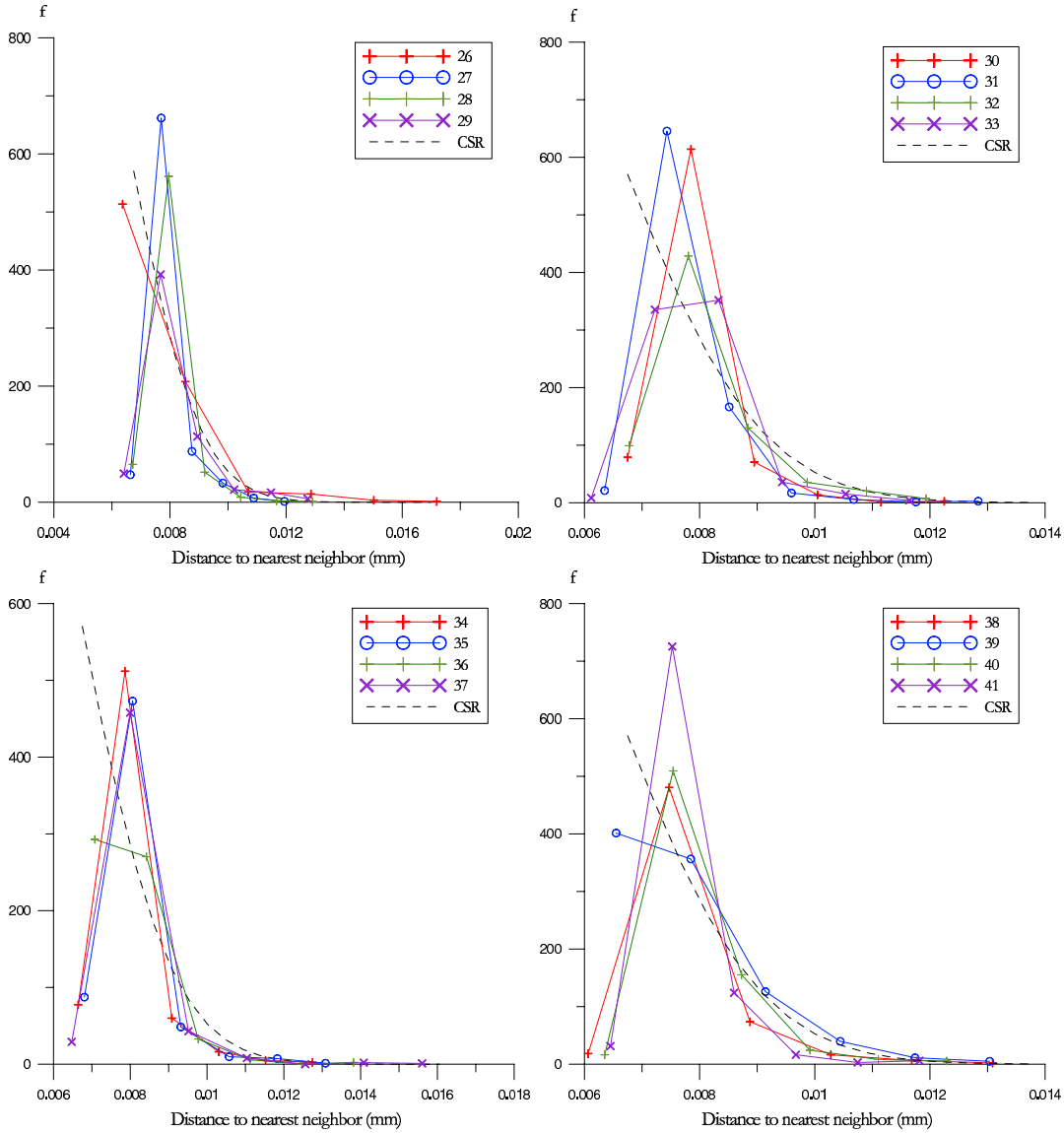

Figure C.10: Second nearest neighbor distance 977-2 (II)

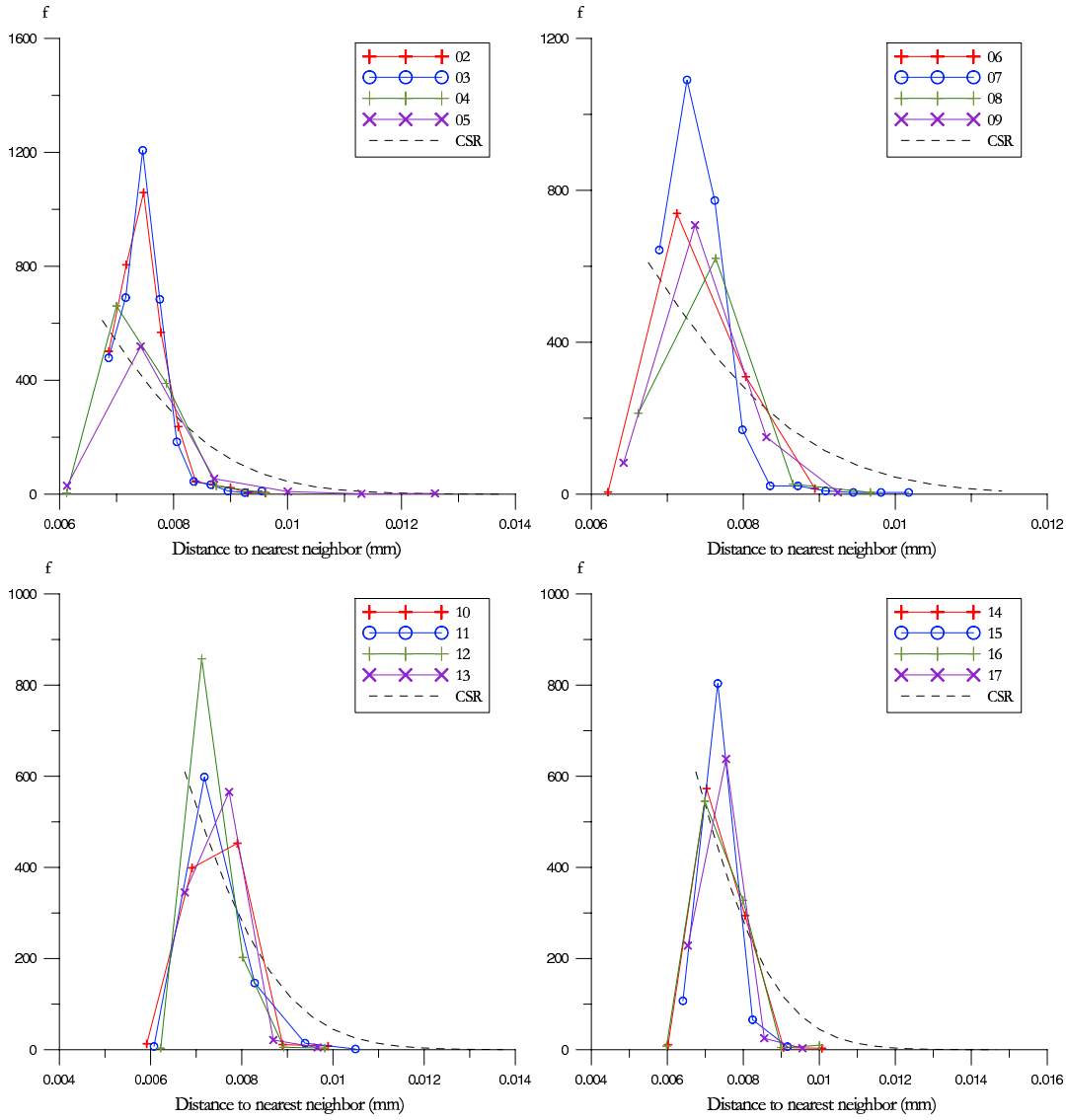

Figure C.11: Second nearest neighbor distance 6376 (I)

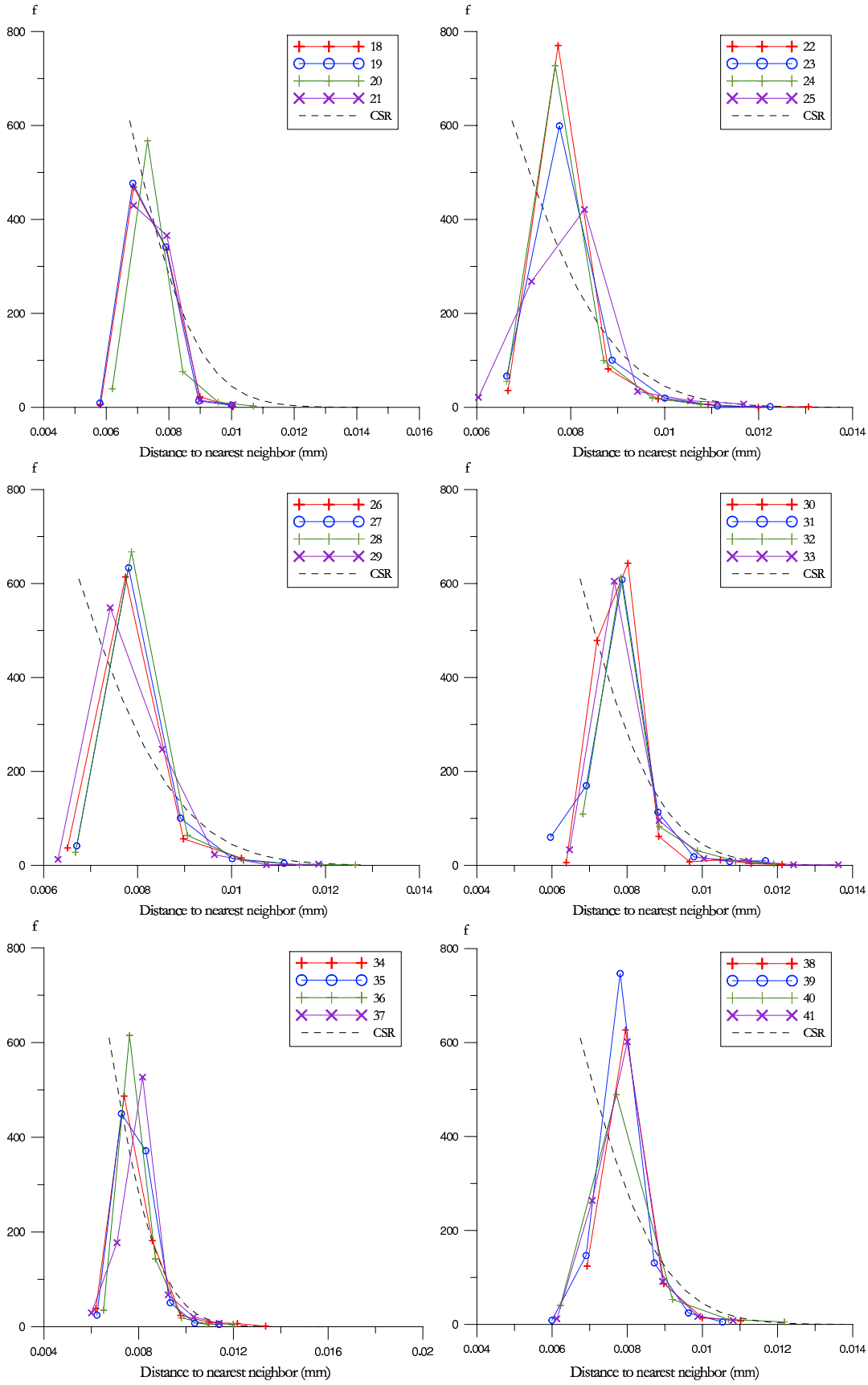

Figure C.12: Second nearest neighbor distance 6376 (II)

C.3 Third nearest neighbor distance

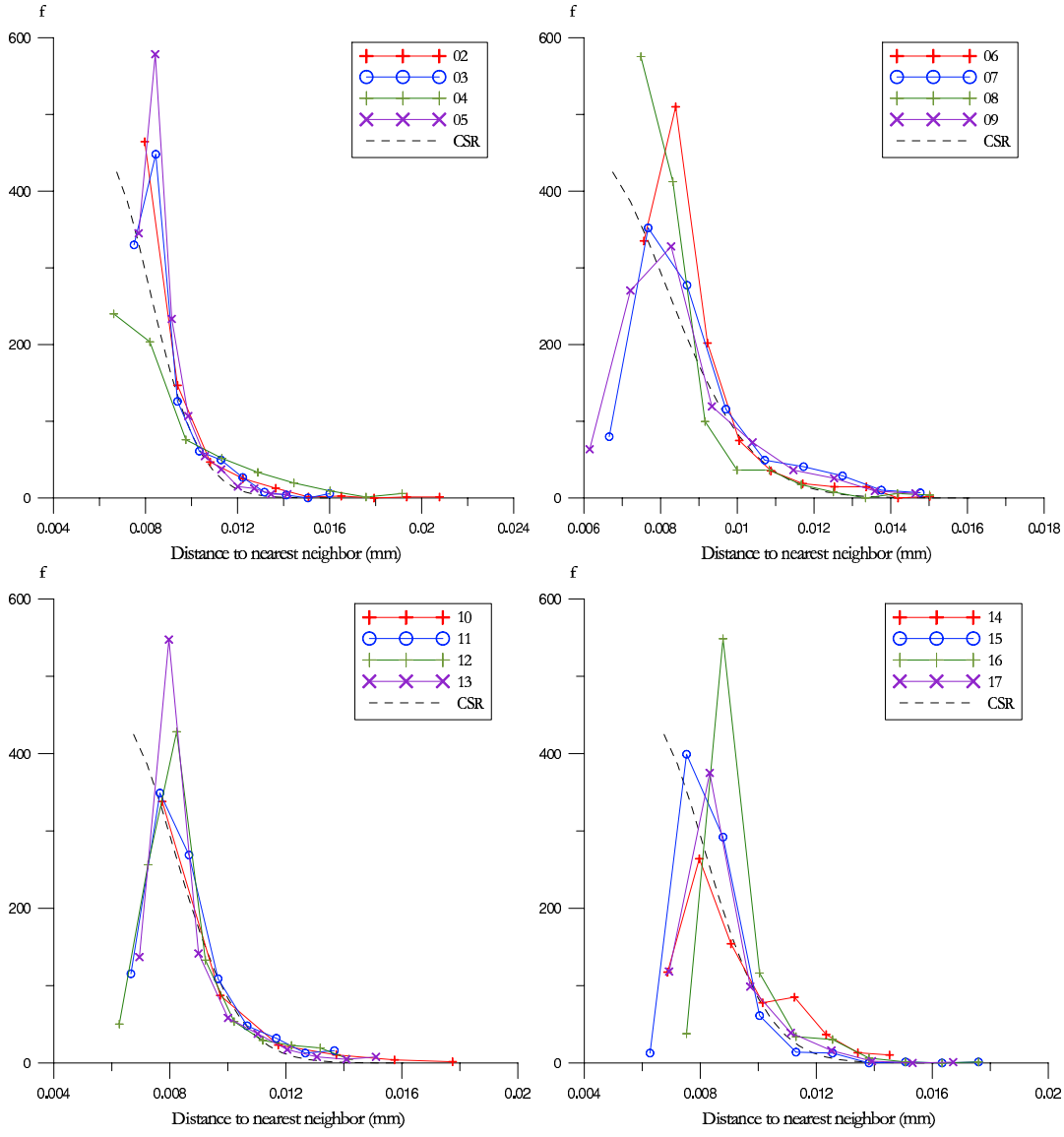

Figure C.13: Third nearest neighbor distance RTM6 (I)

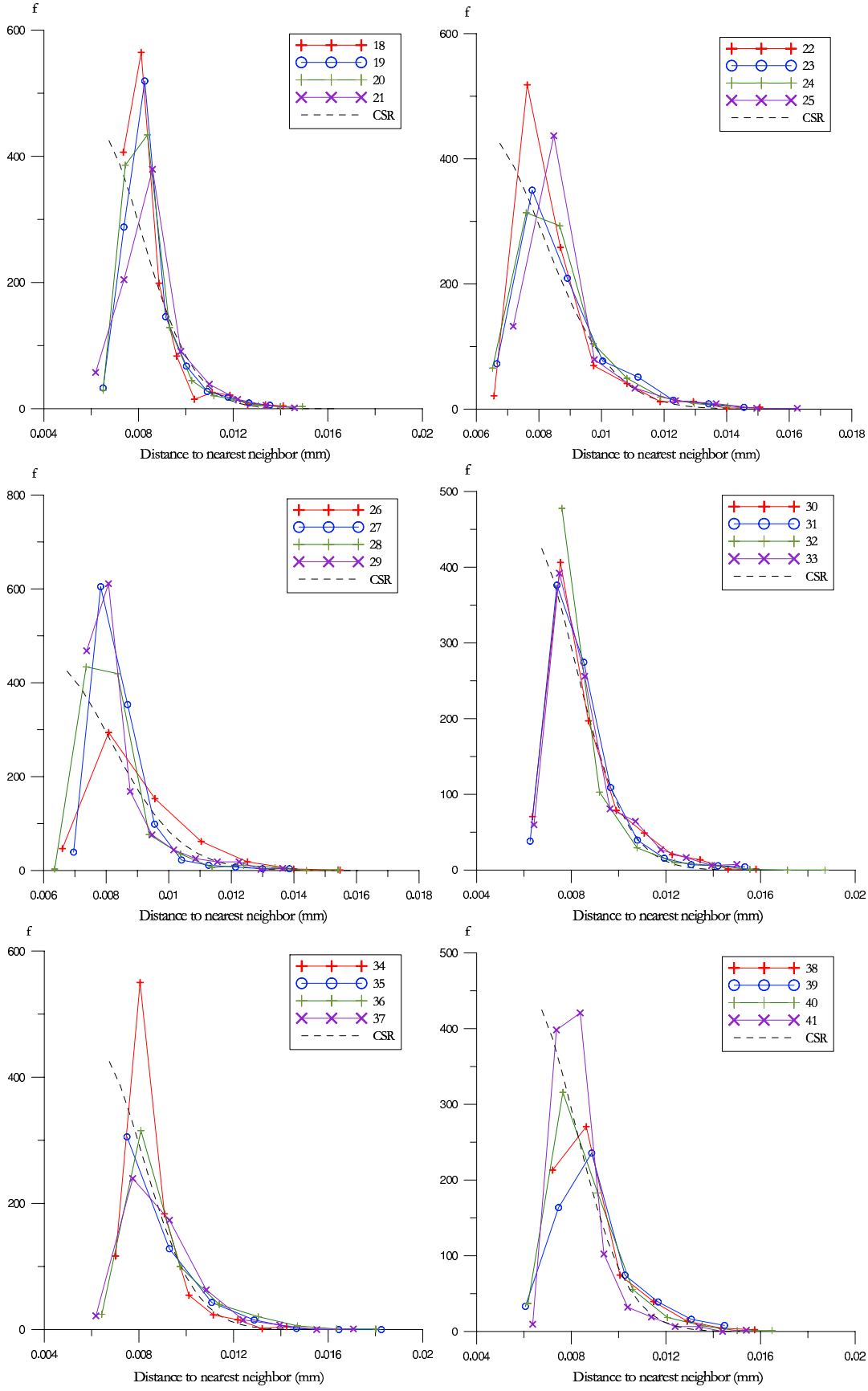

Figure C.14: Third nearest neighbor distance RTM6 (II)

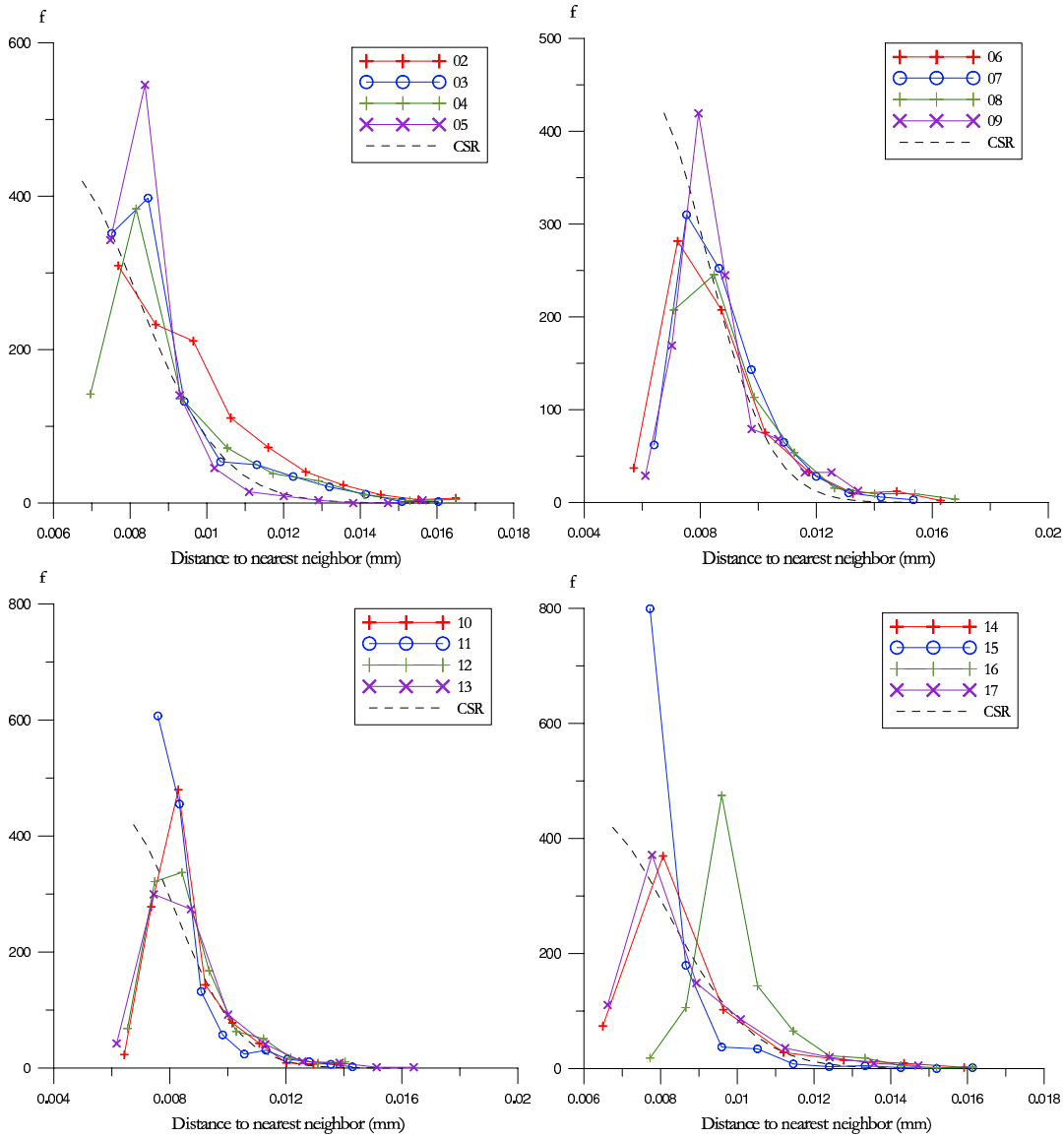

Figure C.15: Third nearest neighbor distance 977-2 (I)

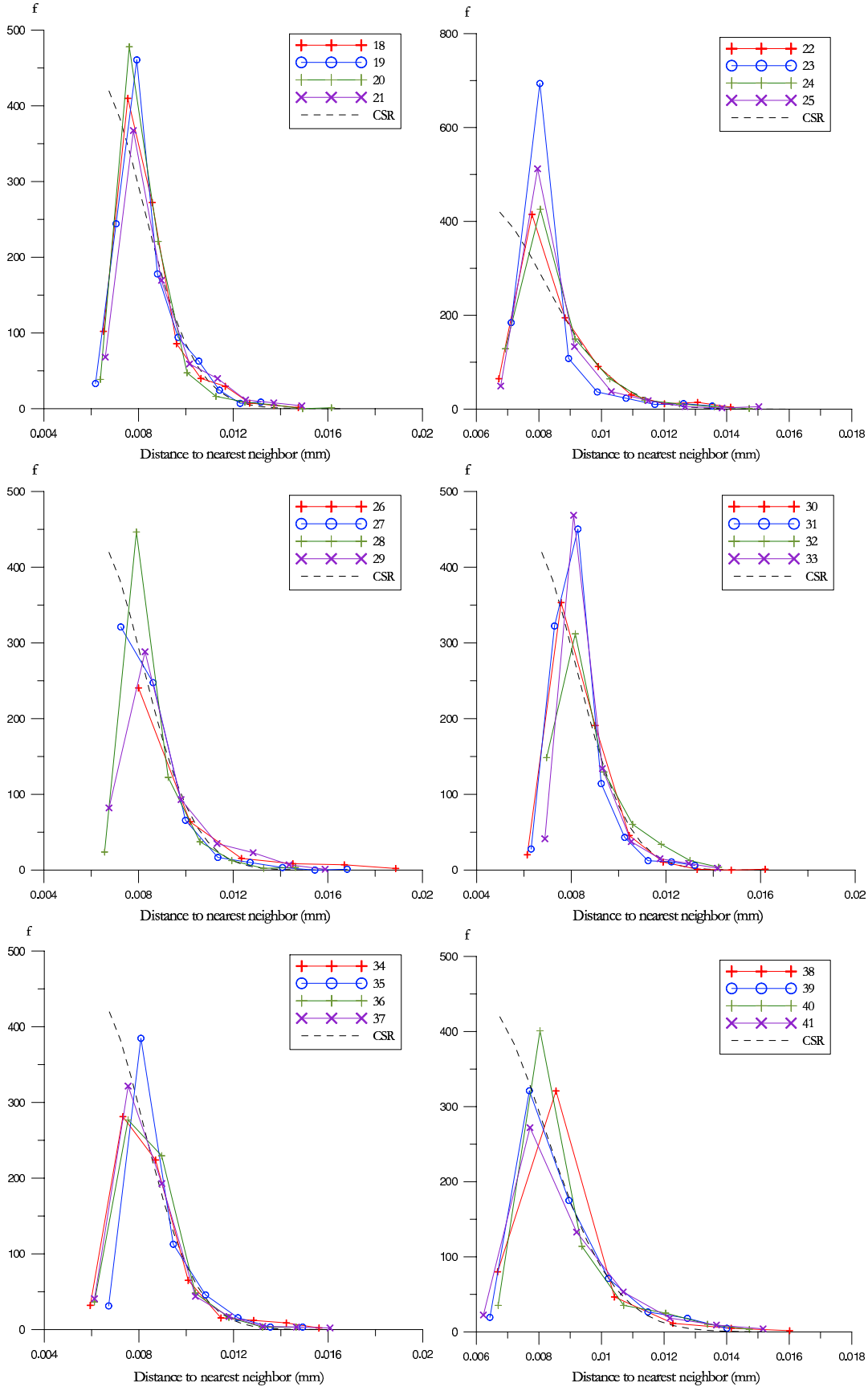

Figure C.16: Third nearest neighbor distance 977-2 (II)

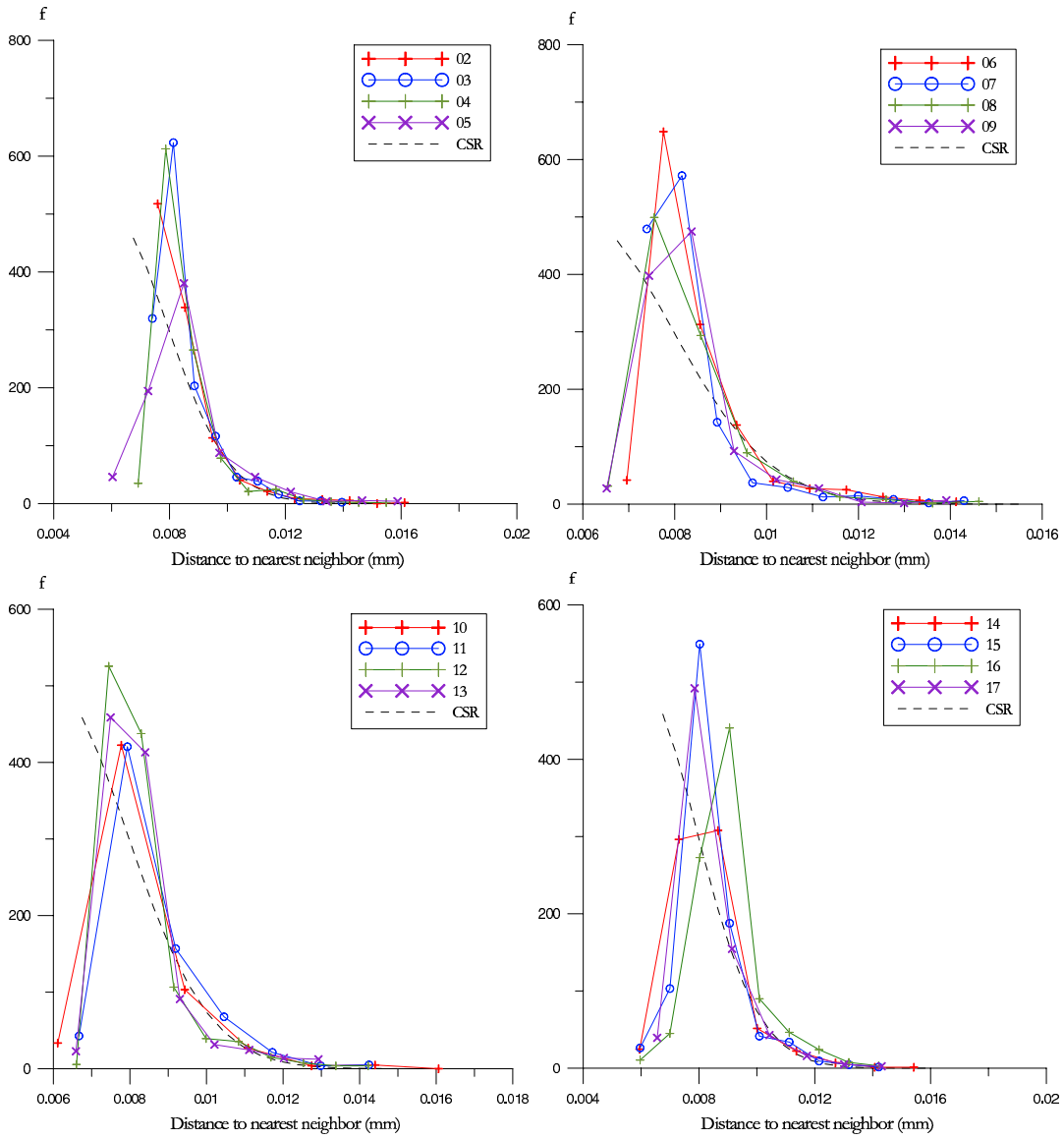

Figure C.17: Third nearest neighbor distance 6376 (I)

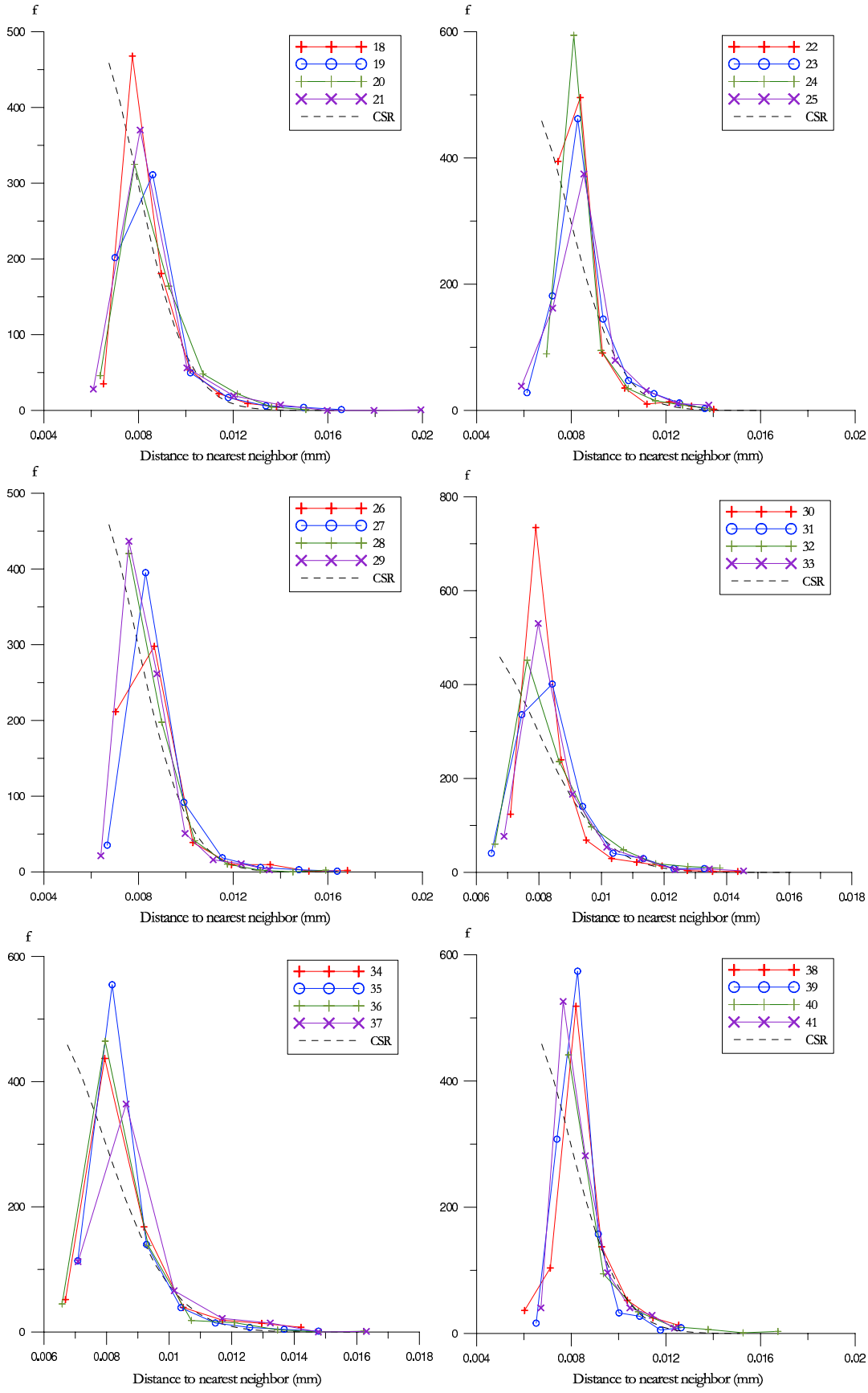

Figure C.18: Third nearest neighbor distance 6376 (II)

C.4 Second-order intensity function

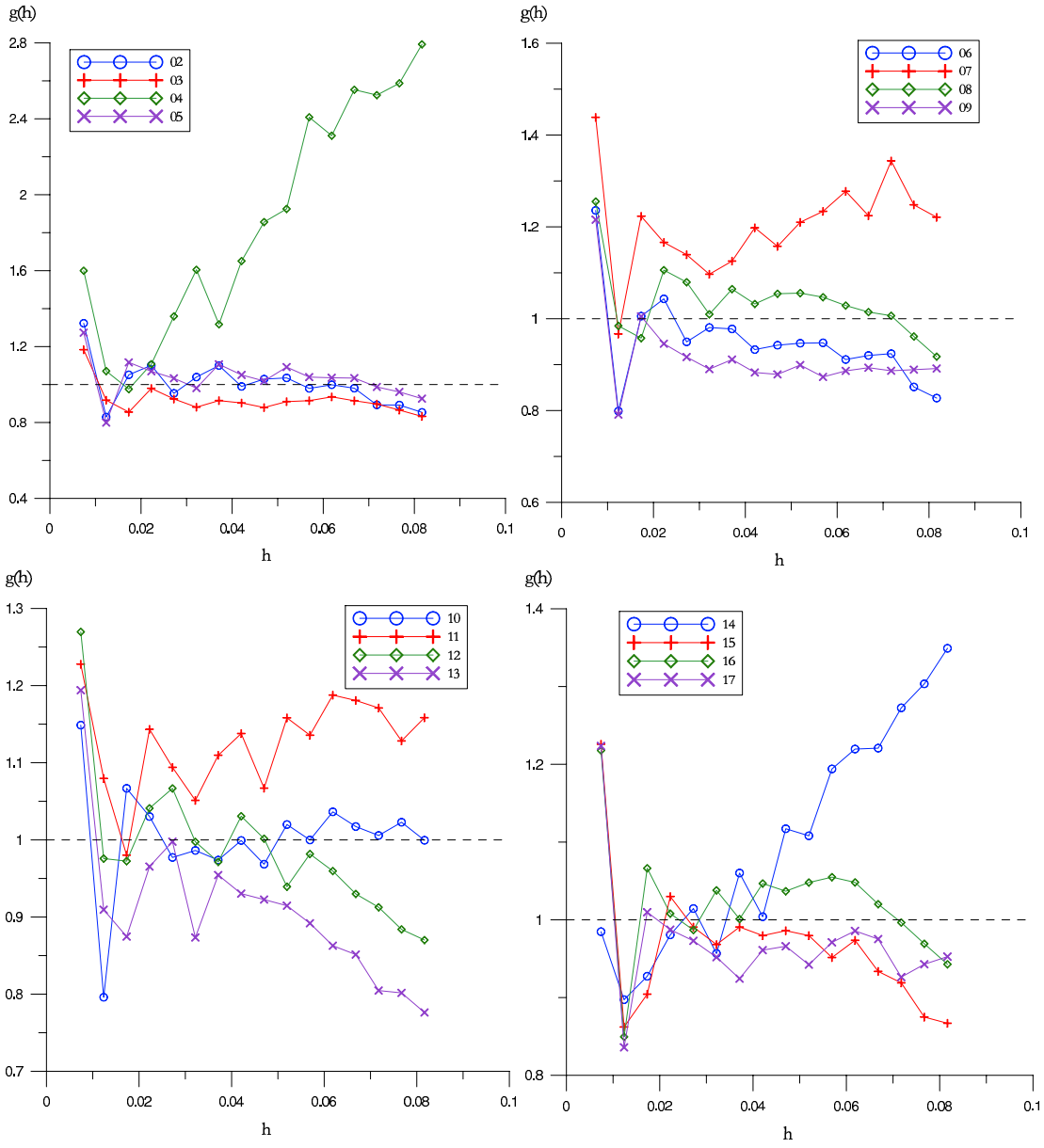

Figure C.19: Second-order intensity function RTM6 (I)

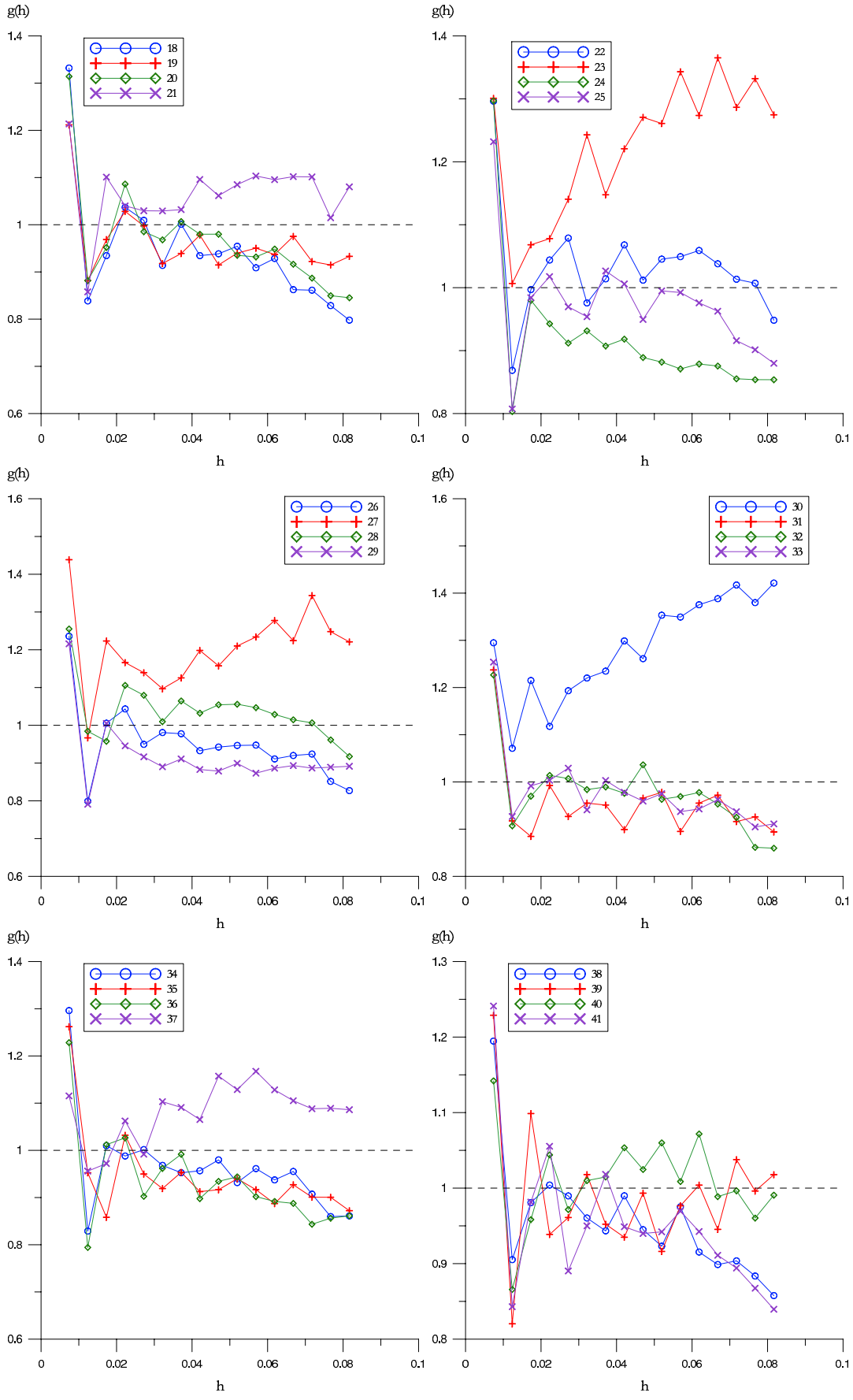

Figure C.20: Second-order intensity function RTM6 (II)

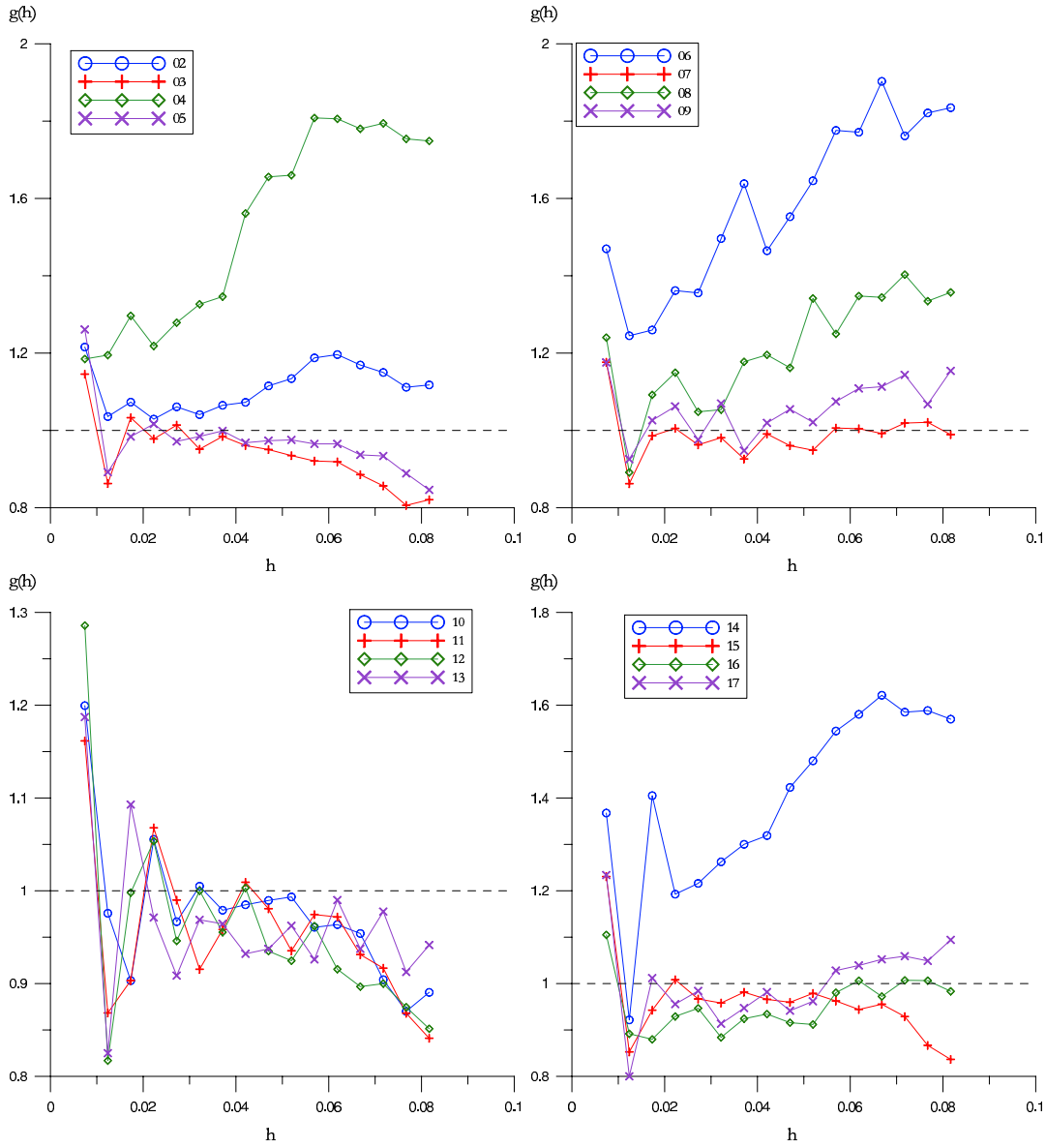

Figure C.21: Second-order intensity function 977-2 (I)

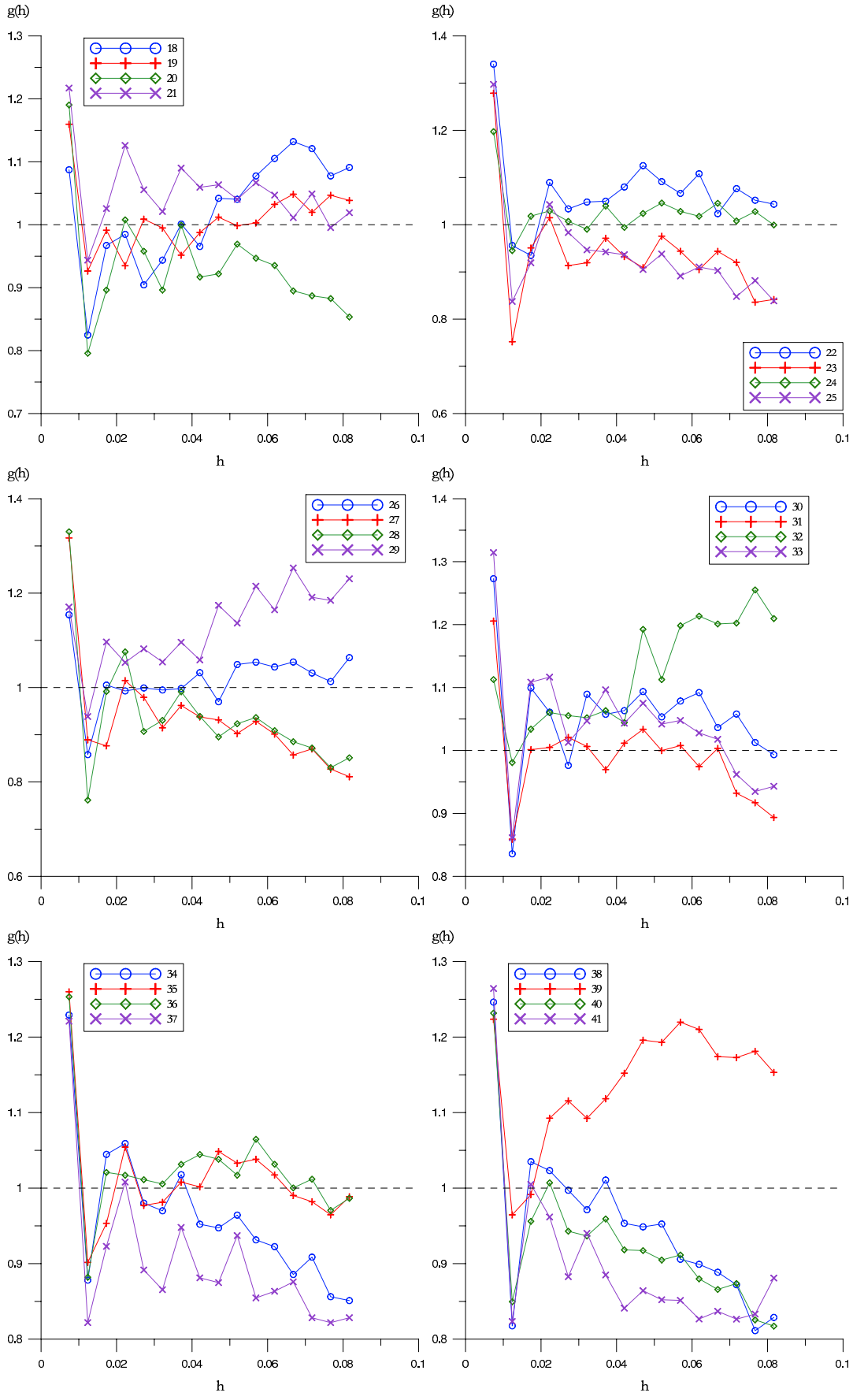

Figure C.22: Second-order intensity function 977-2 (II)

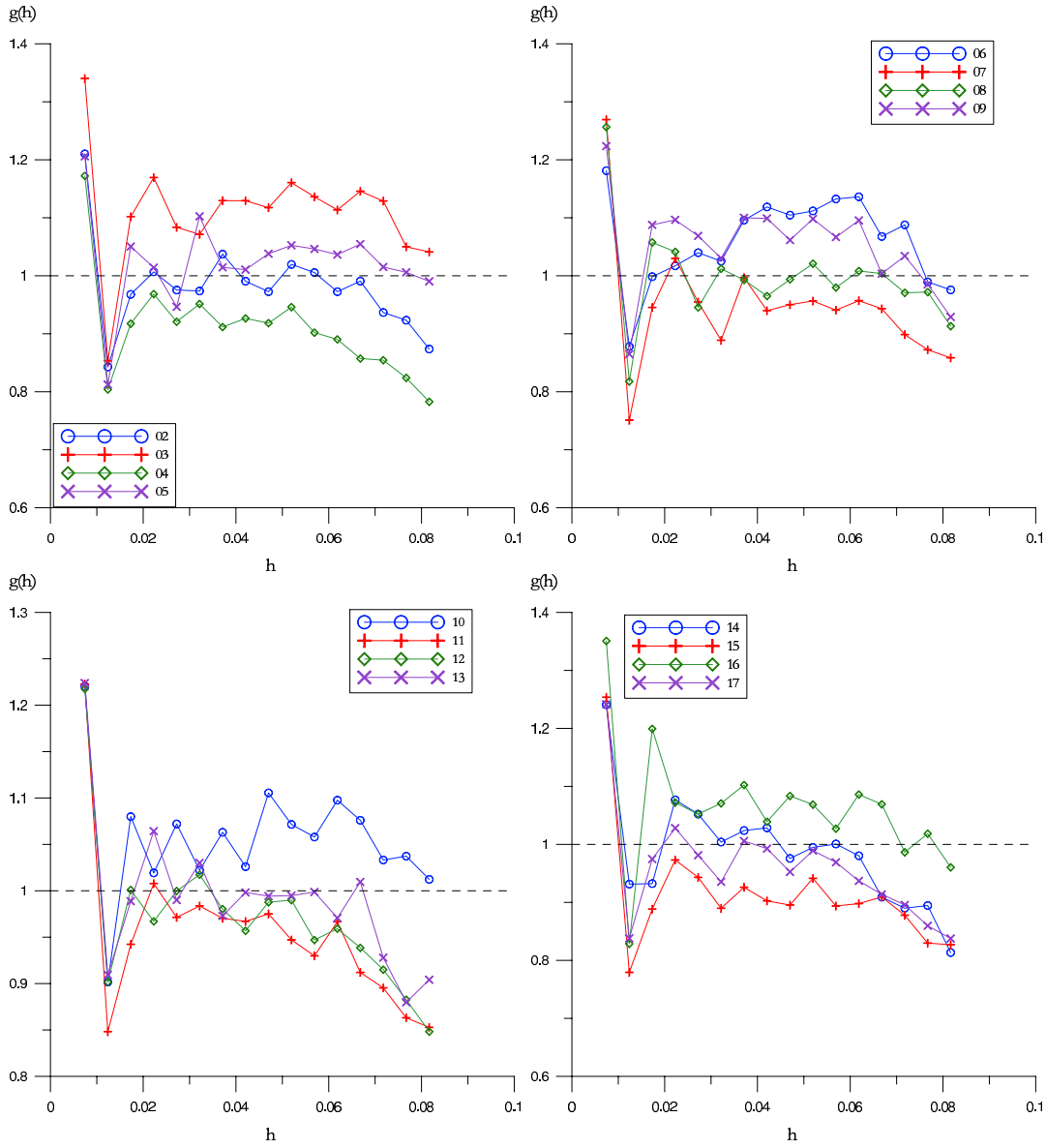

Figure C.23: Second-order intensity function 6376 (I)

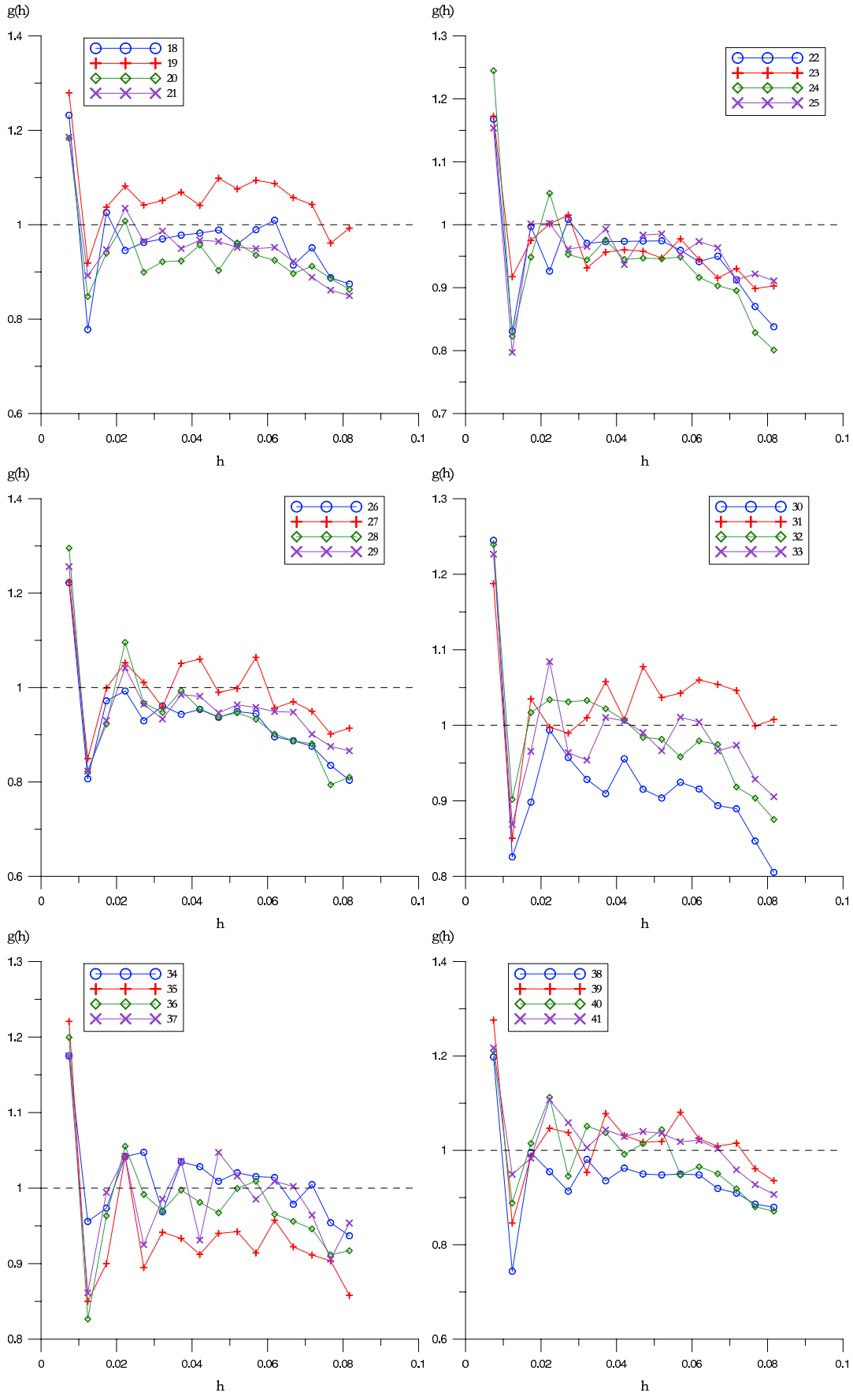

Figure C.24: Second-order intensity function 6376 (II)

C.5 Pair distribution function

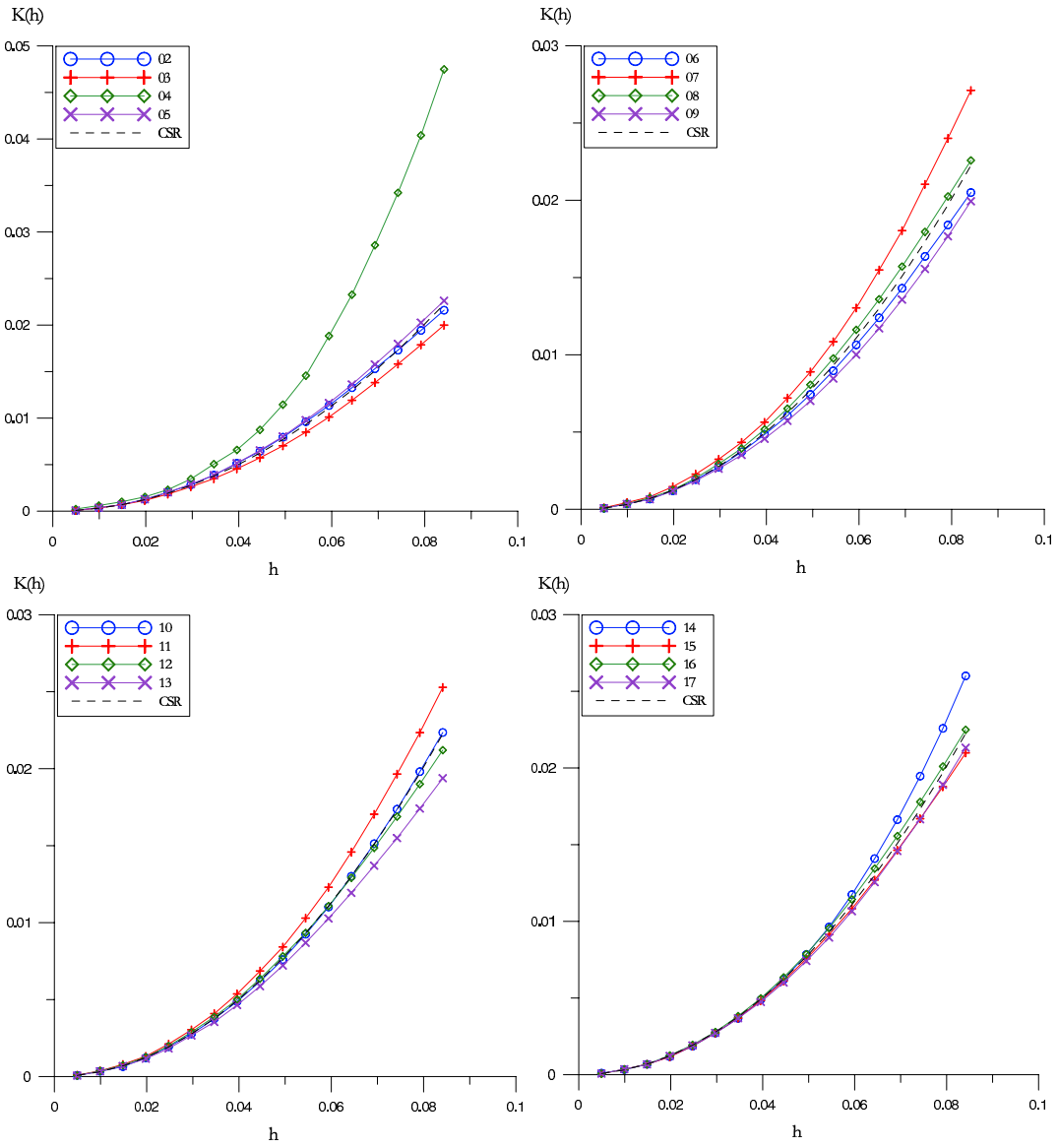

Figure C.25: Pair distribution function RTM6 (I)

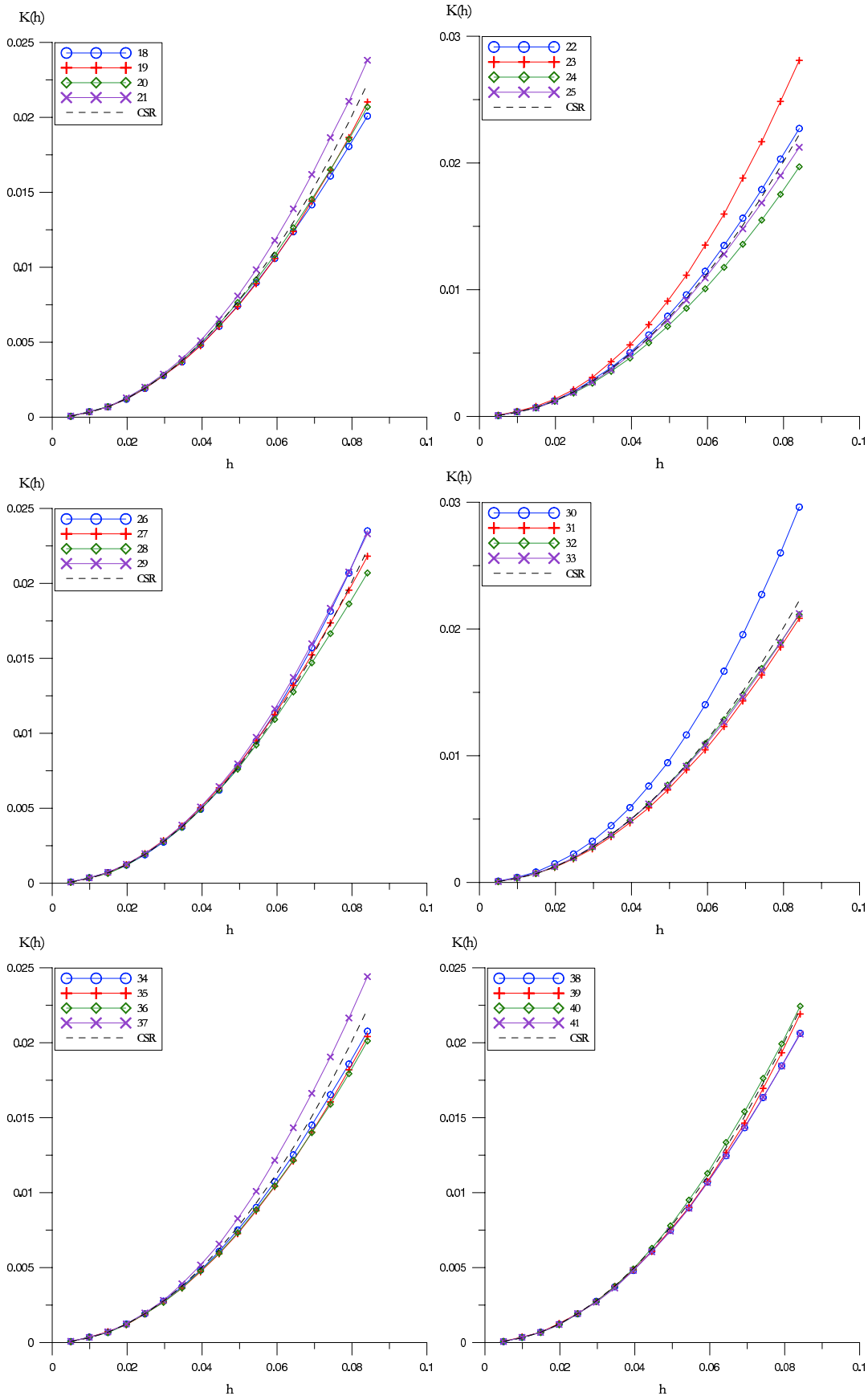

Figure C.26: Pair distribution function RTM6 (II)

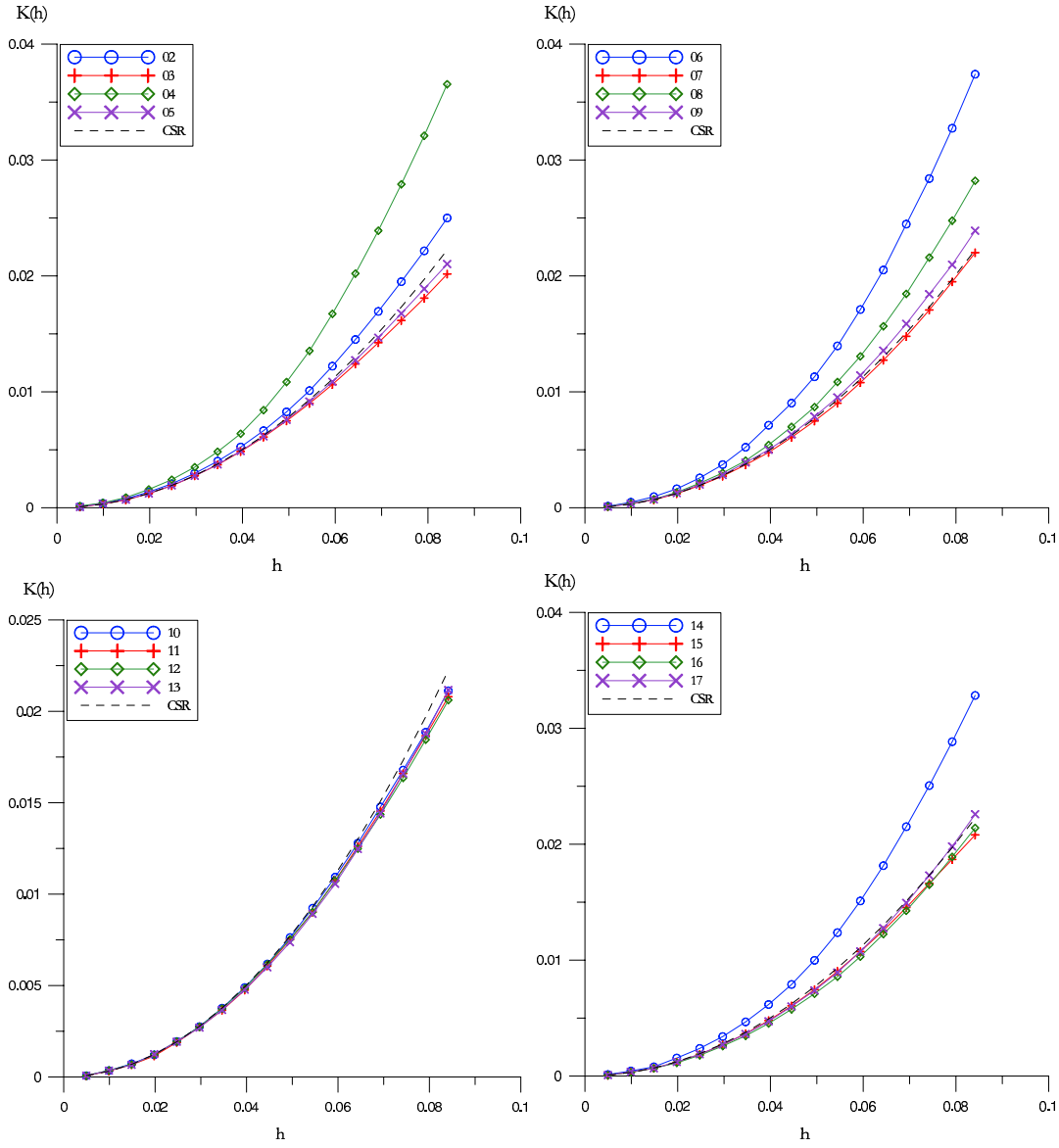

Figure C.27: Pair distribution function 977-2 (I)

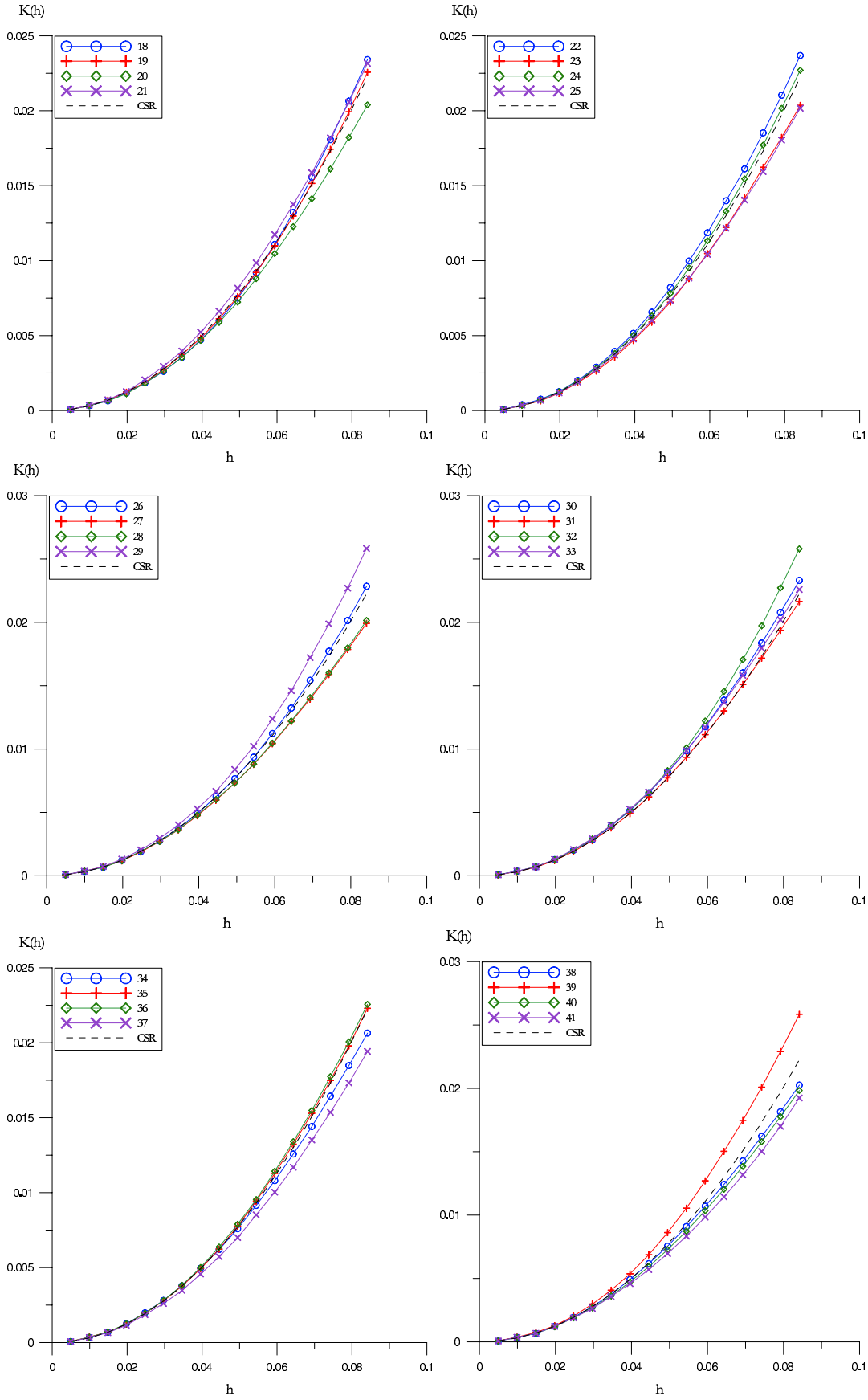

Figure C.28: Pair distribution function 977-2 (II)

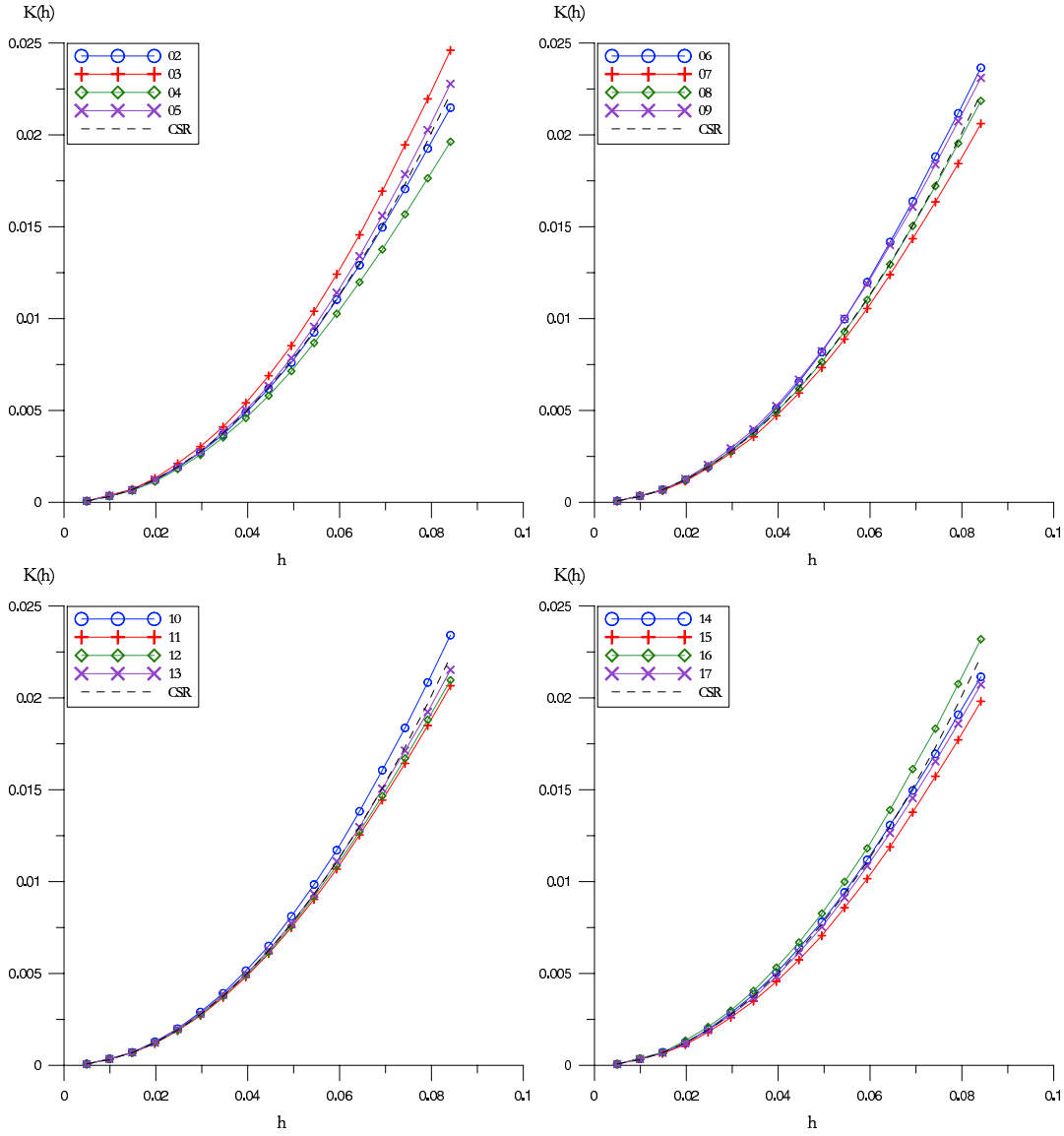

Figure C.29: Pair distribution function 6376 (I)

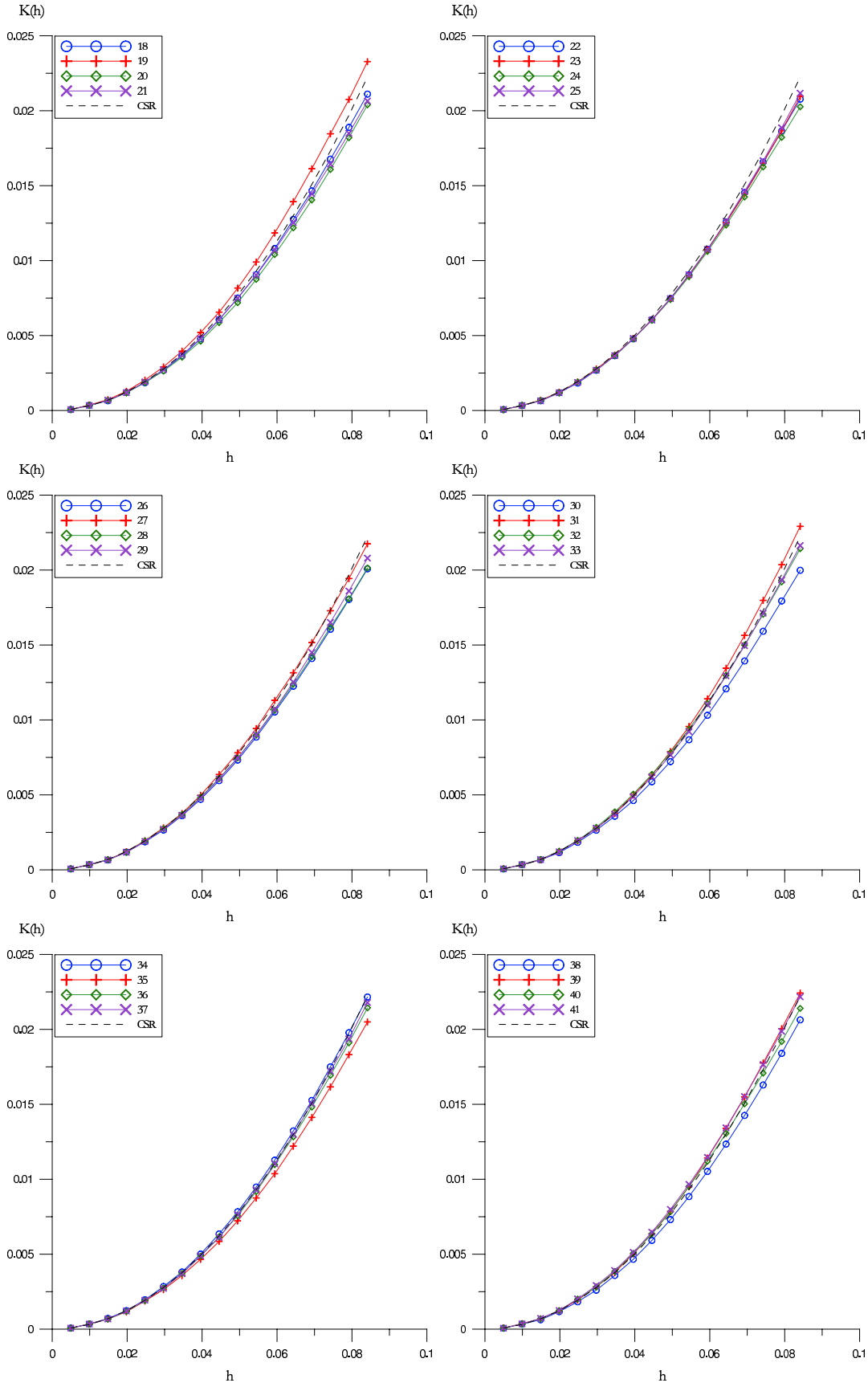

Figure C.30: Pair distribution function 6376 (II)

Bibliography

[1] Probabilistic Engineering Mechanics. Publisher: Elsevier. Website: http://www.sciencedirect.com/science/journal/02668920.

[2] Altair Hypermesh 6.0. - Product Brochure. Electronic document. http://www.altair.com/pdf/hm_pb.pdf, December 2004.

[3] Msc.robust design: Modeling uncertainity to manage risk - electronic document. http://www.mscsoftware.com/assets/2951_RD2004JUNZZZLTDAT.pdf and http://www.mscsoftware.com/products/products_detail.cfm?PI=617, December 2004.

[4] Robust Design Solution - Product Brochure. Electronic document. http://www.ansys.com/assets/brochures/robust-design-solution-1.pdf, December 2004.

[5] M. Abramowitz. Microscopy: Basics and beyond. Technical report, Olympus America Inc., 2003.

[6] E. Adolfsson and P. Gudmundson. Matrix crack initiation and progression in composite laminates subjected to bending and extension. *International Journal of Solids and Structures*, 36:3131–3169, 1999.

[7] J. Aitchison and J. A. Martin-Fernández S. Thió-Henestrosa. Codacourse: An introductory course to compositional data. Course notes. codawork'04 1st compositional data analysis workshop, Department d'Informatica i Matematica Aplicada. Universitat de Girona, 2004.

[8] K. Alzebdeh, A. Al-Ostaz, I. Jasiuk, and M. Ostoja-Starzewski. Fracture of random matrix-inclusion composites: scale effects and statistics. *International Journal of Solids and Structures*, 35(19):2537–2566, 1998.

[9] K. Alzebdeh and M. Ostoja-Starzewski. Micromechanically based stochastic finite elements: length scales and anisotropy. *Probabilistic Engineering Mechanics*, 11:205–214, 1996.

[10] A. Anthoine. Derivation of the in-plane characteristics of masonry through homogenization theory. *International Journal of Solids and Structures*, 32(2):137–163, 1995.

[11] A. Anthoine and P. Pegon. *Numerical Analysis and Modelling of Composite Materials*, chapter Numerical analysis and modelling of the damage and softening of brick masonry. Blackie Academic and Professional, 1999.

[12] L. E. Asp and L. A. Berglund. Effects of a composite-like stress state on the fracture epoxies. *Composites Science and Technology*, 53:27–37, 1995.

[13] L. E. Asp, L. A. Berglund, and R. Talreja. A criterion for crack initiation in glassy polymers subjected to a composite-like stress state. *Composites Science and Technology*, 56:1291–1301, 1996.

[14] L. E. Asp, L. A. Berglund, and R. Talreja. Effects of fibre and interphase on matrix-initiated transverse failure in polymer composites. *Composites Science and Technology*, 56:657–665, 1996.

[15] L. E. Asp, L. A. Berglund, and R. Talreja. Prediction of matrix-initiated transverse failure in polymer composites. *Composites Science and Technology*, 56:1089–1097, 1996.

[16] A. Balacó de Morais. Transverse moduli of continuous-fibre-reinforced polymers. *Composites Science and Technology*, 60:997–1002, 2000.

[17] S.C. Baxter and L.L. Graham. Characterization of random composites using moving-window technique. *Journal of Engineering Mechanics*, 126(4):389–397, 2000.

[18] S.C. Baxter, M.I. Hossain, and L.L. Graham. Micromechanics based random material roperty fields for particulate reinforced composites. *International Journal of Solids and Structures*, 38:9209–9220, 2001.

[19] R. Becker and R.E. Smelser. Simulation of strain localization and fracture between holes in an aluminum sheet. *Journal of the Mechanics and Physics of Solids*, 42(773):773–796, 1994.

[20] Y. Benveniste. A new approach to the application of mori-tanaka's theory in composite materials. *Mechanics of Materials*, 6:147–157, 1987.

[21] M.J. Beran. *Statistical Continuum Theories*. Interscience Publishers, 1968.

[22] J. G. Berryman. Random close packing of hard spheres and disks. *Physical Review A*, 27(2):1053–1061, 1983.

[23] H. J. Böhm. A short introduction to basic concepts of continuum micromechanics. Technical report, Institut für Leichtbau und Flugzeugbau. TU Wien, 2003.

[24] V. V. Bolotin. *Mechanics of Fatigue*. CRC Press, 1999.

[25] A. Borbély, H. Biermann, and O. Hartmann. FE investigation of the effect of particle distribution on the uniaxial stress-strain behaviour of particulate reinforced metal-matrix composites. *Material Science and Engineering A*, 313:34–45, 2001.

[26] B. Bousfield. *Surface Preparation and Microscopy of Materials*. John Wiley and sons, 1992.

[27] G. E. P. Box, W.G. Hunter, and J. S. Hunter. *Statistics for experimenters: an introduction to design, data analysis and model building.* John Wiley and sons, 1978.

[28] L.C. Brinson and W.S. Lin. Comparison of micromechanics methods for effective properties of multiphase viscoelastic composites. *Composite Structures*, 41(3-4):353–367, 1998.

[29] J.R. Brockenborough, S. Suresh, and H.A. Wienecke. Deformation of metal-matrix composites with continuous fibres: geometrical effects of fibre distribution and shape. *Acta Metallica Materialia*, 39(5):735–752, 1991.

[30] Buehler Ltd. Buehler homepage - http://www.buehler.com. Last visited: 17 December 2004.

[31] V.A. Buryachenko, N. J. Pagano, R. Y. Kim, and J. E. Spowart. Quantitative description and numerical simulation of random microstructures of composites and their effective elastic moduli. *International Journal of Solids and Structures*, 40:47–72, 2003.

[32] B. Buttkus. *Spectral Analysis and Filter Theory in Applied Geophysics.* Springer, 2000.

[33] J. Byström. Influence of inclusions distribution on the effective properties of heterogeneous media. *Composites Part B: engineering*, 34:587–592, 2003.

[34] E. Car, F. Zalamea, S. Oller, J. Miquel, and E. Oñate. Numerical simulation of composite materials: two procedures. *International Journal of Solids and Structures*, 39:1967–1986, 2002.

[35] J. F. Caron and A. Ehrlacher. Modelling of fatigue microcracking kinetics in crossply composites and experimental validation. *Composites Science and Technology*, 59:1349–1359, 1999.

[36] C. L. Chiang. *An introduction to stochastic processes and their applications.* Krieger, 1980.

[37] P.Ch. Chou and Pagano N. J. *Elasticity: tensor, dyadic and engineering approaches.* Dover, 1992.

[38] R. M. Christensen. *Mechanics of Composite Materials.* Krieger, 1979.

[39] A. S. Clarke and J. D. Wiley. Numerical simulation of the dense random packing of a binary mixture of hard spheres: Amorphous metals. *Physical Reviews B*, 35(14):7350–7357, 1987.

[40] N. A. C. Cressie. *Statistics for Spatial Data.* John Wiley and sons, 1993.

[41] M. W. Davidson and M. Abramowitz. Optical microscopy. Technical report, National High Magnetic Field Laboratory. The Florida State University. http://microscopy.fsu.edu/primer/opticalmicroscopy.html, 1999.

[42] C. G. Dávila and P. P. Camanho. Failure criteria for frp laminates in plane stress. Technical Memorandum TM-2003-212663, NASA, 2003.

[43] J.M.M. de Kok, H.E.H Meijier, and A.A.J.M Peijs. The influence of matrix plasticity on the failure strain of trasnversely loaded composite materials. In A. Miravete, editor, *Composites Behaviour, ICCM/9*. Woodhead Publishing, 1993.

[44] Department of defense - USA. *Composite Materials Handbook. Volume 2: Polymer matrix composites materials properties.*

[45] K. Dolinski and P. Colombi. Fatigue lifetime under stochastic loading with random overloading pulse trains. *Computer methods in applied mechanics and engineering*, 168:221–241, 1999.

[46] M. Dong and S. Schmauder. Modeling of metal matrix composites by a self-consistent embedded cell approach. *Acta mater.*, 44(6):2465–2478, 1996.

[47] W. J. Drugan and J. R. Willis. A micromechanics-based nonlocal constitutive equation and estimates of representative volume element size for elastic composites. *Journal of Mechanics and Physics of Solids*, 44(4):497–524, 1996.

[48] G. J. Dvorak and M. V. Srinivas. New estimates of overall properties of heterogeneous solids. *Journal of the Mechanics and Physics of Solids*, 47:899–920, 1999.

[49] D. M. Frangopol (ed.). Progress in probabilistic mechanics and structural reliability. *Computers & Structures*, 80(12):1025–1026, 2002.

[50] J. D. Eshelby. *Progress in Solid State Physics*, chapter The continuum theory of lattice defects. Academic, 1956.

[51] J. D. Eshelby. The determination of the elastic field of an ellipsoidal inclusion and related problems. *Proceeding of Royal Society, Series A*, (241):376–396, 1957.

[52] F. Feyel. A multilevel finite element method (FE^2) to describe the response of highly non-linear structures using generalizad continua. *Computer methods in applied mechanics and engineering*, 192:3233–3244, 2003.

[53] J. Fish and A. Ghouali. Multiscale analytical sensivity analysis for composite materials. *International Journal for Numerical Methods in Engineering*, 50:1501–1520, 2001.

[54] J. Fish, Q. Yu, and K. Shek. Computational damage mechanics for composite materials based on mathematical homogenization. *International Journal for Numerical Methods in Engineering*, 45:1657–1679, 1999.

[55] S. K. Gaggar and L.J. Broutman. Effect of matrix ductility and interface treatment on mechanical properties of glass-fiber composites. *Polymer Engineering Science*, 16:537–543, 1976.

[56] E. K. Gamstedt and Sjögren. Micromechanics in tension-compression fatigue of composite laminates containing transverse plies. *Composites Science and Technology*, 59:167–178, 1999.

[57] R. Garcia, J. Batlle, X. Cufí, and J. Amat. Positioning an underwater vehicle through image mosaicking. In *IEEE International Conference on Robotics and Automation (ICRA)*, volume 3, pages 2779–2784. IEEE, 2001.

[58] S. Ghosh, K. Lee, and S. Moorthy. Multiple scale analysis of heterogeneous elastic structures using homogenization theory and Voronoï cell finite element method. *Solids & Structures*, 32(1):27–62, 1995.

[59] S. Ghosh, K. Lee, and S. Moorthy. Two scale analysis of heterogeneous elastic-plastic materials with asymptotic homogenization and Voronoï cell finite element model. *Computer methods in applied mechanics and engineering*, 132:63–116, 1996.

[60] M. Grah, K. Alzebdeh, P. Y. Sheng, M. D. Vaudin, K. J. Bowman, and M. Ostoja-Starzewski. Brittle intergranular failure in 2D microstructures: Experiments and computer simulations. *Acta materialia*, 44(10):4003–4018, 1996.

[61] L. L. Graham and S. C. Baxter. Simulation of local material properties based on moving-window GMC. *Probabilistic Engineering Mechanics*, 16:295–305, 2001.

[62] M. Ostoja-Starzewski (guest editor). Statistical fracture mechanics - special issue. *Engineering Fracture Mechanics*, 57(2-3), 1997.

[63] M. Ostoja-Starzewski (guest editor). Statistical fracture mechanics - special issue. *Engineering Fracture Mechanics*, 58(5-6), 1997.

[64] A. A. Gusev. Representative volume element volume element size for elastic composites: A numerical study. *Journal of the Mechanics and Physics of Solids*, 45(9):1449–1459, 1997.

[65] J. C. Halpin and S. W. Tsai. Environmental factors in in composite materials design. Technical Report AFML TR 67-423, US Air Force, 1967.

[66] Z. Hashin. Failure criteria for unidirectional fiber composites. *Journal of Applied Mechanics*, 47:329–334, 1980.

[67] Z. Hashin. Analysis of composite materials - a survey. *Journal of Applied Mechanics*, 50:481–503, 1983.

[68] Z. Hashin and A. Rotem. A fatigue failure criterion for fiber reinforced materials. *Journal of Composite Materials*, 7:448–464, 1973.

[69] Z. Hashin and S. Shtrikman. A variational approach to the theory of the elastic behaviour of multiphase materials. *Journal of the Mechanics and Physics of Solids*, 11:127–140, 1963.

[70] S. Hazanov. Hill condition and overall properties of composites. *Archive of Applied Mechanics*, 68:385–394, 1998.

[71] D. He and N. N. Ekere. Structure simulation of concentrated suspensions of hard spehrical particles. *American Institute of Chemical Engineers Journal*, 47(1):53–59, 2001.

[72] D. He, N. N. Ekere, and L. Cai. Computer simulation of random packing of unequal particles. *Physical Review E*, 60(6):7098–7104, 1999.

[73] C. Henaff-Gardin, M.C. Lafarie-Frenot, and D. Gamby. Doubly periodic cracking in composite laminates part 1: General in-plane loading. *Composite Structures*, 36:113–130, 1996.

[74] R. Hill. Elastic properties of reinforced solids: Some theoretical principles. *Journal of the Mechanics and Physics of Solids*, 11:357–372, 1963.

[75] M. R. Holl, V. Kumar, J. L. Garbini, and W. R. Murray. Cell nucleation in solid-state polymeric foams: evidence of a triaxial tensile failure mechanism. *Journal of Materials Science*, 34:637–644, 1999.

[76] L. Huyse and M. A. Maes. Random field modeling of elastic properties using homogenization. *Journal of Engineering Mechanics*, 127(1):27–36, 2001.

[77] I. Jasiuk and M. Ostoja-Starzewski (eds.). Micromechanics of random media ii. *International Journal of Solids and Structures*, 35(19):2383–2570, 1998.

[78] J.C.Michel, H.Moulinec, and P.Suquet. Effective properties of composite materials with periodic microstructure: a computational approach. *Computer methods in applied mechanics and engineering*, 172:109–143, 1999.

[79] J.C.Michel, H.Moulinec, and P.Suquet. A computational scheme for linear and non-linear composites with arbitrary phase contrast. *International Journal for Numerical Methods in Engineering*, 52:139–160, 2001.

[80] D. Jeulin and M. Ostoja-Starzewski, editors. *Mechanics of random and multiscale microstructures*. Number 430 in CISM Courses and Lectures. Springer, 2001.

[81] M. Jiang, I. Jasiuk, and M. Ostoja-Starzewski. Apparent elastic and elastoplastic behavior of periodic composites. *International Journal of Solids and Structures*, 39:199–212, 2002.

[82] M. Jiang, M. Ostoja-Starzewski, and I. Jasiuk. Scale-dependent bounds on effective elastoplastic response of random composites. *Journal of the Mechanics and Physics of Solids*, 49:655–673, 2001.

[83] R. A. Johnson and D. W. Wichern. *Applied Multivariate Statistical Analysis*. Prentice-Hall International, 1992.

[84] L. L. Mishnaevsky Jr and S. Schmauder. Continuum mesomechanical finite element modeling in materials development: A state-of-the-art-review. *Applied Mechanics Reviews*, 54(1):49–74, 2001.

[85] M. Kamiński. Stochastic third-order hybrid stress-based finite element method. *Hybrid Methods in Engineering*, 3:25–51, 2001.

[86] M. Kamiński. On probabilistic fatigue models for composite materials. *International Journal of Fatigue*, 24:477–495, 2002.

[87] M. Kamiński and M. Kleiber. Numerical homogenization of n-component composites including stochastic interface defects. *International Journal for Numerical Methods in Engineering*, 47:1001–1027, 2000.

[88] T. Kanit, S. Forest, I. Galliet, V. Mounory, and D. Jeulin. Determination of the size of the representative volume element for random composites: statistical and numerical approach. *International Journal of Solids and Structures*, 40:3647–3679, 2003.

[89] M. Kleiber and T. D. Hien. *The Stochastic Finite Element Method*. John Wiley and sons, 1992.

[90] M. G. Knight, L. C. Wrobel, and J. L. Henshall. Micromechanical response of fibre-reinforced materials using the boundary element technique. *Composite Structures*, 62:341–352, 2003.

[91] L. P. Kollár and G. S. Springer. *Mechanics of Composite Structures*. Cambridge University Press, 2003.

[92] E. Kröner. *Statistical continuum mechanics*. Springer-Verlag, 1972.

[93] K. Lee and S. Ghosh. A microstructure based numerical method for constitutive modeling of composite and porous materials. *Materials Science and Engineering A*, 272:120–133, 1999.

[94] K. Lee, S. Moorthy, and S. Ghosh. Multiple scale computational model for damage in composite materials. *Computer methods in applied mechanics and engineering*, 172:175–201, 1999.

[95] J. W. Leggoe, A. A. Mammoli, M . B. Bush, and X. Z. Hu. Finite elment modelling of deformation in particulate reinforced metal matrix composites with random local microstructure variation. *Acta materialia*, 46(17):6075–6088, 1998.

[96] J. J. Lewandowski, C. Liu, and W. H. Hunt. Effects of matrix microstructure and particle distribution on fracture of an aluminum metal composite. *Material Science and Engineering A*, 107:241–255, 1989. nomes abstract.

[97] S. Li. Modeling of the characteristics of fiber-reinforced composite materials damaged by matrix-cracking. *Composites Science and Technology*, 43(2):185–195, 1992.

[98] S. Li. General unit cells for micromechanical analyses of unidirectional composites. *Composites Part A: Applied Science and Manufacturing*, 32:815–826, 2000.

[99] S. Li. Micromechanics. graduate course notes (ce236). Technical report, Department of Civil and Environmental Engineering. University of California at Berkeley, 2001.

[100] P.E. Magnusen, E. M. Dubensky, and D. A. Koss. The effect of void arrays on void linking during ductile fracture. *Acta Metallurgica*, 36(6):1503–1509, 1988.

[101] L. E. Malvern. *Introduction to the Mechanics of a Continuous Medium*. 1969, Prentice Hall.

[102] T. Matsuda, N. Ohno, H. Tanaka, and T. Shimizu. Effects of fibre distribution on elastic-viscoplastic behavior of long fibre-reinforced laminates. *Mechanical Sciences*, 45:1583–1598, 2003.

[103] F. L. Matthews and R. D. Rawlings. *Composite Materials: Engineering and Science*. Chapman & Hall, 1994.

[104] G. A. Maugin. *The Thermodinamics of Plasticity and Fracture*. Cambridge University Press, 1992.

[105] G. W. Milton. Bounds on the elastic and transport properties of two component composites. *Journal of the Mechanics and Physics of Solids*, 30(3):177–191, 1982.

[106] D. B. Miracle and S. L. Donaldson, editors. *Composites*, volume 1 of *Engineered Materials Handbook*. ASM International, 1987.

[107] O. Mohr. Welche umstande bedingen die elastizitatsgrenzeun den bruch eines materials? *Civilingenieur*, 44:1524–1530 and 1572–1577, 1900.

[108] D.C Montgomery. *Design and Analysis of Experiments*. John Wiley and sons, inc., 2001.

[109] S. Moorthy and S. Ghosh. Adaptativity and convergence in the Voronoi cell finite element model for analyzing heterogeneous materials. *Computer Methods in Applied Mechanics and Engineering*, 185:37–74, 2000.

[110] T. Mori and K. Tanaka. Average stress in matrix and average elastic energy of materials with misfitting inclusions. *Acta Metallurgica*, 21:571–574, 1973.

[111] S. Mucharreira de Azeredo Lopes. *Statistical Analysis of Particle Distributions in Composite Materials*. PhD thesis, University of Sheffield. Department of Probability and Statistics, 2000.

[112] J.A. Nairn. *Comprehensive Composite Materials*, volume 2, chapter Matrix microcracking in Composites, pages 403–432. 2001.

[113] S. Ogihara and N. Takeda. Interaction between transverse cracks and delamination during damage in cfrp cross-ply laminates. *Composites Science and Technology*, 54:395–404, 1995.

[114] J. Ohser and F. Mücklich. *Statistical Analysis of Microstructures in Materials Science*. Statistics in Practice. John Wiley and Sons, 2000.

[115] R. A. Olea. *Geostatistics for engineers and earth scientists*. Kluwer Academic Publishers, 1999.

[116] S. Oller, S. Botello, J. Miquel, and E. O nate. An anisotropic elastic model based on an isotropic formulation. *Engineering Computations*, 12:245–262, 1995.

[117] S. Oller, ate E. Oangle=270, J. Miquel, and S. Botello. A plastic damage model for composite materials. *International Journal of Solids and Structures*, 17:2501–2518, 1996.

[118] M. Ostoja-Starzewski. Random field models of heterogeneous materials. *International Journal of Solids and Structures*, 35(19):2429–2455, 1998.

[119] M. Ostoja-Starzewski. Microstructural disorder, mesoscale finite elements and macroscopic response. *Proceedings of the Royal Society of London*, 455:3189–3199, 1999.

[120] M. Ostoja-Starzewski. *Mechanics of random and multiscale microstructures*, chapter Mechanics of Random Materials: Stochastics, Scale Effects and Computation, pages 93–161. Number 430 in CISM Courses and Lectures. Springer, 2001.

[121] M. Ostoja-Starzewski. Microstructural randomness versus representative volume element in thermomechanics. *Journal of Applied Mechanics*, 69(1):25–35, 2002.

[122] M. Ostoja-Starzewski and I. Jasiuk (Eds.). Micromechanics of random media. *Applied Mechanics Reviews*, 47(1, Part 2), 1994.

[123] M. Ostoja-Starzewski, P.Y. Sheng, and K. Alzabdeh. Spring network models in elasticity and fracture of composites and polycrystals. *Computational Materials Science*, 7:82–93, 1996.

[124] M. Ostoja-Starzewski, P.Y. Sheng, and I. Jasiuk. Damage patterns and constitutive response of random matrix-inclusion composites. *Engineering Fracture Mechanics*, 58(5-6):581–606, 1997.

[125] M. Ostoja-Starzewski and X. Wang. Stochastic finite element as a bridge between random material microstructure and global response. *Computer methods in applied mechanics and engineering*, 168:35–49, 1999.

[126] F. Paris, E. Correa, and J. Cañas. Micromechanical view of failure of the matrix in fibrous composite materials. *Composites Science and Technology*, 63:1041–1052, 2003.

[127] S. L. Phoenix and I. J. Beyerlein. *Comprehensive Composite Materials*, volume 1, chapter Statistical Strength Theory for Fibrous Composite Materials, pages 559–639. 2001.

[128] P. Ponte Castañeda. Exact second-order estimates for the effective properties of nonlinear composite materials. *Journal of the Mechanics and Physics of Solids*, 44(6):827–862, 1996.

[129] G. L. Povirk. Incorporation of microstructural information into models of two-phase materials. *Acta Metalurgica et Materialia*, 43(8):3199–3206, 1995.

[130] A. Puck, J.Kopp, and M. Knops. Guidelines for the determination of the parameters in puck's action plane strength criterion. *Composites Science and Technology*, 62:371–378, 2002.

[131] A. Puck and H. Schürman. Failure analysis of FRP laminates by means of physically based phenomenological models. *Composites Science and Technology*, 58:1045–1067, 1998.

[132] R. Pyrz. Correlation of microstructure variability and local stress field in two-phase materials. *Materials Science and Engineering A*, 177:253–259, 1994.

[133] R. Pyrz. Quantitative descripition of the microstructure of composites. part 1: Morphology of unidirectional composite systems. *Composites Science and Technology*, 50:197–208, 1994.

[134] R. S. Raghava, R.M. Caddell, and G.S.Y. Yeh. The macroscopic yield behavior of polymers. *Journal of Material Science*, 8:225–232, 1973.

[135] B.D. Ripley. The second-order analysis of stationary point processes. *Journal of Applied Probability*, 13:255–266, 1976.

[136] C.P. Robert and G. Casella. *Monte Carlo Statistical Methods*. Springer, 1999.

[137] J.D. Rowatt and P.D. Spanos. Markov chain models for life prediction of composite laminates. *Structural Safety*, 20:117–135, 1998.

[138] J. Sanchez-Hubert and E. Sanchez-Palencia. *Introduction aux méthodes asymptotiques et à l'homogénéisation*. Masson, 1992.

[139] E. Sanchez-Palencia. *Homogenization Techniques for Composite Media*, chapter Boundary Layers and Edge Effects in Composites, pages 121–192. Springer Verlag, 1987.

[140] Z. Shan and A. M. Gokhale. Representative volume element for non-uniform microstructure. *Computational Materials Science*, 24:361–379, 2002.

[141] K. Sobczyk and D. J. Kirkner. *Stochastic Modeling of Microstructures*. Modeling and Simulation in Science, Engineering and Tecnology. Birkhäuser, 2001.

[142] B. Sudret and A. Der Kiureghian. Stochastic finite element methods and reliability: A state-of-the-art report. Technical Report UCB/SEMM-2000/08, Department of Civil Environmental Engineering. University of California, Berkeley, 2000.

[143] J. Summerscales, editor. *Microstructural characterisation of fibre-reinforced composites*. CRC Press - Woodhead Publishing Limited, 2000.

[144] P. Suquet. *Homogenization Techniques for Composite Media*, chapter Elements of homogenization for inelatic solid mechanics, pages 193–279. Springer-Verlag, 1987.

[145] N. Takeda. Characterization of microscopic damage in composite laminates and real-time monitoring by embedded optical fiber sensors. *International Journal of Fatigue*, 24:281–289, 2002.

[146] N. Takeda and S. Ogihara. In situ observation of microscopic failure processes in cfrp cross-ply laminates. *Composites Science and Technology*, 52(2):183–195, 1994.

[147] D.R.S. Talbot. Improved bounds for the effective properties of a nonlinear two-phase elastic composite. *Journal of the Mechanics and Physics of Solids*, 48(6-7):1285–1294, 2000.

[148] D.R.S. Talbot and J.R. Willis. Bounds of third order for the overall response of nonlinear composites. *Journal of the Mechanics and Physics of Solids*, 45(1):87–111, 1997.

[149] D.R.S. Talbot and J.R. Willis. Upper and lower bounds for the overall response of an elastoplastic composite. *Mechanics of Materials*, 28:1–8, 1998.

[150] K. Terada, M. Hori, T. Kyoya, and N. Kikuchi. Simulation of the multi-scale convergence in computational homogenization approaches. *International Journal of Solids and Structures*, 37:2285–2311, 2000.

[151] K. Terada and N. Kikuchi. A class of general algorithms for multi-scale analyses of heterogeneous media. *Computer methods in applied mechanics and engineering*, 190:5427–5464, 2001.

[152] S. Torquato. Effective stiffness tensor of composite media - i. exact series expansions. *Journal of the Mechanics and Physics of Solids*, 45(9):1421–1448, 1997.

[153] S. Torquato. Effective stiffness tensor of composite media - ii. applications to isotropic dispersions. *Journal of the Mechanics and Physics of Solids*, 46(8):1411–1440, 1998.

[154] S. Torquato, T.M. Truskett, and P. G. Debenedetti. Is random close packing of spheres well defined? *Physical Review Letters*, 84(10):2064–2067, 2000.

[155] E. VanMarcke. *Random fields: Analysis and Synthesis.* Massachusetts Institute of Technology, 1988.

[156] S.D. Wang and C. Yan. On composite homogenization theory. In Y. Zhang, editor, *ICCM- 13 International Conference on Composite Materials, Beijing*, 2001.

[157] M. Werwer, A. Cornec, and K. H. Schwalbe. Local strain fields and global plastic response of continuous fibre reinforced metal-matrix composites under transverse loading. *Computational Materials Science*, 12:124–136, 1998.

[158] J. R. Willis. *Lectures on mechanics of random media*, chapter Mechanics of random and multiscale microstructures, pages 221–267. Springer Verlag, 2001.

[159] S. Yang. Utility of microstructure modeling for simulation of micro-mechanical response of composites containing non-uniformly distributed fibres. *Acta Materialia*, 48:2307–2322, 2000.

[160] F. Zalamea. *Tratamiento numérico de Materiales Compuestos mediante la Teoría de Homogeneización.* PhD thesis, Departament de Resistència de materials i Estructures a l'Enginyeria. Universitat Politècnica de Catalunya, 2001.

[161] F. Zalamea, J. M. Canet, and S. Oller. A double scale method for simulating of periodic composite materials. In *European Congress on Computational Methods in Applied Sciences and Engineering, Barcelona CD-ROM*, 2000.

[162] J. Zeman. *Analysis of Mechanical Properties of Fiber-reinforced Composites with Random Microstructure*. Ms. c. thesis, Czech Technical University, 1999.

[163] J. Zeman and M. Sejnoha. Numerical evaluation of effective elastic properties of graphite fibre tow impregnated by polymer matrix. *Journal of the Mechanics and Physics of Solids*, 49(1):69–90, 2001.

[164] O. C. Zienkiewicz and R. L. Taylor. *The Finite Element Method - Volume 1: The Basis*. Butterworth-Heinemann, 2000.